# An Anisotropic Diffusion Model for Brain Tumour Spread

*by*

Amanda Swan

*A thesis submitted in partial fulfillment of the requirements*

*for the degree of*

Doctor of Philosophy

*in*

Applied Mathematics

Department of Mathematical and Statistical Sciences

University of Alberta

# *Abstract*

Gliomas, tumours arising from the glial cells of the nervous system, are some of the most difficult tumours to treat. In particular, glioblastoma are a particularly aggressive glioma subtype carrying a life expectancy of only 14 months. Typically, treatment combines surgery, radiation and chemotherapy where a key component of treatment planning is determining an appropriate treatment region over which to administer radiation therapy. Because gliomas are diffuse, only the main tumour mass shows up using imaging, while many undetectable cancer cells infiltrate the surrounding brain tissue. To account for this, treatment regions typically extend the visible tumour mass by a uniform 2 $c$m margin. We propose that a mathematical model for glioma cell density could help by modelling the spread of cancer cells and contribute to treatment plans that target the largest densities of these undetectable cells.

In this thesis, we focus on the Painter-Hillen model for glioma spread, which uses anisotropic diffusion, allowing the rate of spread of the cells to vary with direction. This is meant to simulate the biological phenomenon where cancer cells spread preferentially along the fibrous white matter tracts within the brain, resulting in tumours having irregular shapes and projections. We establish the utility of this model by implementing it using data from ten patients, in both two and three dimensions. For comparison, a previous

isotropic glioma model, the Swanson model, is used, as it has been applied successfully in a clinical setting. The results of our simulations indicate that the inclusion of anisotropy offers an advantage over the previous model.

Finally, we develop two extensions to the Painter-Hillen model. In Chapter 6, we explore the derivation of a "mass effect" model, using a multiphase model framework. The mass effect model includes the forces induced by the growing mass, introducing a mechanical component to the model. This effect becomes important where a tumour is growing in close proximity to the skull, where the growth in this direction will be impeded by the pressure generated by the increased density. In Chapter 7, we discuss an extension of the Painter-Hillen model, using a transport model framework. The generalization considered allows the turning rate to vary with the direction that a cell is travelling in relation to the underlying structure, since a cell travelling along a fibre will turn less frequently than one travelling perpendicularly. Both of these model extensions have potential for further exploration.

*"First thing we'd climb a tree,*
*and maybe then we'd talk,*
*or sit silently,*
*and listen to our thoughts.*
*With illusions of someday,*
*cast in a golden light,*
*no dress rehearsal,*
*this is our life."*

- Gordon Downie

# *Acknowledgements*

I would like to take this opportunity to thank everyone who has helped me along the way in completing this work.

Firstly, I'd like to thank my supervisors Thomas Hillen and John Bowman for their guidance during the last five years. I would also like to thank the members of our Mathematical Biology Journal Club, who provided valuable feedback and ideas throughout the past five years.

I would also like to thank Albert Murtha for providing access to patient data for our simulations. Being able to apply the model to real patient data really set our work apart and gave it more weight amongst the medical community. Additionally, I would like to thank Russ Greiner, Bret Hoehn and Tatitana Ivanova for their assistance in data processing.

I would like to acknowledge that this work was financially supported by an NSERC CGS D3 award, as well as an Alberta Innovated Technology Futures Graduate Student Scholarship.

Finally, I would like to thank my husband Mark for supporting me throughout the past five years.

# Contents

**1 Introduction** **1**

1.1 Biological Background . . . . . 4

1.1.1 Gliomas . . . . . 4

1.1.2 Anisotropic Diffusion . . . . . 8

1.1.3 Diffusion Tensors . . . . . 12

1.1.4 Magnetic Resonance Imaging . . . . . 14

1.1.5 Diffusion Tensor Imaging . . . . . 23

1.2 Current Landscape . . . . . 27

1.2.1 Standard Treatment Protocol . . . . . 27

1.2.2 The Role of Mathematics . . . . . 29

1.2.3 Established Work . . . . . 32

1.3 Outline . . . . . 39

1.4 Chapter Summary . . . . . 41

**2 A Model for Brain Tumour Spread Using Anisotropic Diffusion** **43**

2.1 Transport Model . . . . . 44

2.1.1 Parabolic Scaling . . . . . 46

2.1.2 Boundary Conditions . . . . . 53

2.2 Defining the Turning Distribution . . . . . 54
2.3 Computing the Second Moment of the von Mises Distribution 59
2.3.1 Two-Dimensional Case . . . . . 60
2.3.2 Three-Dimensional Case . . . . . 68
2.3.3 Limiting Behaviour . . . . . 73
2.4 Classification of the PDE Model . . . . . 76
2.5 Chapter Summary . . . . . 79

**3 Simulations on a Simplified Domain 83**
3.1 One-dimensional Simulations . . . . . 83
3.1.1 Stability of Numerical Method . . . . . 86
3.2 Two-dimensional Simulations . . . . . 88
3.2.1 Numerical Methods . . . . . 89
3.2.2 Simulations on a Simplified Domain . . . . . 94
3.3 Three-dimensional Simulations . . . . . 98
3.3.1 Numerical Methods . . . . . 98
3.3.2 Simulations on a Simplified Domain . . . . . 107
3.4 Chapter Summary . . . . . 112

**4 Implementation on a Real Brain 115**
4.1 Data Processing . . . . . 116
4.2 Metric of Model Performance . . . . . 118
4.3 Obtaining the Cancer Cell Diffusion Tensors . . . . . 121
4.4 Initial Condition
and Growth/Diffusion Rates . . . . . 124
4.5 Parameter Estimation . . . . . 127
4.6 Stopping Criteria . . . . . 131

4.7 Implementing Homogeneous Neumann Boundary Conditions . . . . . 133
4.8 Chapter Summary . . . . . 137

**5 Model Comparison Using Patient Data 139**
5.1 Swanson Model Implementation . . . . . 141
5.1.1 Two-dimensional Numerical Scheme . . . . . 143
5.1.2 Three-dimensional Numerical Scheme . . . . . 145
5.2 Two-Dimensional Results . . . . . 146
5.2.1 Summary of Two-dimensional Results . . . . . 152
5.2.2 Interpretation of Two-dimensional Results . . . . . 152
5.3 Three-dimensional Results . . . . . 155
5.3.1 Summary of Three-dimensional Results . . . . . 161
5.3.2 Interpretation of Three-dimensional Results . . . . . 162
5.4 Reflected-DTI . . . . . 163
5.4.1 Two-dimensional Reflected DTI Results . . . . . 166
5.4.2 Summary of Two-dimensional Reflected DTI Results . 169
5.4.3 Interpretation of Two-dimensional Reflected DTI Results 169
5.4.4 Three-dimensional Reflected DTI Results . . . . . 170
5.4.5 Summary of Three-dimensional Reflected DTI Results 174
5.4.6 Interpretation of Three-dimensional Reflected DTI Results 174
5.5 Treatment Regions . . . . . 175
5.6 Chapter Summary . . . . . 177

**6 The Mass Effect 181**
6.1 Scientific Background . . . . . 182
6.2 Introduction to Continuum Mechanics . . . . . 183

6.2.1 Matter as a Continuum . . . . . 184
6.2.2 Stress Tensors . . . . . 187
6.3 The Multiphase Framework . . . . . 190
6.3.1 Mass Conservation . . . . . 190
6.3.2 Momentum Conservation . . . . . 192
6.3.3 Closing the System . . . . . 195
6.4 Numerical Methods . . . . . 197
6.5 Specifying the Model . . . . . 199
6.5.1 Non-Aggressive Model . . . . . 200
6.5.2 Non-Aggressive Model Results . . . . . 202
6.5.3 Aggressive-Invasion Model . . . . . 204
6.5.4 Aggressive-Invasion Model Results . . . . . 207
6.6 Chapter Summary . . . . . 209

**7 Model with Direction-dependent Turning Rate 211**
7.1 Transport Model Set-up . . . . . 211
7.2 Parabolic Scaling . . . . . 215
7.2.1 Limiting Case: Constant Turning Rate . . . . . 224
7.3 Chapter Summary . . . . . 225

**8 Conclusions 227**
8.1 Discussion . . . . . 227
8.2 Mathematical Challenges . . . . . 229
8.3 Limitations and Extensions . . . . . 230

# List of Tables

1.1 Tumour Grading . . . . . 7
1.2 Previous Work . . . . . 38

4.1 Model Parameters . . . . . 130

5.1 2D Results . . . . . 153
5.2 3D Results . . . . . 161
5.3 2D Reflected Domain Results . . . . . 169
5.4 3D Reflected Domain Results . . . . . 174

# List of Figures


1.1 Glioblastoma . . . . . 6
1.2 Cell Motility . . . . . 10
1.3 Isotropic and Anisotropic Diffusion . . . . . 11
1.4 Diffusion Ellipsoids and Peanuts . . . . . 15
1.5 Axial, Sagittal and Coronal Planes . . . . . 16
1.6 MRI Machine . . . . . 18
1.7 Net Magnetization Vector . . . . . 20
1.8 DTI vs. MRI . . . . . 26
1.9 GTV, CTV and PTV . . . . . 30

2.1 Scalings . . . . . 46
2.2 von Mises Distribution . . . . . 57
2.3 Fisher Distribution . . . . . 58
2.4 Limiting Behaviour . . . . . 77

3.1 1D Diffusion Coefficient . . . . . 86
3.2 1D Solutions . . . . . 87
3.3 Boundary Conditions . . . . . 95
3.4 2D Fibre Domain . . . . . 97
3.5 2D Simple Domain Results . . . . . 99

3.6 3D Fibre Domain . . . . . 109
3.7 3D Simple Domain Results . . . . . 110
3.8 3D Simple Domain Results Slices . . . . . 111

4.1 Segmentation and Skull Stripping . . . . . 118
4.2 Jaccard Index . . . . . 120
4.3 Sample Initial Condition . . . . . 125
4.4 $\alpha$ and $\gamma$ on a Brain Domain . . . . . 128
4.5 $D_{11}$, $D_{22}$ and $D_{33}$ on a Brain Domain . . . . . 129
4.6 Sample Parameter Space . . . . . 132
4.7 Stopping Criteria . . . . . 134
4.8 Boundary Conditions for Convex Domain . . . . . 135

5.1 10 Patient Segmentations . . . . . 140
5.2 Defining the White Matter . . . . . 142
5.3 2D Patient 1 . . . . . 147
5.4 2D Patient 2 . . . . . 148
5.5 2D Patient 3 . . . . . 148
5.6 2D Patient 4 . . . . . 149
5.7 2D Patient 5 . . . . . 149
5.8 2D Patient 6 . . . . . 150
5.9 2D Patient 7 . . . . . 150
5.10 2D Patient 8 . . . . . 151
5.11 2D Patient 9 . . . . . 151
5.12 2D Patient 10 . . . . . 152
5.13 3D Patient 1 . . . . . 156
5.14 3D Patient 2 . . . . . 156
5.15 3D Patient 3 . . . . . 157

5.16 3D Patient 4 . . . . . 157
5.17 3D Patient 5 . . . . . 158
5.18 3D Patient 6 . . . . . 158
5.19 3D Patient 7 . . . . . 159
5.20 3D Patient 8 . . . . . 159
5.21 3D Patient 9 . . . . . 160
5.22 3D Patient 10 . . . . . 160
5.23 Sample Tumour-Free Slices . . . . . 164
5.24 Reflected Segmentations . . . . . 165
5.25 2D Patient 2 Reflected DTI . . . . . 166
5.26 2D Patient 3 Reflected DTI . . . . . 167
5.27 2D Patient 5 Reflected DTI . . . . . 167
5.28 2D Patient 6 Reflected DTI . . . . . 168
5.29 2D Patient 9 Reflected DTI . . . . . 168
5.30 3D Patient 2 Reflected DTI . . . . . 171
5.31 3D Patient 3 Reflected DTI . . . . . 172
5.32 3D Patient 5 Reflected DTI . . . . . 172
5.33 3D Patient 6 Reflected DTI . . . . . 173
5.34 3D Patient 9 Reflected DTI . . . . . 173
5.35 GTV, CTV and PTV . . . . . 176
5.36 Treatment Region Recommendations . . . . . 178

6.1 Subvolume Sequence . . . . . 185
6.2 Constituent Density Limit . . . . . 186
6.3 3D Stress Tensor . . . . . 189
6.4 Non-Aggressive Model Results . . . . . 203
6.5 Aggressive-Invasion Results . . . . . 208

# Abbreviations

| | |
|---|---|
| **DTI** | **D**iffusion **T**ensor **I**maging |
| **MRI** | **M**agnetic **R**esonance **I**maging |
| **ECN** | **E**xtra **C**ellular **N**etwork |
| **ECM** | **E**xtra **C**ellular **M**atrix |
| **GBM** | **G**lio**B**lastoma **M**ultiforme |
| **CNS** | **C**entral **N**ervous **S**ystem |
| **CSF** | **C**erebro**S**pinal **F**luid |
| **PDE** | **P**artial **D**ifferential **E**quation |
| **FA** | **F**ractional **A**nisotropy |
| **CT** | **C**omputed **T**omography |
| **GTV** | **G**ross **T**umour **V**olume |
| **CTV** | **C**linical **T**arget **V**olume |
| **PTV** | **P**lanning **T**arget **V**olume |

# Chapter 1

# Introduction

Cancer is a growing problem of our modern world, as average life expectancies grow. As a result, the need for new solutions and improved treatment methods is ever increasing. With the vast number of genetic and environmental causes, as well as the different organs that can be affected, it has become generally accepted that cancer is not one disease. In fact, it is recognized that there are more than 100 distinct types of disease. Additionally, different types of tumours can even be found within the same organ among different patients [1]. Unfortunately, this heterogeneity makes treatment difficult. Cancer treatments typically include a combination of surgery, radiotherapy, and chemotherapy. While improvements are being made in the treatment of some cancers, the prognosis for others remains poor. For example, stage lV breast cancer has a five year survival rate of 22 % [2], the most common type of prostate cancer has a five year survival of nearly 100 % [3], while glioblastoma (an aggressive brain cancer), on which we focus here, carries a five year survival rate of only 6 % [4].

With such a grim outlook, there remains much room for improvement in

the treatment of gliomas. Many scientists focus on understanding the genetic alterations that cause these tumours to grow, and this certainly offers the potential for developing new therapeutic targets. However, in this work, we focus more on the mesoscopic (cell-level) properties of glioma cells. We will extend the work of Painter and Hillen [5], where a mathematical model was derived describing how a glioma mass grows, based on the characteristics of the individual cells and their movement. The main idea behind the Painter-Hillen model [5] is that the cells use the fibre structure of the brain to advise their movement, and this information is incorporated into a mathematical model to mimic how the cells move. The purpose of such a model is to predict the cancer cell density at each location within a patient's brain. This information can give clinicians an additional tool in treatment planning for radiotherapy. Gliomas are known to be very diffuse in nature, with some cells spreading far from the primary tumour mass. Standard imaging modalities such as Magnetic Resonance Imaging (MRI) and Computed Tomography (CT) are only able to detect the bulk tumour mass, however it is known that the cancer cells have invaded well beyond this boundary. As such, clinicians treat outside the tumour, usually in a uniform 2 $c$m extension beyond what is radiologically visible. The goal of the Painter-Hillen model [5] then is to indicate where more invasion has occured, and where less invasion has occurred, so that the tissue containing the highest concentration of cancer cells more intensively, while the potential damage to healthy tissue can be reduced.

Many attempts at modelling glioma have been made, and the models are becoming more detailed with every iteration. The pioneering paper for this field of modelling was Swanson et al. [6]. They developed a model for glioma spread based on a diffusion model, incorporating the spatial homogeneity of the brain in the form of grey and white matter. Subsequent modelling attempts

have been made by groups such as Jbabdi et al. [7], Clatz et al. [8], Konukoglu et al. [9], Hogea et al. [10], Bondiau et al. [11], Mosayebi et al. [12], Painter and Hillen [5], and Engwer et al. [13]. These models have worked to incorporate more and more of the biological details, and will be discussed in more depth later in this Chapter. As a whole, the aim of all of these modelling attempts is to develop models to be clinically useful and to improve treatment outcomes.

The main focus of this thesis will be the application of the Painter-Hillen model to real patient data. We will use it to simulate tumours using data from patients, and compare the simulated tumours to the actual tumour boundaries. We will compare these results to those of simulations from the Swanson model, showing that the Painter-Hillen model offers improvement. The Painter-Hillen model will then be used to show how treatment regions can be determined, and to demonstrate expected regrowth following treatment.

As an aside to this exploration, we develop a generalization of the Painter-Hillen model using a similar transport equation framework. This model is based on the idea that cells moving in the brain do not turn with a constant rate, but rather with a rate that depends on the direction they are travelling relative to the fibres of the brain. While this particular model will not be applied further in this thesis, it offers the potential for future development.

Additionally, we will derive a second extension to the original Painter-Hillen model incorporating mechanical properties of the tissue. While the Painter-Hillen model extends earlier models by incorporating information about the brain's fibre network, it does not account for pressure generated by the growing tumour mass. In the final chapters, we consider how this effect may be included using a continuum mechanical framework. This work as a whole is highly interdisciplinary, with collaborators from computer science, radiation oncology, and physics.

In the remainder of this chapter, we will discuss some of the biological ideas behind mathematical models of glioma in more detail. Specifically, in Section 1.1.1 we will describe both the origin and treatment of gliomas. In Sections 1.1.2 and 1.1.3 we will introduce the idea of anisotropic diffusion and the mathematical objects we use to quantify it. We will then outline some important imaging modalities that play an important role in the diagnosis and treatment of gliomas in Sections 1.1.4 and 1.1.5. Finally, in Sections 1.2.1-1.2.3 we will describe the current treatment protocol for gliomas as well as the current field of established work in the mathematical modelling of gliomas.

## 1.1 Biological Background

### 1.1.1 Gliomas

In order to understand the terminology describing the various tumours that can arise in the brain and nervous system, it is important to first be familiar with the different cells from which these neoplasms arise [14]. In this work, we focus on gliomas, and typically we will focus on an aggressive subtype of glioma, Glioblastoma Multiforme, or GBM. Gliomas are so named because they arise from the glial cells of the central nervous system. Glial cells are those cells that surround the nerve cells, providing the support necessary for proper functioning. There are three types of glial cell of particular importance: astrocytes, oligodendrocytes, and ependymal cells [14].

Astrocytes are the most numerous of the glial cells, and provide essential nutrients and support to the nerve cells, as well as maintaining the extracellular environment [15]. Following anaplastic transformation, astrocytes may develop into either astrocytomas, or to primary GBMs. In the case where low

grade astrocytomas develop, these will typically progress to (secondary) GBMs eventually [14]. Secondary GBMs tend to occur in those under 45, and make up only about 10 % of all GBMs. The other 90 % occur as primary tumours, without progressing slowly from lower grade lesions [16]. Oligodendrocytes make up the myelin sheath surrounding the axons of the neurons, serving to both protect the axon, and improve the signal transmission. Oligodendrocytes may develop into oligodendrogliomas [15]. Finally, ependymal cells form the lining of the regions of the central nervous system (CNS) that contain cerebrospinal fluid (CSF). These cells, when mutated, can lead to ependyomas, or subependyomas [15].

GBMs are the most aggressive, most deadly, and most difficult to treat of the different types of gliomas. Figure 2.1 shows both a macroscopic (left) and microscopic (right) view of a GBM from a 57-year old woman. The yellow areas in the macroscopic view represent necrotic tissue, whereas the grey areas are active tumour tissue. The microscopic view displays the heterogeneous nature of these tumours, even on a fine spatial scale.

In determining a treatment plan for such tumours, histological grading is a valuable tool used by diagnosticians [17]. A tumour's grade classification reveals how malignant the cells are, and roughly correlates to the prognosis. This process is usually done by taking a tissue sample and observing the microscopic properties of the cells.

Cancer cells are classified as grades I through IV, with IV denoting the most invasive, and most frequently lethal neoplasms [17]. A grade I tumour is defined as having "low proliferative potential", and is often cured through surgical removal alone [17]. Grade II refers to tumours that show low proliferative activity, however are more infiltrative than grade I. These tumours will tend to recur, and some will progress to grades III or IV malignancies.

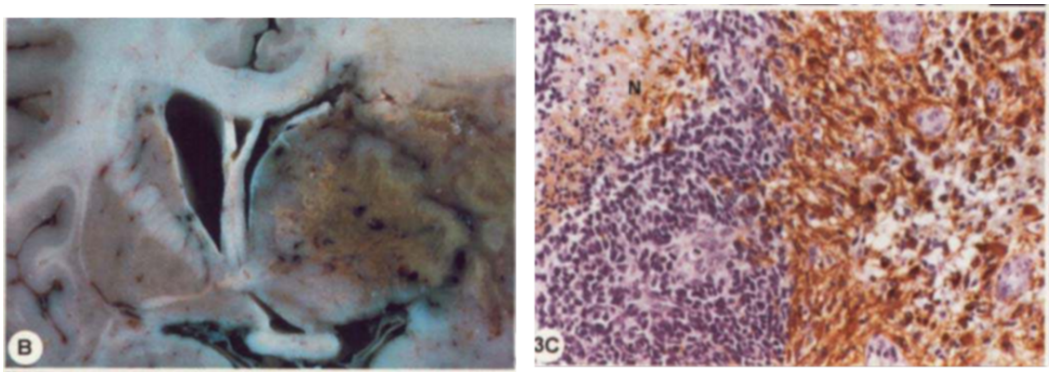


Figure 1.1: Glioblastoma. Macroscopic (left) and microscopic (right) images of a GBM from a 57-year old woman. These images are taken from Figure 3 in Kleihues et al. [14], where we have taken two of the original four panels. The yellow tissue in the macroscopic image shows necrosis, while the grey tissue is active tumour tissue. The microscopic image shows the heterogeneity of this type of tumour even on a very fine spatial scale. It can be seen that some cells maintain a certain degree of differentiation, while others do not.

Grade III tumours show a higher degree of malignancy than grade II, displaying "nuclear atypia and brisk mitotic activity" [17]. These tumours would receive more aggressive treatment, typically incorporating radiotherapy and chemotherapy in addition to surgical resection. Grade IV refers to the highest degree of malignancy, and the most lethal disease. These cells are "cytologically malignant, mitotically active, necrosis-prone" and generally result in the highest rate of recurrence [17]. The various types of gliomas, as well as their respective grades are displayed in Table 1.1. Note that oligoastrocytic tumours are "mixed" tumours, containing abnormal cells of both astrocytic and oligodendrocytic origin [16]. Of particular interest here will be the highest grade, rapidly growing tumours of astrocytic origin: glioblastoma, giant cell glioblastoma and gliosarcoma. Giant cell glioblastoma is a variant of GBM containing giant cells, having many nuclei each [18]. It displays similar characteristic to standard GBM, however does tend to occur in younger patients, having a

median age of onset of 51 years compared to the standard 61 years. It is relatively rare, accounting for between 2 % and 5 % of all GBMs [18]. Gliosarcoma is also a relatively rare subtype of GBM containing cells of glial origin, but also arising from the connective tissue (sarcoma) [19]. It too displays similar characteristics of growth and survival to a standard GBM [19].

| **Astrocytic Tumours** | **Grade** |
|---|---|
| Subependymal giant cell astrocytoma | 1 |
| Pilocytic astrocytoma | 1 |
| Pilomyxoid astrocytoma | 2 |
| Diffuse astrocytoma | 2 |
| Pleomorphic xanthoastrocytoma | 2 |
| Anaplastic astrocytoma | 3 |
| Glioblastoma | 4 |
| Giant cell glioblastoma | 4 |
| Gliosarcoma | 4 |
| **Oligodendroglial Tumours** | **Grade** |
| Oligodendroglioma | 2 |
| Anaplastic Oligodendroglioma | 3 |
| **Oligoastrocytic Tumours** | **Grade** |
| Oligoastrocytoma | 2 |
| Anaplastic Oligoastrocytoma | 3 |
| **Ependymal Tumours** | **Grade** |
| Subependymoma | 1 |
| Myxopapillary ependymoma | 1 |
| Ependymoma | 2 |
| Anaplastic ependymoma | 3 |

Table 1.1: Summary of glioma types and their respective histological grade. Modified from Louis et al. [17].

A discussion of gliomas wouldn't be complete without acknowledging the heterogeneity of the cell types within a particular tumour. In the discussion of the mathematical models, we will refer only to "glioma cells", or "cancer cells", however this is an oversimplification. Not all glioma cells are created

equal, with the recent discovery of glioma stem cells giving researchers valuable information about a particularly important cell subtype. Cancer Stem Cells, or CSCs exhibit characteristics common to normal tissue stem cells. In particular, they are capable of regenerating a tumour [20]. In addition, they are of great importance therapeutically as it is the CSCs that exhibit the greatest resistance to therapy, and pose the biggest challenge to clinicians treating cancer [20].

### 1.1.2 Anisotropic Diffusion

Mathematical modelling using Partial Differential Equations (PDE's) uses relationships between the rates of change in time and space to describe a variable, in this case, cancer cell density. In developing these relationships, it is important to understand the underlying biological mechanisms.

First and foremost, as with any cancer cells, cell division plays an important role [1, 21]. This means that even without cell motility, a tumour will grow in size as the number of cells increases. The second mechanism that we consider in depth, is what we refer to as anisotropic diffusion. The mathematics behind this phenomena will be discussed in detail in the next section, hence we focus here on the biological implications.

The process of diffusion refers to a series of random movements of molecules in a fluid, resulting in a net expansion that will be approximately uniform [22]. This is referred to as isotropic spread. For example, diffusion is the dominant mechanism behind the spreading of a drop of food colouring in water. It is inherently slow, and depends on the microscopic movements of the water molecules. While the path of each individual particle will certainly not be uniform, the average of the motion of all the particles will resemble uniform

spread.

Of course, this type of spread is probably too simplistic for the spread of cancer cells in a heterogeneous medium such as the human brain. The brain is made up of two main types of matter: white matter, and grey matter. White matter has a fibrous structure, consisting of the myelinated axons along which nerve cells send signals and relatively few cell bodies. Conversely, grey matter consists of the glial cells and nerve cell bodies, with a relatively low concentration of both myelinated and unmyelinated axons. This difference in composition causes white matter to appear white, and grey matter to appear grey or yellow/pink [23, 24]. There is a growing body of evidence to indicate that cancer cells will actually use the fibrous white matter tracts to migrate, leading to spread that is decidedly *not* uniform [15, 25, 26]. Figure 1.2 shows a diagram of this invasion. While this figure shows glioma cells travelling not only along the white matter tracts, but also along the blood vessels, for our purposes we focus on the former mechanism. It is this mechanism of spread that can be approximated using Diffusion Tensor Imaging (DTI), as will be discussed in the next subsection.

The tendency of cancer cells to follow white matter tracts results in an apparent increased rate of spread along the direction aligned with the tract. Mathematically, we model this by assigning a higher rate of spread in this direction than in the perpendicular directions. The relative difference in rates depends on where the cell is located within the brain, and can actually be measured, as is discussed in the next subsection. A simple example is illustrated in Figure 1.3. Notice in particular that while isotropic spread leads to a radially symmetric distribution, for anisotropic spread, an ellipsoid shape results.

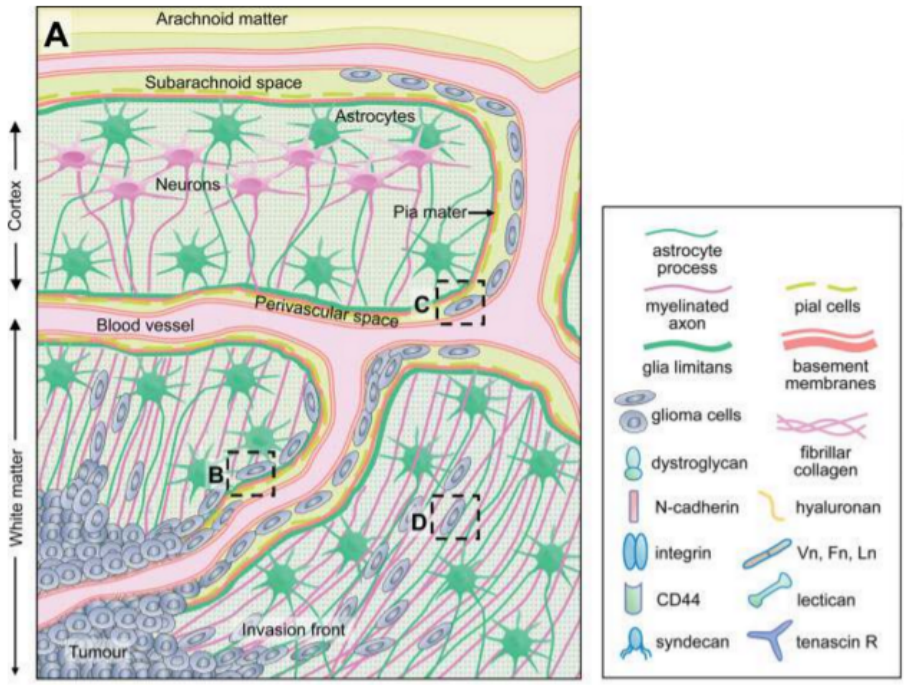


Figure 1.2: Cell Motility. Representation of how glioma cells move along white matter fibres in the brain. Image is modified from Gritsenko et al. [26] where it appears as Figure 2.

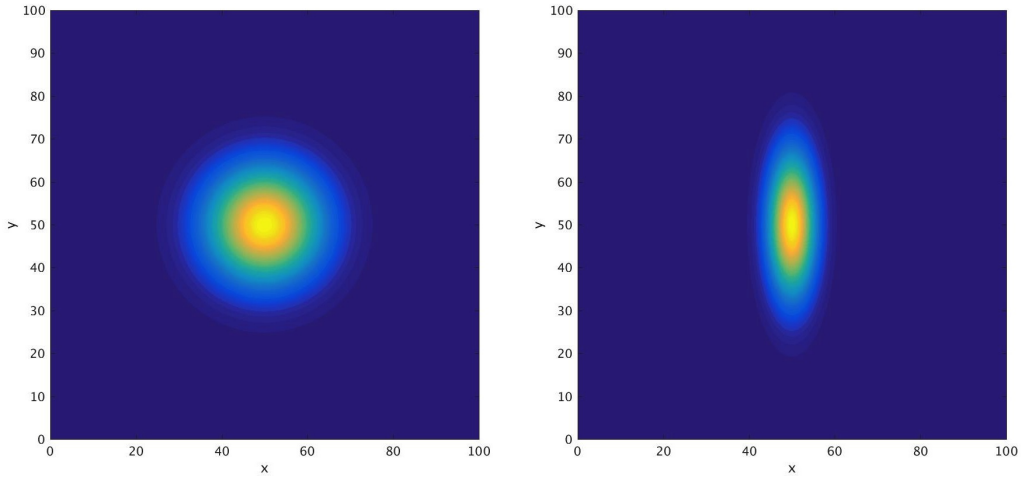


Figure 1.3: Isotropic and Anisotropic Diffusion. Isotropic (left) and anisotropic (right) spread as simulated using Equation 1.1 in MatLab. The blue regions represent low particle density, while the yellow areas represent high particle density. The simulation was started in the centre of the distribution. The key thing to notice is that for isotropic spread, the particles distribute themselves radially symmetrically. For anisotropic spread, the particles spread out in an ellipse shape, with more spread occurring along the y axis, which was assigned a higher rate of spread.

### 1.1.3 Diffusion Tensors

In order to implement anisotropic diffusion in a mathematical model, we need to have some information about the actual rates of spread within the brain. Fortunately, the invention of Diffusion Tensor Imaging, or DTI, helps us to estimate these biological parameters.

To understand DTI, it is first important to understand the diffusion tensor. The brain is a three-dimensional object, and so at each location within the brain, we must define the rates of spread in three dimensions. A scalar quantity could do this if the rates in all directions were equal (isotropic). However, in order to define a direction-dependent (anisotropic) rate of spread, we use a second-order tensor, or a matrix. The entries in a diffusion tensor represent the relative rates of spread in different directions.

The easiest way to interpret a tensor is through the principal directions, and corresponding principal values. These are mathematically equivalent to the eigenvectors and eigenvalues of a matrix. We can use two geometrical representations of the diffusion tensor to better visualize the information contained therein. We first consider these objects in the context of the standard Fickian diffusion equation [5, 27, 28]

$$u_t = \nabla \cdot (D \nabla u)\,, \tag{1.1}$$

where $u$ represents some quantity, i.e., cell density in the context of cancer spread, and $D \in \mathbb{R}^{n \times n}$ is a given symmetric and positive definite matrix. This equation has the fundamental solution

$$u(\boldsymbol{x}, t) = C \exp\left(-\frac{1}{4t} \boldsymbol{x}^T D^{-1} \boldsymbol{x}\right),$$

where $C$ is a normalization coefficient, assuming the random walkers were released at time $t = 0$ from $\boldsymbol{x} = \mathbf{0}$. Then $u(\boldsymbol{x}, t)$ gives the probability of finding a random walker at location $\boldsymbol{x}$ at time $t$. Considering vectors $\boldsymbol{v} \in \mathbb{R}^n$, the level sets of $\boldsymbol{v}^T D^{-1} \boldsymbol{v}$ thus give sets of equal probability in the shape of an ellipsoid, referred to as the **diffusion ellipsoid** [5, 28]. The diffusion ellipsoid associated with positive real number $c$ is given by the set

$$\mathcal{E}_c := \{\boldsymbol{v} \in \mathbb{R}^3 : \boldsymbol{v}^T D^{-1} \theta = c\}. \tag{1.2}$$

Because these ellipsoids will be geometrically similar for any value of $c$, it is often chosen to be 1 for convenience [28]. For tensors in their diagonal form, the ellipsoid can be represented via the principal values $\{\lambda_1, \lambda_2, \lambda_3\}$ of the tensor:

$$\mathcal{E}_1 = \left\{ \boldsymbol{v} \in \mathbb{R}^3 : \left(\frac{v_1}{\sqrt{\lambda_1}}\right)^2 + \left(\frac{v_2}{\sqrt{\lambda_2}}\right)^2 + \left(\frac{v_3}{\sqrt{\lambda_3}}\right)^2 = 1 \right\}.$$

We see that for this case, the diffusion ellipsoid will have semiaxes aligned with the principal directions, whose lengths will be proportional to the square roots of the eigenvalues [27, 28]. In fact, this is true for all diffusion ellipsoids, not just those arising from diagonal tensors [22, 27].

The diffusion tensor can also be visualized via the **diffusion peanut**. The diffusion peanut is obtained by plotting the apparent diffusion coefficient (ADC), given by the map [5, 29]

$$\theta \mapsto ADC_\theta := \theta^T D \theta. \tag{1.3}$$

Peanuts will have their axis aligned in the direction of highest diffusivity, and

will be pinched in directions having lower diffusivity [5]. As an example, we consider two diagonal diffusion tensors, $D_1$ and $D_2$, given by

$$D_1 = \begin{bmatrix} 5 & 0 & 0 \\ 0 & 3 & 0 \\ 0 & 0 & 1 \end{bmatrix}, \qquad D_2 = \begin{bmatrix} 8 & 0 & 0 \\ 0 & 1 & 0 \\ 0 & 0 & 0.2 \end{bmatrix}. \tag{1.4}$$

The resulting ellipsoids and peanuts, as determined via Equations 1.2 and 1.3 respectively, are shown in Figure 1.4. Note that $D_1$ produces an oblate ellipsoid and peanut that is pinched in one direction, while $D_2$ produces a prolate ellipsoid and a peanut pinched in two directions. Note that for the special case of an isotropic tensor, i.e., three equal principal values, both the diffusion ellipsoid and the diffusion peanut will be spherical.

### 1.1.4 Magnetic Resonance Imaging

To understand the physical process of DTI, we first discuss Magnetic Resonance Imaging, or MRI. This imaging modality is based upon applying strong magnetic fields to a tissue in order to obtain a magnetic signal. It offers a safety advantage over techniques such as X-ray computed tomography (CT) scanning, in that no ionizing radiation is used. CT imaging uses radiation of a high enough energy to ionize the atoms in the tissue, creating the possibility of chemical changes to the cells and/or DNA of the patient. While there are risks associated with applying a strong magnetic field to a patient as well, MRI is generally considered to be safer than CT, and is capable of obtaining clearer images [30]. In our discussion of MRI, we will often refer to the three planes of the body: transverse (or axial), sagittal, and coronal. These three planes are shown in Figure 1.5.

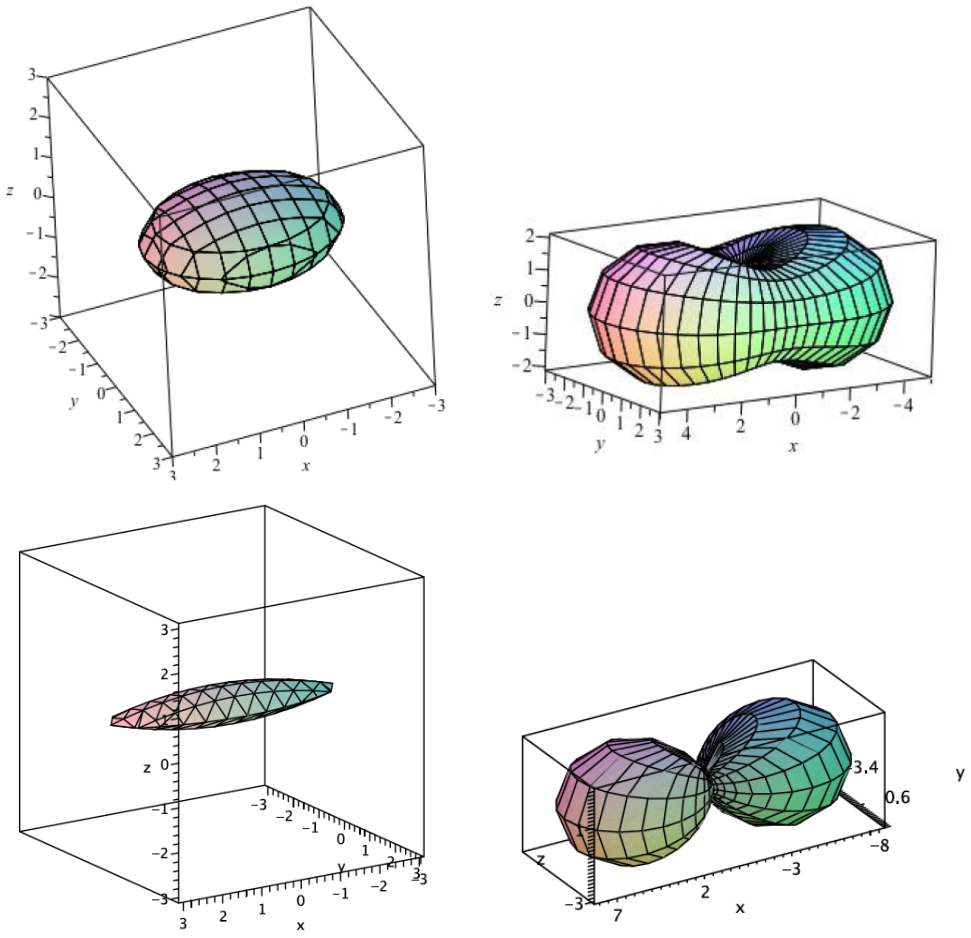

Figure 1.4: Diffusion Ellipsoids and Peanuts. The diffusion ellipsoid (left) and diffusion peanut (right) corresponding to $D_1$ (top), and $D_2$ (bottom). Note that $D_1$ produces a oblate ellipsoid while $D_2$ produces an prolate ellipsoid.

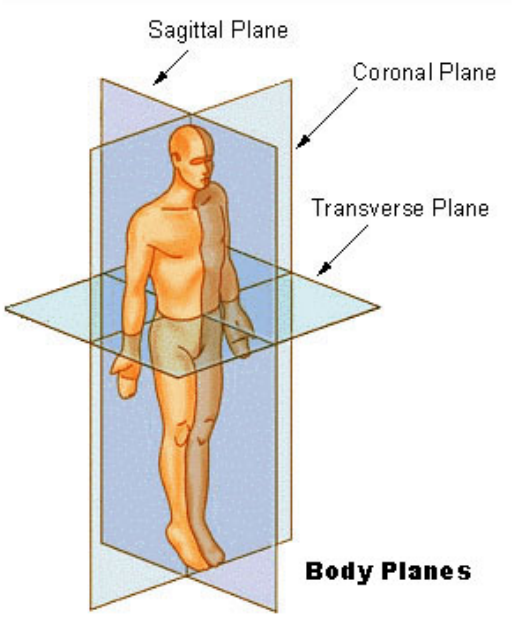


Figure 1.5: Axial, Sagittal and Coronal Planes. The three different planes of the body: Transverse (or Axial), Sagittal and Coronal. Image taken from Wikipedia [31].

An MRI machine is a large piece of equipment consisting of a large tube, called the bore, running through the main magnet. A table extends out from the bore, on which a patient will lie and subsequently be slid inside the bore [32]. MRI machines induce huge magnetic fields, on the order of 0.5–3.0 Tesla. A Tesla is a unit of magnetic field strength equal to 10 000 Gauss. For reference, the earth's magnetic field is around 0.5 Gauss, or $5 \times 10^{-5}$ Tesla [32]. In order to induce this huge magnetic field, typically superconducting magnets are used. A coil is wrapped around a cylinder (or bore) and electricity is run through the coil. Due to the natural resistance of the coil, obtaining large magnetic fields through this method alone is extremely expensive. To remedy this, the coil is submerged in liquid helium at about –269 degrees celsius. This reduces the resistance in the coil to almost 0, allowing for larger magnetic fields to be created with less electricity [32]. This main magnet serves to create a uniform, magnetic field along the axis of the cylinder, which by convention is taken to be along the $z$ axis: [30, 33]

$$B_z = B_0,$$

where $\boldsymbol{B} = (B_x, B_y, B_z)$.

An example of an MRI machine is shown in Figure 1.6. Visible in this image are the table that the patient lies on, the bore through which the table slides for imaging, and the casing containing the superconducting magnet, as well as the radio frequency coils and gradiant magnets (discussed below).

The principle behind MRI is the magnetic moment of hydrogen atoms. The body contains many hydrogen atoms, for example in water and fat molecules [33], making this element an ideal imaging target. Each hydrogen nucleus has its own magnetic moment, because it is spinning and positively charged


Figure 1.6: MRI Machine. Image of a Philips MRI machine. Visible in the image are the table which the patient lies on, the bore through which the table moves for imaging, and the casing containing the magnets. Image taken from [34].

[30]. Due to the random arrangement of these atoms in normal tissue, these tiny magnetic fields usually cancel each other out on average. When an external magnetic field is introduced, however, the magnetic moments of the nuclei will rotate, or precess, about an axis parallel to the magnetic field [30]. The frequency is termed the Larmor frequency, $\omega$, and is proportional to the magnitude of the external magnetic field strength:

$$\omega = \gamma B,$$

where $\gamma$ is the nuclear magnetogyric ratio, and has a value of $2.67 \times 10^8$ Trad/s for the hydrogen nucleus [30, 33]. While their axes of precession will be aligned with the direction of the magnetic field, the nuclei could be rotating counterclockwise about the magnetic field direction (spin-up), or clockwise (spin-down). While the magnetic moments of a spin-up and spin-down pair will cancel, the numbers of each will not be exactly equal, creating a net magnetic moment, represented by the net magnetization vector $\boldsymbol{M}$. The reason for this is energy. Both spin-up and spin-down states are quantum mechanically stable, however the spin-down state requires slightly more energy to achieve, thus more nuclei will end up in the spin-up state than the spin-down [30].

The term "resonance" then refers to the fact that the precessing hydrogen nuclei will only absorb energy in the same frequency as the Larmor frequency. For the magnitudes of magnetic fields used in MRI, this frequency falls within the radio frequency (RF) range of the electromagnetic spectrum [30]. When this energy is absorbed, the effect is that the net magnetization vector $\boldsymbol{M}$ will move towards the $xy$ plane. This is due to the absorption of energy causing nuclei to switch to the spin-down state from spin-up [30]. The phases of the precessing nuclei will also sync up, creating a component of the net

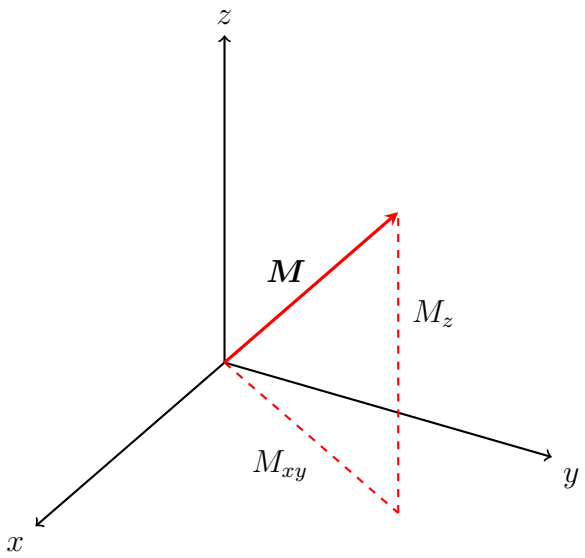


Figure 1.7: Net Magnetization Vector. Figure showing the net magnetization vector $\boldsymbol{M}$, as well as its components.

magnetization vector in the $xy$ plane that will precess about the $z$ axis at the Larmor frequency. This vector as well as the two relevant components are shown in Figure 1.7.

Ultimately, MRI images are created by measuring the signal in the transverse plane to the applied external magnetic field. The signal is measured by RF coils, which also consist of wires wrapped around the central bore. RF coils consist of receiver coils, which receive the signal, and transmission coils, which transmit the RF pulse necessary for tilting the $M$ vector. Images are obtained by measuring the signals emitted following the administration of the RF pulse.

Signals can be measured transversely ($M_{xy}$), or longitudinally ($M_z$), producing different types of images [30]. These are described as follows:

**T1-Relaxation**

We first consider the measurement of the $M_z$ component of the net magnetic moment of a tissue. We assume that initially, $M = M_z$, since the precessions will be out of phase and so $M_{xy} = 0$ initially. Because applying an RF pulse causes the orientation of the $M$ vector to change, the tissue will return to its equilibrium following the administration of the pulse. In doing so, the $M$ vector will return to its original position [30]. Assuming that a 90 degree RF pulse is administered (i.e. so that $M_z$=0 immediately following the pulse), the magnitude of the $M_z$ component will follow an exponential function:

$$M_z = M_0 \left[1 - \exp\left(-\frac{1}{T_1}\right)\right].$$

Upon fitting this function to the $M_z$ relaxation, termed longitudinal relaxation, a characteristic $T_1$ value can be obtained. This $T_1$ value will be different for different tissues [30].

**T2-Relaxation**

T2-relaxation, or transverse relaxation, is caused by a slightly different phenomenon. Following the administration of the RF pulse, all nuclei spins will be in phase, and $M_{xy}$ will be at a maximum. As time passes, each nuclei will return to their own phase dictated by their local environment, and the vector sum of their magnetic moments will return to 0 [30]. This magnitude can be modelled by a decaying exponential:

$$M_{xy} = M_0 \left[\exp\left(-\frac{t}{T_2}\right)\right].$$

Again, different tissues will possess different characteristic $T_2$ values, allowing for distinction between them. While these signals can be measured, the question remains: How do we match a signal to a specific location within a

patient?

Spatial localization is achieved via the application of gradient magnetic fields. In addition to the RF coils, there are gradient magnets that serve to create a non-uniform magnetic field. These are much weaker than the main magnet, having strengths varying between 180-270 Gauss, or 18-27 $m$T [32]. MRI machines have three sets of these gradient coils, one in the $x$, one in the $y$ and one in the $z$ direction. As such, these gradients can be applied in any direction [30]. For example, if a linear gradient field is applied in the $x$ direction, the magnetic field will be

$$B_z(x) = B_{z0} + G_x x,$$

with corresponding Larmor frequency

$$\omega_x = \omega_0 + \gamma G_x x,$$

with $\omega_0$ the Larmor frequency associated with the superconducting magnet field [33]. It is important to note that the direction of the magnetic field remains in the $z$ direction, with only the magnitude following a gradient. Applying a gradient magnetic field in the $z$-direction will cause each location in $z$ to precess with a different frequency. Applying an RF pulse in a small range of frequencies (the bandwidth) will then select an axial slice of appropriate thickness since only the nuclei precessing with the associated frequencies will experience resonance. As such, the slice selection gradient is applied at the same time as the RF pulse [30]. The signal is further localized to the $x$ or $y$ direction using frequency encoding. Another gradient is applied in either the $x$ or $y$ direction, applied at the time of signal measurement (after the slice

selection gradient) [30]. The final direction is localized using phase encoding. This involves applying a gradient perpendicular to that used for both slice selection and frequency encoding, applied after the RF pulse but before the frequency encoding gradient [30]. The result is that when the signal is measured, it may be broken down using a two-dimensional Fourier Analysis into components corresponding to particular phases and frequencies, each of which can be mapped back to a specific location. When the signal strengths are plotted at the appropriate locations, an MRI image is obtained.

### 1.1.5 Diffusion Tensor Imaging

While an understanding of anisotropic diffusion tensors is a crucial element in the modelling of brain tumour spread, it is also important to be able to estimate the values of these parameters within the brain. Fortunately, the technology used in obtaining MRI images can be extended to measure the rates of diffusion of water molecules within the brain. This method is referred to as Diffusion Tensor Imaging, or DTI [35].

DTI works by measuring the diffusion of water molecules in the brain [36]. This diffusion is a naturally occurring phenomenon, and is unaffected by the magnetic field employed in MRI [37]. In the case of fibrous structures such as white matter tracts in the brain, the movement of water molecules along the fibres is relatively unimpeded, while movement perpendicular to the fibres is much more difficult. As such, DTI can be used to determine the presence of white matter tracts [35, 36]. Since the hydrogen nuclei upon which the magnetic fields of MRI work are contained within the diffusing water molecules, the same technology can be used to obtain images. Typically for DTI imaging, a baseline image is obtained without a magnetic gradient, so that a signal loss

may be measured relative to this baseline image. When a magnetic gradient pulse is applied in a particular direction, the phase of precession for the nuclei vary with respect to that direction. When the reverse gradient pulse is applied a short time later, a nuclei that hasn't moved will return to its original phase. Nuclei that have diffused, however, will be slightly out of phase, resulting in a signal loss in that direction [35, 38]. The strength of these pulses are characterized by a coefficient $b$, describing the size of the magnetic field of the pulse [37].

DTI only measures diffusion in the direction of the applied gradient, thus in order to determine the full three-dimensional diffusion tensor, gradients must be applied in at least six directions, corresponding to the six degrees of freedom of the symmetric tensor [36, 38]. It is generally better to apply a gradient in more directions, to obtain a sharper image [38]. DTI offers the ability to obtain information that was not available before the mid-1990's, and in a manner that is non-invasive [36].

The attentive reader may notice that DTI actually measures the diffusion of water molecules. We are, of course, interested in modelling the spread of cancer cells. There have been several methods proposed for converting the water diffusion tensors to cancer cell diffusion tensors, and the process that we use will be described in detail in the next chapter. For now, suffice to say that we choose a scaling that preserves the dominant diffusion direction (the principal direction associated with the largest principal value), as well as the relative anisotropy. These assumptions are based on the fact that for both water and cancer cell diffusion tensors, we expect the dominant direction of diffusion to align with the underlying fibre structure of the brain.

Before concluding our discussion of anisotropic diffusion tensors, let us define an index that will play a big role in the implementation of our model in

later chapters. It is useful to be able to quantify the degree of anisotropy of a given tensor using a single index, referred to in general as a diffusion anisotropy index. While there are different options available for such an index, here we will use the Fractional Anisotropy, or FA [39]. This is the most common choice. It ranges between 0, corresponding to fully isotropic diffusion, and 1, fully anisotropic diffusion [39]. The formulas for $\mathrm{FA}_2$ in two dimensions and $\mathrm{FA}_3$ three dimensions are

$$\mathrm{FA}_2 = \sqrt{\frac{2[(\lambda_1 - D_{\mathrm{av}})^2 + (\lambda_2 - D_{\mathrm{av}})^2]}{\lambda_1^2 + \lambda_2^2}}, \tag{1.5}$$

$$\mathrm{FA}_3 = \sqrt{\frac{3[(\lambda_1 - D_{\mathrm{av}})^2 + (\lambda_2 - D_{\mathrm{av}})^2 + (\lambda_3 - D_{\mathrm{av}})^2]}{2(\lambda_1^2 + \lambda_2^2 + \lambda_3^2)}}, \tag{1.6}$$

where $\lambda_1, \lambda_2$ and $\lambda_3$ are the principal values of a given tensor $D$, in descending order, and $D_{\mathrm{av}} = \mathrm{Tr}\{D\}/2$ for the 2D case, and $D_{\mathrm{av}} = \mathrm{Tr}\{D\}/3$ for the 3D case [39]. Note that for the isotropic case, $D_{\mathrm{av}} = \lambda_1 = \lambda_2 = \lambda_3$ and FA=0. For the fully anisotropic case, FA=1 , the diffusion tensor is singular and only one eigenvalue is non-zero. Other diffusion anisotropy indices include the scaled relative anisotropy (sRA), the volume fraction (VF), or volume ratio (VR), and the lattice Index ($LI_N$) [39]. It has been shown however, that all of these diffusion anisotropy indices give qualitatively similar results when comparing different tensors [39].

Figure 1.8 shows a sample FA variation for an axial brain slice, as well as standard T1-weighted and T2-weighted MRI scans. The dominant diffusive direction, and principal values are also displayed.

We are fortunate enough to have access to the DTI data of actual patients; many of the previous models have been developed without the use of such data.

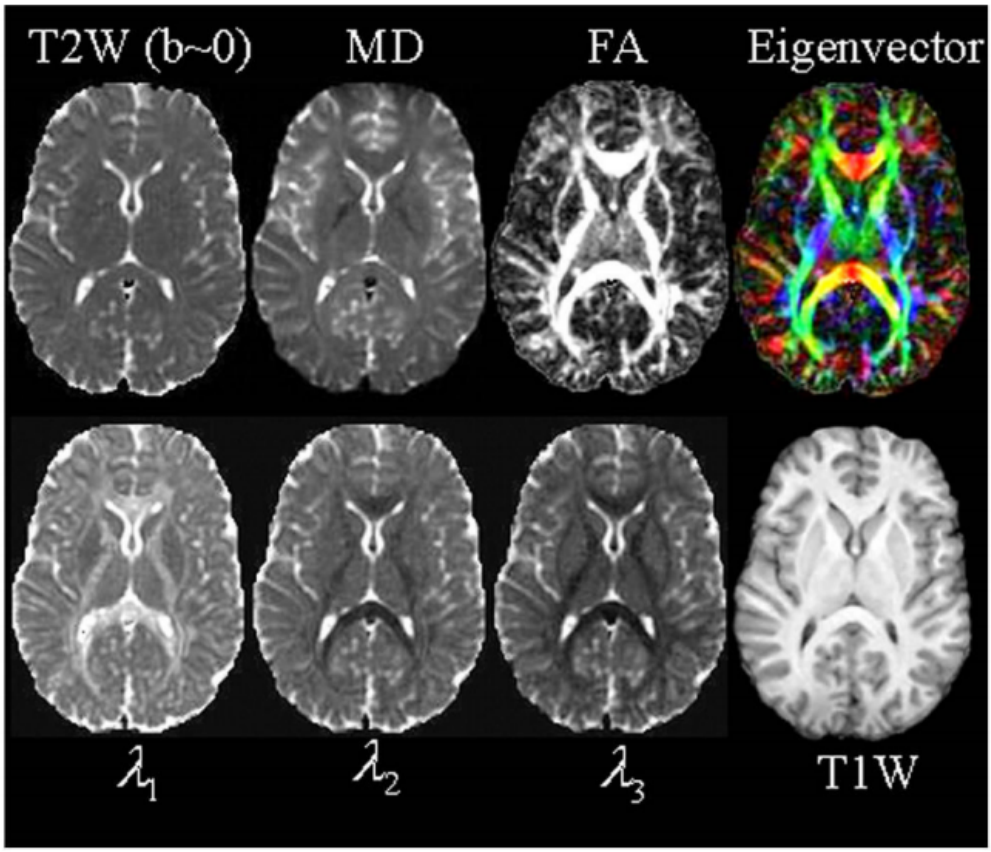


Figure 1.8: DTI vs. MRI. A summary of DTI compared to standard MRI imaging. Taken from [35], where it appears as Figure 4. A spatial map is shown of (from top left) a T2-weighted image, the mean diffusivity, the FA, the principal direction (with direction indicated by colour), the three principal values, in descending order, and a T1-weighted MRI image.

In these instances, researchers typically use what is referred to as **Atlas** data. This is data that is made publicly available, and is usually not specific to one patient. Often, it is built up as the average of many scans from many patients. While patient specific data is considered much better for model validation, it is often difficult to gain access to. Atlas data provides a reasonable alternative in these circumstances.

## 1.2 Current Landscape

### 1.2.1 Standard Treatment Protocol

Current treatment for gliomas is patient specific, and depends on the individual characteristics of their tumour. The preferred first approach would be surgical resection, where as much of the bulk of the tumour is removed as is possible and safe. In many cases, due to the delicate nature of brain tissue, as well as proximity to critical structures, surgical resection is virtually impossible. In these cases, only a biopsy is taken for diagnostic and grading purposes [40]. When brain surgery is possible, it typically takes one of two forms: craniotomy, or intraoperative brain mapping. A craniotomy involves removing a piece of the skull in order to access the brain for surgery. The bone piece is replaced following surgery [41]. Intraoperative brain mapping is a type of brain surgery where the patient is awake, allowing the neurosurgeon to electrically stimulate certain regions of the brain and determine their exact function. This is often done for glioma that may be considered inoperable due to their proximity to critical brain structures, as well as in cases where the tumour boundaries are not well defined. This technique is used in an attempt to maintain brain function following surgery [41]. In addition to improving

survival prognosis, surgery is also often useful in relieving patient symptoms, since removing tumour tissue reduces the intracranial pressure [41].

In addition to surgery, or in some cases instead of, patients will often receive adjuvant therapy. Adjuvant therapy includes both radiotherapy and chemotherapy. Three types of radiation therapy are typically employed to treat these tumours: internal radiation with the GliaSite radiation therapy system, external beam radiation therapy, and stereotactic radiosurgery [41]. Internal radiation is delivered to the hole left following the surgical removal of a tumour via catheter in the form of liquid radiation. In this type of therapy, a radioactive liquid is delivered for several days, and then the catheter is removed [41]. External beam radiotherapy is the modality which this thesis will primarily focus on. It involves the delivery of radiation to the brain from outside of the body via a linear accelerator. A patient would typically receive treatment once per day, five days per week [41]. External beam radiotherapy can be administered to the tumour as well as the surrounding region, or to the entire brain. Additionally, the level of radiation delivered to different regions can be tailored [42]. A discussion of how these treatment regions are defined will be included in the following section. Stereotactic radiosurgery involves a more precise delivery of higher doses of radiation to the tumour, while sparing the surrounding tissue. This is achieved by delivering the radiation from many different directions, resulting in a higher total dose [41].

It is also standard for glioma patients to receive chemotherapy, usually temozolomide [43]. Bevacizumab, an antiangiogenic agent has also recently been approved for use in glioma therapy [43]. These chemotherapeutic agents are typically administered following surgery and radiotherapy [41].

### 1.2.2 The Role of Mathematics

The main challenge in treating gliomas is the fact that a significant portion of the tumour is "invisible" from a clinician's perspective. If it were possible to better determine where the cancer cells had invaded the most, then treatment could be better targeted to areas where the greatest number of malignant cells could be killed. As mentioned earlier, modelling the "cancer cell" density is an oversimplification, as a tumour is really a heterogeneous mass containing different cell subtypes, however, for the time being we do not consider individual subpopulations and focus only on the density of cancer cells.

As a result of the microscopic invasion by cancer cells of the surrounding brain tissue, the treatment region typically involves a uniform 2$c$m extension of the visible glioma mass [12]. This process is shown in Figure 1.9. In the figure, several regions that are typically used for radiation treatment are outlined. The GTV, or Gross Tumour Volume corresponds to the visible tumour mass as it appears on a scan. The CTV, or Clinical Target Volume is a uniform 1.5 $c$m extension. The PTV or Planning Target Volume accounts for any uncertainties in the delivery of the prescribed dose, extending 0.5 $c$m further than the CTV, for a total of 2 $c$m. While using a uniform extension of the GTV is a good starting point, the anisotropic nature of glioma spread means that cancer cells will have invaded further in some directions than in others, meaning that it may be more beneficial in terms of both survival and quality of life to treat further in some directions, and not as far in others. This is where mathematical models offer the potential to help.

Through simulating the growth of a tumour, we can predict cell density levels in regions that cannot be seen on a scan. As such, an accurate mathematical model can help clinicians to determine a better therapeutic region

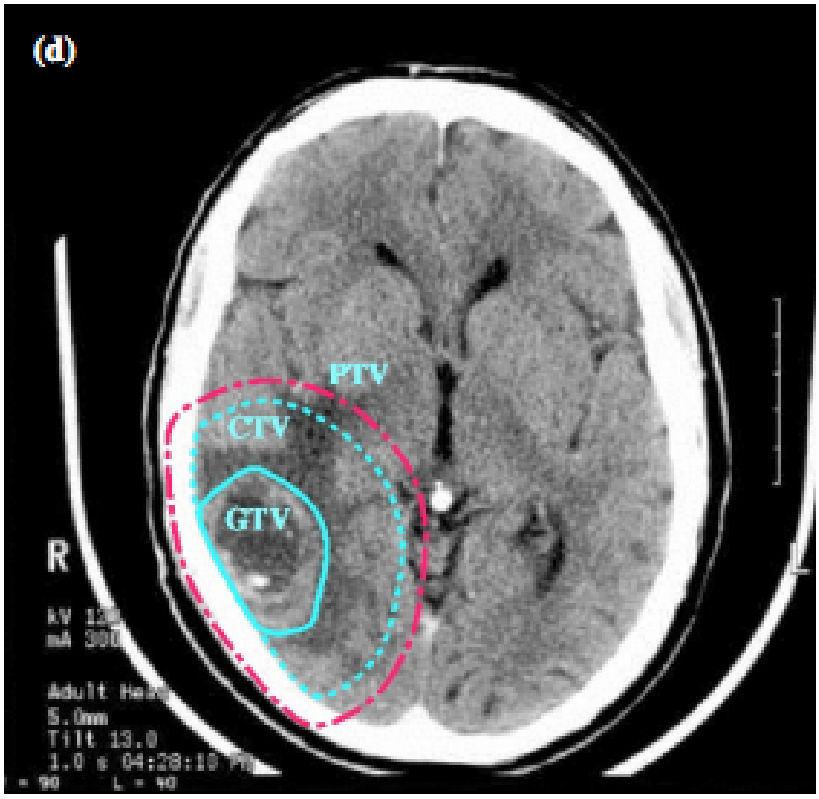


Figure 1.9: GTV, CTV and PTV. The various treatment volumes for a glioma patient. The GTV, or Gross Tumour Volume, indicates the bulk of the tumour as can be seen on a scan. The CTV, or Clinical Target Volume represents the uniform 2$cm$ extension that is typically chosen for treatment, and the PTV, or Planning Target Volume is a slight extension of this allowing for uncertainties in delivering the radiation dose. This image is modified from Burnet et al. [42], where is appears as Figure 4.

than what could be estimated based on scans alone. There are several groups who have had success with using mathematical models in a clinical setting.

In particular, Swanson's group at the Mayo Clinic in Phoenix, Arizona has developed several methods for applying mathematical models for diagnosis and treatment. In Wang et al. [44], in 2009, the group looked at quantitative measures for proliferation and invasion rates for individual patients, and how to connect these to a prognosis. A therapeutic response index was also proposed, using their model to simulate regrowth without treatment, and comparing the results to the actual growth after treatment. This allows for the effectiveness of a given treatment to be quantified. In 2010, in Rockne et al. [45], Swanson's group used these results coupled with a model for cell-killing by radiation to predict response to external beam radiotherapy on a patient-specific basis, with a high degree of accuracy. Clinicians can then use this information to help design treatment plans for individual patients. This work was further developed in Neal et al. in 2013 [46].

In a different vein, Anderson and Chaplain [47] developed both a discrete and a continuous model for angiogenesis. The process of angiogenesis describes the formation of new blood vessels, and while this process is a normal part of embryogenesis or wound healing, tumours produce chemical signals that induce angiogenesis for their own benefit [47]. This irregular network of vessels surrounding a tumour can make treatment more challenging as it can be difficult to predict the chemotherapeutic dose that the tumour receives. McDougall et al. [48], along with Anderson and Chaplain, coupled the original angiogenesis model with models for fluid flow in order to predict the amount of fluid that would reach a tumour.

In this work, we describe a model based on cell growth and anisotropic diffusion. Of course, in a real biological system, there is far more than these two

factors at play. Additional properties such as cell adhesion and vasculature could affect the tumour growth, however we focus only on the most significant mechanisms here. The goal of biological modelling using mathematics is to capture the most important aspects of the biology, without producing a convoluted, complicated model. Usually these models are built up from simple models, with new aspects being added at each model iteration [49]. This will be discussed in the established work section.

### 1.2.3 Established Work

In describing the previous work, we will make several distinctions between the models. The first distinction will be whether or not the model uses diffusion tensors (anisotropic), or just a coefficient (isotropic). In addition to the diffusion rates, the diffusion operator itself is important. Most of the models below use a standard "Fickian" diffusion, based on Fick's first law. We briefly mentioned this in the discussion of diffusion tensors, where Fickian diffusion obeys the following PDE:

$$u_t + \nabla \cdot J = 0,$$

with $J$ the classical Fickian diffusion $J = -D\nabla u$ [49], driven by the gradient of the density function ($u(\boldsymbol{x}, t)$). For the classic Fick's law, $D$ is a scalar diffusion coefficient. The diffusion model of this form then follows

$$u_t = \nabla \cdot (D\nabla u). \tag{1.7}$$

Fick's law can also be extended for anisotropic diffusion. If $D$ is a symmetric positive-definite tensor of diffusion coefficients, then the flux is still

$J = -D\nabla u$, and the diffusion model is

$$u_t = \nabla \cdot (D\nabla u) = \sum_{i=1}^{n} \sum_{j=1}^{n} \frac{\partial}{\partial x_i} \left( D_{ij} \frac{\partial u}{\partial x_j} \right). \tag{1.8}$$

Alternatively, we will talk about a "Fully Anisotropic" diffusion operator, so named because it contains the classic Fickian diffusion operator as well as an additional advection term. This operator will be derived from a transport equation model in Chapter 2, and obeys the following PDE:

$$u_t = \nabla\nabla : (Du) = \sum_{i=1}^{n} \sum_{j=1}^{n} \frac{\partial}{\partial x_i} \frac{\partial}{\partial x_j} (D_{ij} u), \tag{1.9}$$

where $n$ is the dimension of the model (2 or 3), and : is used to denote the contraction of two tensors. This will be defined more precisely in Chapter 2. The big difference between these two operators is that while only one derivative is applied to $D$ in Fickian diffusion as in Equation (1.8), in fully anisotropic diffusion, both derivatives are applied to $D$. In fact, the Fickian diffusion operator is contained in the fully anisotropic diffusion operator, as well as an additional advection term. Specifically, Equation (1.9) can be expanded via the product rule to

$$u_t = \nabla \cdot (D\nabla u) + \nabla \cdot ((\nabla^T D)u).$$

Most of the models for glioma spread include, in addition to diffusion and advection, cell division in the form of a growth term. The growth term is usually of one of the following three types [5, 6, 50]:

$$\textbf{Exponential:} \quad u_t + \nabla \cdot J = ru,$$

where $r$ is the growth rate, or a logistic growth as given by

$$\textbf{Logistic:} \quad u_t + \nabla \cdot J = ru\left(1 - \frac{u}{K}\right),$$

or

$$\textbf{Gompertz:} \quad u_t + \nabla \cdot J = r \ln\left(\frac{K}{u}\right) u,$$

where $K$ gives the carrying capacity for both logistic and Gompertz growth.

The first diffusion model for brain tumour spread was developed in 2000 by Swanson et al. [6]. This model was groundbreaking as it was the first effort that had been made to use mathematical models to predict glioma growth. While this model included both cell growth and diffusion, it incorporated a spatially varying diffusion coefficient with no anisotropy, and was termed the Proliferation-Infiltration (P.I.) model. The growth was modelled using an exponential function. This work made the distinction between white and grey matter, setting the diffusion coefficient to be 5 times higher in the white matter vs. the grey matter, as per available data [6]. The PDE used in the Swanson P.I. model is

$$u_t = \nabla \cdot (D\nabla u) + ru, \tag{1.10}$$

where $D$ is the diffusion coefficient, $r$ is the growth rate and $u(\boldsymbol{x}, t)$ is the cancer cell density. Initially, this work was only theoretical, however Swanson's group went on to lead the way in applying mathematical models to glioma treatment planning. They have made great strides in terms of applying their models in a personalized medicine framework, incorporating diffusion, growth and even treatment simulations [6, 44–46, 49, 51–54] . Because of this work, much of the foundation has been laid when it comes to translating the mathematical modelling of glioma into actual clinical treatment plans [53, 54].

Swanson's work was extended in Jbabdi et al. [7], where they incorporated anisotropy into the glioma growth model, replacing the diffusion coefficient with a tensor. This work represented a significant step forward, incorporating anisotropy into the original PI model. The anisotropic glioma growth model was used to simulate brain tumour spread using a DTI scan of a healthy individual, and the results were compared to the shapes of real segmented tumours. A parameter was also introduced to scale the water diffusion tensors, in an attempt to better simulate the spread of cancer cells.

Glioma modelling was moved along further in 2005 by Clatz et al. [8], who developed the first derivation of a mass effect. They modelled growth and infiltration using the P.I. model with the addition of diffusion tensors as per Jbabdi et al. [7]. The mass effect equation was derived via a momentum equation, considering all of the sources of momentum and requiring their conservation. Clatz et al. simulated tumour growth using atlas data, and the validity of their model was established by comparing the simulation result to the actual growth of a patient's tumour over a period of six months.

Hogea et al. [10] proposed another model in 2008, that included both growth and infiltration, as well as a mass effect. Here, the cell density is modelled using a reaction-diffusion-advection equation, given by

$$u_t = \nabla \cdot (D\nabla u) - \nabla \cdot (u\mathbf{v}) + r(u), \tag{1.11}$$

where once again, $u(\boldsymbol{x}, t)$ represents the space and time-dependent cancer cell density. The first term on the right hand side is the standard Fickian diffusion operator with a diffusion tensor, the second is the advection (drift) term, and the last is the reaction, or growth term. They then go on to solve a set of continuum mechanics equations to determine the velocity profile, in a

manner similar to the work of [8]. The major contribution of this work was the method for fitting the parameters, which involved deriving and solving a PDE constrained optimization problem.

The work of Clatz et al. [8] was carried further by the same research group in 2008, in the paper of Bondiau et al. [11]. They too simulated glioma spread using a combination of growth, proliferation (with anisotropic tensors) and mass effect. Here, they introduce parameters that allow for the mechanical aspects of growth, as well as the diffusion to be tuned to a specific patient. Once again, they simulate their model using atlas data, and test its performance by comparing it to the growth of a real glioma over a six month period.

While previous models had focused on modelling cell density, Konukoğlu et al. [55] developed in 2006 the first model that focussed instead on invasion margins. Instead of trying to model the time evolution of the tumour, they tried to extrapolate the invisible cell profile from the visible tumour mass. This is done by matching travelling wave solutions of the classic Fisher-Kolmogorov equation to the tumour mass data. Konukoğlu et al. extended this work in 2010, incorporating real patient DTI data, and validating their model for two real patients.

This idea was taken a step further by Mosayebi et al. in 2012 [12], where they proposed a model for the tumour boundary that assumed that the brain fibres induce a Riemannian metric on the brain domain. They then proposed using a geodesic distance on this space to define the Clinical Target Volume, as opposed to the standard Euclidean distance currently used in clinical practice. This group was able to test their model using patient data from 11 patients, something that few of the other groups had access to.

The model that will be considered in this work in detail is that of Painter and Hillen [5] of 2013. We will discuss both the development and theory

behind the model (Chapter 2), and then apply it to real patient data (Chapters 3-5). The Painter-Hillen model again uses anisotropic diffusion tensors to model glioma spread, however it is the only model to use the "fully anisotropic" Fokker–Planck diffusion operator discussed above in Equation 1.9. The derivation of this model also leads to a natural method for scaling of the DTI data, introducing a parameter that can be tuned to a specific patient. Specifically, the Painter-Hillen model is given by the PDE

$$u_t = \nabla\nabla : (D_c u) + ru(1-u), \tag{1.12}$$

where $r$ is the growth rate and $D_c$ is the anisotropic diffusion tensor. The : operator represents a double tensor contraction, and is expanded in Equation (1.9). The details of the Painter-Hillen model will be discussed in the chapters that follow.

The most recent model for glioma spread was developed by Engwer et al. [13] in 2014. It is an extension of the Painter-Hillen model, including explicitly the adhesion mechanisms connecting the glioma cells to the white matter tracts. The model derivation results in a model that is slightly different from the Painter-Hillen model, an advection-reaction-diffusion equation similar to Equation 1.11, as compared to the more standard reaction-diffusion models. The source of the advection though is different from that of Hogea et al. [10]. In their model, the mass effect induced the advection, where in Engwer et al. [13], it is the adhesion dynamics that induce the advective effect.

Mosayebi et al. [12] provide a table summarizing the previous models. We reproduce that table here, as well as adding several other models that are relevant, or have been developed since their paper was published. This information is shown in Table 1.2

| Paper | Model | Tensor | Source of tensor | Comparison |
|---|---|---|---|---|
| Swanson et al. (2000) | D | IT | N/A | N/A |
| Jbabdi et al. (2005) | D | DT | Healthy case | Visual |
| Clatz et al. (2005) | DM | DT | Atlas | 1 Patient |
| Konukoglu et al. (2006) | D | DT | Atlas | Synthetic |
| Hogea et al. (2007) | DM | DT | Atlas | 1 Patient |
| Bondiau (2008) | DM | DT | Atlas | 1 Patient |
| Konukoglu et al. (2010) | D | DT | Real tensors | 2 Patients |
| Mosayebi (2012) | D | DT | Real tensors | 11 Patients |
| Painter and Hillen (2013) | D | DT | Real tensors | 1 Patient |
| Engwer et al. (2014) | D | DT | Atlas | 1 Patient |
| This Thesis | D | DT | Real tensors | 10 Patients |

Table 1.2: Table modified from [12] summarizing previous models and contributions. We have added several other relevant models, most of which have been developed since their paper was published. For model categorization, D=Diffusion, DM=Diffusion and Mass Effect, IT= Isotropic Tensor, DT=Diffusion Tensor.

While there have been many people working on glioma models over the last decade or more, there has been very limited use of patient data or attempts at validation. While the most basic P.I. model has since been implemented in a clinical setting, this is not true for most of the other models. Table 1.2 also shows that Mosayebi et al. compared their model to a significant number of patients. In this thesis, we will establish the utility of the Painter-Hillen model [5], by comparing it to the P.I. model using simulations on real patient data. The ultimate goal will be to implement the Painter-Hillen model in a clinical setting, in a manner similar to the P.I. model.

Additionally, we will describe a method for incorporating a "mass effect" into the fully anisotropic Painter-Hillen model. The mass effect refers to the fact that we will incorporate the deformation of the brain into the model. We will see that the mechanical deformation of the brain is quite important

when a tumour is growing near the skull boundary. While there have been many different implementations of such an effect in glioma models, there is not yet a well-established way to include the mechanics. Here, we will present a simple, straight-forward incorporation of the mass effect built up from the fundamentals of continuum mechanics.

## 1.3 Outline

In the next chapter, we will rigorously develop the mathematics behind the anisotropic diffusion model for glioma spread. The technique of Hillen et al. [56] for computing the second moment of von Mises Fisher distributions will also be summarized. We will then establish the existence and uniqueness of solutions of the Painter-Hillen model using existing theory of partial differential equations (PDEs).

The numerical solution of fully anisotropic diffusion equations is not straightforward, hence in Chapter 3, we discuss the numerical methods used in simulating the Painter-Hillen model. We then show the results of these numerics for simple domains in one, two and three dimensions. The use of a simple domain serves to highlight the model behaviour in a controlled environment, so that we can observe how the cancer cell distribution tends to spread along synthetic "fibres" in the absence of the more complicated brain domains.

In Chapter 4, we discuss the patient data that is used here, as well as address the challenges encountered in applying the model to real patient data. These include data preprocessing such as segmentation and skull-stripping, initial conditions, boundary conditions, stopping criteria, parameter fitting, and a metric for model performance.

The main results are showcased in Chapter 5, where we actually apply the

Painter-Hillen model to data from ten patients. We first discuss in more detail the P.I. model of Swanson et al. [6], and discuss the results of applying this model to our patient set. We will then apply the anisotropic Painter-Hillen model to the same ten patients, and compare the results quantitatively using the metric discussed in Chapter 4. The result is that the Painter-Hillen model offers an improvement over the original P.I. model. We also introduce the idea of estimating missing DTI data by taking advantage of the symmetry of the brain, and perform simulations on this new data for a subset of the original patient set. After establishing the validity of the Painter-Hillen model, we showcase how it may be applied in a clinical setting.

In Chapter 6, we develop the mass effect model theory, starting with the fundamentals of continuum mechanics. The mass effect takes into account the mechanical response of the brain tissue to the pressure generated by the growing tumour. This is done by introducing the ideas of mass conservation and momentum conservation, and combining them into a coupled PDE system modelling both cancer cells and the healthy brain tissue surrounding them. We also consider simulations of the mass effect model in one dimension, demonstrating the deformation effect.

In Chapter 7 we derive an alternative model with a slightly different biological motivation. In this model, the cells' turning rate will depend on the underlying biological structure. This is motivated by the idea that a cell travelling in line with a fibre will turn less frequently than one moving perpendicularly. After performing a similar derivation to that done in Chapter 2, an interesting alternative model is derived, with its own biological interpretation. This model can be seen as a generalization of the Painter-Hillen model, and we verify that the original Painter-Hillen model is recovered upon considering a constant turning rate. While the model derived in Chapter 7

will not be developed further in this thesis, it offers the potential for further exploration/simulation.

Finally, in Chapter 8 we will draw conclusions from all of this, as well as discuss the model shortcomings and future work. Based on the results of this thesis, the Painter-Hillen model will open doors for future validation and inspire new developments in glioma treatment design.

## 1.4 Chapter Summary

Gliomas are tumours arising from the glial cells of the nervous system. The most aggressive type of glioma, grade IV astrocytoma, or glioblastoma multiforme, is a very aggressive tumour carrying a poor prognosis, with an expected survival of only 14 months from diagnosis. Glioma cells are characterized by a tendency to spread into the brain tissue, and as a result, the boundaries of these tumours are diffuse, with a large degree of spread beyond what can be imaged. This diffuse nature of glioma spread, coupled with the delicate nature of brain tissue, makes treatment of gliomas a challenge. As such, clinicians typically define a treatment region that includes the bulk tumour mass that is visible on a scan, as well as a uniform $2c$m extension to this region to account for the invisible spread. We propose that a mathematical model could help define a more accurate extension based on an individual patient's brain structure.

It has been shown that cancer cells in the brain have a preferential movement direction aligned with the white matter tracts. White matter is made up of bundles of nerves, and as such is fibrous in nature. When cancer cells move along these fibres, their pattern of spread leads to tumour shapes that often show projections in certain directions. This directed movement can be

modelled through the use of anisotropic diffusion, where the rate of spread is allowed to vary with direction. These different rates of spread are encoded into a diffusion model through the use of a diffusion tensor.

The advent of Diffusion Tensor Imaging, or DTI, has allowed clinicians to measure the rates of diffusion in each direction, at each location within a patient's brain. DTI technology therefore allows us to apply an anisotropic diffusion model to simulate the spread of glioma cells along the white matter tracts. Such a model was derived by Painter and Hillen [5], and we will focus on this model specifically, which we refer to as the Painter-Hillen model.

There have been many attempts at glioma modelling, in particular, Swanson et al. [6, 44–46, 49, 51–54] have had success in applying glioma models in a clinical setting. The ultimate goal of this work will be to implement the Painter-Hillen model clinically, inspired by the success of Swanson et al.

# Chapter 2

# A Model for Brain Tumour Spread Using Anisotropic Diffusion

In this work, we will be applying the fully anisotropic diffusion model of Painter and Hillen [5] to patient data, and comparing it to the Swanson P.I. model [6]. The fully anisotropic diffusion model was developed rigorously from the underlying biological fundamentals, see References [5, 57–60]. In this Chapter, we will explain the derivation, highlighting the key features of this particular model. Additionally, we will describe the scaling technique of Painter and Hillen [5] for obtaining the cancer cell diffusion tensors from the measured water diffusion tensors. As such, Sections 2.1 and 2.2 serve as review with no new results. Section 2.3 however, does contain a new computation.

## 2.1 Transport Model

In many biological systems, organisms move with some spatial awareness of their surroundings. As such, a suitable model for such spread must incorporate environmental information. One can attempt to describe an individual organism's migration path, or consider the density of organisms on a macroscopic scale. It turns out that these two types of approaches are not entirely independent, and are in fact, closely linked.

In our case, we are considering how cancer cells migrate in a heterogenous environment containing white matter tracts. As mentioned above, the white matter tracts actually play an important role in how the cells travel through the environment. We refer to this as contact guidance, which describes how the cells respond to directional information in the environment [60].

We will begin the derivation of the Painter-Hillen model by formulating a transport model describing how each individual cell will move. This is based on a correlated random walk [58] involving 'runs' and 'turns'. A run is defined as an organism moving through space with a constant velocity, with a turn being a change in that velocity. Three parameters describe this type of movement: (1) the mean speed, (2) the mean turning rate, and (3) the turning angle distribution [58]. We can go on to formulate an integro-differential equation to describe this movement.

We begin by defining $p(t, \boldsymbol{x}, \boldsymbol{v})$ to be the density of cells at time $t$, location $\boldsymbol{x}$ and travelling with velocity $\boldsymbol{v}$. We have that $t > 0$, $\boldsymbol{x} \in \mathbb{R}^n$ and $\boldsymbol{v} \in V \subset \mathbb{R}^n$. In the case of the brain, we will ultimately be considering $n = 3$, but will also consider the intermediate cases of $n = 1, 2$. We then derive an equation describing how that density can change. Our transport equation model is thus

given by [58]

$$p_t(t, \boldsymbol{x}, \boldsymbol{v}) + \boldsymbol{v} \cdot \nabla p(t, \boldsymbol{x}, \boldsymbol{v}) = \mathcal{L}p(t, \boldsymbol{x}, \boldsymbol{v}). \tag{2.1}$$

The second term on the left hand side describes the cells' movement through space, as this is just simple transport with velocity $\boldsymbol{v}$. The term on the right hand side however, describes the cells' turning, hence we refer to $\mathcal{L}p(t, \boldsymbol{x}, \boldsymbol{v})$ as the *turning operator*. In our case, it is defined as [5, 28, 60]

$$\mathcal{L}p(t, \boldsymbol{x}, \boldsymbol{v}) = -\mu p(t, \boldsymbol{x}, \boldsymbol{v}) + \mu \int_V q(t, \boldsymbol{x}, \boldsymbol{v}, \boldsymbol{v'}) p(t, \boldsymbol{x}, \boldsymbol{v'}) d\boldsymbol{v'}. \tag{2.2}$$

The first term describes cells turning out of current velocity $\boldsymbol{v}$, while the second term describes cells turning into velocity $\boldsymbol{v}$ from all other velocities $\boldsymbol{v'}$. The *turning rate* is given by $\mu$ and is for the time being assumed to be constant. The last term is a kernel term, and $q(t, \boldsymbol{x}, \boldsymbol{v}, \boldsymbol{v'})$ is called the turning kernel, or *turning distribution*. We describe $q(t, \boldsymbol{x}, \boldsymbol{v}, \boldsymbol{v'})$ as being the probability density that a cell at time $t$ and spatial location $\boldsymbol{x}$, moving with velocity $\boldsymbol{v'}$ will turn into velocity $\boldsymbol{v}$. It is through this distribution that we can incorporate information about the cell's environment. Since $q(t, \boldsymbol{x}, \boldsymbol{v}, \boldsymbol{v'})$ is a distribution, we must define it so that [5]:

1. $q(t, \boldsymbol{x}, \boldsymbol{v}, \boldsymbol{v'}) \geq 0$, and
2. $\int_V q(t, \boldsymbol{x}, \boldsymbol{v}, \boldsymbol{v'})\, d\boldsymbol{v} = 1$.

Before proceeding, we make several assumptions that will in turn simplify the subsequent mathematical derivations. The first assumption is that the cells' new direction will be independent of the old direction. Biologically speaking, this means that as a cancer cell approaches a white matter tract, it doesn't matter from what direction it was coming. The only direction that matters is that of the white matter tract. Mathematically speaking, this means

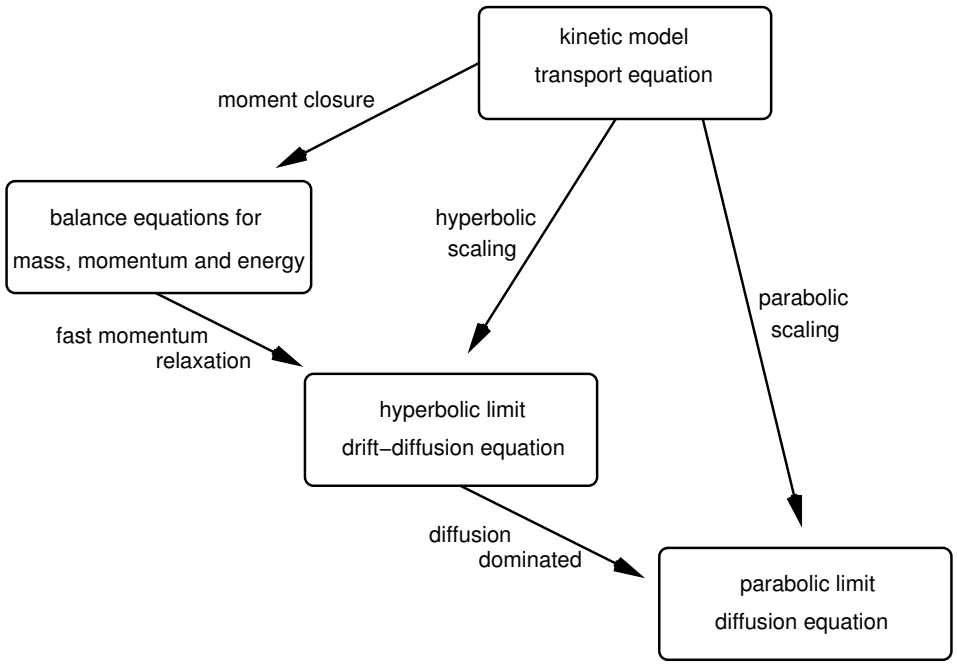


Figure 2.1: Scalings. Figure relating the different scalings and limit equations. Taken from [58] where it appears as Figure 1.

that $q(t, \boldsymbol{x}, \boldsymbol{v}, \boldsymbol{v'}) \approx q(t, \boldsymbol{x}, \boldsymbol{v})$. Additionally, we will assume that the fibre network is fixed in time, so that $q(t, \boldsymbol{x}, \boldsymbol{v}) \approx q(\boldsymbol{x}, \boldsymbol{v})$. Finally, we will assume that the distribution is symmetric, so that a cell has the same probability of turning "up" or "down" a fibre, i.e. $q(\boldsymbol{x}, \boldsymbol{v}) = q(\boldsymbol{x}, -\boldsymbol{v})$ [5].

### 2.1.1 Parabolic Scaling

There are at least three principal ways in which we may perform scaling of transport equations. These are:

(i) parabolic,

(ii) hyperbolic, and

(iii) moment closure.

It turns out that the parabolic scaling is the most important of the three in our case, although the other two scalings can also lead to the parabolic limit [58]. The motivation for this scaling comes from the space and time scales of the problem at hand. In the case of a brain tumour, a typical mesoscopic spatial scale would be on the order of $10\mu$m, whereas a typical macroscopic spatial scale would be on the order of 1 cm. In terms of time, cells would move on the order of seconds, while macroscopically, a tumour grows on the order of months. In order to go from the mesoscopic scale to the macroscopic scale spatially, we need to define $X = \epsilon \boldsymbol{x}$ where $\boldsymbol{x}$ is the mesoscopic spatial variable, $X$ is the macroscopic spatial variable, and $\epsilon = 10^{-3}$. The change in the time scales is much larger however, thus we would define $\tau = \epsilon^2 t$, where $t$ is the mesoscopic time variable and $\tau$ is the macroscopic time scale.

Now we have motivated the proper scaling to use for this problem, but before we proceed, we will make a few simplifying assumptions. These are:

(A1) The speed will remain constant, and we will vary only direction, i.e. $V \subset s\mathbb{S}^{n-1}$, where $s$ is the speed.

(A2) The turning distribution will not change with time, and the probability of turning into new velocity $\boldsymbol{v}$ is independent of old velocity $\boldsymbol{v}'$ as discussed above, so $q(t, \boldsymbol{x}, \boldsymbol{v}, \boldsymbol{v}') = q(\boldsymbol{x}, \boldsymbol{v})$.

(A3) The turning distribution is symmetric, with $q(\boldsymbol{x}, \boldsymbol{v}) = q(\boldsymbol{x}, -\boldsymbol{v})$.

The assumption that the speed is constant is not necessary, but will greatly simplify the analysis. The extension to non-constant speed is possible, but for our purposes not necessary. The assumption that the turning distribution is independent of time is perhaps too simple, as this is equivalent to assuming that the fibre structure is fixed in time. We know that as the tumour grows,

the brain around it may be deformed, causing $q$ to change. We will address this issue in Chapter 7, and for now consider this assumption to be valid. The assumption that $q$ is independent of $\boldsymbol{v}'$ however is reasonable, as we are simply neglecting inertia.

As we stated above, the parabolic scaling computation begins with an appropriate rescaling of both time and space, i.e.,[60]

$$X = \epsilon \boldsymbol{x}, \quad \text{and} \quad \tau = \epsilon^2 t. \tag{2.3}$$

If we apply these scalings to Equation (2.1), we obtain the scaled transport equation

$$\epsilon^2 p_\tau(\tau, X, \boldsymbol{v}) + \epsilon \boldsymbol{v} \cdot \nabla p(\tau, X, \boldsymbol{v}) = \mathcal{L} p(\tau, X, \boldsymbol{v}). \tag{2.4}$$

Note that the gradient is now taken with respect to $X$. We will then take an asymptotic expansion of $p(\tau, X, \mathbf{v})$ in $\epsilon$, recalling that $\epsilon \ll 1$ [60]:

$$p(\tau, X, \boldsymbol{v}) = p_0(\tau, X, \boldsymbol{v}) + \epsilon p_1(\tau, X, \boldsymbol{v}) + \epsilon^2 p_2(\tau, X, \boldsymbol{v}) + O(\epsilon^3). \tag{2.5}$$

The next step is to substitute Equation (2.5) into Equation (2.4) and match orders of $\epsilon$, however, before we proceed, we will study several properties of the turning operator, which will be needed in this analysis. Let us first define the macroscopic cell density by integrating over all velocities [59]:

$$\bar{p}(\tau, X) = \int_V p(\tau, X, \boldsymbol{v}) d\boldsymbol{v}. \tag{2.6}$$

Then, since our turning distribution is independent of the old velocity ($\boldsymbol{v}'$), we can rewrite the turning operator as

$$\mathcal{L}p(\tau, X, \boldsymbol{v}) = \mu \left( q(X, \boldsymbol{v}) \bar{p}(\tau, X) - p(\tau, X, \boldsymbol{v}) \right).$$

We first need to determine the kernel of $\mathcal{L}$, so that we know where we can invert our operator. An arbitrary function $\phi(\tau, X, \boldsymbol{v})$ is in the kernel of $\mathcal{L}$ if

$$\begin{aligned} & \mathcal{L}\phi(\boldsymbol{v}) = 0 \\ \iff \quad & \mu \left( q(X, \boldsymbol{v}) \bar{\phi} - \phi(\boldsymbol{v}) \right) = 0 \\ \iff \quad & q(X, \boldsymbol{v}) \bar{\phi} = \phi(\boldsymbol{v}). \end{aligned}$$

Since $\bar{\phi}$ does not depend on $\boldsymbol{v}$, we have that the kernel of $\mathcal{L}$ is simply the span of $q$, or $\langle q(X, \cdot) \rangle$. For short, we denote this $\langle q \rangle$. We will therefore define our space to be a weighted $L^2$ space, with weighting $q^{-1}$, denoted by $L^2_{q^{-1}}(V)$. The weighting appears in the inner product, so that the product of two functions $g(\boldsymbol{v})$ and $f(\boldsymbol{v})$ is given by [28, 60]

$$\langle f(\boldsymbol{v}), g(\boldsymbol{v}) \rangle_{L^2_{q^{-1}}} = \int_V f(\boldsymbol{v}) g(\boldsymbol{v}) \, \frac{d\boldsymbol{v}}{q(X, \boldsymbol{v})}.$$

Now we may compute the pseudoinverse on the complement of the kernel, i.e., on $\langle q \rangle^\perp$. We compute the inverse by starting with a function $\psi \in \langle q \rangle^\perp$ as in [60], and solving for the corresponding $\phi \in \langle q \rangle^\perp$ with

$$\mathcal{L}\phi(\boldsymbol{v}) = \psi(\boldsymbol{v}).$$

Substituting this in, we obtain

$$\mu\left(q(X,\boldsymbol{v})\bar{\phi}-\phi(\boldsymbol{v})\right)=\psi(\boldsymbol{v}). \tag{2.7}$$

Since $\phi\in\langle q\rangle^{\perp}$, we have that

$$\begin{aligned}
& \langle\phi,q\rangle=0\\
\iff\quad & \int_V \phi(\boldsymbol{v})q(X,\boldsymbol{v})\,\frac{d\boldsymbol{v}}{q(X,\boldsymbol{v})}=0\\
\iff\quad & \int_V \phi(\boldsymbol{v})\,d\boldsymbol{v}=0\\
\iff\quad & \bar{\phi}=0.
\end{aligned}$$

Substituting this result into Equation (2.7), we get

$$-\mu\phi(\boldsymbol{v})=\psi(\boldsymbol{v}),$$

giving

$$\phi(\boldsymbol{v})=-\frac{1}{\mu}\psi(\boldsymbol{v}). \tag{2.8}$$

Thus the pseudoinverse of the turning operator is defined as multiplication by $-1/\mu$ [60]. Now that we have defined some properties of our function space as well as our operator, we can proceed with matching the coefficients for orders of $\epsilon$ from the left and right hand sides of Equation (2.4). Substituting Equation (2.5) into Equation (2.4), we have:

$\epsilon^0$ :

$$\begin{aligned}
&\mathcal{L}p_0(\tau,x,\boldsymbol{v})=0\\
\Rightarrow\ &\mu(q(X,\boldsymbol{v})\bar{p}_0(\tau,X)-p_0(\tau,X,\boldsymbol{v}))=0\\
&\Rightarrow p_0(\tau,X,\boldsymbol{v})=q(X,\boldsymbol{v})\bar{p}_0(\tau,X),
\end{aligned} \tag{2.9}$$

where

$$\bar{p}_0(\tau, X) = \int_V p_0(\tau, X, \boldsymbol{v}) d\boldsymbol{v}.$$

Then for $\epsilon^1$, we have [60]

$\epsilon^1$ :

$$(\nabla \cdot \boldsymbol{v}) p_0 = \mathcal{L} p_1. \tag{2.10}$$

In order to solve for $p_1$, we use the pseudoinverse of $\mathcal{L}$ defined above. To apply this, we first need to verify that $(\nabla \cdot \boldsymbol{v}) p_0 \in \langle q \rangle^{\perp}$. This condition is equivalent to $\langle (\nabla \cdot \boldsymbol{v}) p_0, q \rangle = 0$ in $L^2_{q^{-1}}(V)$, so we compute

$$\int_V (\nabla \cdot \boldsymbol{v}) p_0(\tau, X, \boldsymbol{v}) \cancel{q(X, \boldsymbol{v})} \frac{d\boldsymbol{v}}{\cancel{q(X, \boldsymbol{v})}} = \nabla \cdot \int_V \boldsymbol{v} q(X, \boldsymbol{v}) d\boldsymbol{v} \bar{p}_0(\tau, X),$$

where we have substituted for $p_0$ using Equation (2.9). We therefore have that the left hand side of Equation (2.10) is in $\langle q \rangle^{\perp}$ whenever the turning distribution obeys the condition [60]

$$\mathbf{E}_q = \int_V \boldsymbol{v} q(X, \boldsymbol{v}) \, d\boldsymbol{v} = 0.$$

Since we are assuming $q$ to be symmetric, this condition will be satisfied. We can therefore solve Equation (2.10) for $p_1$ by inverting $\mathcal{L}$ as per Equation 2.8:

$$p_1(\tau, X, \boldsymbol{v}) = -\frac{1}{\mu} \nabla \cdot \boldsymbol{v} p_0(\tau, X, \boldsymbol{v}). \tag{2.11}$$

Now we will see that matching coefficients of $\epsilon^2$, and substituting in the earlier results will give a closed PDE for the macroscopic cell density $\bar{p}_0$:

$\epsilon^2$ :

$$p_{0,\tau}(\tau, X\boldsymbol{v}) + \boldsymbol{v} \cdot \nabla p_1(\tau, X, \boldsymbol{v}) = \mathcal{L} p_2(\tau, X, \boldsymbol{v}).$$

Integrating both sides over $V$ gives

$$\int_V p_{0,\tau}(\tau, X, \boldsymbol{v})\, d\boldsymbol{v} + \int_V \boldsymbol{v} \cdot \nabla p_1(\tau, X, \boldsymbol{v})\, d\boldsymbol{v} = \int_V \mathcal{L} p_2(\tau, X, \boldsymbol{v})\, d\boldsymbol{v}. \qquad (2.12)$$

Now we evaluate each integral:

$$\begin{aligned}
\int_V \mathcal{L} p_2(\tau, X, \boldsymbol{v})\, d\boldsymbol{v} &= \mu \left( \int_V q(X, \boldsymbol{v}) \bar{p}_2(\tau, X)\, d\boldsymbol{v} - \int_V p_2(\tau, X, \boldsymbol{v})\, d\boldsymbol{v} \right) \\
&= \mu \left( \bar{p}_2(\tau, X) \underbrace{\int_V q(X, \boldsymbol{v})\, d\boldsymbol{v}}_{=1} - \bar{p}_2(\tau, X) \right) \\
&= 0.
\end{aligned}$$

Substituting Equation (2.9) for $p_0$ into the first term on the left hand side of Equation 7.14, we also have

$$\begin{aligned}
\int_V p_{0,\tau}(\tau, X, \boldsymbol{v})\, d\boldsymbol{v} &= \int_V \bar{p}_{0,\tau}(\tau, X) q(X, \boldsymbol{v})\, d\boldsymbol{v} \\
&= \bar{p}_{0,\tau}.
\end{aligned}$$

Finally, substituting Equation (2.10) for $p_1$ into the second term on the left hand side of Equation 7.14 we have

$$\begin{aligned}
\int_V \boldsymbol{v} \cdot \nabla p_1(\tau, X, \boldsymbol{v})\, d\boldsymbol{v} &= -\frac{1}{\mu} \int_V \boldsymbol{v} \cdot \nabla (\nabla \cdot \boldsymbol{v}) p_0(\tau, X, \boldsymbol{v})\, d\boldsymbol{v} \\
&= -\frac{1}{\mu} \int_V (\boldsymbol{v} \cdot \nabla)(\nabla \cdot \boldsymbol{v})(\bar{p}_0(\tau, X) q(X, \boldsymbol{v}))\, d\boldsymbol{v} \\
&= -\frac{1}{\mu} \partial_i \partial_j \left( \int_V v_i v_j q(X, \boldsymbol{v})\, d\boldsymbol{v} \right) \bar{p}_0(\tau, X),
\end{aligned}$$

where we have used repeated indices to indicate summation. Putting these all back into Equation (7.14), we obtain a closed form PDE [60]:

$$\bar{p}_{0,\tau}(\tau, X) = \nabla\nabla : (D(X)\bar{p}_0(\tau, X)),$$

where the macroscopic diffusion tensor $D(X)$ is proportional to the variance-covariance matrix of the turning distribution $q$ [5, 60]:

$$D(X) = \frac{1}{\mu}\int_V \boldsymbol{v}\boldsymbol{v}^T q(X, \boldsymbol{v})\, d\boldsymbol{v}. \tag{2.13}$$

The : operator indicates a double contraction of the tensor $(D(x)\bar{p}_0(\tau, X))$. For example, $T : U = T_{ij}U_{ij}$, where repeated indices represent a sum [61]. Then, taking $\nabla\nabla = \partial_i\partial_j$ we have that

$$\nabla\nabla : (D(X)\bar{p_0}) = \partial_i\partial_j(D_{ij}(X)p_0(\tau, X)).$$

To simplify notation, we let $\boldsymbol{x} = X$ define the macroscopic spatial variable, $t = \tau$ define the macroscopic temporal variable, and $u(\boldsymbol{x}, t) = \bar{p}_0(\tau, X)$ define the macroscopic cell density. Additionally, we will let $D_c(\boldsymbol{x}) = D(X)$ define the cancer cell diffusion tensor. Then the diffusion of the cancer cells is described by the PDE

$$u_t = \nabla\nabla : (D_c(\boldsymbol{x})u(\boldsymbol{x}, t)), \tag{2.14}$$

which uses the Painter-Hillen fully anisotropic diffusion operator [5].

### 2.1.2 Boundary Conditions

In order to completely define our model, we must specify the appropriate boundary conditions. In this case, we will not be allowing cells to diffuse

through the skull, hence we will employ homogeneous Neumann boundary conditions. Mathematically, we represent this as

$$\boldsymbol{\eta} \cdot \nabla(D(\mathbf{x})u) = 0 \text{ on } \partial\Omega, \tag{2.15}$$

where $\boldsymbol{\eta}$ is the outward unit normal to the boundary $\partial\Omega$. This condition ensures that the flux over the boundary will be 0, since cells cannot pass through the skull.

## 2.2 Defining the Turning Distribution

Choosing an appropriate turning distribution $q(X, \boldsymbol{v})$ is an important component of the modelling process, and there are a number of ways to choose this distribution. We discussed the diffusion ellipsoid and the diffusion peanut in Chapter 1, both of which offer potential methods for defining this distribution. Both correspond to a unique diffusion tensor, as is proven here.

**Theorem 2.1.** *Assume $D \in \mathbb{R}^{n\times n}$ is a symmetric and positive definite matrix. Then for a given constant c, the associated diffusion ellipsoid of Equation (1.2) and the diffusion peanut of Equation (1.3) are unique.*

*Proof.* We begin by showing that the peanut uniquely defines an associated symmetric tensor. Given $f(\theta) = \theta^T D\theta$, assume that we have two symmetric tensors $D_1$ and $D_2$, with $D_1 \neq D_2$. Assume that they define the same peanut, i.e.

$$\theta^T D_1\theta = \theta^T D_2\theta \quad \forall\theta \in \mathbb{S}^{n-1}.$$

Then by linearity

$$\theta^T(D_1 - D_2)\theta = 0.$$

Now defining $C = D_1 - D_2$, and employing the summation convention for repeated indices

$$\theta_i C_{ij} \theta_j = 0 \quad \forall i, j \leq n,$$

where $n$ is the dimension of the tensor. Then

$$\theta_i \theta_j C_{ij} = 0,$$

and in general, $\theta_i \neq 0$, $\theta_j \neq 0$, therefore since $C$ is symmetric by the symmetry of $D_1$ and $D_2$, we have that $C_{ij} = 0$ for all $i, j \leq n$. Therefore $C = \mathbf{0}$, and $D_1 = D_2$. For the diffusion ellipsoid, consider two ellipsoids $E_1$ and $E_2$ defined from tensors $D_1$ and $D_2$ respectively, i.e.

$$E_1 = \{\theta^T D_1^{-1} \theta = 1\}, \quad E_2 = \{\theta^T D_2^{-1} \theta = 1\}.$$

Now we will assume that $E_1 = E_2 = E$ and show that we must then have $D_1 = D_2$. If $E_1 = E_2$, then

$$\theta^T D_1^{-1} \theta = \theta^T D_2^{-1} \theta, \quad \forall \theta \in E.$$

By the same argument as for the peanut, we have

$$D_1^{-1} = D_2^{-1}.$$

Thus both the diffusion peanut and diffusion ellipse uniquely define an associated symmetric diffusion tensor.

□

For our model, we are considering a cancer cell sitting at a given location,

and need to define the probabilities of this cell travelling in any given direction. Naturally, if it is sitting on a fibre, we want to define the turning distribution such that it is most likely to travel either "up" the fibre or "down" the fibre. We do this by selecting a von Mises distribution to be our turning distribution in two dimensions, and a von Mises-Fisher, or simply Fisher distribution in three dimensions. The von Mises and Fisher distributions are the result of wrapping a normal distribution around either a circle, or a sphere, respectively [56]. The result is that there will be a peak in a specified direction. Since DTI allows us to measure the dominant direction of diffusion at each spot within the brain, we will select our turning distribution so that the peak occurs in this direction. In our case, if $\phi_1$ is the eigenvector corresponding to the dominant eigenvalue, then we do not distinguish between $\phi_1$ and $-\phi_1$. This is because when a cell approaches a fibre, we assume that it has equal probability of travelling 'up' the fibre as travelling 'down' the fibre. As such, we will use a von Mises distribution having a peak at $\phi_1$ and also at $-\phi_1$. This is referred to as the bimodal von Mises distribution, or bimodal Fisher distribution [56]. An example of a unimodal von Mises distribution is shown in Figure 2.2 (a), having a peak in direction $(1,0)^T$. A bimodal von Mises distribution is shown in Figure 2.2 (b), with peaks at $\pm(1,0)^T$.

If we are considering the two-dimensional case, then we represent a given direction by a unit vector $\boldsymbol{n} \in \mathcal{S}^1$. We will represent the direction of the peak by $\boldsymbol{\gamma} \in \mathcal{S}^1$, where $\boldsymbol{\gamma}$ will be the dominant eigenvector obtained via DTI in unit vector form. The unimodal von Mises distribution is therefore given by

$$q(\boldsymbol{n}) = \frac{1}{2\pi I_0(k)} e^{k\boldsymbol{n}\cdot\boldsymbol{\gamma}}, \tag{2.16}$$

where $I_0(k)$ is the modified Bessel function of first kind of order 0, and $k$ is what

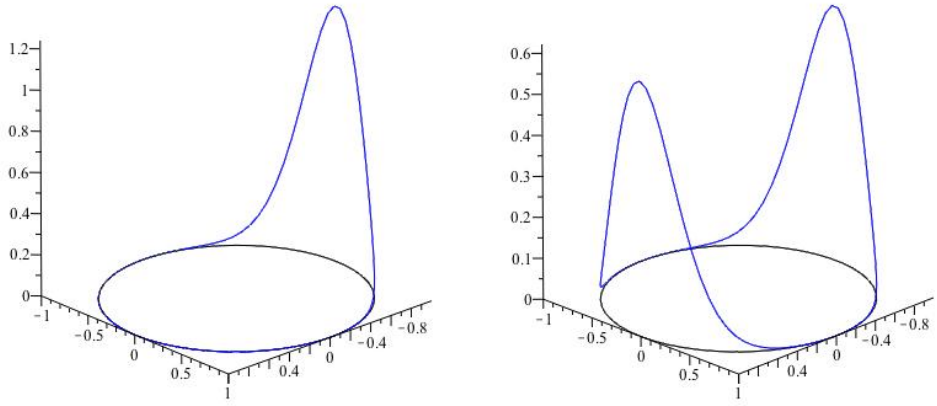


Figure 2.2: von Mises Distribution. (a) An example of a unimodal von Mises distribution with $\boldsymbol{\gamma} = (1, 0)^T$. (b) An example of a bimodal von Mises distribution with peaks at $\pm(1, 0)^T$.

we call the concentration parameter. The factor in front of the exponential ensures normalization. The concentration parameter controls the width of the peak, and thus the strength of the directional dependence. As such, $k$ will be proportional to the fractional anisotropy mentioned in Chapter 1, Equations (1.5) and (1.6). For example, in a region near a white matter tract, the fractional anisotropy will be high, and thus the concentration parameter will be high, resulting in a sharp narrow peak. In isotropic regions where $k \approx 0$, the turning distribution will resemble a uniform distribution and movement will be random with no directional influence. The constant of proportionality will be referred to as $\kappa$, the anisotropy parameter. We therefore define $k(\boldsymbol{x}) = \kappa \text{FA}(\boldsymbol{x})$, where $\text{FA}(\boldsymbol{x})$ is the fractional anisotropy defined in Equations (1.5) and (1.6). We will discuss $\kappa$ in more detail in Chapter 5. The value of $\kappa$ will be considered fixed for a given patient, and spatial dependence of $k$ will be introduced through the FA value. Note that as $k \to 0$, we obtain the uniform distribution. Both $\boldsymbol{\gamma}(\boldsymbol{x})$ and $k(\boldsymbol{x})$ will depend on space, since both will be

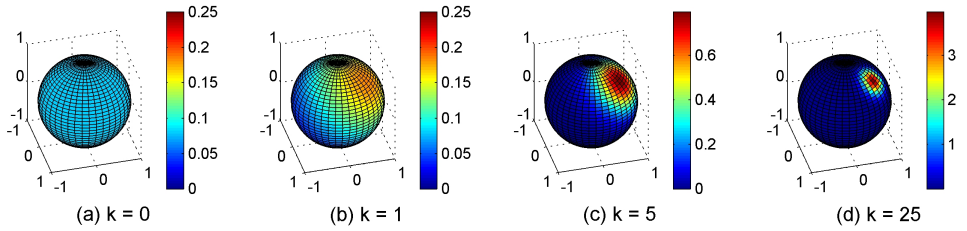


Figure 2.3: Fisher Distribution. The Fisher distribution with $\boldsymbol{\gamma} = (\frac{1}{2}, \frac{1}{2}, \frac{\sqrt{2}}{2})$ for increasing values of the concentration parameter $k$ (left to right).

obtained from the spatially varying DTI data.

In order to obtain the bimodal version, we take a linear combination of distributions with peaks at $\pm\boldsymbol{\gamma}$. To preserve normalization, a factor of $\frac{1}{2}$ is also introduced. The bimodal distribution is therefore given by

$$q_B(\boldsymbol{n}) = \frac{1}{4\pi I_0(k)} \left(e^{k\boldsymbol{n}\cdot\boldsymbol{\gamma}} + e^{-k\boldsymbol{n}\cdot\boldsymbol{\gamma}}\right).$$

The three-dimensional Fisher distribution[1] has the same form, however the normalization coefficient is slightly different:

$$q(\boldsymbol{n}) = \frac{k}{4\pi \sinh(k)} e^{k\boldsymbol{n}\cdot\boldsymbol{\gamma}} \tag{2.17}$$

with corresponding bimodal form

$$q_B(\boldsymbol{n}) = \frac{k}{8\pi \sinh(k)} \left(e^{k\boldsymbol{n}\cdot\boldsymbol{\gamma}} + e^{-k\boldsymbol{n}\cdot\boldsymbol{\gamma}}\right).$$

Figure 2.3 shows the Fisher distribution with $\boldsymbol{\gamma} = (\frac{1}{2}, \frac{1}{2}, \frac{\sqrt{2}}{2})$ for increasing values of $k$. This is taken from [56] where it appears as Figure 2.

[1]Not to be confused with the statistical F-distribution.

## 2.3 Computing the Second Moment of the von Mises Distribution [2]

As seen in Equation (2.13), in order to compute the cancer cell diffusion tensor, we must compute the second moment of the turning distribution. It turns out that this is not entirely trivial to do, and traditionally involves explicitly computing increasingly complicated integrals. Here we will use the technique of Hillen et al. [56], which instead takes advantage of the divergence theorem to simplify computations in higher dimensions. We will compute the second moment of both the unimodal von Mises and Fisher distributions, and extend this result to the bimodal cases for both two and three dimensions. It is the bimodal result that will be of interest for our modelling. Additionally, we will show that the second moments will tend to the isotropic tensors as the concentration parameter $k$ tends to 0, as would be expected.

Before beginning with the computations, we will define some properties of Bessel functions and modified Bessel functions which we will make use of. We denote by $J_n(x)$ the Bessel functions of first kind, and define [56]

$$I_n(x) := (-i)^{-n} J_n(ix) \tag{2.18}$$

to be the modified Bessel functions of first kind. We also have an explicit definition of the modified Bessel functions [56]:

$$I_n(k) = \frac{1}{2\pi} \int_0^{2\pi} \cos(n\phi) e^{k\cos(\phi)} d\phi. \tag{2.19}$$

[2] The material in this subsection is based on a paper that has been submitted for publication. The explicit form of the three-dimensional variance-covariance matrix of the three-dimensional Fisher distribution, as shown in Theorem 2.4, is a new result.

Additionally, the Bessel functions satisfy the following recursive relation [56]

$$\frac{d}{dx}(x^n J_n(x)) = x^n J_{n-1}(x). \tag{2.20}$$

Finally, for $n \geq 0$, we have [56]

$$J_{n+1}(x) = \frac{2n}{x} J_n(x) - J_{n-1}(x). \tag{2.21}$$

These relations will be useful in computing the resulting integrals in the two-dimensional case.

### 2.3.1 Two-Dimensional Case

We first consider the two-dimensional case. Traditionally, these computations would be done by explicitly computing the integrals component wise. While possible, this method is tedious. We instead use the method of Hillen et al. [56] which uses the divergence theorem.

We begin by computing the first moment, or the expectation of the von Mises distribution given in Equation (2.16). We will make use of this calculation in the computation of the second moment. We will call this the expectation $\mathbf{E}[q]$, defined as

$$\mathbf{E}[q] = \int_{\mathcal{S}^1} \boldsymbol{n} q(\boldsymbol{n}) d\boldsymbol{n}.$$

Then applying Equation (2.16), we have

$$\mathbf{E}[q] = \frac{1}{2\pi I_0(k)} \int_0^{2\pi} \boldsymbol{n} e^{k\cos\theta} d\theta,$$

where $\theta$ is the angle between $\boldsymbol{n}$ and $\boldsymbol{\gamma}$. Then we could integrate this component

wise to determine the expectation vector, but instead we introduce a test vector $\boldsymbol{a}$ [56]:

$$\boldsymbol{a} \cdot \mathbf{E}[q] = \frac{1}{2\pi I_0(k)} \boldsymbol{a} \cdot \int_0^{2\pi} \boldsymbol{n} e^{k \cos\theta} d\theta.$$

Bringing the test vector inside the integral and replacing $\cos\theta$ by the corresponding dot product, we have

$$\boldsymbol{a} \cdot \mathbf{E}[q] = \frac{1}{2\pi I_0(k)} \int_0^{2\pi} \boldsymbol{n} \cdot \left(\boldsymbol{a} e^{k \cos \boldsymbol{n} \cdot \boldsymbol{\gamma}}\right) d\theta.$$

Applying the divergence theorem to this integral, it becomes

$$\begin{aligned}
\boldsymbol{a} \cdot \mathbf{E}[q] &= \frac{1}{2\pi I_0(k)} \int_{\mathbb{B}_1(0)} \frac{\partial}{\partial \boldsymbol{v}} \left(\boldsymbol{a} e^{k \cos \boldsymbol{v} \cdot \boldsymbol{\gamma}}\right) d\boldsymbol{v} \\
&= \frac{1}{2\pi I_0(k)} \int_{\mathbb{B}_1(0)} k a_i \gamma_i e^{k \boldsymbol{v} \cdot \boldsymbol{\gamma}} d\boldsymbol{v} \\
&= \frac{1}{2\pi I_0(k)} \boldsymbol{a} \cdot k\boldsymbol{\gamma} \int_0^1 \int_0^{2\pi} e^{rk\cos\theta} r dr d\theta,
\end{aligned}$$

where $\mathcal{B}_1(0)$ is the unit ball centred at the origin. Applying the definition of Bessel functions in Equation (2.19) with $n = 0$, this is simply

$$\begin{aligned}
\boldsymbol{a} \cdot \mathbf{E}[q] &= \boldsymbol{a} \frac{1}{2\pi I_0(k)} \cdot k\boldsymbol{\gamma} \int_0^1 2\pi r I_0(rk) dr \\
&= \boldsymbol{a} \cdot \frac{1}{I_0(k)} k\boldsymbol{\gamma} \int_0^1 r I_0(rk) dr. \qquad (2.22)
\end{aligned}$$

To solve this integral, we make use of some of the recursive properties of Bessel and modified Bessel functions outlined above. We first use Equation (2.18) to rewrite our integrand [56]:

$$r I_0(rk) = \frac{irk J_0(irk)}{ik} = \frac{1}{ik} \left(irk J_0(irk)\right).$$

We then make use of Equation (2.20) to get

$$\frac{1}{ik}\left(irkJ_0(irk)\right) = \frac{1}{ik}\frac{d}{dx}(xJ_1(x))|_{x=irk}.$$

We rewrite this in terms of the $r$ derivative, so that we may apply the fundamental theorem of calculus. We thus have

$$\frac{1}{ik}\frac{d}{dx}(xJ_1(x))|_{x=irk} = \frac{1}{ik}\frac{d}{dr}(rJ_1(irk)).$$

Substituting this result back into our integral in Equation (2.22), and using the fundamental theorem of calculus to solve, we get [56]

$$\int_0^1 rI_0(rk)dr = \frac{1}{ik}\int_0^1 \frac{d}{dr}(rJ_1(irk))dr = \frac{1}{ik}\left(J_1(ik) - 0\cdot J_1(0)\right) = \frac{1}{ik}J_1(ik). \tag{2.23}$$

Finally, by the definition of the modified Bessel function, Equation (2.18), we have

$$\frac{1}{ik}J_1(ik) = \frac{1}{ik}iI_1(k) = \frac{I_1(k)}{k}. \tag{2.24}$$

Substituting this back in, we obtain [56]

$$\boldsymbol{a}\cdot\mathbf{E}[q] = \boldsymbol{a}\cdot\frac{1}{I_0(k)}k\boldsymbol{\gamma}\frac{I_1(k)}{k},$$

$$\Rightarrow \mathbf{E}[q] = \frac{I_1(k)}{I_0(k)}\boldsymbol{\gamma}, \tag{2.25}$$

since $\boldsymbol{a}$ was an arbitrary test vector.

Now we will compute the second moment of the von Mises distribution.

The variance-covariance matrix of a turning distribution $q$ is defined as [56]

$$\begin{aligned}\mathrm{Var}[q] &= \int_{\mathbb{S}^{n-1}} (\boldsymbol{n} - \mathbf{E}[q])(\boldsymbol{n} - \mathbf{E}[q])^T q(\boldsymbol{n}) d\boldsymbol{n} \\ &= \int_{\mathbb{S}^{n-1}} \boldsymbol{n}\boldsymbol{n}^T q(\boldsymbol{n}) d\boldsymbol{n} - 2\mathbf{E}[q] \underbrace{\int_{\mathbb{S}^1} \boldsymbol{n}^T q(\boldsymbol{n}) d\boldsymbol{n}}_{=\mathbf{E}[q]^T} + \mathbf{E}[q]\mathbf{E}[q]^T \underbrace{\int_{\mathbb{S}^{n-1}} q(\boldsymbol{n}) d\boldsymbol{n}}_{=1} \\ &= \int_{\mathbb{S}^{n-1}} \boldsymbol{n}\boldsymbol{n}^T q(\boldsymbol{n}) - \mathbf{E}[q]\mathbf{E}[q]^T. \end{aligned} \tag{2.26}$$

Since the variance of $q$ is a second-order tensor (matrix), it is appropriate to use two test vectors $\boldsymbol{a}$ and $\boldsymbol{b}$, and to work with the double contraction obtained using these two test vectors. We thus proceed in a similar fashion as for the computation of the expectation, and since $\mathbf{E}[q]$ is known, we work to compute

$$\begin{aligned}\boldsymbol{a}^T \int_{\mathbb{S}^1} \boldsymbol{n}\boldsymbol{n}^T q(\boldsymbol{n}) d\boldsymbol{n}\boldsymbol{b} &= \frac{1}{2\pi I_0(k)} \int_{\mathbb{S}^1} a_i n_i b_j n_j e^{k n_l \gamma_l} d\boldsymbol{n} \\ &= \frac{1}{2\pi I_0(k)} \int_{\mathbb{S}^1} n_i \left(a_i b_j n_j e^{k n_l \gamma_l}\right) d\boldsymbol{n}\end{aligned}$$

at which point we once again apply the divergence theorem. Transforming this to an integral over $\mathbb{B}_1(0)$ and applying the product rule gives

$$\begin{aligned}\boldsymbol{a}^T \int_{\mathbb{S}^1} \boldsymbol{n}\boldsymbol{n}^T q(\boldsymbol{n}) d\boldsymbol{n}\boldsymbol{b} &= \frac{1}{2\pi I_0(k)} \int_{\mathbb{B}_1(0)} \frac{\partial}{\partial v_i} \left(a_i b_j v_j e^{k v_l \gamma_l}\right) d\boldsymbol{v} \\ &= \frac{1}{2\pi I_0(k)} \left[\int_{\mathbb{B}_1(0)} a_i b_i e^{k\boldsymbol{v}\cdot\boldsymbol{\gamma}} d\boldsymbol{v} + \int_{\mathbb{B}_1(0)} a_i (\boldsymbol{v}\cdot\boldsymbol{b}) k\gamma_i e^{k\boldsymbol{v}\cdot\boldsymbol{\gamma}} d\boldsymbol{v}\right] \\ &= \frac{1}{2\pi I_0(k)} \left[\underbrace{\boldsymbol{a}\cdot\boldsymbol{b} \int_{\mathbb{B}_1(0)} e^{k\boldsymbol{v}\cdot\boldsymbol{\gamma}} d\boldsymbol{v}}_{I} + \underbrace{k\boldsymbol{a}\cdot\boldsymbol{\gamma}\boldsymbol{b}\cdot \int_{\mathbb{B}_1(0)} \boldsymbol{v} e^{k\boldsymbol{v}\cdot\boldsymbol{\gamma}} d\boldsymbol{v}}_{II}\right].\end{aligned} \tag{2.27}$$

At this point we will consider the two integrals above separately. Starting

with $I$, writing it explicitly in polar coordinates, we have

$$\int_{\mathbb{B}_1(0)} e^{k\boldsymbol{v}\cdot\boldsymbol{\gamma}} d\boldsymbol{v} = \int_0^1 \int_{\mathbb{S}^1} e^{rk\boldsymbol{n}\cdot\boldsymbol{\gamma}} r dr d\boldsymbol{n}$$

The integral over $\mathbb{S}^1$ is simply the total mass of the von Mises distribution with $k = rk$, times the normalization coefficient $2\pi I_0(rk)$, hence [56]

$$\begin{aligned}\int_0^1 \int_{\mathbb{S}^1} e^{rk\boldsymbol{n}\cdot\boldsymbol{\gamma}} r dr d\boldsymbol{n} &= \int_0^1 2\pi r I_0(rk) dr \\ &= 2\pi \frac{I_1(k)}{k},\end{aligned}$$

where we made use of a calculation already performed in the expectation computation, using the properties of Bessel functions, see Equations (2.23) and (2.24). Now we turn our attention to the second integral, $II$. Writing it out explicitly using polar coordinates, we have

$$\begin{aligned}\int_{\mathbb{B}_1(0)} e^{k\boldsymbol{v}\cdot\boldsymbol{\gamma}} d\boldsymbol{v} &= \int_0^1 \int_{\mathbb{S}^1} r\boldsymbol{n} e^{rk\boldsymbol{n}\cdot\boldsymbol{\gamma}} r dr d\boldsymbol{n} \\ &= \int_0^1 r^2 \int_{\mathbb{S}^1} \boldsymbol{n} e^{rk\boldsymbol{n}\cdot\boldsymbol{\gamma}} d\boldsymbol{n} dr.\end{aligned}$$

The integral over the unit circle is simply $2\pi I_0(rk)$ times the expectation of the von Mises distribution with $k = rk$. Then

$$\int_0^1 r^2 \int_{\mathbb{S}^1} \boldsymbol{n} e^{rk\boldsymbol{n}\cdot\boldsymbol{\gamma}} d\boldsymbol{n} dr = 2\pi\boldsymbol{\gamma} \int_0^1 r^2 I_1(rk) dr, \tag{2.28}$$

as is given by Equation (2.25). In order to compute this last integral, we will use the Bessel function properties. Rewriting the integrand:

$$r^2 I_1(rk) = -\frac{1}{ik^2} J_1(irk),$$

from the definition of the modified Bessel functions, and using Equation (2.20), we have

$$-\frac{1}{ik^2}J_1(irk) = -\frac{1}{ik^2}\frac{d}{dx}(x^2 J_2(x)|_{x=irk}.$$

Since $i, k$ are constants,

$$-\frac{1}{ik^2}\frac{d}{dx}(x^2 J_2(x)|_{x=irk} = -\frac{1}{k}\frac{d}{dr}(r^2 J_2(irk)).$$

Substituting this back into Equation (2.28) and applying the fundamental theorem of calculus, we have [56]

$$\begin{aligned}\int_{B_1(0)} \boldsymbol{v} e^{k\boldsymbol{v}\cdot\boldsymbol{\gamma}} d\boldsymbol{v} &= -2\pi\boldsymbol{\gamma}\int_0^1 \frac{1}{k}\frac{d}{dr}(r^2 J_2(irk))dr \\ &= -2\pi\boldsymbol{\gamma}J_2(ik) \\ &= 2\pi\boldsymbol{\gamma}\frac{I_2(k)}{k}.\end{aligned}$$

Now substituting our solved integrals back into Equation (2.27), we have

$$\begin{aligned}\boldsymbol{a}^T\int_{\mathbb{S}^1} \boldsymbol{n}\boldsymbol{n}^T q(\boldsymbol{n})\, d\boldsymbol{n}\, \boldsymbol{b} &= \frac{1}{2\pi I_0(k)}\left[(\boldsymbol{a}\cdot\boldsymbol{b})2\pi\frac{I_1(k)}{k} + (k\boldsymbol{a}\cdot\boldsymbol{\gamma})2\pi\boldsymbol{\gamma}\frac{I_2(k)}{k}\right] \\ &= \boldsymbol{a}\left(\frac{1}{k}\frac{I_1(k)}{I_0(k)}\mathbb{I}_2 + \boldsymbol{\gamma}\boldsymbol{\gamma}^T\frac{I_2(k)}{I_0(k)}\right)\boldsymbol{b},\end{aligned}$$

where $\mathbb{I}_2$ is the two-dimensional identity matrix. Then, because $\boldsymbol{a}$ and $\boldsymbol{b}$ were arbitrary test vectors, we have [56]

$$\int_{S^1} \boldsymbol{n}\boldsymbol{n}^T q(\boldsymbol{n}) d\boldsymbol{n} = \frac{1}{k}\frac{I_1(k)}{I_0(k)}\mathbb{I}_2 + \boldsymbol{\gamma}\boldsymbol{\gamma}^T\frac{I_2(k)}{I_0(k)}. \tag{2.29}$$

We can then apply Equation (2.21) with $n = 1$, to get

$$\int_{S^1} \boldsymbol{n}\boldsymbol{n}^T q(\boldsymbol{n}) d\boldsymbol{n} = \frac{1}{2}\mathbb{I}_2 + \frac{I_2(k)}{I_0(k)}\left(\boldsymbol{\gamma}\boldsymbol{\gamma}^T - \frac{1}{2}\right).$$

We substitute this formula into Equation (2.26), along with the expectation given in Equation (2.25) to get [56]

$$\begin{aligned}
\mathrm{Var}[q] &= \int_{\mathbb{S}^1} \boldsymbol{n}\boldsymbol{n}^T q(\boldsymbol{n}) d\boldsymbol{n} - \mathbf{E}[q]\mathbf{E}[q]^T \\
&= \frac{1}{2}\mathbb{I}_2 + \frac{I_2(k)}{I_0(k)}\left(\boldsymbol{\gamma}\boldsymbol{\gamma}^T - \frac{1}{2}\mathbb{I}_2\right) - \left(\frac{I_1(k)}{I_0(k)}\right)^2 \boldsymbol{\gamma}\boldsymbol{\gamma}^T \\
&= \frac{1}{2}\left(1 - \frac{I_2(k)}{I_0(k)}\right)\mathbb{I}_2 + \left(\frac{I_2(k)}{I_0(k)} - \left(\frac{I_1(k)}{I_0(k)}\right)^2\right)\boldsymbol{\gamma}\boldsymbol{\gamma}^T.
\end{aligned}$$

Then, we summarize these results in the following Lemma.

**Lemma 2.2.** *[56] Let $\boldsymbol{\gamma} \in \mathbb{S}^1$ be a given unit vector, and consider the two-dimensional von Mises distribution given by*

$$q(\boldsymbol{n}) = \frac{1}{2\pi I_0(k)} e^{k\boldsymbol{n}\cdot\boldsymbol{\gamma}}, \quad \boldsymbol{n} \in \mathbb{S}^1.$$

*Then the expectation and variance of $q$ are:*

$$\mathbf{E}[q] = \frac{I_1(k)}{I_0(k)}\boldsymbol{\gamma},$$

$$\mathrm{Var}[q] = \frac{1}{2}\left(1 - \frac{I_2(k)}{I_0(k)}\right)\mathbb{I}_2 + \left(\frac{I_2(k)}{I_0(k)} - \left(\frac{I_1(k)}{I_0(k)}\right)^2\right)\boldsymbol{\gamma}\boldsymbol{\gamma}^T.$$

### Bimodal Distibribution

Of particular interest in our models are the moment calculations for the bimodal von Mises distribution, i.e.

$$q_B(\boldsymbol{n}) = \frac{1}{4\pi I_0(k)} \left( e^{k\boldsymbol{n}\cdot\boldsymbol{\gamma}} + e^{-k\boldsymbol{n}\cdot\boldsymbol{\gamma}} \right).$$

Since this distribution is symmetric, we have $\mathbf{E}[q_B] = \mathbf{0}$. This can be easily seen by applying Equation (2.25) to the two individual distributions. We then have

$$\mathbf{E}[q_B] = \frac{I_1(k)}{I_0(k)} (\boldsymbol{\gamma} - \boldsymbol{\gamma}) = \mathbf{0}. \tag{2.30}$$

For the second moment, since $\mathbf{E}[q_B] = 0$, Equation (2.26) gives

$$\mathrm{Var}[q_B] = \int_{\mathbb{S}^1} \boldsymbol{n}\boldsymbol{n}^T q_B(\boldsymbol{n}) d\boldsymbol{n},$$

which is given in Equation (2.29) by

$$\int_{\mathbb{S}^1} \boldsymbol{n}\boldsymbol{n}^T q_B(\boldsymbol{n}) d\boldsymbol{n} = \frac{1}{2} \left( 1 - \frac{I_2(k)}{I_0(k)} \right) \mathbb{I}_2 + \frac{I_2(k)}{I_0(k)} \boldsymbol{\gamma}\boldsymbol{\gamma}^T,$$

thus we have [56]

$$\mathrm{Var}[q_B] = \frac{1}{2} \left( 1 - \frac{I_2(k)}{I_0(k)} \right) \mathbb{I}_2 + \frac{I_2(k)}{I_0(k)} \boldsymbol{\gamma}\boldsymbol{\gamma}^T. \tag{2.31}$$

We again summarize these results in a corollary.

**Corollary 2.3.** *[56] Let $\boldsymbol{\gamma} \in \mathbb{S}^1$ be a given unit vector, and consider the two-dimensional bimodal von Mises distribution given by*

$$q(\boldsymbol{n}) = \frac{1}{4\pi I_0(k)} \left( e^{k\boldsymbol{n}\cdot\boldsymbol{\gamma}} + e^{-k\boldsymbol{n}\cdot\boldsymbol{\gamma}} \right), \quad \boldsymbol{n} \in \mathbb{S}^1.$$

*Then the expectation and variance of $q$ are:*

$$\mathbf{E}[q] = \mathbf{0},$$

$$\mathrm{Var}[q] = \frac{1}{2}\left(1 - \frac{I_2(k)}{I_0(k)}\right)\mathbb{I}_2 + \frac{I_2(k)}{I_0(k)}\boldsymbol{\gamma}\boldsymbol{\gamma}^T. \tag{2.32}$$

### 2.3.2 Three-Dimensional Case

We next consider the three-dimensional case. The variance for this case was previously unknown, hence this computation represents a new result. We will thus compute the expectation and the variance-covariance matrix of the Fisher distribution, defined in Equation (2.17). We begin as in two dimensions, by computing the expectation. Introducing an arbitrary test vector $\boldsymbol{a}$, we have [56]

$$\begin{aligned}
\boldsymbol{a}\cdot\mathbf{E}[q] &= \boldsymbol{a}\cdot\int_{\mathbb{S}^2}\boldsymbol{n}q(\boldsymbol{n})d\boldsymbol{n} \\
&= \int_{\mathbb{S}^2} n_i(a_i q(\boldsymbol{n}))d\boldsymbol{n} \\
&= \int_{\mathbb{B}_1(0)}\frac{\partial}{\partial v_i}\left(a_i\frac{k}{4\pi\sinh k}e^{k\gamma_l v_l}\right)d\boldsymbol{v}
\end{aligned}$$

where we have applied the divergence theorem, and explicitly written in the formula for the Fisher distribution. Taking the derivative, and explicitly writing the resulting integral, we have

$$\begin{aligned}
\boldsymbol{a}\cdot\mathbf{E}[q] &= a_i\int_{\mathbb{B}_1(0)}\frac{k^2\gamma_i}{4\pi\sinh k}e^{k\boldsymbol{\gamma}\cdot\boldsymbol{v}}d\boldsymbol{v} \\
&= \boldsymbol{a}\cdot\boldsymbol{\gamma}k\int_{\mathbb{B}_1(0)}\frac{k}{4\pi\sinh k}e^{k\boldsymbol{\gamma}\cdot\boldsymbol{v}}d\boldsymbol{v} \\
&= \boldsymbol{a}\cdot\boldsymbol{\gamma}\int_0^1\frac{r^2k^2}{4\pi\sinh k}\int_{\mathbb{S}^2}e^{rk\boldsymbol{\gamma}\cdot\boldsymbol{n}}d\boldsymbol{n}dr.
\end{aligned}$$

The inner integral is simply $\frac{4\pi \sinh kr}{rk}$ times the total mass of the Fisher distribution with $k = kr$, so this reduces to

$$\begin{aligned}
&= \boldsymbol{a} \cdot \boldsymbol{\gamma} \frac{k}{\sinh k} \int_0^1 r \sinh krdr \\
&= \boldsymbol{a} \cdot \boldsymbol{\gamma} \frac{k}{\sinh k} \left[ \frac{r}{k} \cosh kr - \frac{1}{k^2} \sinh kr \right|_0^1 \\
&= \boldsymbol{a} \cdot \boldsymbol{\gamma} \frac{k}{\sinh k} \left[ \frac{\cosh k}{k} - \frac{\sinh k}{k^2} \right] \\
&= \boldsymbol{a} \cdot \boldsymbol{\gamma} \left( \coth k - \frac{1}{k} \right),
\end{aligned}$$

where integration by parts was used to solve the integral. Then, since $\boldsymbol{a}$ was an arbitrary test vector, the expectation is given by [56]

$$\mathbf{E}[q] = \left( \coth k - \frac{1}{k} \right) \boldsymbol{\gamma}. \tag{2.33}$$

In order to compute the variance via Equation (2.26), we must compute the second moment of the Fisher distribution. We do this in a similar fashion to the two-dimensional case, beginning with two arbitrary test vectors $\boldsymbol{a}$ and $\boldsymbol{b}$ [56]. Then

$$\begin{aligned}
\boldsymbol{a}^T \int_{\mathbb{S}^2} \boldsymbol{n}\boldsymbol{n}^T q(\boldsymbol{n})\, d\boldsymbol{n}\, \boldsymbol{b} &= \int_{\mathbb{S}^2} a_i n_i n_j b_j q(\boldsymbol{n}) d\boldsymbol{n} \\
&= \int_{\mathbb{S}^2} n_i (a_i n_j b_j q(\boldsymbol{n})) d\boldsymbol{n}.
\end{aligned}$$

Applying the divergence theorem, substituting in the Fisher distribution,

and expanding out the product rule, we have [56]

$$\begin{aligned}\int_{\mathbb{S}^2} n_i(a_i n_j b_j q(\boldsymbol{n}))d\boldsymbol{n} &= \int_{\mathbb{B}_1(0)} \frac{\partial}{\partial v_i}\left(a_i v_j b_j \frac{k}{4\pi\sinh k} e^{k\gamma_l v_l}\right) d\boldsymbol{v} \\ &= \int_{\mathbb{B}_1(0)} a_i b_i \frac{k}{\sinh k} e^{k\boldsymbol{\gamma}\cdot\boldsymbol{v}} d\boldsymbol{v} + \int_{\mathbb{B}_1(0)} a_i(\boldsymbol{v}\cdot\boldsymbol{b})\frac{k^2\gamma_i}{4\pi\sinh k} e^{k\boldsymbol{\gamma}\cdot\boldsymbol{v}} d\boldsymbol{v} \\ &= \underbrace{\boldsymbol{a}\cdot\boldsymbol{b}\int_{\mathbb{B}_1(0)} \frac{k}{\sinh k} e^{k\boldsymbol{\gamma}\cdot\boldsymbol{v}} d\boldsymbol{v}}_{I} + \underbrace{\boldsymbol{a}\cdot\boldsymbol{\gamma}\boldsymbol{b}\cdot\int_{\mathbb{B}_1(0)} \frac{k^2}{4\pi\sinh k}\boldsymbol{v} e^{k\boldsymbol{\gamma}\cdot\boldsymbol{v}} d\boldsymbol{v}}_{II}.\end{aligned} \tag{2.34}$$

We will once again consider these two integrals separately. Beginning with $I$, we have

$$\int_{\mathbb{B}_1(0)} \frac{k}{\sinh k} e^{k\boldsymbol{\gamma}\cdot\boldsymbol{v}} d\boldsymbol{v} = \frac{1}{k}\coth k - \frac{1}{k^2}, \tag{2.35}$$

which we computed in our calculation of the expectation. Now for $II$, we have

$$\int_{\mathbb{B}_1(0)} \boldsymbol{v} e^{k\boldsymbol{\gamma}\cdot\boldsymbol{v}} d\boldsymbol{v} = \int_0^1 \int_{\mathbb{S}^2} r\boldsymbol{n} e^{rk\boldsymbol{\gamma}\cdot\boldsymbol{n}} r^2 d\boldsymbol{n} dr.$$

The inner integral is simply $\frac{4\pi\sinh kr}{rk}$ times the expectation of the Fisher distribution with $k = rk$, hence this is equal to

$$\begin{aligned}\int_{\mathbb{B}_1(0)} \boldsymbol{v} e^{k\boldsymbol{\gamma}\cdot\boldsymbol{v}} d\boldsymbol{v} &= \int_0^1 \frac{4\pi\sinh rk}{rk}\left(\coth rk - \frac{1}{rk}\right) r^3 dr\boldsymbol{\gamma} \\ &= 4\pi\left[\int_0^1 \frac{r^2}{k}\cosh rk dr - \int_0^1 \frac{r}{k^2}\sinh rk dr\right]\boldsymbol{\gamma}.\end{aligned}$$

Using integration by parts to evaluate the integrals, we have

$$\begin{aligned}
&\int_{\mathbb{B}_1(0)} \boldsymbol{v} e^{k\boldsymbol{\gamma}\cdot\boldsymbol{v}} d\boldsymbol{v} \\
&\quad = \frac{4\pi}{k^4}\left\{\left[(k^2r^2+2)\sinh(kr) - 2kr\cosh(kr)\right]_0^1 - \left[kr\cosh(kr) - \sinh(kr)\right]_0^1\right\}\boldsymbol{\gamma} \\
&\quad = 4\pi\left[\left(\frac{\sinh k}{k^2} - \frac{2\cosh k}{k^3} + \frac{2\sinh k}{k^4}\right) - \left(\frac{\cosh k}{k^3} - \frac{\sinh k}{k^4}\right)\right]\boldsymbol{\gamma} \\
&\quad = 4\pi\left(\frac{\sinh k}{k^2} - \frac{3\cosh k}{k^3} + \frac{3\sinh k}{k^4}\right)\boldsymbol{\gamma}.
\end{aligned}$$

Then

$$\int_{\mathbb{B}_1(0)} \frac{k^2}{4\pi\sinh k} \boldsymbol{v} e^{k\boldsymbol{\gamma}\cdot\boldsymbol{v}} d\boldsymbol{v} = \left(1 - \frac{3}{k}\coth k + \frac{3}{k^2}\right)\boldsymbol{\gamma}. \tag{2.36}$$

Now substituting Equations (2.35) and (2.36) into Equation (2.34), we obtain [56]

$$\boldsymbol{a}^T \int_{\mathbb{S}^2} \boldsymbol{n}\boldsymbol{n}^T q(\boldsymbol{n}) d\boldsymbol{n}\boldsymbol{b} = \boldsymbol{a}^T\boldsymbol{b}\left(\frac{\coth k}{k} - \frac{1}{k^2}\right) + \boldsymbol{a}^T\boldsymbol{\gamma}\boldsymbol{\gamma}^T\boldsymbol{b}\left(1 - \frac{3\coth k}{k} + \frac{3}{k^2}\right).$$

We then conclude

$$\int_{\mathbb{S}^2} \boldsymbol{n}\boldsymbol{n}^T q(\boldsymbol{n}) d\boldsymbol{n} = \left(\frac{\coth k}{k} - \frac{1}{k^2}\right)\mathbb{I}_3 + \left(1 - \frac{3\coth k}{k} + \frac{3}{k^2}\right)\boldsymbol{\gamma}\boldsymbol{\gamma}^T. \tag{2.37}$$

In order to conclude the variance computation, we must combine this result, along with the expectation with Equation (2.26). Doing so gives [56]

$$\begin{aligned}
\mathrm{Var}[q] &= \left(\frac{\coth k}{k} - \frac{1}{k^2}\right)\mathbb{I}_3 + \left(1 - \frac{3\coth k}{k} + \frac{3}{k^2}\right)\boldsymbol{\gamma}\boldsymbol{\gamma}^T + \left(\coth k - \frac{1}{k}\right)^2\boldsymbol{\gamma}\boldsymbol{\gamma}^T \\
&= \left(\frac{\coth k}{k} - \frac{1}{k^2}\right)\mathbb{I}_3 + \left(1 - \frac{\coth k}{k} + \frac{2}{k^2} - \coth^2 k\right)\boldsymbol{\gamma}\boldsymbol{\gamma}^T.
\end{aligned} \tag{2.38}$$

We summarize these results in the following theorem.

**Theorem 2.4.** *[56] Let $\boldsymbol{\gamma} \in \mathbb{S}^2$ be a given unit vector, and consider the three-dimensional Fisher distribution given by*

$$q(\boldsymbol{n}) = \frac{k}{4\pi \sinh k} e^{k\boldsymbol{n}\cdot\boldsymbol{\gamma}}, \quad \boldsymbol{n} \in \mathbb{S}^2.$$

*Then the expectation and variance of $q$ are:*

$$\boldsymbol{E}[q] = \left(\coth k - \frac{1}{k}\right)\boldsymbol{\gamma},$$

$$Var[q] = \left(\frac{\coth k}{k} - \frac{1}{k^2}\right)\mathbb{I}_3 + \left(1 - \frac{\coth k}{k} + \frac{2}{k^2} - \coth^2 k\right)\boldsymbol{\gamma}\boldsymbol{\gamma}^T.$$

The computations for two and three dimensions were very similar, with the main difference being the integrals that are evaluated, which depend on the particular normalization coefficients. This is the major advantage of this technique; while the traditional method for calculating moments becomes much increasingly tedious in higher dimensions, this method using the divergence theorem generalizes easily to higher dimensions.

### Bimodal Distibribution

Again, for our modelling purposes, it is the bimodal distribution that is of interest. As in the two-dimensional case, the expectation is simply $\mathbf{0}$, since the distribution is symmetric. As such, Equation (2.26) tells us that the variance should be given by Equation (2.37). This is summarized in the following corollary [56].

**Corollary 2.5.** *[56] Let $\boldsymbol{\gamma} \in \mathbb{S}^2$ be a given unit vector, and consider the three-dimensional bimodal Fisher distribution given by*

$$q(\boldsymbol{n}) = \frac{1}{4\pi I_0(k)} \left( e^{k\boldsymbol{n}\cdot\boldsymbol{\gamma}} + e^{-k\boldsymbol{n}\cdot\boldsymbol{\gamma}} \right), \quad \boldsymbol{n} \in \mathbb{S}^1.$$

*Then the expectation and variance of $q$ are:*

$$\boldsymbol{E}[q_B] = \mathbf{0},$$

$$Var[q_B] = \left( \frac{\coth k}{k} - \frac{1}{k^2} \right) \mathbb{I}_3 + \left( 1 - \frac{3\coth k}{k} + \frac{3}{k^2} \right) \boldsymbol{\gamma}\boldsymbol{\gamma}^T. \tag{2.39}$$

### 2.3.3 Limiting Behaviour

As $k \to 0^+$, both the von Mises and Fisher (unimodal and bimodal) distributions tend to a uniform distribution. As such, we would expect that as $k \to 0^+$, the expectation of each should go to 0, and the variance-covariance matrices should be purely isotropic, i.e., the coefficients of the dyadic tensors should go to 0, leaving only the coefficients of the identity matrices. In this section, we consider the limits of the coefficients in both two and three dimensions, and show that the isotropic tensors result.

#### Two dimensions

In two dimensions, the limits are very straight forward, and we can plug in $k = 0$ directly, with no issues. We have that

$$\lim_{k\to 0^+} \frac{I_2(k)}{I_0(k)} = \lim_{k\to 0^+} \frac{I_1(k)}{I_0(k)} = 0,$$

hence $\mathbf{E}[q] = \mathbf{0}$, $\mathbf{E}[q_B] = 0$ (trivially), and $\mathrm{Var}[q] = \mathrm{Var}[q_B] = \frac{1}{2}\mathbb{I}_2$.

### Three dimensions

The situation in three dimensions is not so straight forward. Simply setting $k = 0$ in the coefficients causes undefined values, thus the limits must be taken carefully. Let us first define the following coefficients as functions of $k$:

$$\begin{aligned} a(k) &= \coth k - \frac{1}{k}, \\ b(k) &= \frac{\coth k}{k} - \frac{1}{k^2}, \\ c(k) &= 1 - \frac{\coth k}{k} + \frac{2}{k^2} - \coth^2 k, \\ d(k) &= 1 - \frac{3\coth k}{k} + \frac{3}{k^2}. \end{aligned}$$

Then we have for the unimodal case

$$\begin{aligned} \mathbf{E}[q] &= a(k)\boldsymbol{\gamma}, \\ \mathrm{Var}[q] &= b(k)\mathbb{I}_3 + c(k)\boldsymbol{\gamma}\boldsymbol{\gamma}^T, \end{aligned}$$

and for the bimodal case

$$\begin{aligned} \mathbf{E}[q_B] &= \mathbf{0}, \\ \mathrm{Var}[q_B] &= b(k)\mathbb{I}_3 + d(k)\boldsymbol{\gamma}\boldsymbol{\gamma}^T. \end{aligned}$$

We can compute the limits analytically for each of these coefficients. Beginning with $a(k)$, we have

$$\lim_{k\to 0^+} a(k) = \lim_{k\to 0^+} \coth k - \frac{1}{k},$$

which we rewrite into an indeterminate form and apply successive l'Hôpital's

rules to:

$$\begin{aligned}\lim_{k\to 0^+} \frac{k-\tanh k}{k\tanh k} &= \lim_{k\to 0^+} \frac{1-\operatorname{sech}^2 k}{\tanh k + k\operatorname{sech}^2 k} \\ &= \lim_{k\to 0^+} \frac{2\operatorname{sech}^2 k\tanh k}{\operatorname{sech}^2 + (1-2\operatorname{sech} k)\operatorname{sech}^2 k} \\ &= 0.\end{aligned}$$

We compute the limit of $b(k)$ in a similar fashion; rewriting it into an indeterminate form, and repeatedly applying l'Hôpital's rule:

$$\begin{aligned}\lim_{k\to 0^+} b(k) &= \lim_{k\to 0^+} \frac{\coth k}{k} - \frac{1}{k^2} \\ &= \lim_{k\to 0^+} \frac{k-\tanh k}{k^2\tanh k} \\ &= \lim_{k\to 0^+} \frac{1-\operatorname{sech}^2 k}{2k\tanh k + k^2\operatorname{sech}^2 k} \\ &= \lim_{k\to 0^+} \frac{2\operatorname{sech}^2 k\tanh k}{2k\operatorname{sech}^2 k + 2\tanh k - 2k^2\operatorname{sech}^2 k\tanh k + 2k\operatorname{sech}^2 k} \\ &= \lim_{k\to 0^+} \frac{-4\operatorname{sech}^2 k\tanh^2 k = 2\operatorname{sech}^4 k}{6\operatorname{sech}^2 k - 12k\operatorname{sech}^2 k\tanh k - 2k^2(\operatorname{sech}^4 k - 2\operatorname{sech}^2 k\tanh^2 k)} \\ &= \frac{1}{3}.\end{aligned}$$

To compute the limit of $c(k)$ and $d(k)$, we can make use of the limits that we've already computed. To compute $c(k)$, we have

$$\begin{aligned}\lim_{k\to 0^+} c(k) &= \lim_{k\to 0^+} 1 - \frac{\coth k}{k} + \frac{2}{k^2} - \coth^2 k \\ &= \lim_{k\to 0^+} 1 - \underbrace{\left(\frac{\coth k}{k} - \frac{1}{k^2}\right)}_{b(k)} + \frac{1}{k^2} - \coth^2 k \\ &= \lim_{k\to 0^+} \frac{2}{3} + \left(\frac{1}{k} + \coth k\right)\left(\frac{1}{k} - \coth k\right),\end{aligned}$$

where we have used the fact that the limit of $b(k)$ is $1/3$, and factored using difference of two squares. Then rewriting we have

$$\begin{aligned}\lim_{k\to 0^+} \frac{2}{3} + \left(\frac{1}{k} + \coth k\right)\left(\frac{1}{k} - \coth k\right) &= \lim_{k\to 0^+} \frac{2}{3} - (1 - k\coth k)b(k) \\ &= \lim_{k\to 0^+} \frac{2}{3} - \frac{1}{3}\left(1 + \frac{k}{\sinh k}\right) \\ &= \frac{2}{3} - \frac{2}{3} = 0.\end{aligned}$$

Finally, taking the limit of $d(k)$, we have

$$\begin{aligned}\lim_{k\to 0^+} d(k) &= \lim_{k\to 0^+} 1 - \frac{3\coth k}{k} + \frac{3}{k^2} \\ &= \lim_{k\to 0^+} 1 - 3\left(\frac{\coth k}{k} - \frac{1}{k^2}\right) \\ &= 1 - 3\lim_{k\to 0^+} c(k) \\ &= 1 - 3\left(\frac{1}{3}\right) = 0.\end{aligned}$$

These results can be confirmed numerically by plotting the coefficients as functions of $k$. The result of this is shown in Figure 2.4. We can see that the numerical limits match with those computed analytically.

## 2.4 Classification of the PDE Model

Because $q(\boldsymbol{x}, \cdot)$ is a regular probability distribution, its variance-covariance matrix will be symmetric positive-definite. We thus conclude that $D_c$ as given by Equation (2.13) is positive definite [5]. Mathematically speaking, this means that

$$\boldsymbol{x}^T D_c \boldsymbol{x} = D_{ij} x_i x_j > 0,$$

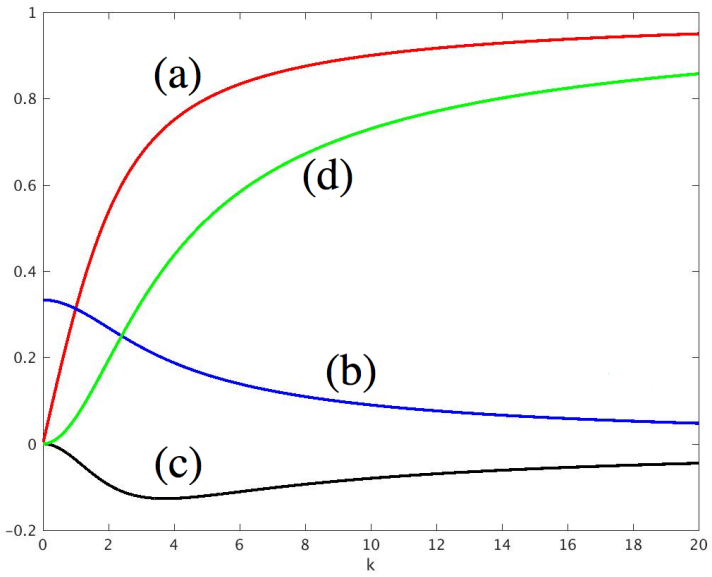


Figure 2.4: Limiting Behaviour. (a) Plot of the coefficients $a(k), b(k), c(k)$ and $d(k)$ vs. $k$. Note that for $k \to 0$, $a, c, d \to 0$, while $b \to 1/3$.

for all $\boldsymbol{x} \in \mathbb{R}^n$, $\boldsymbol{x} \neq 0$, where we have used repeated indices to indicate summation. A natural consequence of this is that when $\theta \in \mathbb{S}^{n-1}$, there will be a lower bound for the quadratic form, i.e.,

$$\theta^T D_c \theta = D_{ij}\theta_i\theta_j \geq k > 0, \tag{2.40}$$

for all $\theta \in \mathbb{S}^{n-1}$. We can use this result to show that Equation (2.14) is a parabolic PDE. We follow the definition of Evans [62] for classifying a second order linear PDE as parabolic. Following the notation of Evans, we consider

a PDE of the following form [62]

$$\begin{cases} u_t(t,\boldsymbol{x}) + Lu(t,\boldsymbol{x}) = f(\boldsymbol{x}) & \text{in} \quad U_T \\ u(t,\boldsymbol{x}) = 0 & \text{on} \quad \partial U \times [0,T] \\ u(0,\boldsymbol{x}) = g(\boldsymbol{x}) & \text{on} \quad U \times \{t=0\}, \end{cases}$$

where $U_T$ is the domain, and $f(\boldsymbol{x})$ and $g(\boldsymbol{x})$ are prescribed functions. Then $L$ represents a second-order partial differential operator that takes the form [62]

$$Lu(t,\boldsymbol{x}) = -\sum_{i,j=1}^{n} a^{ij}(\boldsymbol{x},t)u_{x_i x_j} + \sum_{i=1}^{n} b^i(\boldsymbol{x},t)u_{x_i} + c(\boldsymbol{x},t)u. \tag{2.41}$$

Then a parabolic PDE is defined as follows:

**Definition 2.6.** (Evans [62]) We say that the partial differential operator $\frac{\partial}{\partial t} + L$ is (uniformly) parabolic if there exists a constant $C > 0$ such that

$$\sum_{i,j=1}^{n} a^{ij}(\boldsymbol{x},t)\xi_i\xi_j \geq C|\xi|^2, \tag{2.42}$$

for all $(\boldsymbol{x},t) \in U_T, \xi \in \mathbb{R}^n$.

In the case of the fully anisotropic diffusion operator of Equation (2.14), $Lu$ is defined as

$$Lu(t,\boldsymbol{x}) = -\nabla\nabla : (D_c(\boldsymbol{x})u(t,\boldsymbol{x})) = \partial_i\partial_j \left( D_c(\boldsymbol{x})_{ij} u(t,\boldsymbol{x}) \right).$$

Expanding out the full three-dimensional operator, and recalling that $D_c$ is

symmetric, we can define the coefficients of Equation (2.41) as follows:

$$a = \begin{bmatrix} D_{11} & D_{12} & D_{13} \\ D_{12} & D_{22} & D_{23} \\ D_{13} & D_{23} & D_{33} \end{bmatrix} = D_c,$$

$$b = \begin{pmatrix} 2D_{11x_1} + 2D_{13x_3} + 2D_{12x_2} \\ 2D_{12x_1} + 2D_{23x_3} + 2D_{22x_2} \\ 2D_{13x_1} + 2D_{33x_3} + 2D_{23x_2} \end{pmatrix},$$

and

$$c = D_{11x_1x_1} + D_{22x_2x_2} + D_{33x_3x_3} + 2D_{13x_1x_3} + 2D_{23x_2x_3} + 2D_{12x_1x_2}.$$

Now dividing both side of Equation (2.42) by $|\xi|^2$, we have

$$\bar{\xi}^T a \bar{\xi} \geq C,$$

where $\bar{\xi} = \xi/|\xi|$ is a unit vector. Now since $a = D_c$, this is exactly equivalent to Equation (2.40), and so the condition in Equation (2.42) is satisfied for $C = k$, and the operator $\partial_t + \nabla\nabla : D_c(\boldsymbol{x})$ is parabolic. A nice consequence of this is that the classical existence and uniqueness theorems for parabolic PDE's apply [5, 62], For these results, see Robinson [63].

## 2.5 Chapter Summary

In this chapter, we reviewed the details of the derivation of the Painter-Hillen model of [5]. We began by setting up a transport equation modelling the movement of individual cells, parameterized by space $\boldsymbol{x}$, time $t$ and velocity

$\boldsymbol{v}$. The movement depends on the turning rate $\mu$, as well as the turning distribution $q(\boldsymbol{x}, \boldsymbol{v})$. The turning distribution defines the probability that a cell at location $\boldsymbol{x}$ will turn into velocity $\boldsymbol{v}$. We wanted to incorporate the fact that cells move along the white matter tracts into the model, hence we used a bimodal von Mises distribution (in two dimensions) or a bimodal Fisher distribution (in three dimensions), having a peak in the direction of the fibre tract.

While the transport equation models cell movement on an individual basis, we were ultimately interested in a model for the macroscopic cell density. To obtain the macroscopic model, a parabolic scaling was performed due to the difference in spatial and temporal scales at the cellular level as compared to the macroscopic scale. The result was that the macroscopic PDE describing glioma spread is given by

$$u_t = \nabla\nabla : (D_c(\boldsymbol{x})u(\boldsymbol{x}, t)),$$

where

$$D_c(\boldsymbol{x}) = \frac{1}{\mu}\int_V \boldsymbol{v}\boldsymbol{v}^T q(\boldsymbol{x}, \boldsymbol{v})\, d\boldsymbol{v}$$

is the macroscopic cancer cell diffusion tensor, computed as the second moment of the turning distribution.

To fully determine the diffusion tensor for the Painter-Hillen model, we calculated the second moment of the turning distribution. While a formula exists for the two-dimensional von Mises case, we were not able to find the formula for the second moment of the three-dimensional Fisher distribution. As such, we employed a novel moment calculation technique that uses the divergence theorem to simplify the integrals. We therefore obtained a formula

for the diffusion tensor in three dimensions, analogous to the result in two dimensions. We confirmed the validity of this result by exploring the limiting behaviour as the distribution tends towards a uniform distribution. The result was that as we tended towards a uniform distribution, the diffusion tensor tended towards an isotropic tensor, as expected.

Finally, we confirmed that the resulting operator is parabolic, so that the classical existence and uniqueness results apply.

# Chapter 3

# Simulations on a Simplified Domain

To get a better understanding of the solutions to the Painter-Hillen model of Equation (1.12) when applied to real patient data, we will first apply it to a simple domain. Additionally, we will use these results to validate the model and the code. We will begin with the simple one-dimensional case and work up to the three-dimensional case. A simplified artificial domain is used in both two and three dimensions to demonstrate how the model behaves when a white matter tract is encountered. In Chapters 4 and 5, we will use the numerical methods and boundary conditions derived in this chapter and apply the Painter-Hillen model to more complicated real brain domains.

## 3.1 One-dimensional Simulations

We begin with the one-dimensional case. For this particular case, anisotropy does not exist, as there is only one direction of spread. There will therefore

be no diffusion tensor, instead just a scalar diffusion coefficient. We use this example to introduce the numerical method, and to explore the numerical and analytical steady-state behaviour.

While the diffusion coefficient does not vary directionally, we do allow it to vary spatially. We therefore begin with the PDE

$$\begin{cases} u_t = (D(x)u)_{xx} & \text{in } [0,L]\times\mathbb{R}^+, \\ u(x,0) = g(x) & \text{on } [0,L]\times\{t=0\}, \\ \frac{\partial(Du)}{\partial x} = 0 & \text{at } x = 0, L, \end{cases} \tag{3.1}$$

where $u$ represents the cell density, $D(x) \in C^2$ is the diffusion coefficient and the domain is defined as $x \in [0,L]\times\mathbb{R}^+$. The initial condition is prescribed by $g(x)$. Note that we have applied the fully anisotropic diffusion operator of Painter and Hillen [5], derived in Chapter 2. We have chosen homogeneous Neumann boundary conditions to simulate cells being unable to pass through the skull (boundary). Making the substitution $\phi(x,t) = D(x)u(x,t)$ reduces the system to a straight-forward diffusion equation

$$\begin{cases} \phi_t = D(x)\phi_{xx} & \text{in } [0,L]\times\mathbb{R}^+, \\ \phi(x,0) = D(x)g(x) & \text{on } [0,L]\times\{t=0\}, \\ \frac{\partial\phi}{\partial x} = 0 & \text{at } x = 0, L. \end{cases} \tag{3.2}$$

We will transform solutions of Equation (3.2) by dividing by $D(x)$ to obtain solutions of Equation (3.1). We also note that while Equation (3.2) has steady state solutions $\phi(x) = C$, where $C$ is a constant, Equation (3.1) has steady state solutions $u(x) = C/D(x)$. We used a simple finite differencing scheme with a forward Euler time stepping, and a centred difference in space, i.e.,

simulating Equation (3.2):

$$\frac{\phi_i^{n+1} - \phi_i}{\tau} = \frac{D_i(\phi_{i+1}^n - 2\phi_i^n + \phi_{i-1}^n)}{h^2}, \tag{3.3}$$

where $\tau$ is the time step and $h$ is the spatial step. The numerical solution is given by $\phi_i^n$, with time level indicated by the superscripts $n$ and $n+1$, while the spatial level is indicated by the subscripts $i$, $i+1$ and $i-1$. The discrete diffusion coefficient is given by $D_i = D(x_i)$, with $D(x)$ defined as

$$D(x) = \begin{cases} 0.5 & \text{if } 0 \leq x \leq 0.1, \\ 20e^{(-((x-0.2)^2))} + 0.5 - 20e^{-0.01} & \text{if } 0.1 < x < 0.3, \\ 0.5 & \text{if } 0.3 \leq x \leq 0.7, \\ -20e^{(-((x-0.8)^2))} + 0.5 + 20e^{-0.01} & \text{if } 0.7 < x < 0.9, \\ 0.5 & \text{if } 0.9 \leq x \leq 1, \end{cases}$$

which describes enhanced diffusion when $0.1 \leq x \leq 0.3$, and reduced diffusion when $0.7 \leq x \leq 0.9$. The spatial dependence of $D(x)$ is shown in Figure 3.1. Finally, the initial condition was chosen to be a straight line, i.e.,

$$g(x) = \frac{1}{2}x.$$

The plot on the top of Figure 3.2 shows the solutions to Equation (3.1) for different numbers of iterations, after applying the scheme in Equation (3.3) and the initial condition stated above. It appears that solutions are tending towards a steady state, as is confirmed in the plot on the bottom of Figure 3.2. This plot shows the agreement of the long term numerical behaviour with the analytical steady state. Recall that Equation (3.1) has steady states of

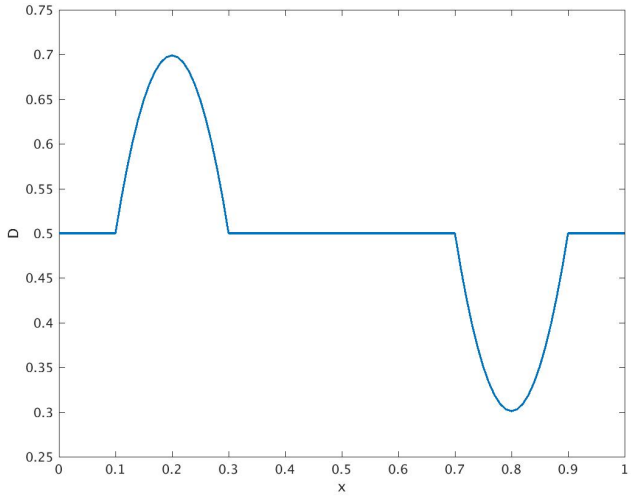


Figure 3.1: 1D Diffusion Coefficient. The spatially dependent diffusion coefficient $D(x)$. It is chosen to display enhanced diffusion when $0.1 \leq x \leq 0.3$, and reduced diffusion when $0.7 \leq x \leq 0.9$.

the form $C/D(x)$, as can be seen in the plot.

We see from the simulations that the long-term numerical behaviour matches with the theoretical steady state. We also see that the highest values of the steady state solution correspond to the smallest values of the diffusion coefficient. This initially may seem counterintuitive, but in fact makes sense. Where the diffusion coefficient is high, all of the cells diffuse away more quickly than they diffuse into this region, resulting in the local minimum observed in the plot.

### 3.1.1 Stability of Numerical Method

In order to simulate Equation (3.2), we used an explicit finite difference scheme, with forward time and centred space. Here we derive a necessary condition for stability. To do this, we will use the method of von Neumann stability analysis.

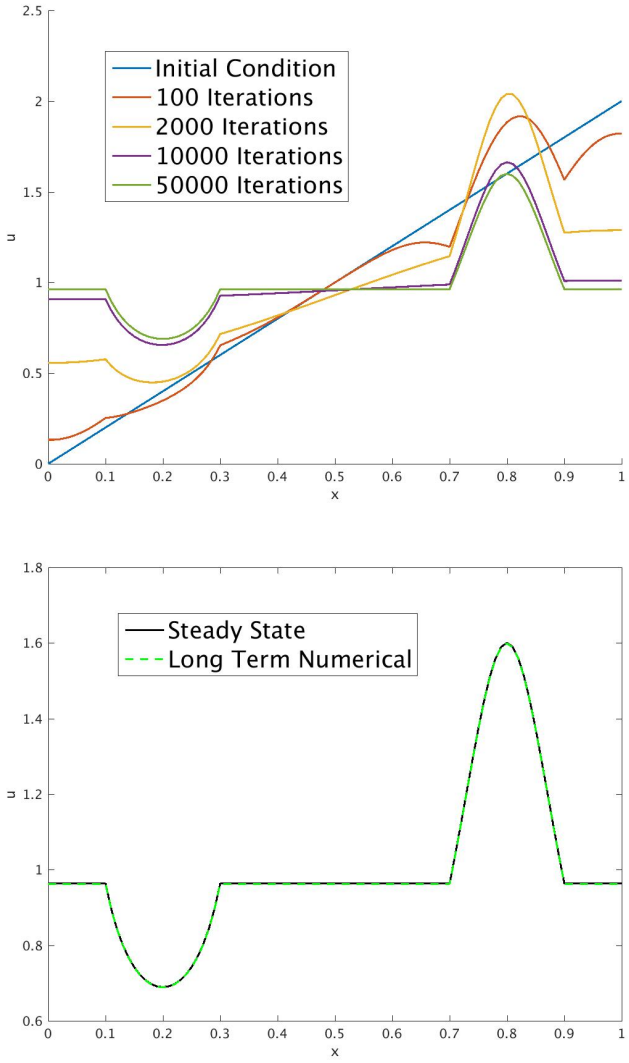


Figure 3.2: 1D Solutions. (a) Plot of solutions to Equation (3.1), for 0, 100, 2000, 10000 and 50000 iterations. (b) Plot of the long term numerical behaviour (50000 iterations) with the theoretical steady state solution.

We follow the explanation as in [64], though the method can be found in many sources. Recall that we are using the discretization shown in Equation (3.3). We begin by substituting in a single Fourier mode $\phi_j^n = \xi^n e^{ikjh}$, where $k$ is the wave number and $jh = x$. For stability, we require that the ratio $|\xi^{n+1}/\xi^n| < 1$. We note here that $n$ represents the time level. Plugging this mode into the above scheme and simplifying, we get

$$\frac{\xi^{n+1}}{\xi^n} = 1 - 2\frac{D(x)\tau}{h^2} + 2\frac{D(x)\tau}{h^2} i \sin(kh),$$

where we have used the fact that $e^{ikh} - e^{-ikh} = 2i\sin(kh)$. We therefore see that, because $|\sin(kh)| \leq 1$, we have

$$\left|\frac{\xi^{n+1}}{\xi^n}\right| = \left|1 - 2\frac{D(x)\tau}{h^2} + 2\frac{D(x)\tau}{h^2} i \sin(kh)\right| \leq \left(1 - 2\frac{D(x)\tau}{h^2}\right)^2 + \left(2\frac{D(x)\tau}{h^2}\right)^2.$$

A necessary condition for stability is that $\xi^{n+1}/\xi^n < 1$. We thus have a condition on stability:

$$\frac{2D(x)k}{h^2} < 1 \iff D(x)\frac{\tau}{h^2} < \frac{1}{2}.$$

We thus must keep this condition in mind for our simulations. We omit the stability analysis for higher dimensions, but assume a similar condition exists.

## 3.2 Two-dimensional Simulations

While the one-dimensional simulations give us valuable information about the relationship between steady states and diffusion rates, it has little applicability in the case of brain tumours, and ultimately we will need to look at higher dimensional simulations. We now consider a two-dimensional simulation and

a diffusion coefficient that is both spatially dependent and anisotropic, corresponding to the situation that we would expect to find within the brain. We will also now add a logistic growth term, intended to simulate cell division. This growth term takes the form

$$u_t = ru(1-u),$$

where $r$ defines the growth rate. Logistic growth behaves like exponential growth when the cell density is small, but will tend to 0 as the cell density approaches a carrying capacity (1 in this case). This growth will be included in the numerical methods described in the following sections.

To begin with, we will consider a simplified domain containing a vertical fibre and a horizontal fibre and see how the solution distribution varies due to the presence of these fibres. The purpose of looking at these solutions is so that we may observe the behaviour of the Painter-Hillen model without the complication of a brain domain.

### 3.2.1 Numerical Methods

Because the diffusion tensors are symmetric, as can be seen from the calculation of the second moment of the bimodal von Mises distribution in Chapter 2, we may define the tensor with three parameters: $\alpha$, $\gamma$ and $\beta$. These correspond to the three degrees of freedom in the two-dimensional, spatially dependent diffusion tensor. The two-dimensional Painter-Hillen model given in Equation (1.12), with logistic growth added, can then be written as

$$u_t = \nabla\nabla : \left( \begin{bmatrix} \alpha(\boldsymbol{x}) & \beta(\boldsymbol{x}) \\ \beta(\boldsymbol{x}) & \gamma(\boldsymbol{x}) \end{bmatrix} \right) u + ru(1-u), \tag{3.4}$$

which expands to

$$u_t = (\alpha(\boldsymbol{x})u)_{x_1x_1} + (\beta(\boldsymbol{x})u)_{x_1x_2} + (\beta(\boldsymbol{x})u)_{x_2x_1} + (\gamma(\boldsymbol{x})u)_{x_2x_2} + ru(1-u).$$

Following the natural substitution that was done in the one-dimensional case, let

$$\begin{aligned} v_1 &= \alpha(\boldsymbol{x})u, \\ v_2 &= 2\beta(\boldsymbol{x})u, \\ v_3 &= \gamma(\boldsymbol{x})u. \end{aligned}$$

We can compute the following numerical second derivatives:

$$(v_1)^n_{x_1x_1} = \frac{(v_1)^n_{i+1,j} - 2(v_1)^n_{i,j} + (v_1)^n_{i-1,j}}{h_1^2}, \tag{3.5}$$

$$(v_2)^n_{x_1x_2} = (v_2)^n_{x_2x_1} = \frac{(v_2)^n_{i+1,j+1} - (v_2)^n_{i-1,j+1} - (v_2)^n_{i+1,j-1} + (v_2)^n_{i-1,j-1}}{4h_1h_2}, \tag{3.6}$$

$$(v_3)^n_{x_2x_2} = \frac{(v_3)^n_{i,j+1} - 2(v_3)^n_{i,j} + (v_3)^n_{i,j-1}}{h_2^2}, \tag{3.7}$$

where $h_1$ is the $x_1$ spatial step, $h_2$ is the $x_2$ spatial step and $n$ indicates the time level. The $i$ subscripts indicate the $x_1$ direction, while the $j$ subscripts indicate the $x_2$ direction. We then use a forward Euler time-stepping scheme, and obtain the following finite difference scheme:

$$u^{n+1}_{i,j} = k\left((v_1)^n_{x_1x_1} + (v_2)^n_{x_1x_2} + (v_3)^n_{x_2x_2} + ru^n_{i,j}(1-u^n_{i,j}))\right) + u^n_{i,j}, \tag{3.8}$$

where $k$ gives the time step and the second derivatives are given by Equations (3.5)-(3.7) for spatial level $(i,j)$.

### Boundary Conditions

We stated in the introduction of the model, that we would be using no-flux boundary conditions. For this particular model, this is equivalent to

$$\boldsymbol{n} \cdot (\nabla \cdot (D(\boldsymbol{x})u)) = 0,$$

where $\boldsymbol{n}$ is the outward unit normal from the boundary. Because this condition is difficult to implement numerically, we instead take a different approach to ensure that our numerical scheme conserves mass (in the absence of growth). We begin by writing out the full numerical discretization described above:

$$\begin{aligned}\frac{u_{i,j}^{n+1} - u_{i,j}^{n}}{k} = &\frac{(v_1)_{i+1,j}^{n} - 2(v_1)_{i,j}^{n} + (v_1)_{i-1,j}^{n}}{h_1^2} \\ &+ \frac{(v_2)_{i+1,j+1}^{n} - (v_2)_{i+1,j-1}^{n} - (v_2)_{i-1,j+1}^{n} + (v_2)_{i-1,j-1}}{4h_1h_2} \\ &+ \frac{(v_3)_{i,j+1}^{n} - 2(v_3)_{i,j}^{n} + (v_3)_{i,j-1}^{n}}{h_1^2}. \end{aligned} \tag{3.9}$$

Taking the double sum over the domain of the left hand side, this gives

$$\begin{aligned}&\frac{1}{k}\left[\sum_{i=1}^{M}\sum_{j=1}^{N} u_{i,j}^{n+1} - \sum_{i=1}^{M}\sum_{j=1}^{N} u_{i,j}^{n}\right] = \\ &\frac{1}{k}\left[(\text{Total mass at time } n+1) - (\text{Total mass at time } n)\right]. \end{aligned} \tag{3.10}$$

Note that for this section we are assuming a rectangular domain where $x$ goes between $x_1$ and $x_M$, and $y$ goes between $y_1$ and $y_N$. In order to ensure conservation of mass, the mass at time $n+1$ must equal the mass at time $n$, and so the quantity on the left hand side of Equation (3.10) must be equal to 0. To ensure this, we will take the same double sum over the discretization on

the right hand side of Equation (3.9) and force the resulting expression to be 0. We therefore want to force the following condition:

$$\begin{aligned}
0 =& \frac{1}{h_1^2}\sum_{i=1}^{M}\sum_{j=1}^{N}\left((v_1)^n_{i+1,j} - 2(v_1)^n_{i,j} + (v_1)^n_{i-1,j}\right) \\
&+\frac{1}{4h_1h_2}\sum_{i=1}^{M}\sum_{j=1}^{N}\left((v_2)^n_{i+1,j+1} - (v_2)^n_{i+1,j-1} - (v_2)^n_{i-1,j+1} + (v_2)^n_{i-1,j-1}\right) \\
&+\frac{1}{h_2^2}\sum_{i=1}^{M}\sum_{j=1}^{N}\left((v_3)^n_{i,j+1} - 2(v_3)^n_{i,j} + (v_3)^n_{i,j-1}\right).
\end{aligned}$$

Since we are now working only with time level $n$, we drop the time label. Reindexing, we obtain

$$\begin{aligned}
0 =& \frac{1}{h_1^2}\sum_{j=1}^{N}\left[\sum_{i=2}^{M+1}(v_1)_{i,j} - 2\sum_{i=1}^{M}(v_1)_{i,j} + \sum_{i=0}^{M-1}(v_1)_{i,j}\right] \\
&+\frac{1}{4h_1h_2}\sum_{j=1}^{N}\left[\sum_{i=2}^{M+1}(v_2)_{i,j+1} - \sum_{i=2}^{M+1}(v_2)_{i,j-1} - \sum_{i=0}^{M-1}(v_2)_{i,j+1} + \sum_{i=0}^{M-1}(v_2)_{i,j-1}\right] \\
&+\frac{1}{h_2^2}\sum_{j=1}^{N}\left[\sum_{i=2}^{M+1}(v_3)_{i,j} - 2\sum_{i=1}^{M}(v_3)_{i,j} + \sum_{i=0}^{M-1}(v_3)_{i,j}\right].
\end{aligned}$$

We therefore have a number of telescoping sums. Removing all overlapping terms that are subtracted off, we are left with an expression involving boundary terms:

$$\begin{aligned}
0 =& \frac{1}{h_1^2}\sum_{j=1}^{N}[(v_1)_{M+1,j} - (v_1)_{M,j} + (v_1)_{0,j} - (v_1)_{1,j}] \\
&+\frac{1}{4h_1h_2}\sum_{j=1}^{N}[(v_2)_{M,j+1} + (v_2)_{M+1,j+1} - (v_2)_{0,j+1} - (v_2)_{1,j+1} \\
&+(v_2)_{0,j-1} + (v_2)_{1,j-1} - (v_2)_{M,j-1} - (v_2)_{M+1,j-1}]
\end{aligned}$$

$$+\frac{1}{h_2^2}\sum_{i=1}^{M}[(v_3)_{i,N+1} - (v_3)_{i,N} + (v_3)_{i,0} - (v_3)_{i,1}].$$

There are a number of ways to choose the $v_i$s to ensure that this condition is met, however, we will choose the simplest set of boundary conditions:

$$\begin{aligned}
(v_1)_{M+1,j} &= (v_1)_{M,j}, \\
(v_1)_{0,j} &= (v_1)_{1,j}, \quad \text{for } 1 \le j \le N, \\
(v_3)_{i,N+1} &= (v_3)_{i,N}, \\
(v_3)_{i,0} &= (v_3)_{i,1}, \quad \text{for } 1 \le i \le M, \\
(v_2)_{1,j} &= -(v_2)_{0,j}, \\
(v_2)_{M+1,j} &= -(v_2)_{M,j}, \quad \text{for } 1 \le j \le N.
\end{aligned} \tag{3.11}$$

These conditions fully define the needed boundary points for the second derivatives with respect to $x_1$ and $x_2$ ($v_1$ and $v_3$), but only partially define the conditions on the mixed second derivative ($v_2$). A sample $(3 \times 3)$ square domain is shown in Figure 3.3, along with the associated boundary points. Because of the numerical stencils used in calculating the derivatives, $v_1$ need only be defined on the white boundary points to the left and right of the domain. Similarly, $v_3$ need only be defined on the white boundary points above and below the domain. For the mixed second derivative, however, $v_2$ must be defined on all of the white points, and the blue corner points. The condition above defines $v_2$ only on the white boundary points to the left and right of the domain, however we notice that the summation over the second derivative discretization has an equivalent representation:

$$\frac{1}{4h_1h_2}\sum_{j=1}^{N}\left[\sum_{i=2}^{M+1}(v_2)_{i,j+1}-\sum_{i=2}^{M+1}(v_2)_{i,j-1}-\sum_{i=0}^{M-1}(v_2)_{i,j+1}+\sum_{i=0}^{M-1}(v_2)_{i,j-1}\right]=$$
$$\frac{1}{4h_1h_2}\sum_{i=1}^{M}\left[\sum_{j=2}^{N+1}(v_2)_{i+1,j}-\sum_{j=2}^{N+1}(v_2)_{i-1,j}-\sum_{j=0}^{N-1}(v_2)_{i+1,j}+\sum_{j=0}^{N-1}(v_2)_{i-1,j}\right],$$

which gives conditions on $v_2$ for the white boundary points above and below the domain:

$$\begin{aligned}(v_2)_{i,0} &= -(v_2)_{i,1},\\ (v_2)_{i,N+1} &= -(v_2)_{i,N} \text{ for } 1 \le i \le M.\end{aligned} \tag{3.12}$$

Finally, $v_2$ for the corner points can be defined to satisfy the above conditions as

$$\begin{aligned}(v_2)_{M+1,N+1} &= -(v_2)_{M,N+1} = -(v_2)_{M+1,N} = (v_2)_{M,N},\\ (v_2)_{M+1,0} &= -(v_2)_{M,0} = -(v_2)_{M+1,1} = (v_2)_{M,1},\\ (v_2)_{0,0} &= -(v_2)_{0,1} = -(v_2)_{1,0} = (v_2)_{1,1},\\ (v_2)_{0,N+1} &= -(v_2)_{0,N} = -(v_2)_{1,N+1} = (v_2)_{1,N}.\end{aligned} \tag{3.13}$$

It turns out that we do not need explicit boundary conditions on $u$ itself, as all derivatives are computed using $v_1$, $v_2$ and $v_3$, hence the set of conditions given for $v_1$, $v_2$ and $v_3$ is sufficient.

### 3.2.2 Simulations on a Simplified Domain

Now we will solve this system numerically using the explicit finite difference scheme just described. We will solve it on what we will refer to as a "simplified

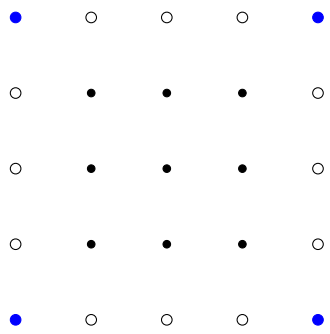

Figure 3.3: Boundary Conditions. Grid representing a simple $3 \times 3$ grid and accompanying ghost points to satisfy the boundary conditions outlined in this section. The points of the domain are shown in black, while the ghost points are shown in white and blue. A distinction is made between "edge" points (white) and "corner" points (blue).

domain", meaning that it is not the full brain data, but rather artificially defined DTI data. We will define this data to approximate a vertical fibre and a horizontal fibre, crossing in the middle of a square domain of size $(100 \times 100)$. We will then initialize a Gaussian distribution and observe how the cell density interacts with this domain as it diffuses according to Equation (1.9). To set up the artificial domain, we will approximately follow the procedure outlined in Painter and Hillen [5], which we will extend to three dimensions in the next section.

To begin, we will initialize an artificial DTI dataset following Equation (24) from Painter and Hillen [5]:

$$\begin{aligned}
\alpha(x, y) &= 0.5 - d_1(x, y) + d_2(x, y), \\
\beta(x, y) &= 0, \\
\gamma(x, y) &= 0.5 + d_1(x, y) - d_2(x, y),
\end{aligned}$$

where

$$d_1(x,y) = 0.25e^{-0.05(x-50)^2}, \text{ and } d_2(x,y) = 0.25e^{0.5(y-50)^2}.$$

Recall that $\alpha$ is the (1,1) component of the two-dimensional diffusion tensor, $\gamma$ is the (2,2) component, and $\beta$ defines the off-diagonals of the symmetric tensor, as per Equation (3.4). This serves to create a thin fibre in the $x$ direction, and a wider fibre in the $y$ direction. Once the artificial DTI dataset is constructed, it is scaled according to the procedure described in Chapter 2 to obtain $D_c$ for three different values of the anisotropy parameter: $\kappa$=0, $\kappa$ =10 and $\kappa$ =50. The artificial DTI data, as well as the results of these scalings are shown in Figure 3.4. We can see in this image that when observing the $\alpha$ parameter, it is high along the horizontal fibre and low along the vertical fibre. Since the diffusion tensor we are using is diagonal, $\alpha$ represents the principal value associated with the vector $[1,0]^T$. Similarly, $\gamma$ represents the principal value associated with the vector $[0,1]^T$, and hence is high along the vertical fibre, and low along the horizontal fibre. We also note that as $\kappa$ increases from 0 to 50, the bands get darker, indicating a stronger directional tendency.

For the initial condition, we define

$$g(x,y) = 0.1e^{-\left((x-35)^2+(y-35)^2\right)},$$

so that we have a sharp Gaussian centered at the point (35,35). This is meant to simulate a small tumour beginning to grow. A growth rate of $r = 0.3$ is used, while the diffusion tensors are scaled by setting $\frac{1}{\mu^2} = 0.5$.

Simulation results are shown for $t = 0$ (the initial condition), $t = 8$. $t = 16$, $t = 24$ and $t = 32$ in Figure 3.5. The resulting simulations are greatly affected

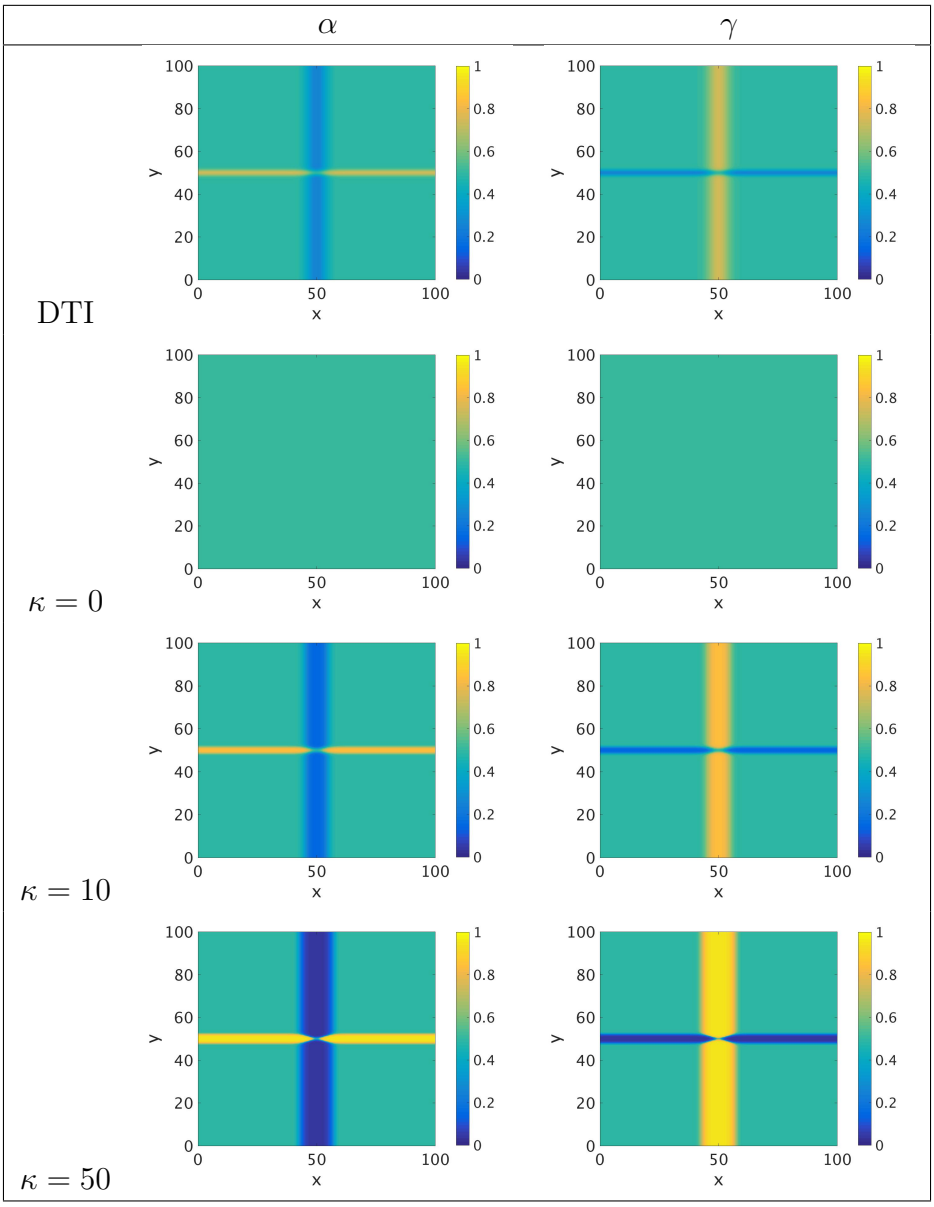


Figure 3.4: 2D Fibre Domain. Plot of the diagonal components, $\alpha$ (left) and $\gamma$ (right), for the two-dimensional diffusion tensor. The first row shows the artificially defined DTI data, with subsequent rows showing the result of scaling the DTI data according to the procedure in Chapter 2 for varying values of the anisotropy parameter. The second row corresponds to $\kappa = 0$ (isotropic), the third row corresponds to $\kappa = 10$, and the bottom row to $\kappa = 50$. The colour indicates the value of $\alpha$ (left) and $\gamma$ (right), with yellow=high and blue=low. Notice that the directional tendency increases with increasing $\kappa$.

by the anisotropy parameter. The higher the value of $\kappa$, the more the cells diffuse along the white matter fibres. The top row of Figure 3.5 shows the results after different numbers of iterations, for $\kappa = 0$. For this case, the spread is isotropic and the resulting distribution is radially symmetric. The cells spread over the fibres without even noticing their presence. The second row of Figure 3.5 shows the results after different numbers of iterations for $\kappa = 10$. For this case, we can see that the cell density distribution begins to expand along the fibres. This effect is seen even more strongly in the bottom row, where $\kappa = 50$. We also see that the cells tend to collect along the fibres, particularly for higher values of $\kappa$. This is because the rate of spread along the fibres is much higher than the rate of spread perpendicularly, making it difficult for cells to move off of a fibre. We will see in Chapters 4 and 5 that $\kappa$ will play an important role in the simulation of real patients' gliomas.

## 3.3 Three-dimensional Simulations

It is most realistic to consider simulations in three dimensions since the brain is a three-dimensional object. Many of the ideas from two dimensions extend in a natural way when another dimension is added.

### 3.3.1 Numerical Methods

We begin again with the model Equation (1.9). Again, we have that the three-dimensional diffusion tensor is symmetric, thus we define 6 individual quantities: $D_{11}(\boldsymbol{x})$, $D_{12}(\boldsymbol{x})$, $D_{13}(\boldsymbol{x})$, $D_{22}(\boldsymbol{x})$, $D_{23}(\boldsymbol{x})$, and $D_{33}(\boldsymbol{x})$. Writing

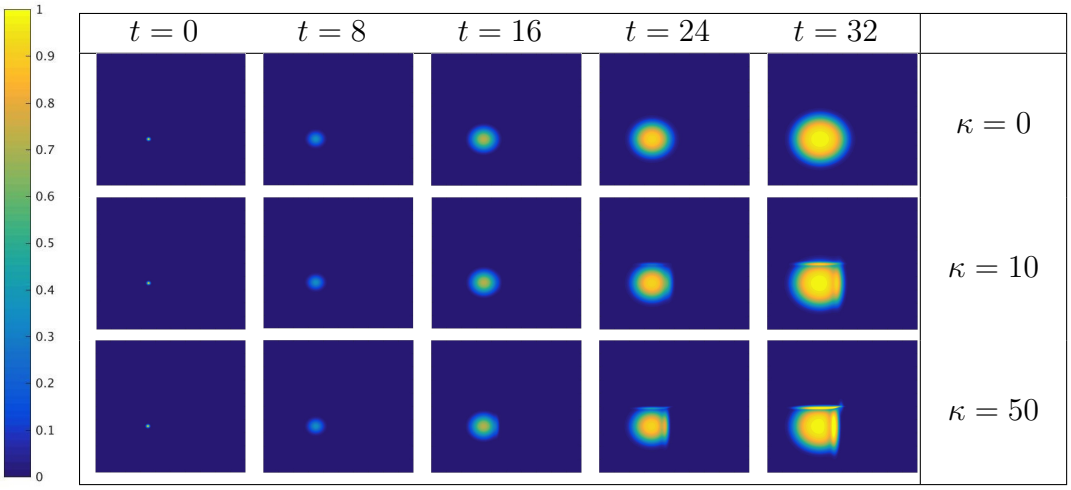


Figure 3.5: 2D Simple Domain Results. The results of simulating Equation (3.4) for varying values of the anisotropy parameter, and varying time points. The first row corresponds to $\kappa = 0$, the second to $\kappa = 10$, and the third to $\kappa$=50. The columns correspond to time points of $t = 0$, 8, 16, 24 and 32, respectively. The colour corresponds to cell density, with yellow=high and dark blue=low. Notice that for increasing $\kappa$, cells have a stronger tendency to follow the fibres. They also have a tendency to collect on the fibres for higher $\kappa$, as movement in the perpendicular directions is greatly reduced.

this out, we have

$$u_t = \nabla\nabla : \left( \begin{bmatrix} D_{11}(\mathbf{x}) & D_{12}(\mathbf{x}) & D_{13}(\mathbf{x}) \\ D_{12}(\mathbf{x}) & D_{22}(\mathbf{x}) & D_{23}(\mathbf{x}) \\ D_{13}(\mathbf{x}) & D_{23}(\mathbf{x}) & D_{33}(\mathbf{x}) \end{bmatrix} u \right) + ru(1-u), \tag{3.14}$$

and this can be expanded to

$$\begin{aligned} u_t = (D_{11}(\mathbf{x})u)_{xx} + (D_{12}(\mathbf{x})u)_{xy} + (D_{13}(\mathbf{x})u)_{xz} + (D_{12}(\mathbf{x})u)_{yx} + (D_{22}(\mathbf{x})u)_{yy} \\ + (D_{23}(\mathbf{x})u)_{yz} + (D_{13}(\mathbf{x})u)_{zx} + (D_{23}(\mathbf{x})u)_{zy} + (D_{33}(\mathbf{x})u)_{zz} + ru(1-u). \end{aligned} \tag{3.15}$$

As we did in two dimensions, we will make the following substitutions:

$$\begin{aligned} v_1 &= D_{11}u, \\ v_2 &= D_{22}u, \\ v_3 &= D_{33}u, \\ v_4 &= 2D_{12}u, \\ v_5 &= 2D_{13}u, \\ v_6 &= 2D_{23}u. \end{aligned}$$

We compute the following numerical second derivatives

$$(v_1)^n_{xx} = \frac{(v_1)^n_{i+1,j,l} - 2(v_1)^n_{i,j,l} + (v_1)^n_{i-1,j,l}}{h_1^2}, \tag{3.16}$$

$$(v_2)^n_{yy} = \frac{(v_2)^n_{i,j+1,l} - 2(v_2)^n_{i,j,l} + (v_2)^n_{i,j-1,l}}{h_2^2}, \tag{3.17}$$

$$(v_3)^n_{zz} = \frac{(v_3)^n_{i,j,l+1} - 2(v_3)^n_{i,j,l} + (v_3)^n_{i,j,l-1}}{h_3^2}, \tag{3.18}$$

$$(v_4)^n_{yx} = (v_4)^n_{xy} = \frac{(v_4)^n_{i+1,j+1,l} - (v_4)^n_{i-1,j+1,l} - (v_4)^n_{i+1,j-1,l} + (v_4)^n_{i-1,j-1,l}}{4h_1h_2}, \tag{3.19}$$

$$(v_5)^n_{zx} = (v_5)^n_{xz} = \frac{(v_5)^n_{i+1,j,l+1} - (v_5)^n_{i-1,j,l+1} - (v_5)^n_{i+1,j,l-1} + (v_5)^n_{i-1,j,l-1}}{4h_1h_3}, \tag{3.20}$$

$$(v_6)^n_{zy} = (v_6)^n_{yz} = \frac{(v_6)^n_{i,j+1,l+1} - (v_6)^n_{i,j+1,l-1} - (v_6)^n_{i,j-1,l+1} + (v_6)^n_{i,j-1,l-1}}{4h_2h_3}, \tag{3.21}$$

$$\tag{3.22}$$

where $h_1$ is the spatial step for $x$, $h_2$ is the spatial step for $y$ and $h_3$ is the spatial step for $z$. The $i$ subscripts correspond to $x$, the $j$ subscripts to $y$, and the $l$ subscripts to $z$. Using a forward Euler scheme in time, we then have the following scheme for $u$:

$$\begin{aligned} & u^{n+1}_{i,j,l} \\ &= k\left((v_1)^n_{xx} + (v_2)^n_{yy} + (v_3)^n_{zz} + (v_4)^n_{xy} + (v_5)^n_{xz} + (v_6)^n_{yz}) + ru^n_{i,j}(1 - u^n_{i,j})\right) + u^n_{i,j,l} \end{aligned}$$

where $k$ is the time step and the second derivatives are computed as in Equations (3.16)-(3.22) for spatial level $(i, j)$.

### Boundary Conditions

In three dimensions, we again have no-flux boundary conditions, as we wish to prevent cells from diffusing through the skull in order to have a realistic biological model. Note however that in this chapter we consider only rectangular domains. We will use a similar process to derive the boundary conditions to that which was used to derive the two-dimensional conditions, ensuring that mass in conserved. We begin by once again writing out the full numerical discretization described above (without the growth term):

$$\frac{u^{n+1}_{i,j,l} - u^n_{i,j,l}}{k} = \frac{(v_1)^n_{i+1,j,l} - 2(v_1)^n_{i,j,l} + (v_1)^n_{i-1,j,l}}{h_1^2}$$

$$
\begin{aligned}
&+ \frac{(v_2)^n_{i,j+1,l} - 2(v_2)^n_{i,j,l} + (v_2)^n_{i,j-1,l}}{h_2^2} \\
&+ \frac{(v_3)^n_{i,j,l+1} - 2(v_3)^n_{i,j,l} + (v_3)^n_{i,j,l-1}}{h_3^2} \\
&+ \frac{(v_4)^n_{i+1,j+1,l} - (v_4)^n_{i-1,j+1,l} - (v_4)^n_{i+1,j-1,l} + (v_4)^n_{i-1,j-1,l}}{4h_1h_2} \\
&+ \frac{(v_5)^n_{i+1,j,l+1} - (v_5)^n_{i-1,j,l+1} - (v_5)^n_{i+1,j,l-1} + (v_5)^n_{i-1,j,l-1}}{4h_1h_3} \\
&+ \frac{(v_6)^n_{i,j+1,l+1} - (v_6)^n_{i,j+1,l-1} - (v_6)^n_{i,j-1,l+1} + (v_6)^n_{i,j-1,l-1}}{4h_2h_3}. \quad (3.23)
\end{aligned}
$$

Taking the triple sum over the domain of the left hand side, this will give

$$
\begin{aligned}
&\frac{1}{k}\left[\sum_{i=1}^{M}\sum_{j=1}^{N}\sum_{l=1}^{P} u^{n+1}_{i,j,l} - \sum_{i=1}^{M}\sum_{j=1}^{N}\sum_{l=1}^{P} u^{n}_{i,j,l}\right] = \\
&\frac{1}{k}\left[(\text{Total mass at time } n+1) - (\text{Total mass at time } n)\right]. \quad (3.24)
\end{aligned}
$$

For this section we are assuming a cube domain where we still have $x$ between $x_1$ and $x_M$, and $y$ between $y_1$ and $y_N$, however now we have a third dimension $z$ between $z_1$ and $z_P$. In order to ensure conservation of mass, the mass at time $n+1$ must equal the mass at time $n$, and so the quantity on the left hand side of Equation (3.24) must be equal to 0. To ensure this, we take the same triple sum over the discretization on the right hand side and force the resulting expression to be 0. We therefore want to force the following condition:

$$
\begin{aligned}
0 =& \frac{1}{h_1^2}\sum_{i=1}^{M}\sum_{j=1}^{N}\sum_{l=1}^{P}\left((v_1)^n_{i+1,j,l} - 2(v_1)^n_{i,j,l} + (v_1)^n_{i-1,j,l}\right) \\
&+ \frac{1}{h_2^2}\sum_{i=1}^{M}\sum_{j=1}^{N}\sum_{l=1}^{P}\left((v_2)^n_{i,j+1,l} - 2(v_2)^n_{i,j,l} + (v_2)^n_{i,j-1,l}\right)
\end{aligned}
$$

$$
\begin{aligned}
&+\frac{1}{h_3^2}\sum_{i=1}^{M}\sum_{j=1}^{N}\sum_{l=1}^{P}\left((v_3)_{i,j,l+1}^n-2(v_3)_{i,j,l}^n+(v_3)_{i,j,l-1}^n\right)\\
&+\frac{1}{4h_1h_2}\sum_{i=1}^{M}\sum_{j=1}^{N}\sum_{l=1}^{P}\left((v_4)_{i+1,j+1,l}^n-(v_4)_{i-1,j+1,l}^n-(v_4)_{i+1,j-1,l}^n+(v_4)_{i-1,j-1,l}^n\right)\\
&+\frac{1}{4h_1h_3}\sum_{i=1}^{M}\sum_{j=1}^{N}\sum_{l=1}^{P}\left((v_5)_{i+1,j,l+1}^n-(v_5)_{i-1,j,l+1}^n-(v_5)_{i+1,j,l-1}^n+(v_5)_{i-1,j,l-1}^n\right)\\
&+\frac{1}{4h_2h_3}\sum_{i=1}^{M}\sum_{j=1}^{N}\sum_{l=1}^{P}\left((v_6)_{i,j+1,l+1}^n-(v_6)_{i,j+1,l-1}^n-(v_6)_{i,j-1,l+1}^n+(v_6)_{i,j-1,l-1}^n\right).
\end{aligned}
$$

Since we are now working only with time level $n$, we drop the time label. Reindexing, we obtain

$$
\begin{aligned}
0=&\frac{1}{h_1^2}\sum_{j=1}^{N}\sum_{l=1}^{P}\left[\sum_{i=2}^{M+1}(v_1)_{i,j,l}-2\sum_{i=1}^{M}(v_1)_{i,j,l}+\sum_{i=0}^{M-1}(v_1)_{i,j,l}\right]\\
&+\frac{1}{h_2^2}\sum_{i=1}^{M}\sum_{l=1}^{P}\left[\sum_{j=2}^{N+1}(v_2)_{i,j,l}-2\sum_{j=1}^{N}(v_2)_{i,j,l}+\sum_{j=0}^{N-1}(v_2)_{i,j,l}\right]\\
&+\frac{1}{h_3^2}\sum_{i=1}^{M}\sum_{j=1}^{N}\left[\sum_{l=2}^{P+1}(v_3)_{i,j,l}-2\sum_{l=1}^{P}(v_3)_{i,j,l}+\sum_{l=0}^{P-1}(v_3)_{i,j,l}\right]\\
&+\frac{1}{4h_1h_2}\sum_{l=1}^{P}\sum_{j=1}^{N}\left[\sum_{i=2}^{M+1}(v_4)_{i,j+1,l}-\sum_{i=0}^{M-1}(v_4)_{i,j+1,l}-\sum_{i=2}^{M+1}(v_4)_{i,j-1,l}+\sum_{i=0}^{M-1}(v_4)_{i,j-1,l}\right]\\
&+\frac{1}{4h_1h_3}\sum_{i=1}^{M}\sum_{j=1}^{N}\left[\sum_{l=2}^{P+1}(v_5)_{i+1,j,l}-\sum_{l=0}^{P-1}(v_5)_{i+1,j,l}-\sum_{l=2}^{P+1}(v_5)_{i-1,j,l}+\sum_{l=0}^{P-1}(v_5)_{i-1,j,l}\right]\\
&+\frac{1}{4h_2h_3}\sum_{i=1}^{M}\sum_{l=1}^{P}\left[\sum_{j=2}^{N+1}(v_6)_{i,j,l+1}-\sum_{j=0}^{N-1}(v_6)_{i,j,l+1}-\sum_{j=2}^{N+1}(v_6)_{i,j,l-1}+\sum_{j=0}^{N-1}(v_6)_{i,j,l-1}\right].
\end{aligned}
$$

Once again, we have a number of telescoping sums, with only certain

boundary terms left over. The resulting condition is

$$\begin{aligned}
0 =&\frac{1}{h_1^2}\sum_{j=1}^{N}\sum_{l=1}^{P}[(v_1)_{M+1,j,l} - (v_1)_{M,j,l} + (v_1)_{0,j,l} - (v_1)_{1,j,l}] \\
&+\frac{1}{h_2^2}\sum_{i=1}^{M}\sum_{l=1}^{P}[(v_2)_{i,N+1,l} - (v_2)_{i,N,l} + (v_2)_{i,0,l} - (v_2)_{i,1,l}] \\
&+\frac{1}{h_3^2}\sum_{i=1}^{M}\sum_{j=1}^{N}[(v_3)_{i,j,P+1} - (v_3)_{i,j,P} + (v_3)_{i,j,0} - (v_3)_{i,j,1}] \\
&+\frac{1}{4h_1h_2}\sum_{l=1}^{P}\sum_{j=1}^{N}[(v_4)_{M+1,j+1,l} + (v_4)_{M,j+1,l} - (v_4)_{0,j+1,l} - (v_4)_{1,j+1,l} \\
&\qquad\qquad - (v_4)_{M+1,j-1,l} - (v_4)_{M,j-1,l} + (v_4)_{0,j-1,l} + (v_4)_{1,j-1,l}] \\
&+\frac{1}{4h_1h_3}\sum_{i=1}^{M}\sum_{j=1}^{N}[(v_5)_{i+1,j,P+1} + (v_5)_{i+1,j,P} - (v_5)_{i+1,j,0} - (v_5)_{i+1,j,1} \\
&\qquad\qquad - (v_5)_{i-1,j,P+1} - (v_5)_{i-1,j,P} + (v_5)_{i-1,j,0} + (v_5)_{i-1,j,1}] \\
&+\frac{1}{4h_2h_3}\sum_{i=1}^{M}\sum_{l=1}^{P}[(v_6)_{i,N+1,l+1} + (v_6)_{i,N,l+1} - (v_6)_{i,0,l+1} - (v_6)_{i,1,l+1} \\
&\qquad\qquad - (v_6)_{i,N+1,l-1} - (v_6)_{i,N,l-1} + (v_6)_{i,0,l-1} + (v_6)_{i,1,l-1}].
\end{aligned}$$

As in two dimensions, there is not a unique method for choosing the boundary conditions so that conservation of mass is satisfied, however we will choose the conditions that are the simplest, and that make the most sense. Recall that for the mixed second derivatives, we obtain two sets of conditions which can be seen by rewriting the sums, as was done in two dimensions. We will omit this step here. We therefore obtain conditions on $v_1$:

$$
\begin{aligned}
(v_1)_{0,j,l} &= (v_1)_{i,j,l}, \\
(v_1)_{M+1,j,l} &= (v_1)_{M,j,l}, \quad \text{for } 1 \le j \le N, 1 \le l \le P,
\end{aligned} \tag{3.25}
$$

and on $v_2$:

$$
\begin{aligned}
(v_2)_{0,j,l} &= (v_2)_{i,j,l}, \\
(v_2)_{M+1,j,l} &= (v_2)_{M,j,l}, \quad \text{for } 1 \le j \le N, 1 \le l \le P,
\end{aligned} \tag{3.26}
$$

and on $v_3$:

$$
\begin{aligned}
(v_3)_{0,j,l} &= (v_3)_{i,j,l}, \\
(v_3)_{M+1,j,l} &= (v_3)_{M,j,l}, \quad \text{for } 1 \le j \le N, 1 \le l \le P.
\end{aligned} \tag{3.27}
$$

The conditions on $v_4$ are given by:

$$
\begin{aligned}
(v_4)_{M+1,j,l} &= -(v_4)_{M,j,l}, \\
(v_4)_{0,j,l} &= -(v_4)_{1,j,l}, \quad \text{for } 1 \le j \le N, 1 \le l \le P, \\
(v_4)_{i,N+1,l} &= -(v_4)_{i,N,l}, \\
(v_4)_{i,0,l} &= -(v_4)_{i,1,l}, \quad \text{for } 1 \le i \le M, 1 \le l \le P,
\end{aligned} \tag{3.28}
$$

with edge conditions

$$
\begin{aligned}
(v_4)_{M+1,N+1,l} &= (v_4)_{M,N,l}, \\
(v_4)_{M+1,0,l} &= (v_4)_{M,1,l}, \\
(v_4)_{0,0,l} &= (v_4)_{1,1,l},
\end{aligned}
$$

$$(v_4)_{0,M+1,l} = (v_4)_{1,M,l}, \quad \text{for } 1 \le l \le P. \tag{3.29}$$

The conditions on $v_5$ are

$$\begin{aligned}
(v_5)_{i,j,P+1} &= -(v_5)_{i,j,P}, \\
(v_5)_{i,j,0} &= -(v_5)_{i,j,1}, \quad \text{for } 1 \le i \le M, 1 \le j \le N \\
(v_5)_{M+1,j,l} &= -(v_5)_{M,j,l}, \\
(v_5)_{0,j,l} &= -(v_5)_{1,j,l}, \quad \text{for } 1 \le j \le N, 1 \le l \le P,
\end{aligned} \tag{3.30}$$

with edge conditions

$$\begin{aligned}
(v_5)_{M+1,j,P+1} &= (v_5)_{M,j,P}, \\
(v_5)_{M+1,j,0} &= (v_5)_{M,j,1}, \\
(v_5)_{0,j,0} &= (v_5)_{1,j,1}, \\
(v_5)_{0,j,P+1} &= (v_5)_{1,j,P}, \quad \text{for } 1 \le j \le N.
\end{aligned} \tag{3.31}$$

Finally, the conditions on $v_6$ are given by

$$\begin{aligned}
(v_6)_{i,j,P+1} &= -(v_6)_{i,j,P}, \\
(v_6)_{i,j,0} &= -(v_6)_{i,j,1}, \quad \text{for } 1 \le i \le M, 1 \le j \le N \\
(v_6)_{i,N+1,l} &= -(v_6)_{i,N,l}, \\
(v_6)_{i,0,l} &= -(v_6)_{i,1,l}, \quad \text{for } 1 \le i \le M, 1 \le l \le P,
\end{aligned} \tag{3.32}$$

with edge conditions

$$\begin{aligned}(v_6)_{i,N+1,P+1} &= (v_6)_{i,N,P},\\ (v_6)_{i,N+1,0} &= (v_6)_{i,N,1},\\ (v_6)_{i,0,0} &= (v_6)_{i,1,1},\\ (v_6)_{i,0,P+1} &= (v_6)_{i,1,P}, \quad \text{for } 1 \leq i \leq M. \end{aligned} \tag{3.33}$$

### 3.3.2 Simulations on a Simplified Domain

Now we will implement the numerical method just described on a three-dimensional simplified domain. We will follow the method of the two dimensional domain, creating an artificial fibre in each dimension: $x$, $y$ and $z$, and using a cube domain of dimension $(100 \times 100 \times 100)$. The purpose of these simulations is to show the behaviour of the model on a basic domain before implementing it on a more complicated brain domain. Extending the method of Painter and Hillen [5], we define the artificial DTI data as

$$\begin{aligned}D_{11}(x,y,y) &= 0.5 + d_2(y,z) - d_3(x,z) - d_1(x,y),\\ D_{12}(x,y,z) &= 0,\\ D_{22}(x,y,z) &= 0.5 + d_3(x,z) - d_1(x,y) - d_2(y,z),\\ D_{23}(x,y,z) &= 0,\\ D_{33}(x,y,z) &= 0.5 + d_1(x,y) - d_3(x,z) - d_2(y,z),\\ D_{13}(x,y,z) &= 0,\end{aligned}$$

where

$$d_1(x,y) = 0.25e^{\left(-0.05\left((x-50)^2+(y-50)^2\right)\right)},$$
$$d_2(y,z) = 0.25e^{\left(-0.5\left((y-50)^2+(z-50)^2\right)\right)},$$
$$d_3(x,z) = 0.25e^{\left(-0.05\left((x-50)^2+(z-50)^2\right)\right)}.$$

This artificial DTI data is then scaled as per the method described in Chapter 2 to determine $D_c$. We use the same three values of $\kappa$: 0, 10 and 50. The original DTI data are plotted as isosurfaces of $D_{11}$, $D_{22}$ and $D_{33}$ on the top of Figure 3.6, to demonstrate the artificial fibre domain. The results of the scalings for $\kappa = 0, 10$ and 50 are shown on the bottom, in the first, second and third columns of Figure 3.6, respectively. The first row is a slice through the centre ($z = 50$) of the three-dimensional $D_{11}$, showing the fibres in the $x$- and $y$-directions. The value of $D_{11}$ is high in the fibre parallel to the $x$-direction, since this is the principal value corresponding to the vector $[1,0,0]^T$. The second row shows a slice through the centre of $D_{22}$ ($z = 0$), again showing the fibres in the $x$- and $y$-directions. This component, however is high in the fibre aligned with the $y$-direction, since it represents the principal value corresponding to the vector $[0,1,0]^T$. Finally, the third row shows a slice through the middle ($y = 50$) of $D_{33}$. This shows the fibres in the $x$- and $z$-directions, having a high value in the fibre aligned with the $z$-direction, as this is the principal value associated with the vector $[0,0,1]^T$.

We define a three-dimensional Gaussian as the initial condition, this time centred at (40,40,40). Then

$$g(x,y,z) = e^{-\left((x-40)^2+(x-40)^2+(x-40)^2\right)}.$$

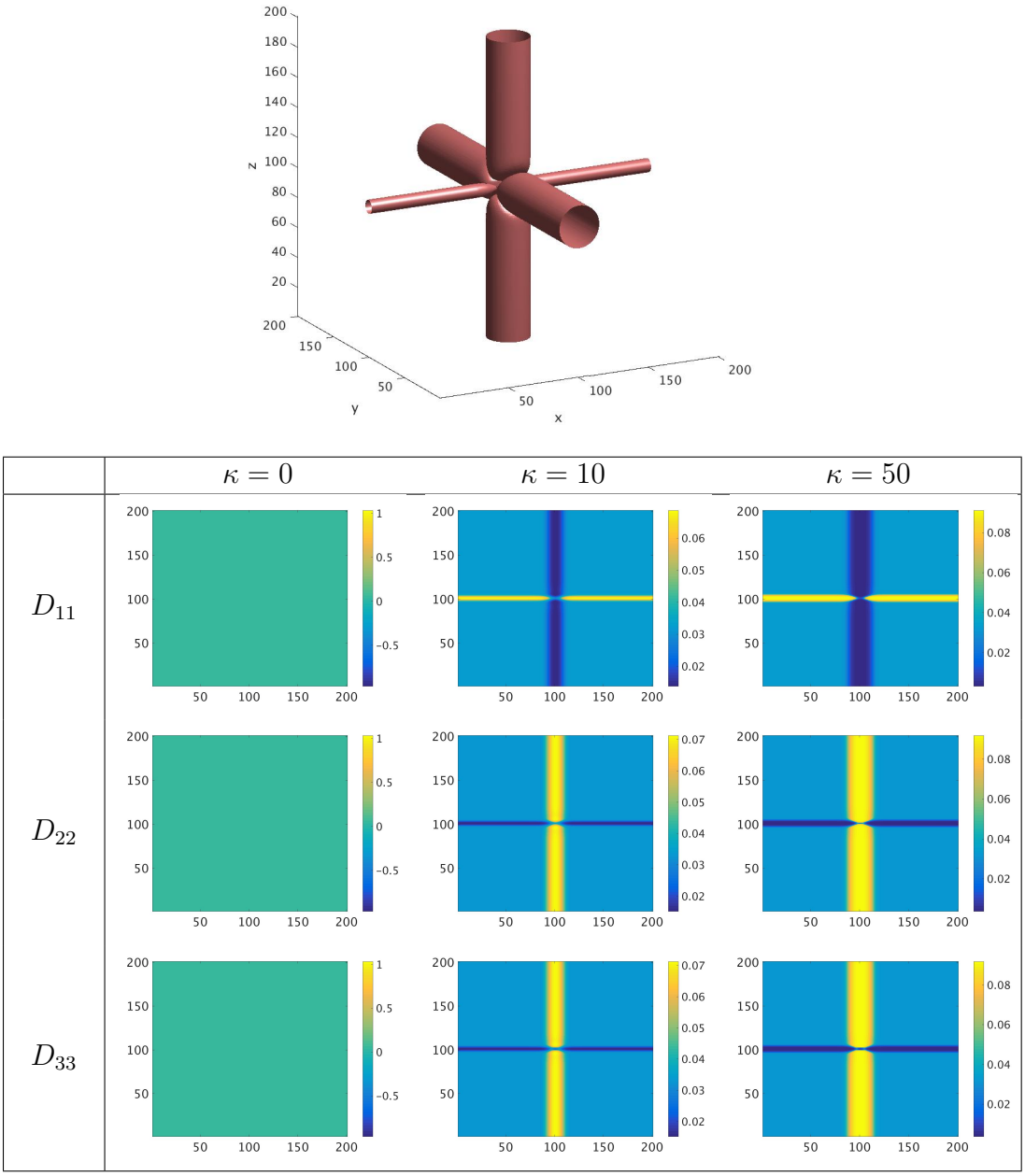


Figure 3.6: 3D Fibre Domain. The DTI fibre structure plotted as level sets of $D_{11}$, $D_{22}$ and $D_{33}$ (top). Slices through the middle of $D_{11}$ (z=50), $D_{22}$ (z=50) and $D_{33}$ (y=50) in rows one, two and three respectively (bottom). The columns correspond to different values of the anisotropy parameter: $\kappa = 0$ (left), $\kappa = 10$ (middle) and $\kappa = 50$ (right).

A growth rate of $r = 0.06$ is used, and the diffusion tensors are scaled by setting $\frac{s}{\mu^2}$=0.1. Once again, we look at the results of for three different time points for three values of the anisotropy parameter: $\kappa = 0$, $\kappa = 10$ and $\kappa = 50$. The results of these simulations are shown in Figure 3.7.

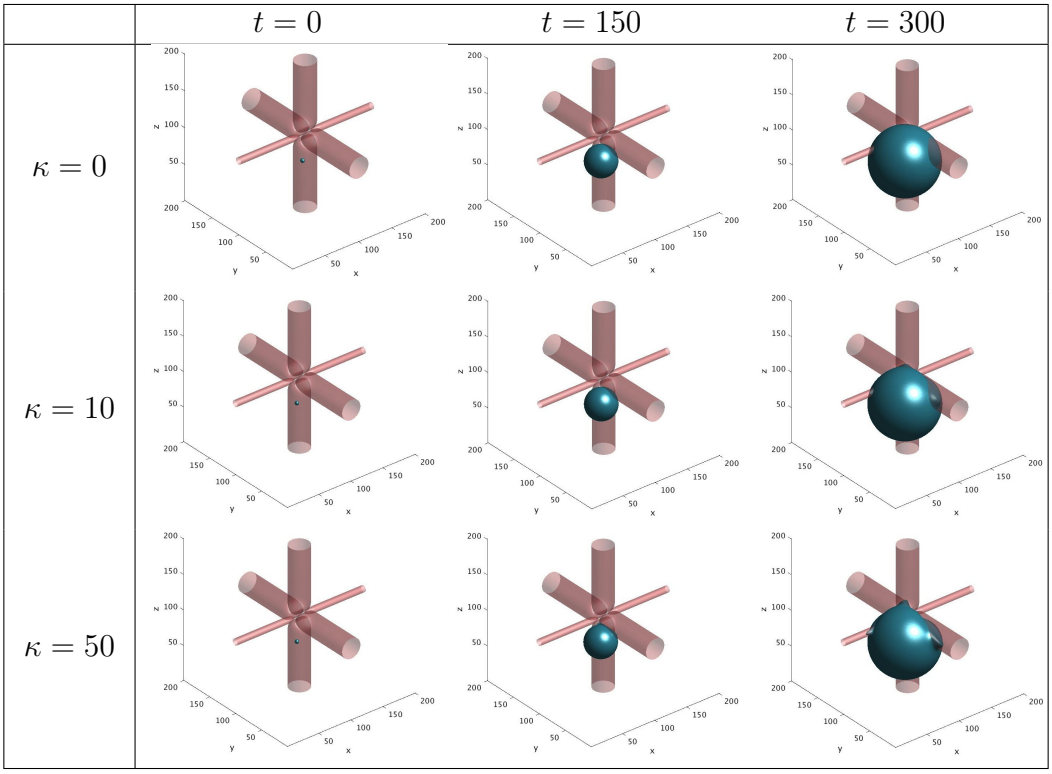


Figure 3.7: 3D Simple Domain Results. Results for the three-dimensional simulations. The fibre structure is shown in pink, and a level set of $u = 0.16$ is shown of the solution to Equation 3.14 is shown in green. The first row corresponds to $\kappa = 0$, the second row to $\kappa = 10$ and the third row to $\kappa = 50$. The first column shows the initial condition, the second column shows the time point $t = 150$, and the last column shows results for $t = 300$. It can be seen that for higher $\kappa$ values, the distribution spreads along the fibre when it is encountered. Additionally, the distribution spreads very slowly across the fibre due to the relatively low rate of spread in this direction.

The resulting distributions grow isotropically outside of the fibres, resulting in spherical shapes. Level sets for $u = 0.16$ are shown in Figure 3.7 for three

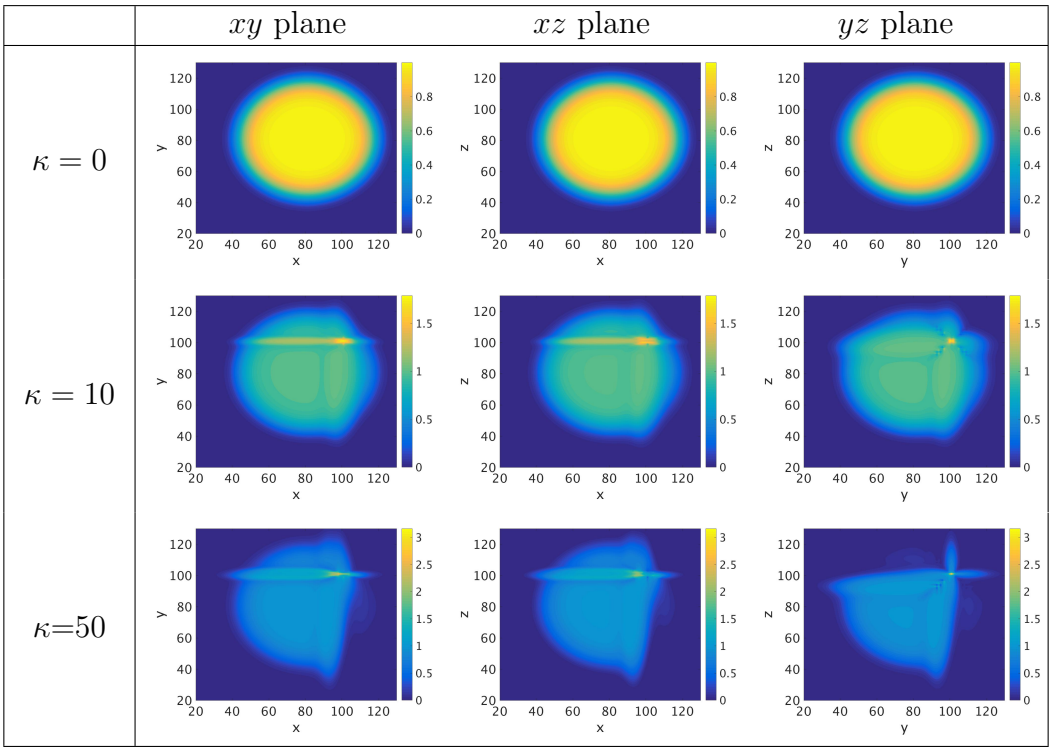


Figure 3.8: 3D Simple Domain Results Slices. Results for the three-dimensional simulations. To better show the anisotropic spread, slices through the middle of the domain are shown in the $xy$ plane (column 1), the $xz$ plane (column 2) and the $yz$ plane (column 3). Results are shown for $\kappa = 0$ (row 1), $\kappa = 10$ (row 2) and $\kappa = 50$ (row 3). By looking at the two dimensional slices, the spread along the fibres can be seen more easily. Additionally, it can be observed that cells that spread onto the fibres tend to remain there as the rate of spread in the perpendicular directions in relatively low.

different values of $\kappa$. We observe that for $\kappa = 0$, the growing cell distribution ignores the fibres, growing isotropically everywhere and giving spherical distributions. For $\kappa = 10$, the cell distribution spreads out along the fibres when it encounters them. This effect is seen even more strongly for $\kappa = 50$. Additionally, the cell distribution cannot spread easily through the fibre as the relative rate of diffusion in this direction is very low. As was mentioned following the two-dimensional simulations, the anisotropy parameter $\kappa$ will play an important role in fitting the model to patient data. To better see these results, Figure 3.8 shows two dimensional slices through the cell density distribution. Slices are shown in the $xy$ plane (column 1), the $xz$ plane (column 2) and the $yz$ plane (column 3). From this view, the anisotropic spread is more clearly visible.

## 3.4 Chapter Summary

In this chapter, we saw how solutions to the Painter-Hillen model of Equation (1.12) actually evolved with time when using a simple, easy-to-control domain. We began by considering a simple one-dimensional case. This case is not the most interesting, as there is no anisotropy in one dimension. Starting with this case allowed us to test the numerical method, as well as get an idea about the steady state behaviour. It was also straight forward to analyze the stability of the numerical method in one dimension.

The results were more interesting in two dimensions, as we introduced anisotropy in this case. We set up a rectangular domain containing two artificial "fibres" crossing in the centre, and defined an initial condition meant to represent a growing tumour. We then observed how solutions behaved when they encountered the fibres. We saw that the solutions showed greater spread

along the fibres, as the model was derived to do. This case also showed how solutions behaved for different values of $\kappa$. Since a higher value of $\kappa$ corresponds to a stronger directional tendency for the cells, the higher $\kappa$ values showed even more spread along the fibre directions than did the lower $\kappa$ values. This is more difficult to see in the full three-dimensional model, as everywhere not on the fibres, the spread is isotropic, hence a large portion of the isosurface is spherical. At the point where the sphere meets the fibres, however, the effect of the anisotropy was seen. The use of the anisotropic operator introduced a new challenge when it came to mass conservation. Standard techniques for implementing no-flux boundary conditions were not sufficient for this case, and so we explicitly derived the appropriate conditions. While the process was tedious, the resulting conditions were easy to implement numerically.

Finally, we considered how solutions behaved for the full three-dimensional model. The numerics for the two-dimensional case extend quite naturally to three dimensions, including the derivation of the boundary conditions. While the computations became a bit more tedious, the resulting conditions were analogous to the two-dimensional boundary conditions. We set up a parallelepiped domain, this time containing three fibres crossing, one in each direction. When observing how the solutions behaved when the fibres were encountered, the results were consistent with the two-dimensional case. Solutions showed a higher degree of spread along the fibre directions, with higher values of $\kappa$ corresponding to higher degrees of spread.

# Chapter 4

# Implementation on a Real Brain

In this Chapter, we will bring together the background motivation from Chapter 1, the model from Chapter 2 and the numerical method developed in Chapter 3. Instead of the artificial domain developed in Chapter 3, we will implement the model using real patient DTI data, and real brain domains. The patient data was made available to us by Dr. Albert Murtha. Working with patient data comes with its own set of logistical challenges, and in this chapter we will discuss how to deal with these challenges, before performing the simulations in Chapter 5.

We begin by discussing the pre-processing of the DTI data in Section 4.1. This process translates the data measured via DTI into a useable form for inputting into the Painter-Hillen model. We then, in Section 4.2 define a metric for model performance, establishing a manner for comparing simulation results to the existing tumours. We go on in Section 4.3 to review the formulas from Chapter 2 for computing the cancer cell diffusion tensors from the measured DTI data, as well as describe the process for extracting the two-dimensional tensors from the measured three-dimensional tensors. Next we

consider biologically realistic values for parameters such as the growth rate and relative size for the diffusion tensors in Sections 4.4 and 4.5. Finally, we describe how to implement an appropriate stopping condition in Section 4.6, and how the boundary conditions are applied on a brain domain as opposed to the rectangular domain of Chapter 3 in Section 4.7.

## 4.1 Data Processing

When dealing with real patient data, there is some pre-processing that must be done before the model can be applied. The data cannot be simply extracted from the imaging machines and plugged directly into the model. Before we received the patient data, it had already undergone several data processing steps for registration, skull stripping and tumour segmentation. This processing was all done by Russ Greiner's lab in computer science [65, 66].

The first issue with using patient brain data, is that there may not be consistency between image positioning. This means that scans cannot be compared directly, as a patient's head positioning may be slightly different for different scans. As such, the images must be aligned by comparing similar structures on different images and rotating or translating them so that they match up properly. This process is called *registration*. While more complicated non-linear registrations like that described in Cobzas et al. [67] can be employed, in this particular case these more sophisticated techniques did not offer an improvement over more simple linear registration methods. Hence, the data was registered using a linear method [12].

The second pre-processing step that was done to the data was *skull stripping*. The original scans contain both the brain and the skull, however brain tumours do not spread into the skull. When simulating the Painter-Hillen

model, the boundary should be the edge of the brain, and the domain should not include the skull. To manually delineate where this boundary should be is not an easy task. Our computer science colleagues developed an automated algorithm that removes the skull, creating a perfect domain for model simulations [65, 66]. This algorithm uses a similar technique as for segmentation, which is described in the following paragraphs.

The final, and perhaps most crucial part of the data processing is the *tumour segmentation*. Segmentation refers to the delineation of a tumour boundary using an MRI image. This process is often done manually by a clinician. However, this can introduce a bias and a human error into the process. Additionally, these results are not reproducible. Russ Greiner's group has developed an automated tumour segmentation tool based on MRI histograms. This technique looks at the intensity of various pixels within an MRI image and generates a histogram, showing the number of pixels in the image having a designated intensity. This is done because absolute intensity levels can vary from image to image, depending on many factors, including the specific machine, and the parameters used during image acquisition [68]. The technique used in [65] and [66] uses thresholding, where inflection points of the MRI histogram are used to define specific threshold intensity values for a particular image. These different thresholds coupled with several different imaging modalities (i.e., T1-MRI, T2-MRI) are then used to separate out particular structures or regions of interest within the brain. This is also the method used to separate the skull from the brain tissue in skull stripping. The thresholding technique for both skull-stripping and segmentation is demonstrated in Figure 4.1 [65].

All of the patient data that we received has been segmented and hence includes the tumour boundaries. It is these segmented tumour boundaries

that we use as the standard to compare the Painter-Hillen results to. Since we will be simulating cell density, we will thus be comparing a level set of the simulated density function to the actual segmented boundary. Based on the images used to delineate the boundaries, it has been estimated that the segmented boundary corresponds to a cell density of 0.16 [51], and hence this is the value we use for comparison in the following Chapter.

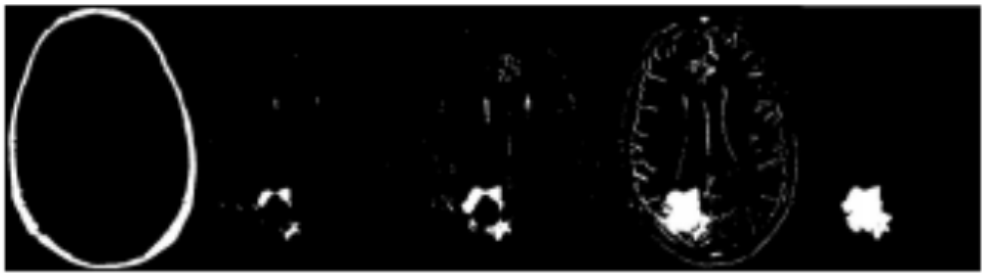

Figure 4.1: Segmentation and Skull Stripping. A demonstration of the skull stripping algorithm, as well as the tumour segmentation algorithm. Taken from [65], where it appears as Figure 4.The thresholding technique creates a high contrast between certain anatomical regions on the scans, allowing for them to be separated from the rest of the scan.

## 4.2 Metric of Model Performance

In the Chapter 5, we compare the performance of the Painter-Hillen model to the performance of the Swanson P.I. model. In order to do this in an objective, quantitative way, it is necessary to determine an appropriate metric for model performance. There are two main things we considered in choosing a metric:

1. **Information available:** Since we have no information about the cell density of the actual tumours, we cannot compare cell density values to evaluate the model fit. The only information we have about the real

tumours is their boundaries, hence we are limited to metrics comparing boundaries.

2. **Ease of implementation:** some metrics are significantly faster and more efficient to evaluate than others. A simple, easy to implement metric is preferred over something more complicated.

Konukoglu et al. [9] proposed a method for comparing similarity between two cell density functions by comparing successive contours. This method could be adapted to compare single contours as well. For example, let $A = \{\boldsymbol{x} | u(\boldsymbol{x}, t) \geq u_0\}$, where $u_0$ is the threshold of detection in the medical image (0.16 in our case) and $B = \{\boldsymbol{x}$-values contained within the automatic segmentation image$\}$. Then we can compute the error defined by

$$\begin{aligned} \epsilon(t) &= \frac{1}{2}\left[\text{dist}(A, B) + \text{dist}(B, A)\right], \\ \text{dist}(A, B) &= \frac{1}{\#A}\sum_{a \in A} \text{dist}_{\min}(a, B), \end{aligned} \tag{4.1}$$

where $\text{dist}_{\min}(a, B)$ is the minimum distance in the Euclidean sense between the point $a$ and the set $B$, and $\#A$ denotes the cardinality of the set $A$ [9]. While a model fit could be evaluated by computing this error value, it is a bit complicated to actually calculate. As such, we also consider an alternative method.

Inspired by the validation of Mosayebi et al. [12], we will use the Jaccard Index to evaluate the fit of the Painter-Hillen and Swanson P.I. model simulations. This is a measure of similarity between finite sample sets. Taking $A$ and $B$ to be as defined above, we compute the Jaccard Index $J(A, B)$ as [12]

$$J(A, B) = \frac{|A \cap B|}{|A \cup B|}. \tag{4.2}$$

The result is that when the union of the two sets is small relative to the intersection, the ratio approaches 1. When the union is large relative to the intersection, the ratio approaches 0. As such, in order to obtain the best model fit, we aim to get the Jaccard Index as large as possible, with a maximum value of 1. Figure 4.2 shows an example of two sets with a low Jaccard Index (left), and two sets with a high Jaccard Index (right).

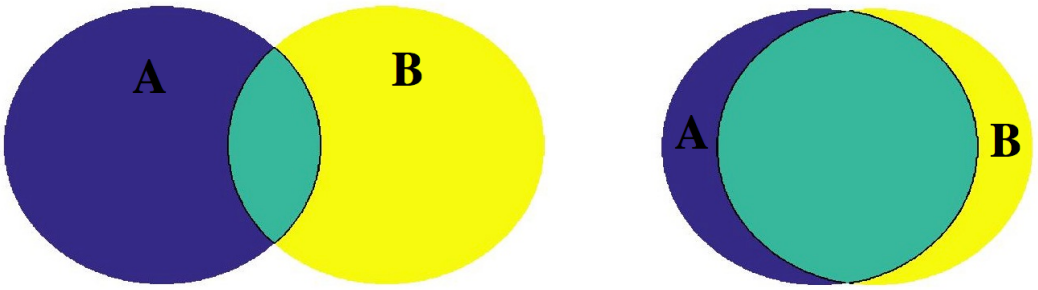


Figure 4.2: Jaccard Index. Figure showing two sets having (a) Jaccard Index = 0.100 (b) Jaccard Index=0.634.

The Jaccard Index offers a couple of advantages over other metrics, such as the error function described in Equation (4.1). The first advantage is that it penalizes both undergrowth and overgrowth, so that in order to get a truly good model fit, the sets must match up everywhere. The second advantage is its simplicity. Not only is it simple to understand, but implementation is straightforward and is not computationally expensive. As such, we will use it as our metric of choice going forward.

## 4.3 Obtaining the Cancer Cell Diffusion Tensors

Before we proceed with the two-dimensional simulations, we first comment on how to obtain the two-dimensional tensors when the data is in three dimensions. The data obtained from DTI is in the form of two-dimensional axial slices that are discretized in a uniform mesh, with a three-dimensional diffusion tensor given at each mesh point. A typical axial slice is shown in Figure 1.5 in our discussion of MRI in Chapter 1. For the case of three-dimensional simulations of Section 5.3, we will use a series of these slices to obtain the movement information in all three dimensions. In the case of the two-dimensional simulations of Section 5.2 however, we need only the information in the plane of consideration.

Mathematically speaking, we are looking for the diffusion tensor $D_2$ such that

$$u^{\mathrm{T}} D_2 u = v^{\mathrm{T}} D_3 v,$$

where $u = \begin{pmatrix} a \\ b \end{pmatrix}$, $v = \begin{pmatrix} a \\ b \\ 0 \end{pmatrix}$, and $D_3$ is the three-dimensional tensor given by the DTI data. Writing this out, we have

$$\begin{pmatrix} a & b & 0 \end{pmatrix} \begin{pmatrix} d_{11} & d_{12} & d_{13} \\ d_{21} & d_{22} & d_{23} \\ d_{31} & d_{32} & d_{33} \end{pmatrix} \begin{pmatrix} a \\ b \\ 0 \end{pmatrix} = \begin{pmatrix} a & b \end{pmatrix} \begin{pmatrix} c_{11} & c_{12} \\ c_{21} & c_{22} \end{pmatrix} \begin{pmatrix} a \\ b \end{pmatrix},$$

where the $d_{ij}$ are the components of $D_3$ and the $c_{ij}$ are the components of $D_2$. Recall that DTI tensors are always symmetric, since in measuring the diffusion,

the rate is computed along a given line and no distinction is made between the two directions along that line. Taking advantage of this symmetry, we have that $d_{ij} = d_{ji}$ and $c_{ij} = c_{ji}$. The resulting equation is therefore:

$$a^2 d_{11} + 2abd_{12} + b^2 d_{22} = a^2 c_{11} + 2abc_{12} + b^2 c_{22}$$

$$\iff a^2(d_{11} - c_{11}) + 2ab(d_{12} - c_{12}) + b^2(d_{22} - c_{22}) = 0, \tag{4.3}$$

and so we have that

$$D_2 = \begin{pmatrix} d_{11} & d_{12} \\ d_{21} & d_{22} \end{pmatrix}$$

in order for Equarion (4.3) to be true for general $a$ and $b$, i.e., $D_2$ is the projection of $D_3$ onto the first two coordinates.

### Calculating Cancer Cell Tensors from DTI Data

To calibrate the Painter-Hillen model of Equation (1.12) to realistic parameter values, we consider the general arguments from Chapter 2 in the context of specific patient data. DTI measures diffusion tensors through the diffusion of water molecules in the brain, whereas the diffusion tensor used in the Painter-Hillen model of Equation (1.12) represents the diffusion of cancer cells. The tensors resulting from the DTI measurements roughly correspond to the location of the white matter tracts, meaning that there will be a lot of similarities between the water diffusion tensors and the cancer cell diffusion tensors. In particular (as seen in Chapter 2), the dominant direction of diffusion for the water molecules, given by the principal direction of the DTI tensor, will be the dominant direction of diffusion for the cancer cell diffusion tensor. In addition, if a particular DTI tensor has a higher FA value than a second DTI

tensor, then the corresponding cancer cell diffusion tensors will share the same relationship. The parabolic scaling derivation of Chapter 2 revealed that the cancer cell diffusion tensors can be computed as the second moment of the turning distribution associated with the DTI tensor, as per Equation (2.13).

It was discussed in Chapter 2 that there are several ways of choosing a turning distribution, each having their merits. In this thesis, we will use a bimodal von Mises distribution approach in two dimensions, and the equivalent bimodal Fisher distribution approach in three dimensions. We saw in Chapter 2 that for these distributions, the moments can be calculated, however it is not always a trivial process. In Chapter 2, we made use of a novel divergence theorem approach and computed the second moments of the bimodal von Mises distribution and the bimodal Fisher distribution. The resulting formula in two dimensions is as given in Equation (2.32), and the resulting formula in three dimensions is as given in Equation (2.39). These formulas both depend on both a concentration parameter $k(\boldsymbol{x})$ and a vector $\gamma(\boldsymbol{x})$. It is through these two quantities that the DTI data is incorporated into the cancer cell diffusion tensors.

Recall that the concentration parameter $k(\boldsymbol{x})$ controls the width of the distribution, with a higher value of $k$ resulting in a narrower, sharper peak. We want areas with stronger directional tendencies, or higher fractional anisotropy, or FA values (recall Equations (1.5) and (1.6)), to be associated with narrower distributions, hence we choose $k$ proportional to the fractional anisotropy, i.e.

$$k(\boldsymbol{x}) = \kappa \mathrm{FA}(\boldsymbol{x}). \tag{4.4}$$

Biologically speaking, this means that when a cell encounters a fibre, it will have a stronger tendency to turn into the fibre direction.

We have thus introduced an anisotropy parameter $\kappa$ as one of the parameters that can be used to fit the Painter-Hillen model of Equation (1.12) to patient data. Note that when $\kappa = 0$ the distribution becomes uniform, and the spread becomes isotropic. This might be suitable for particularly spherical tumour shapes.

## 4.4 Initial Condition and Growth/Diffusion Rates

The formula for the initial condition is given by

$$u_0(\boldsymbol{x}) = e^{-\left(\frac{(\boldsymbol{x}-\boldsymbol{x}_0)\cdot(\boldsymbol{x}-\boldsymbol{x}_0)}{\epsilon}\right)}, \tag{4.5}$$

where $\epsilon = 0.0001$ $c\text{m}^2$ controls the standard deviation of the distribution, and $\boldsymbol{x}_0 = (x_0, y_0)$ in two dimensions, and $\boldsymbol{x}_0 = (x_0, y_0, z_0)$ in three dimensions. This represents the initial point where the tumour originated, and has units of $c$m so that $u_0(\boldsymbol{x})$ is a dimensionless cell density with carrying capacity of 1. The initial distributions are then scaled so that the maximum value of the cell density is 1, representing a cell or small group of cells where the tumour started to grow. A sample initial condition for Patient 1 can be seen in Figure 4.3. In this particular case, $\boldsymbol{x}_0 = (13.52, 11.95)$.

For the growth rate and the diffusion rates, it is important to use values that reflect reality. For the growth rate $r$, this is straight forward as we use $r = 0.012/$ day in two dimensions, taken from [6]. In three dimensions, we use a slightly higher value to maintain a comparable growth/diffusion balance. The same paper gives a biologically realistic value for the diffusion coefficient within the brain of $d_{\text{ref}} = 0.0013$ $\text{cm}^2/\text{day}$ for isotropic spread. Because the

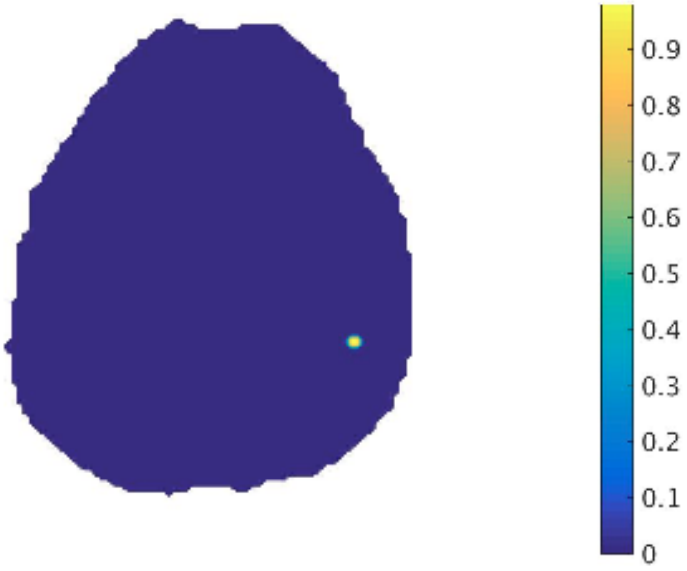


Figure 4.3: Sample Initial Condition. A sample initial condition $u_0(\boldsymbol{x})$ for Patient 1 as defined by Equation (4.5). A sharp Gaussian distribution is used, centered at $\boldsymbol{x}_0$, simulating a cell or small group of cells where the tumour originated. In this particular example, $\boldsymbol{x}_0 = (13.52, 11.95)$.

Painter-Hillen model uses not only a spatially variant diffusion coefficient, but diffusion tensors having different rates of diffusion in different directions, the tensors are scaled so that the average rate of diffusion is equal to $d_{\text{ref}}$. We first define what is meant by "average". For each tensor, the average rate of diffusion is given by the mean of the eigenvalues. Hence, for a particular tensor $D_c(\boldsymbol{x})$:

$$d_{\text{avg}}(\mathbf{x}) = \frac{\text{Tr}(D_c(\mathbf{x}))}{N},$$

where $\text{Tr}(D_c)$ js the trace of the tensor, and $N$ is the dimension. Note that $d_{\text{avg}}$ is a scalar value. Because these tensors also vary spatially, they are also averaged spatially, and scaled by choosing $\frac{1}{\mu}$ in Equation (2.13) such that

$$\frac{1}{|\Omega|}\int_{\Omega}\frac{\text{Tr}(D_c(\mathbf{x}))}{N}d\mathbf{x} = d_{\text{ref}},$$

where $\Omega$ is the brain domain.

We have thus outlined the procedure for computing both the two and three dimensional diffusion tensors. As an example, some of the tensor coefficients are plotted in Figures 4.4 and 4.5. These coefficients are plotted for Patient 1.

For the two-dimensional simulations, the axial slice of consideration is chosen to be that with the largest section of the tumour present, intended to approximate a slice through the centre of the tumour. Figure 4.4 shows the two diagonal components of the two-dimensional tensor, with the images on the left showing the spatial distribution of $\alpha(\boldsymbol{x})$ as defined in Equation (3.4). Recall that this value will be high when the dominant direction of diffusion is horizontal. The images on the right show the spatial distribution of $\gamma(\boldsymbol{x})$, which is higher where the dominant direction of diffusion is vertical. The top row shows the results for a $\kappa$ value of 2, while the bottom row shows the results

for $\kappa = 20$. A clear difference between the two rows can be seen, where the fibres are more strongly defined for the higher $\kappa$ value.

Figure 4.5 shows similar plots for Patient 1 in three dimensions. Again, slices are shown through the same axial slice of consideration, but now the three diagonal components of the three-dimensional diffusion tensor are shown: $D_{11}$, $D_{22}$ and $D_{33}$, respectively. These quantities correspond roughly to fibres in the $x$ direction, fibres in the $y$ direction and fibres in the $z$ direction. The first row shows the results for $\kappa = 2$, while the second row shows the results for $\kappa = 20$. Again, the fibres are much more distinct for the higher $\kappa$ value. This shows that defining the concentration parameter $k(\boldsymbol{x})$ depends both on the structure of the brain, incorporated through the fractional anisotropy, and through the patient-specific anisotropy parameter $\kappa$. This parameter indicates how strong the cancer cell's tendency is to follow the underlying structure.

## 4.5 Parameter Estimation

For the Painter-Hillen model of Equation (1.12), there are either 3 (in two dimensions) or 4 (in three dimensions) parameters that can be used to fit the model. These are:

$\kappa$: The anisotropy parameter that we will selectively tune for each specific patient, see Equation (4.4). This parameter controls the width of the peaks in the von Mises distributions, and consequently how sensitive the cells are to the underlying structure. Varying $\kappa$ can dramatically change the shape of the resulting cancer cell distribution. We assume $\kappa$ is spatially consistent for each patient, and should be thought of as a characteristic of the cancer cells. (In future model iterations, $\kappa$ could

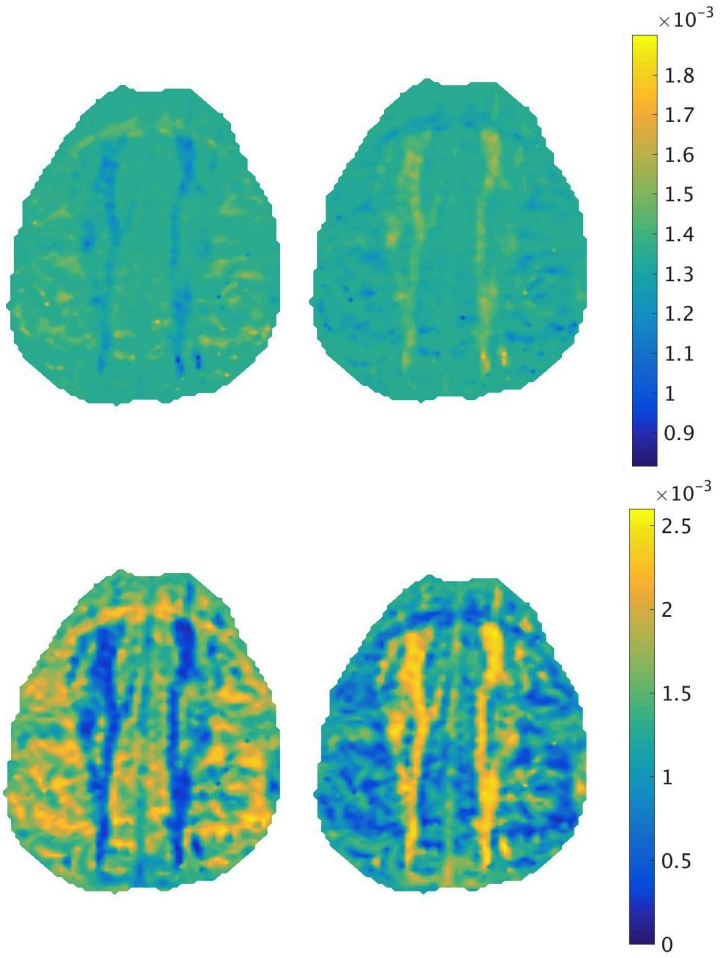


Figure 4.4: $\alpha$ and $\gamma$ on a Brain Domain. Plots showing the spatial distribution of the diagonal elements of the two-dimensional diffusion tensors for Patient 1. The axial slice of consideration is chosen as the slice containing the largest portion of the tumour. The left column shows $\alpha(\boldsymbol{x})$ as defined in Equation (3.4), and the right column shows $\gamma(\boldsymbol{x})$. The top row shows the results for $\kappa = 2$, while the bottom row shows the results for $\kappa = 20$. Note that the fibres are far more pronounced for higher values of $\kappa$.

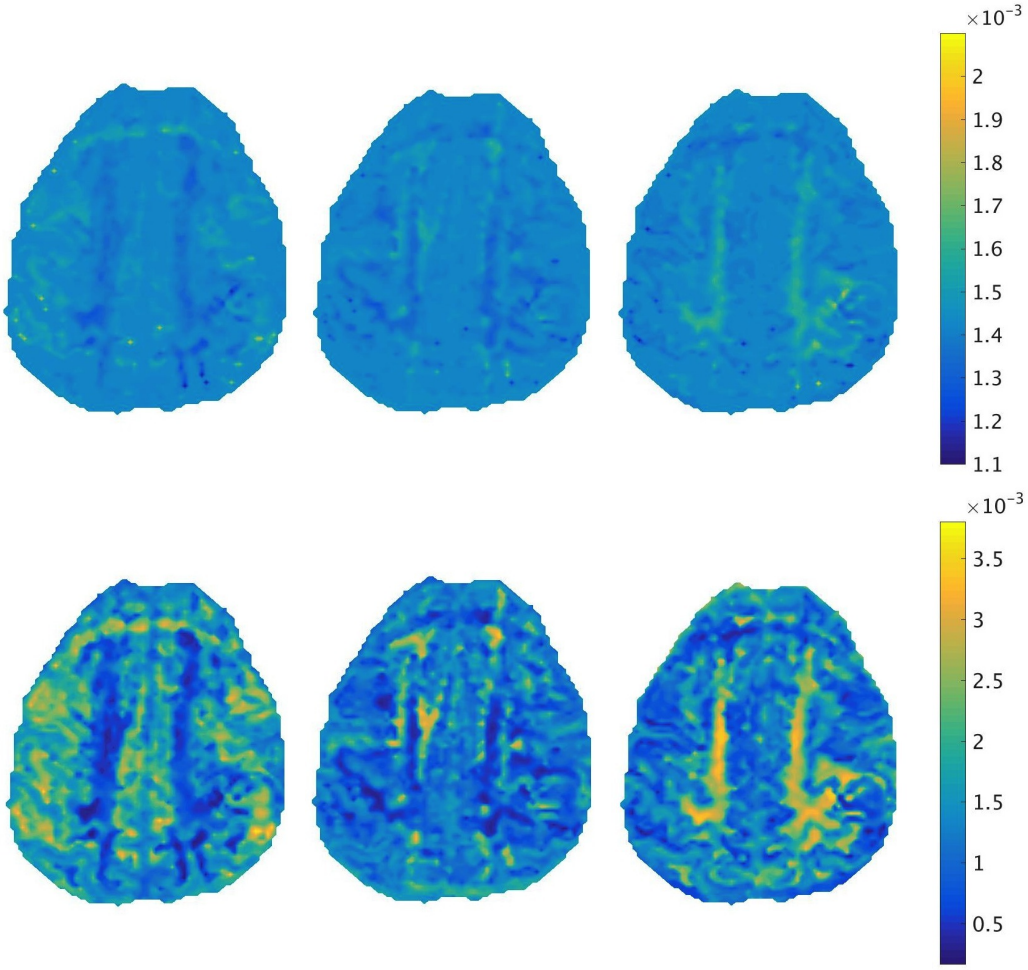


Figure 4.5: $D_{11}$, $D_{22}$ and $D_{33}$ on a Brain Domain. Plots showing the spatial distribution of the diagonal elements of the three-dimensional diffusion tensors for Patient 1. These plots are shown for the same axial slice of consideration as for the two-dimensional case. The first column shows $D_{11}$, roughly corresponding to fibres in the $x$-direction, while the middle column shows $D_{22}$, roughly corresponding to fibres in the $y$-direciton, and the last column shows $D_{33}$, roughly corresponding to fibres in the $z$-direction. The first row shows results for $\kappa = 2$, while the second row shows results for $\kappa = 20$. Note that the fibres are more pronounced for the higher value of $\kappa$.

| Model | two dimensions | three dimensions |
|---|---|---|
| Painter-Hillen | $\kappa, x_0, y_0$ | $\kappa, x_0, y_0, z_0$ |
| Swanson P.I. | $x_0, y_0$ | $x_0, y_0, z_0$ |

Table 4.1: Table showing the parameters that must be fit for each model in both two and three dimensions.

vary spatially within a specific patient.)

$(x_0, y_0)$: The coordinates of the initial position for the initial distribution in two dimensions. In other words, the sharp Gaussian function is centred at $(x_0, y_0)$.

$(x_0, y_0, z_0)$: The coordinates of the initial position for the initial distribution in three dimensions. We expect $z_0$ to be near the slice containing the maximum tumour area.

We will also be fitting the Swanson P.I. model of Equation (1.10), as will be discussed in more detail in Chapter 5. Then depending on the model used, as well as the dimension of the simulation, there could be anywhere from 2 to 4 parameters to fit. The parameters that must be fit are summarized in Table 4.1.

This fitting is currently done in a combination manual-automatic manner. The most probable initial condition is selected by observing the tumour segmentation, and then an exhaustive search is done in the region surrounding this point. The anisotropy parameter is chosen in a similar manner, with an initial guess based on the shape of the tumour, followed by an exhaustive search surrounding that value. Future development will work towards further automating this process.

For example, consider fitting the Swanson P.I. model in two dimensions. We choose this as an example because it contains only two parameters that

need to be fit (the two coordinates of the initial condition), and thus can provide a useful visual plot of the Jaccard Index of Equation (4.2) over the parameter space. The model is initialized at each spatial location in the chosen region, and the Jaccard Index is assigned to that location. Figure 4.6 shows the results of such a plot for Patient 1. The parameters that give the maximum Jaccard Index are then selected as the initial condition.

In general, when determining parameter values for model fitting, the idea of likelihood is central. The likelihood provides a method for determining the set of model parameters most likely to result in a particular observed distribution [69]. More specifically, the process of evaluating the model for a wide variety of parameter values, followed by the computation of the Jaccard index, relates to the idea of Approximate Bayesian computation (ABC). ABC doesn't actually involve the evaluation of a likelihood function, and as such is very useful in the complex models arising in the different areas of mathematical biology [70].

## 4.6 Stopping Criteria

When running the simulations, it is not known what the final time should be, as we do not know how long each tumour took to grow. As such, the Jaccard Index of Equation (4.2) is used to determine an appropriate stopping criterion. As the simulated tumours begin to grow, they will first be smaller than the actual tumour, meaning that as they grow larger, the Jaccard Index will increase. At some point, this index is maximized, and after this point, the simulated tumour will outgrow the actual tumour, causing the Jaccard Index to decrease. It is at this point of optimal Jaccard Index that the simulation is stopped. See Figure 4.7 to see how this works for Patient 1. Notice that there is some transient behaviour for small times, before the diffusion and growth

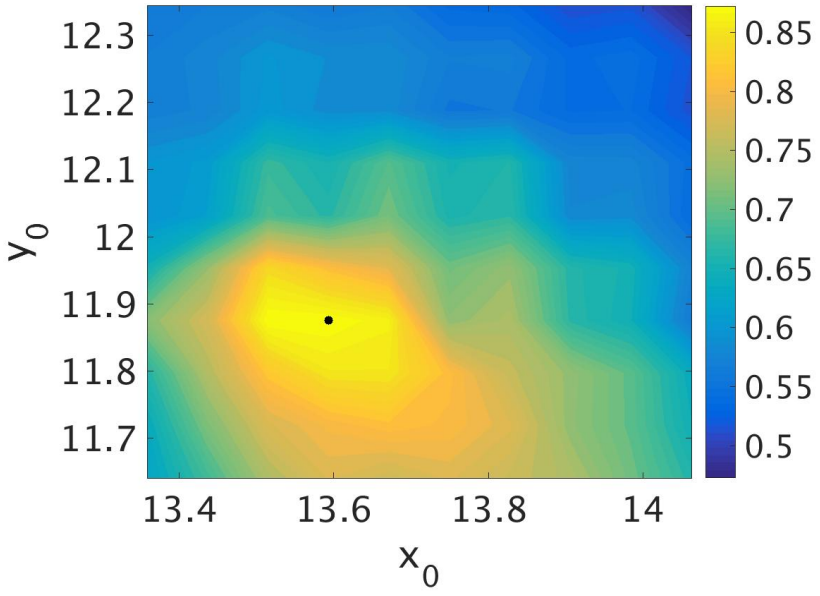


Figure 4.6: Sample Parameter Space. Figure showing the Jaccard Index plotted over the parameter space for the Swanson P.I. model. Patient 1 is shown as an example. The optimum value occurs at $(x_0, y_0)$=(13.6,11.9), hence this is selected as the initial condition. This is marked on the plot as a black dot.

find an appropriate balance.

## 4.7 Implementing Homogeneous Neumann Boundary Conditions

In Chapter 3, we discussed how to implement the boundary conditions to ensure that the numerical scheme conserves mass. Recall that we use no-flux boundary conditions, so that cancer cells can not diffuse through the skull. The skull has been removed from the patient data that will be used, via the segmentation procedure outlined above. It is not necessary to repeat the whole derivation of the previous chapter, however a few extra conditions are required for a convex brain domain vs. a rectangular domain. Figure 3.3 showed the different possible points on the boundary of a rectangular domain, and explained how to deal with them. We illustrate the use of a real brain domain in Figure 4.8, where we again have the black interior points, the white boundary points and the blue corner points. Corner points are defined as being diagonally adjacent to one internal point, while white boundary points are in contact via the numerical stencil with exactly one interior point. Using a convex brain domain introduces a new class of points, as is shown in Figure 4.8. These points are shown in red, and consist of boundary points that are in contact with more than one interior point in the context of the numerical stencil.

Both the white and blue boundary points are handled in the same manner as they were in Equations (3.11)-(3.13) for two dimensions, and Equations (3.25)-(3.33) in three dimensions. For the red points, mass conservation is achieved by averaging the value of the given quantity on the interior points

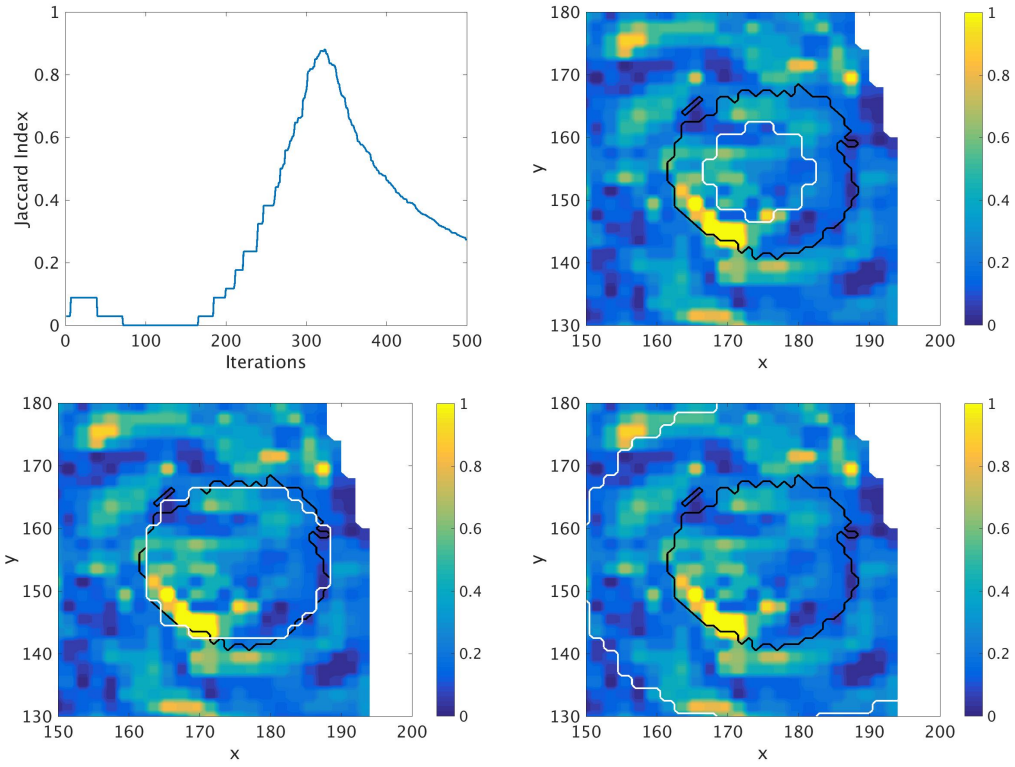


Figure 4.7: Stopping Criteria. (i) Figure showing how the Jaccard Index of Equation (4.2) changes with the number of iterations. As an example, the Painter-Hillen model is applied in two dimensions for Patient 1. As more iterations are run, the Jaccard Index increases, however, after some maximum is reached, it will begin to decrease again as the simulated tumour outgrows the actual tumour. This is shown in the image in the first row, first column as $J(t)$. The other three images show plots of the simulated tumour boundary (white) and the actual tumour boundary (black) for $t = 250$, $t = 323$ and $t = 500$, plotted over the fractional anisotropy. In the second column of the first row, this plot corresponds to $t = 250$, where $J(t)$ is increasing and when the simulated tumour is smaller than the actual tumour. In the first column of the second row, the plot shows the optimal value of the Jaccard Index at $t = 323$ and indicates where the algorithm should stop. The final plot corresponds $t = 500$, where $J(t)$ is decreasing and when the simulated tumour has outgrown the actual tumour. These results are for a sample model run on a sample patient, but are qualitatively consistent across all models and patients.

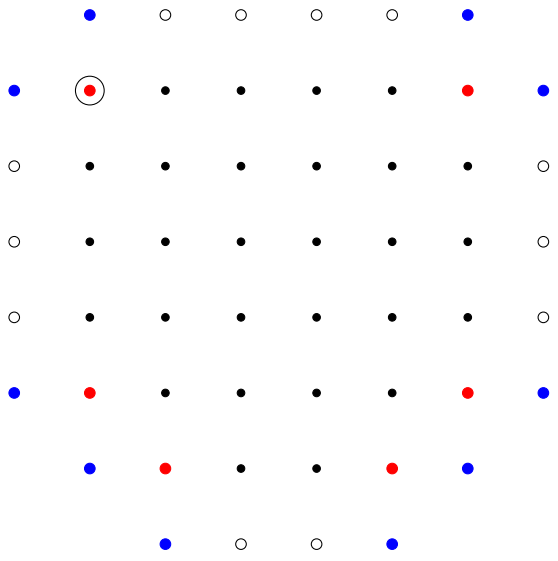

Figure 4.8: Boundary Conditions for Convex Domain. Grid showing the different categories of boundary points encountered with a convex brain domain. The blue points and white points were present in the rectangular domain of Chapter 3, while the red points are new to the brain domain. The points of the domain itself are shown in black, while the ghost points are shown in white, blue and red. The white points are the "edge" points of the rectangular domain of Chapter 3, while the blue points are the "corner" points from the same example. The red points represent a new class of ghost points that are only present for a convex domain.

with respect to the correct stencil. In two dimensions, $(v_1)$ and $(v_3)$ can be defined as in the rectangular domain case, since each red point will only be horizontally adjacent to one interior point, and vertically adjacent to one interior point. For example, consider the circled red point in Figure 4.8. In this case, the boundary conditions are given as follows:

$$\begin{aligned}(v_1)_{i,j} &= (v_1)_{i+1,j},\\ (v_3)_{i,j} &= (v_3)_{i,j-1},\\ (v_2)_{i,j} &= -((v_2)_{i+1,j} + (v_2)_{i,j-1})/2.\end{aligned}$$

For the other red points, the conditions are defined analogously. In three dimensions we again have the same types of points as before, however now we allow for a boundary point that is in contact with more than one interior point with respect to the numerical stencil. For a sample three-dimensional "red" point, the boundary conditions are given by:

$$\begin{aligned}(v_1)_{i,j,l} &= (v_1)_{i+1,j,l},\\ (v_2)_{i,j,l} &= (v_3)_{i,j-1,l},\\ (v_3)_{i,j,l} &= (v_3)_{i,j1,l+1},\\ (v_4)_{i,j,l} &= -((v_2)_{i+1,j,l} + (v_2)_{i,j-1,l})/2,\\ (v_5)_{i,j,l} &= -((v_2)_{i+1,j,l} + (v_2)_{i,j,l+1})/2,\\ (v_6)_{i,j,l} &= -((v_2)_{i,j,l+1} + (v_2)_{i,j-1,l})/2.\end{aligned}$$

The other cases are once again determined analogously. Note that these conditions assume that each "red" boundary point is in contact with at most two interior points with respect to each stencil. In practice, for the patient

data, this is a reasonable assumption.

## 4.8 Chapter Summary

In this chapter, we described in detail the challenges associated with applying the Painter-Hillen model to real patient data, and outlined our methods for dealing with these challenges.

The first challenge when dealing with real patient data, particularly when medical imaging machines are involved, is translating this data into a useable format. The first issue to deal with was aligning images taken from the same patient, by matching up specific identifiable regions. This is referred to as registration. The next step involved removing the skull from the images so that the "boundary" used in the simulations was actually the boundary of the brain tissue, and not the patient's head. The final step was to obtain a segmentation of the tumour boundary based on the patient scans. The segmentation will then be used to evaluate the fit of model simulations for the Painter-Hillen model of Equation (1.12) and the Swanson P.I. model of Equation 1.10. All of this work was done by colleagues in computer science [65, 66].

The next issue was defining a method for evaluating the performance of both the Painter-Hillen and Swanson P.I. models. Ideally, the metric should provide an objective, quantitative manner of comparison. While there are many metrics to choose from, we are limited by the fact that we do not have any information about the actual cell density, hence can only compare tumour boundaries. As such, we chose the Jaccard Index as our metric of choice, as per Mosayebi et al. [12]. The Jaccard Index offers a simple, easy to implement method for computing the similarity between two sets by comparing the size

of their intersect to the size of their union.

While the idea of converting the DTI data into the proper tensors for cancer cell spread was introduced in Chapter 2, we reviewed it here in the context of patient data. It is also important to consider the orders of magnitude for the tensor components, as well as the growth rate. In addition to these fixed parameters, there were certain patient-specific parameters to determine. Namely, the starting point for the initial condition, as well as the anisotropy parameter $\kappa$. The method for choosing these parameter values was discussed.

Finally, we discussed how to determine the appropriate stopping condition, as well as the proper boundary conditions. To determine the appropriate stopping time for each simulation, we discussed how to optimize the Jaccard Index over time in order to find the best possible match between the segmented and simulated tumours. As for the boundary conditions, a careful analysis of irregular convex domains enabled us to maintain a mass conserving numerical scheme. The ideas developed in this chapter will be applied in Chapter 5 when both the Painter-Hillen model and the Swanson P.I. model are applied to real patient data.

# Chapter 5

# Model Comparison Using Patient Data

Thus far, we have discussed the derivation of the Painter-Hillen model of Equation (1.12), as well as the numerical method for implementing it, and the details of applying it to patient data. In this chapter, we present the results of using the Painter-Hillen model on 10 real patients from the Cross Cancer Institute. While we have more data available (54 patients total) for further model validations, here we consider the results using 10 randomly selected patients. This is due to computational limitations, and our belief that the 10 patients presented here give a good cross-section of tumour types and sizes. Figure 5.1 shows two-dimensional cross sections through the centre of each patient's tumour, with the slice containing the largest portion of the tumour shown. These images show the shapes and sizes of each tumour that we are attempting to simulate.

It is clear from these images why an anisotropic model would be useful. In examining MRI images of patients' tumours, it is difficult if not impossible

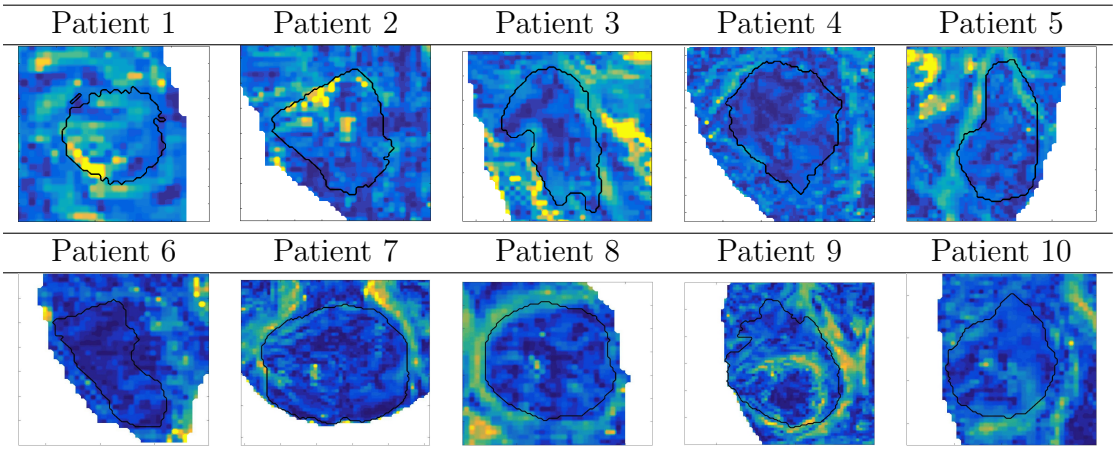


Figure 5.1: 10 Patient Segmentations. Segmentations through the largest two-dimensional slice of each patient's glioma. The underlying colours correspond to the fractional anisotropy (FA), with the tumour boundary as determined via automatic segmentation shown in black.

to estimate cell density, and often only the tumour boundary is delineated. Furthermore, on images of these type (T2-images), it is estimated that a detection threshold of approximately 0.16 exists [51], with any lower cancer cell densities being invisible on scans. If the model is able to accurately reproduce the tumour boundary, then we expect that the cell densities predicted everywhere are close to reality as well. This would allow clinicians to use our model output in determining an appropriate treatment region, with the goal of killing the most cancer cells possible.

To evaluate the Painter-Hillen model of Equation (1.12) in an objective, quantitative sense, we compare the simulation results to those of the Swanson model of Equation (1.10) discussed in the introduction [6]. This model is also referred to colloquially as the proliferation-invasion (P.I.) model, and has been used extensively in clinical settings to assist in treatment planning [6, 44–46, 49, 51–54]. It is for this reason that we choose it as a benchmark for comparison of the Painter-Hillen model performance. If we can improve upon

its performance, then we could potentially improve upon current treatment standards.

The goal of simulating both the Painter-Hillen model and the P.I. model is to reproduce the tumour boundary as determined from the automated segmentation procedure. It should be noted that there is no guarantee that this is a completely accurate tumour boundary, however it is reasonable to assume that it provides a good estimate for comparison. Since both models simulate the cell density, and not the tumour boundary, we will use the 0.16 level set in each case to compare to the segmented boundary.

## 5.1 Swanson Model Implementation

While we introduced the Swanson model in Chapter 1, here we outline its implementation in more detail. The model is given by the PDE

$$u(\boldsymbol{x},t)_t = \nabla \cdot (D(\boldsymbol{x})\nabla u(\boldsymbol{x},t)) + ru(\boldsymbol{x},t), \tag{5.1}$$

where $r$ is once again the growth rate, and the spatially dependent scalar diffusion coefficient is defined as

$$D(\boldsymbol{x}) = \begin{cases} D_g & \text{if } \boldsymbol{x} \in \text{ grey matter,} \\ D_w & \text{if } \boldsymbol{x} \in \text{ white matter.} \end{cases}$$

We use $u(\boldsymbol{x},t)$ to represent the cancer cell density, as before. Because of the increased diffusivity in the white matter, Swanson takes $D_w = 5D_g$ [6]. Note also that this model uses an exponential growth, while the Painter-Hillen model uses a logistic growth. It will be seen in the cell density plots that this

growth will make a difference in the tumour composition. Recall also that while $D$ is spatially dependent, it is piecewise constant and has no directional dependence. In order for the numerical scheme to make sense, we assume a smooth interpolation between $D_g$ and $D_w$ so that the function is continuous.

There remains the question of how to separate the brain into white matter and grey matter. In [6], an online database is used that distinguishes between grey and white matter, however since we are applying this model to patient data, we will need to make the distinction for each patient individually. This will be done using a threshold FA value, with the assumption that white matter will have an FA value $> 0.25$, while grey matter will have an FA value $\leq 0.25$. This value is consistent with that used in fibre tracking, see for example [71] or [72]. The results of such a division are shown in figure 5.2 for a sample three-dimensional axial slice for Patient 1.

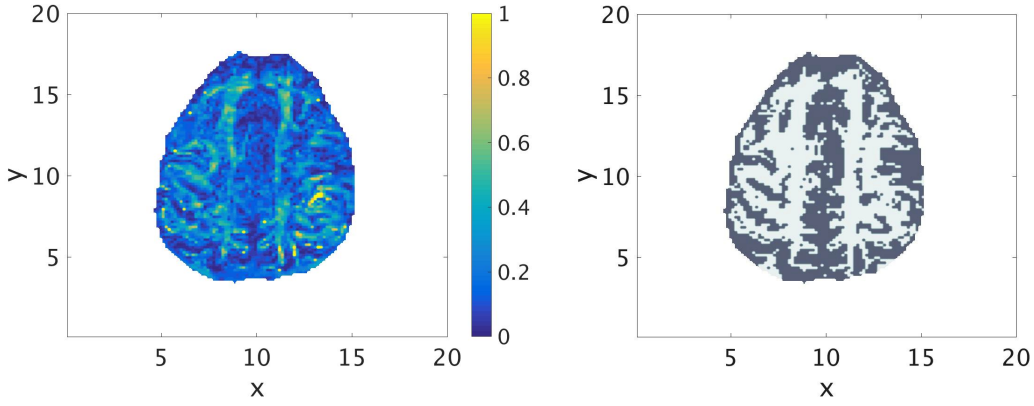


Figure 5.2: Defining the White Matter. (a) Plot showing the FA on a scale from 0 (dark blue) to 1 (yellow) for Patient 1. Note that anything with a value above 0.25 will be classified as white matter. (b) Plot showing the corresponding distinction between grey and white matter. The white matter appears white, while the grey matter appears grey.

The main difference between the Swanson P.I. model and the Painter-

Hillen model is the inclusion of the anisotropic diffusion tensors. While the Swanson P.I. model includes a spatially varying diffusion coefficient, it is scalar in nature and does not vary with direction. The Painter-Hillen model includes a spatially varying diffusion tensor, so that the rate of spread varies not only in space, but with direction. This allows cells to spread faster along a fibre than in the perpendicular direction. Additionally, the Painter-Hillen model includes the fully anisotropic diffusion operator of Equation (2.14), discussed in detail in Chapter 2, while the Swanson P.I. model uses a more standard diffusion operator where only one spatial derivative is applied to the diffusion coefficient. The final difference lies in the growth function. The Painter-Hillen model uses a logistic growth, that behaves like exponential growth at low density values, but tends to 0 as the density approaches 1. The Swanson model uses an exponential growth. We believe the logistic growth to be more realistic, as there is a limiting density within the brain.

### 5.1.1 Two-dimensional Numerical Scheme

To numerically implement this model, we begin by expanding Equation (5.1) into a diffusion term and an advection term:

$$u(\boldsymbol{x},t)_t = \nabla D(\boldsymbol{x}) \cdot \nabla u(\boldsymbol{x},t) + D(\boldsymbol{x})\nabla^2 u + ru(\boldsymbol{x},t), \tag{5.2}$$

where $\nabla^2$ represents the standard Laplacian. To explain the numerical method, we assume that $D(x)$ is differentiable, an assumption that will be relaxed later. In two dimensions, 5.2 expands to

$$u_t(\boldsymbol{x},t) = \underbrace{D_x u_x + D_y u_y}_{\text{Advective terms}} + \underbrace{D(x)(u_{xx} + u_{yy})}_{\text{Diffusive terms}} + ru(\boldsymbol{x},t).$$

For the advective terms, we will use a first-order upwind scheme to promote positivity. Consider first just the $D_x u_x$ term. The same technique is used for the $D_y u_y$ term. First, we compute $D_x$ at each location $i, j$ using a centred difference scheme:

$$\frac{\partial D^n_{i,j}}{\partial x} \approx \frac{D^n_{i+1,j} - D^n_{i-1,j}}{2h_1}, \tag{5.3}$$

where $h_1$ is the spatial step in the $x$-direction. This $D_x$ value then denotes the velocity for the advection, hence the $u$ partial derivative is computed based on the sign of $D_x$. Then [73]

$$\frac{\partial u^n_{i,j}}{\partial x} \approx \begin{cases} \frac{u^n_{i,j} - u^n_{i-1,j}}{h_1} & \text{if } D_x \leq 0 \\ \frac{u^n_{i+1,j} - u^n_{i,j}}{h_1} & \text{if } D_x > 0 \end{cases}. \tag{5.4}$$

The $D_y u_y$ term is computed numerically the same way. For the diffusive terms, a standard centred difference scheme is used for the second derivatives. The numerical scheme is therefore [74]

$$\begin{aligned} u^n_{i,j} + 1 = k[&D^n_{xi,j} u^n_{xi,j} + D^n_{yi,j} u^n_{yi,j} \\ &+ D_{i,j} \left( \frac{u^n_{i+1,j} - 2u^n_{i,j} + u^n_{i-1,j}}{h_1^2} + \frac{u^n_{i,j+1} - 2u^n_{i,j} + u^n_{i,j-1}}{h_2^2} \right) + r u_{i,j}] + u^n_{i,j}, \end{aligned}$$

where $D^n_{xi,j}$, $u^n_{xi,j}$, $D^n_{yi,j}$ and $u^n_{yi,j}$ are computed as described in Equations (5.3) and (5.4). If $D(x)$ is discontinuous, as for Equation (5.1), we use the same discretization.

### Boundary Conditions

Because this model uses a more traditional diffusion operator, the boundary conditions are more straight-forward than they were for the Painter-Hillen

model. Assuming that the model is applied to domain $\Omega$, the boundary conditions are defined on $\partial\Omega$. Writing the Swanson model using the flux $\boldsymbol{J}$, we have

$$u(x,t)_t = -\nabla \cdot \boldsymbol{J},$$

where $\boldsymbol{J}$ is the standard Fickian flux,

$$\boldsymbol{J} = -D\nabla u.$$

Writing the boundary condition in terms of the normal vector $\eta$, we want the projection of the flux in the direction of the normal to be 0, or

$$\boldsymbol{\eta} \cdot \boldsymbol{J} = 0, \text{ on } \partial\Omega.$$

Assuming that in general $D \neq 0$, this condition is equivalent to

$$\eta \cdot \nabla u = 0, \text{ on } \partial\Omega \tag{5.5}$$

### 5.1.2 Three-dimensional Numerical Scheme

In three dimensions, we assume again that $D(x)$ is differentiable and we write Equation (5.2) as

$$u_t(\boldsymbol{x},t) = \underbrace{D_x u_x + D_y u_y + D_z u_z}_{\text{Advective terms}} + \underbrace{D(x)(u_{xx} + u_{yy} + u_{zz})}_{\text{Diffusive terms}} + ru(\boldsymbol{x},t).$$

The two-dimensional methods generalize naturally for three dimensions. Consider first just the $D_x u_x$ term again. The same technique is used for the $D_y u_y$ term and the $D_z u_z$. We compute $D_x$ at each location $i, j$ as we did in

two-dimensions:

$$\frac{\partial D^n_{i,j,l}}{\partial x} \approx \frac{D^n_{i+1,j,l} - D^n_{i-1,j,l}}{2h_1}.$$

Then [73]

$$\frac{\partial u^n_{i,j,l}}{\partial x} \approx \begin{cases} \frac{u^n_{i,j,l} - u^n_{i-1,j,l}}{h_1} & \text{if } D_x \leq 0, \\ \frac{u^n_{i+1,j,l} - u^n_{i,j,l}}{h_1} & \text{if } D_x > 0. \end{cases}$$

The $D_y u_y$ and $D_z u_z$ terms are computed numerically the same way. For the diffusive terms, a standard centred difference scheme is used for the second derivatives. The numerical scheme is therefore

$$\begin{aligned} u^n_{i,j,l} + 1 = k[&D^n_{x i,j,l} u^n_{x i,j,l} + D^n_{y i,j,l} u^n_{y i,j,l} + D^n_{z i,j,l} u^n_{z i,j,l} \\ &+ D_{i,j,l}\left(\frac{u^n_{i+1,j,l} - 2u^n_{i,j,l} + u^n_{i-1,j,l}}{h_1^2} + \frac{u^n_{i,j+1,l} - 2u^n_{i,j,l} + u^n_{i,j-1,l}}{h_2^2}\right. \\ &\left. + \frac{u^n_{i,j,l+1} - 2u^n_{i,j,l} + u^n_{i,j,l-1}}{h_2^2}\right) + r u_{i,j,l}] + u^n_{i,j,l}. \end{aligned}$$

The description of the two-dimensional case for the boundary conditions generalizes easily to three dimensions, with Equation (5.5) holding.

## 5.2 Two-Dimensional Results

Here we show the simulation results of the Painter-Hillen model of Equation (1.12) simulations, as well as the Swanson P.I. model of Equation (5.1). Each figure corresponds to the results for one patient, with the Painter-Hillen simulation on the left, and the Swanson P.I. model simulation on the right. The automatically segmented tumour boundary is plotted in black, while the model predicted boundary is shown in white. The top row of each figure shows these boundaries overlaid on the FA plot to give an idea about the brain architecture

of that particular patient, and the bottom row shows the cell density function. A discussion of these results will follow.

**Patient 1**

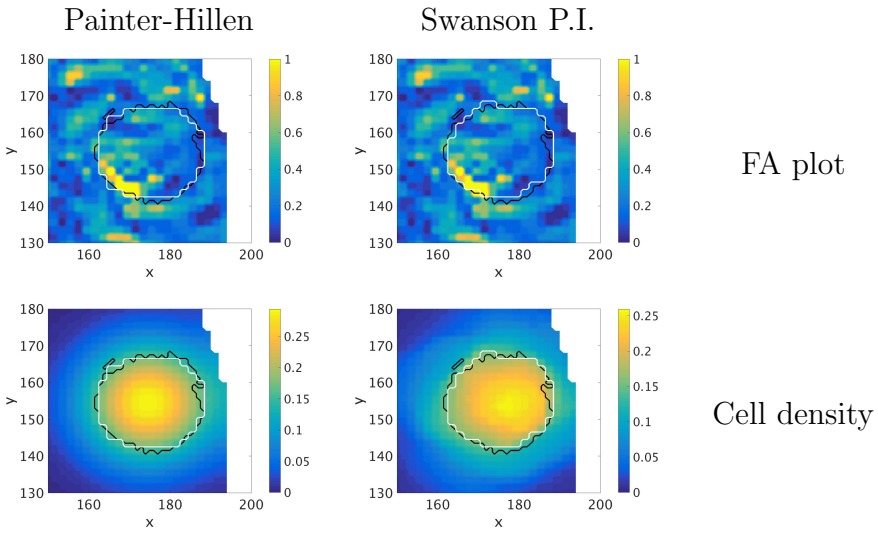


Figure 5.3: 2D Patient 1. Two-dimensional simulation results for Patient 1. The result on the left is the result for the Painter-Hillen model, while the result on the right is from the Swanson P.I. model. The black line denotes the segmented tumour, and the white line corresponds to the model-predicted boundary.

**Patient 2**

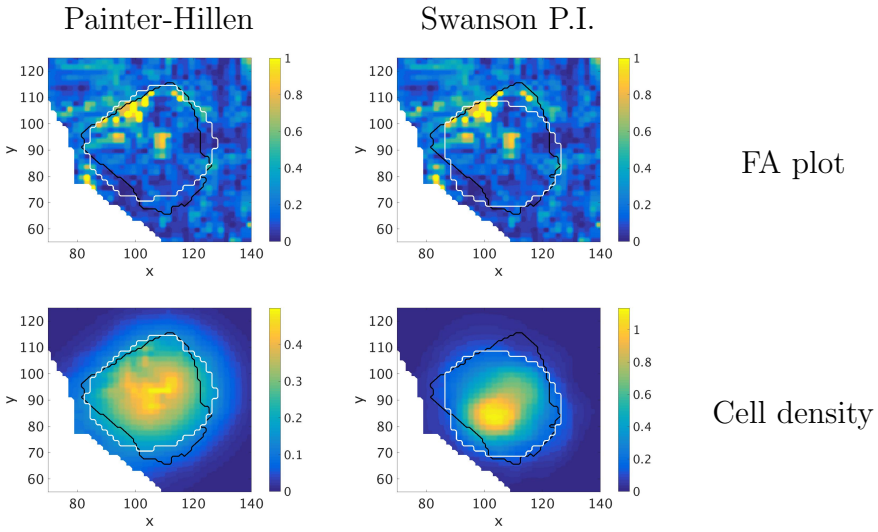


Figure 5.4: 2D Patient 2. Two-dimensional simulation results for Patient 2. Left: Painter-Hillen model, right: Swanson P.I. model. Black contour=segmented tumour, white contour=model-predicted boundary..

**Patient 3**

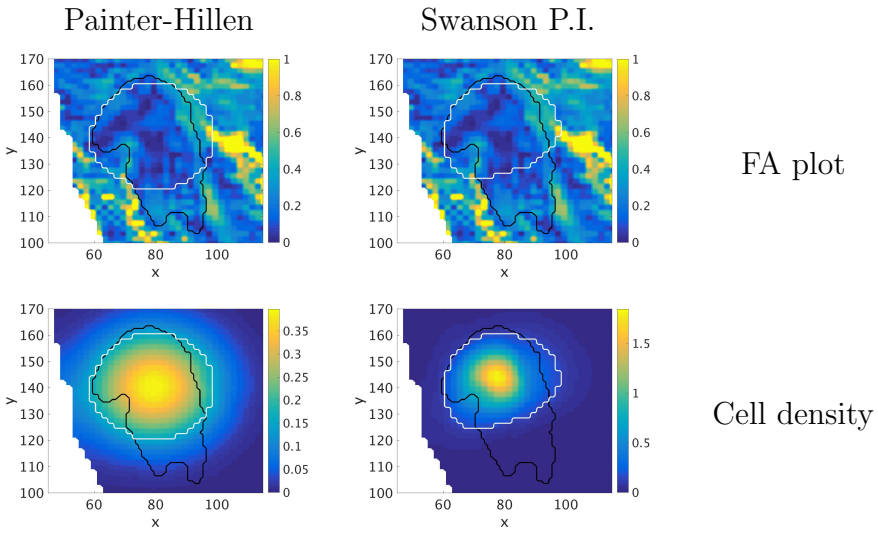


Figure 5.5: 2D Patient 3. Two-dimensional simulation results for Patient 3. Left: Painter-Hillen model, right: Swanson P.I. model. Black contour=segmented tumour, white contour=model-predicted boundary.

**Patient 4**

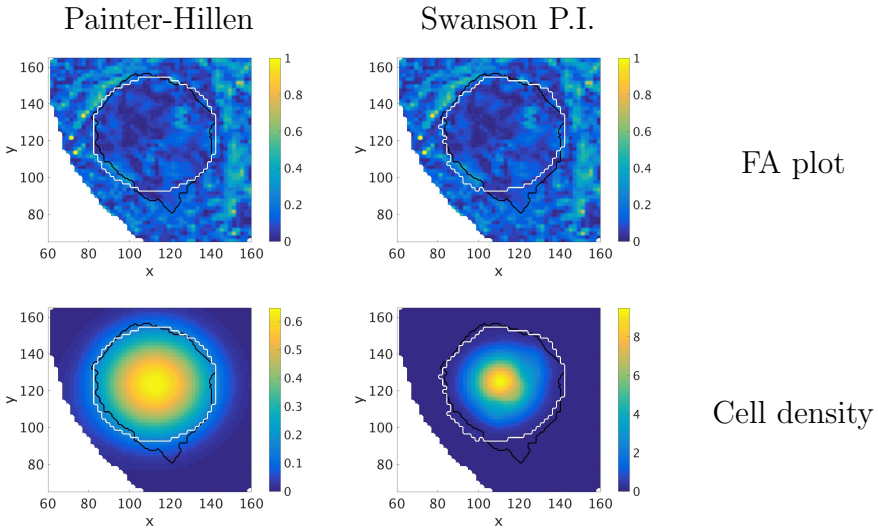


Figure 5.6: 2D Patient 4. Two-dimensional simulation results for Patient 4. Left: Painter-Hillen model, right: Swanson P.I. model. Black contour=segmented tumour, white contour=model-predicted boundary.

**Patient 5**

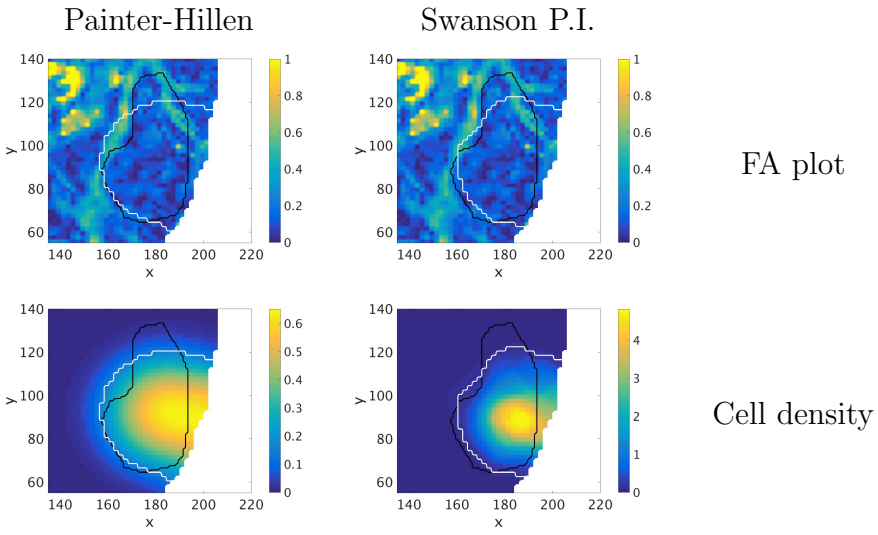


Figure 5.7: 2D Patient 5. Two-dimensional simulation results for Patient 5. Left: Painter-Hillen model, right: Swanson P.I. model. Black contour=segmented tumour, white contour=model-predicted boundary.

**Patient 6**

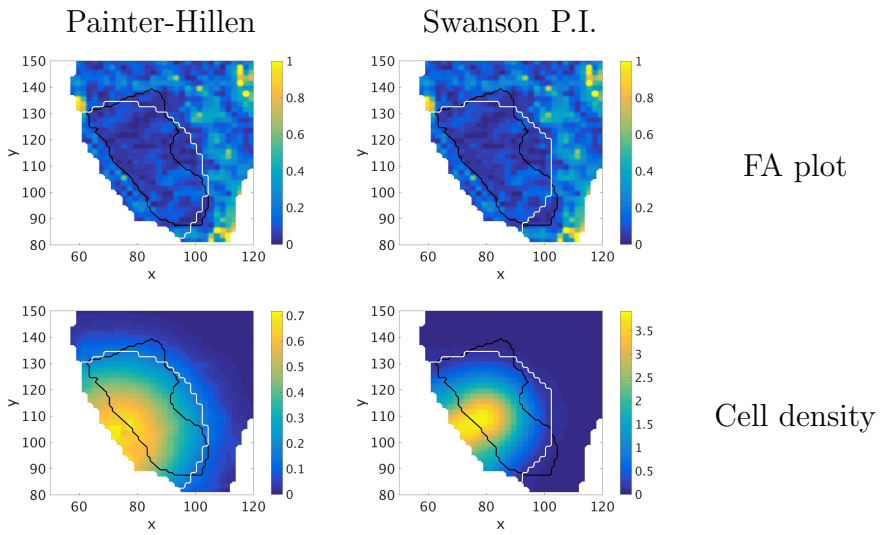


Figure 5.8: 2D Patient 6. Two-dimensional simulation results for Patient 6. Left: Painter-Hillen model, right: Swanson P.I. model. Black contour=segmented tumour, white contour=model-predicted boundary.

**Patient 7**

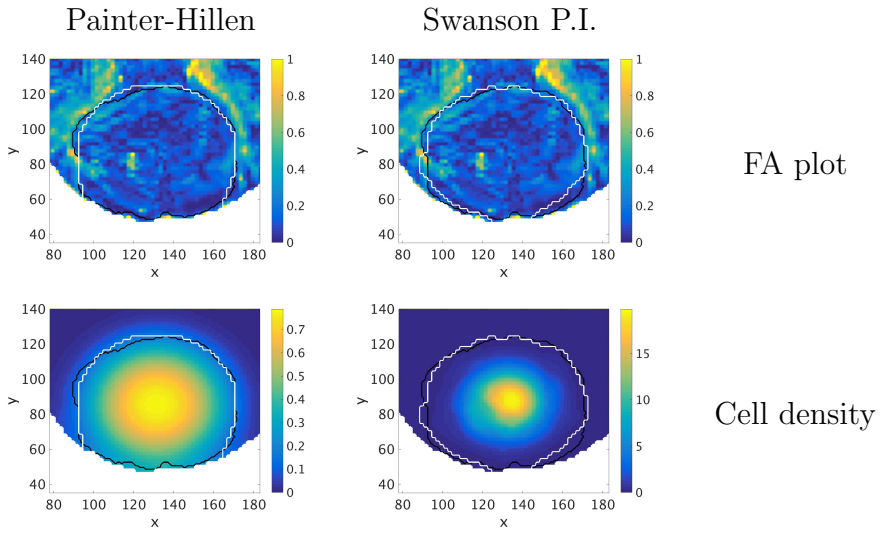


Figure 5.9: 2D Patient 7. Two-dimensional simulation results for Patient 7. Left: Painter-Hillen model, right: Swanson P.I. model. Black contour=segmented tumour, white contour=model-predicted boundary.

**Patient 8**

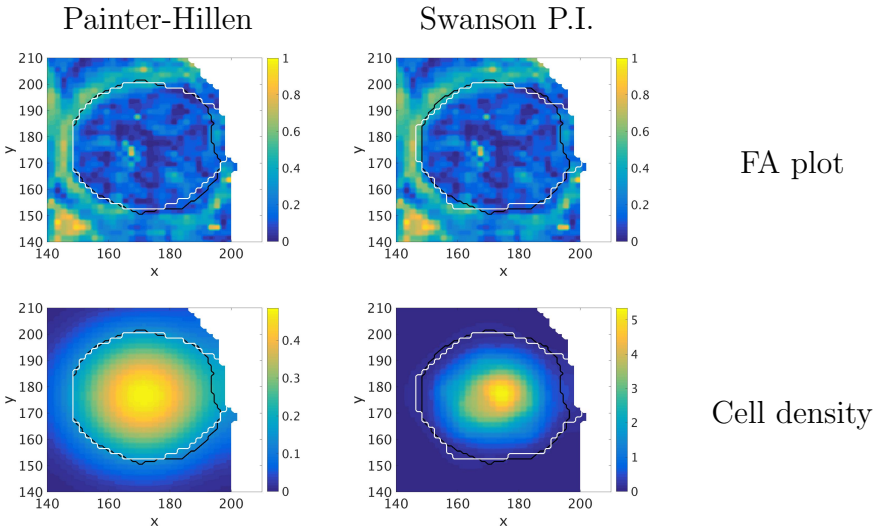


Figure 5.10: 2D Patient 8. Two-dimensional simulation results for Patient 8. Left: Painter-Hillen model, right: Swanson P.I. model. Black contour=segmented tumour, white contour=model-predicted boundary.

**Patient 9**

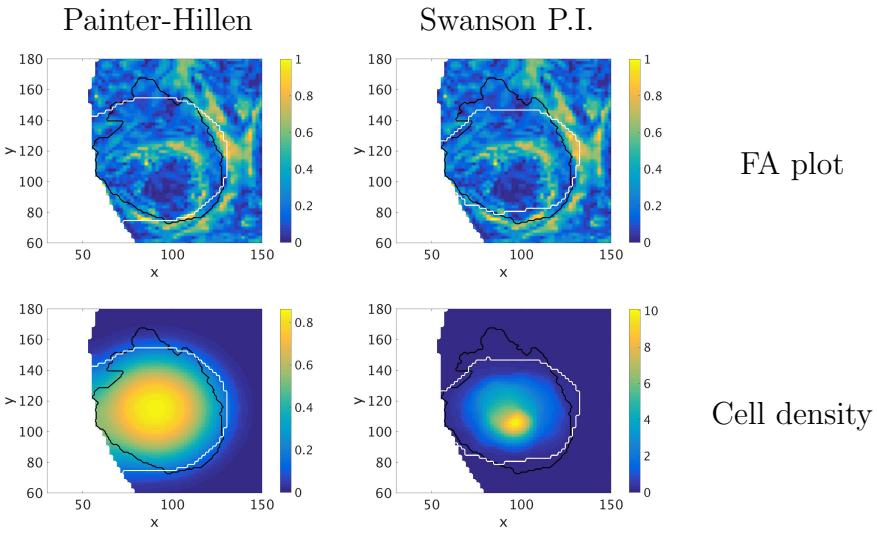


Figure 5.11: 2D Patient 9. Two-dimensional simulation results for Patient 9. Left: Painter-Hillen model, right: Swanson P.I. model. Black contour=segmented tumour, white contour=model-predicted boundary.

**Patient 10**

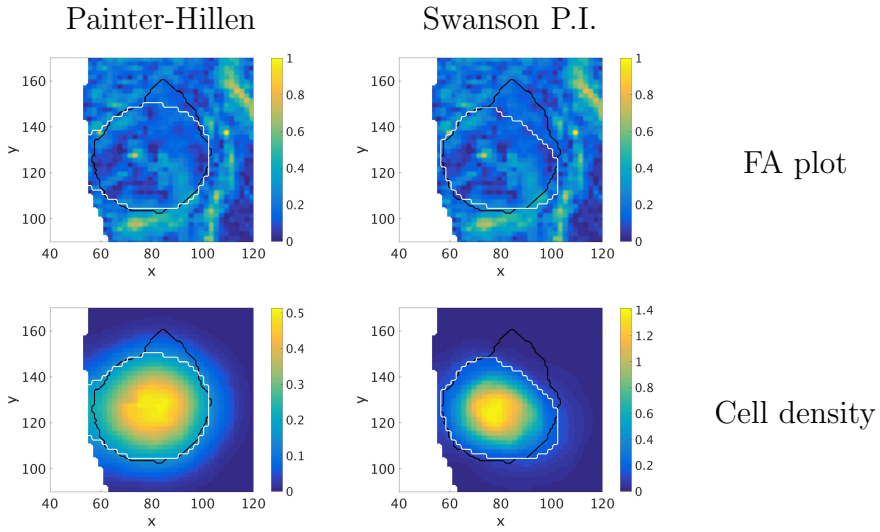


Figure 5.12: 2D Patient 10. Two-dimensional simulation results for Patient 10. Left: Painter-Hillen model, right: Swanson P.I. model. Black contour=segmented tumour, white contour=model-predicted boundary.

### 5.2.1 Summary of Two-dimensional Results

Here we summarize the results of the two-dimensional simulations, shown in Table 5.1. The Jaccard Index for each model and for each patient is shown, as well as the value of the anisotropy parameter, $\kappa$, for the anisotropic Painter-Hillen model.

### 5.2.2 Interpretation of Two-dimensional Results

The first thing that we notice about the two-dimensional results is that the Painter-Hillen shows an improvement in fit over the Swanson P.I. model in nine out of ten cases. This is encouraging, since the Painter-Hillen model includes more of the underlying biological mechanisms. One thing that we notice, however is that the optimal value of the anisotropy parameter $\kappa$ tends to be

| Patient | Painter-Hillen | $\kappa$ | Swanson |
|---|---|---|---|
| 1 | 0.8811 | 0 | 0.8803 |
| 2 | 0.7809 | 3 | 0.7786 |
| 3 | 0.6467 | 1 | 0.5639 |
| 4 | 0.8633 | 1 | 0.8377 |
| 5 | 0.6424 | 0 | 0.6582 |
| 6 | 0.6263 | 5 | 0.6072 |
| 7 | 0.9241 | 0.5 | 0.9057 |
| 8 | 0.9075 | 0.5 | 0.8819 |
| 9 | 0.7994 | 0.5 | 0.7689 |
| 10 | 0.8406 | 2.5 | 0.7581 |

Table 5.1: 2D Results. Table showing the Jaccard Indices for 10 patients for the Painter-Hillen model and the Swanson P.I. model in two dimensions. The corresponding $\kappa$ value that maximized the Jaccard Index for the Painter-Hillen model is also shown.

low, indicating a weak dependency of the tumour growth on the underlying structure. This issue will be discussed further in the discussion following the three-dimensional results, where a potential fix is suggested and implemented.

Looking at the cell density plots in Figures 5.3 through 5.12, we notice the difference in the distributions. Because the Swanson model implements an exponential growth, the tumours tend to have very dense cores with densities that drop off rather rapidly. Additionally, the range in density values is much higher, with the centres of the tumours simulated using the Swanson P.I. model attaining very high density values. This phenomenon is not observed with the Painter-Hillen model due to the use of a logistic growth function.

Considering certain patients specifically, we can see that the Painter-Hillen offers a qualitative advantage over the Swanson P.I. model in certain cases as well. Looking for example at Patient 2, as seen in Figure 5.4, it can be seen that the contour for the Painter-Hillen model more closely follows the segmented tumour boundary, while the Swanson P.I. model misses a large

portion in the upper right hand corner. Patient 3 was a particularly difficult patient to fit, due to the irregular shape of the tumour, as seen in Figure 5.5. While neither model obtained a great fit, the Painter-Hillen model offered a significant advantage over the Swanson P.I. model, displaying the power of the anisotropy. We will see later, in Section 5.4 that it is actually possible to achieve an even better fit for this patient using the anisotropy of the other brain hemisphere.

Patients 5 and 6 represent a failure of both models, as seen in Figure 5.7 and 5.8. Since the fitting was done in a completely objective, quantitative manner, the best fit was obtained by growing a tumour out from the boundary, which does not match the segmented tumour shapes. A large part of the reason for this is due to the absence of mechanical effects in both the Painter-Hillen and the Swanson model. If a real tumour were growing near the skull, there would be a build-up of pressure, causing it to progress more slowly in that direction. This idea will be addressed in Chapter 6. It should also be noted that for tumours having a very isotropic shape, both models were able to replicate them with a high degree of accuracy. We will attempt to improve upon the results for the patients having the lowest five Jaccard Indices, i.e. Patients 2, 3, 5, 6, and 9 in Section 5.4.

In the above simulations, and in those that follow, we have used a single value for $r$ and a single value for $D$. Changing these values, and in particular the balance between growth and diffusion, i.e., $r/D$, could provide better model fits. For example, Gu et al. [52] considered estimating these parameters on a patient-specific basis using multiple time points. Because we are already estimating a number of parameters, we have currently only considered fixed values for $r$ and $D$. However, incorporating a more patient-specific estimation of these parameters should be considered in the future.

## 5.3 Three-dimensional Results

In this section, we show the results of applying both the Painter-Hillen model of Equation (1.12) and the Swanson P.I. model of Equation (5.1) in three dimensions to the same ten patients as for the two-dimensional case. This should be a more realistic situation, since the brain exists in three dimensions, and not as a collection of two-dimensional slices. In general, however, we expect the fits to be poorer, since it is more difficult to fit the full three-dimensional model. In the following figures, the first row shows the 0.16 isosurface of the cancer cell density $u(\boldsymbol{x}, t)$, meant to represent the tumour boundary as it would appear in a scan [51]. This value is used as it has been estimated that this is the approximate cell density threshold that appears in the MRI scans. The first column shows the best fit of the Painter-Hillen model, while the second column shows the best fit of the Swanson model. The last column shows the tumour as it was automatically segmented from the scans. The second row shows a two-dimensional slice through the largest part of the tumour, to show specifically how close the fit is. As in the two-dimensional results, the white line corresponds to the simulated tumour boundary (0.16 level set of $u(\boldsymbol{x}, t)$), while the black line shows the tumour segmentation. The first column shows this image for the Painter-Hillen model, while the second column shows the same for the Swanson model. The last image shows the fractional anisotropy in the slice in which the simulated Painter-Hillen tumour was initiated.

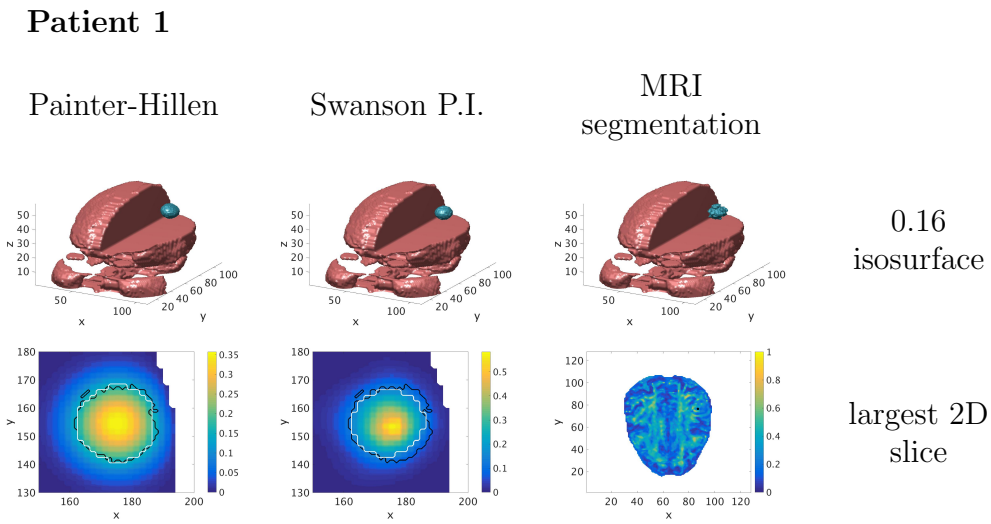


Figure 5.13: 3D Patient 1. Simulation results for Patient 1 in three dimensions. The first column shows the results for the Painter-Hillen model, the second column for the Swanson P.I. model. The third column shows the tumour segmentation in the first row, and the initial condition overlaid onto the FA in the second row.

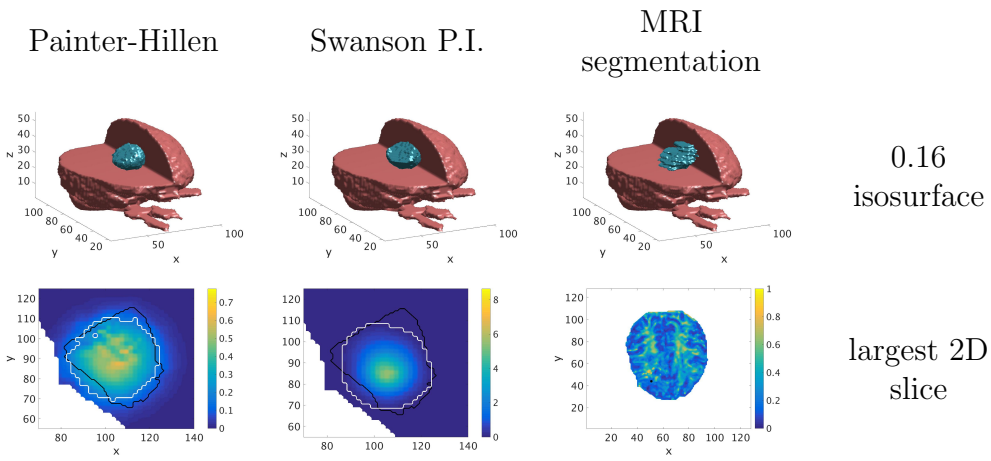


Figure 5.14: 3D Patient 2. Simulation results for Patient 2 in three dimensions. The first column shows the results for the Painter-Hillen model, the second column for the Swanson P.I. model. The third column shows the tumour segmentation in the first row, and the initial condition overlaid onto the FA in the second row.

**Patient 3**

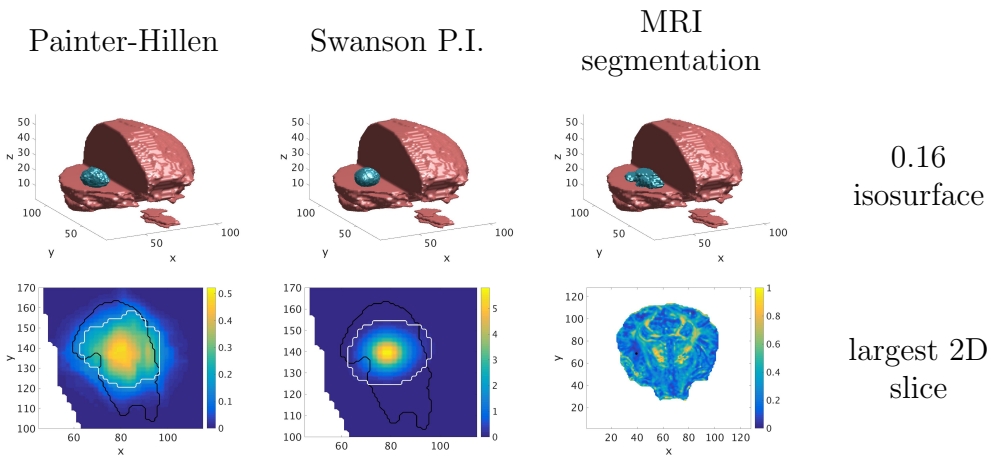


Figure 5.15: 3D Patient 3. Simulation results for Patient 3 in three dimensions. The first column shows the results for the Painter-Hillen model, the second column for the Swanson P.I. model. The third column shows the tumour segmentation in the first row, and the initial condition overlaid onto the FA in the second row.

**Patient 4**

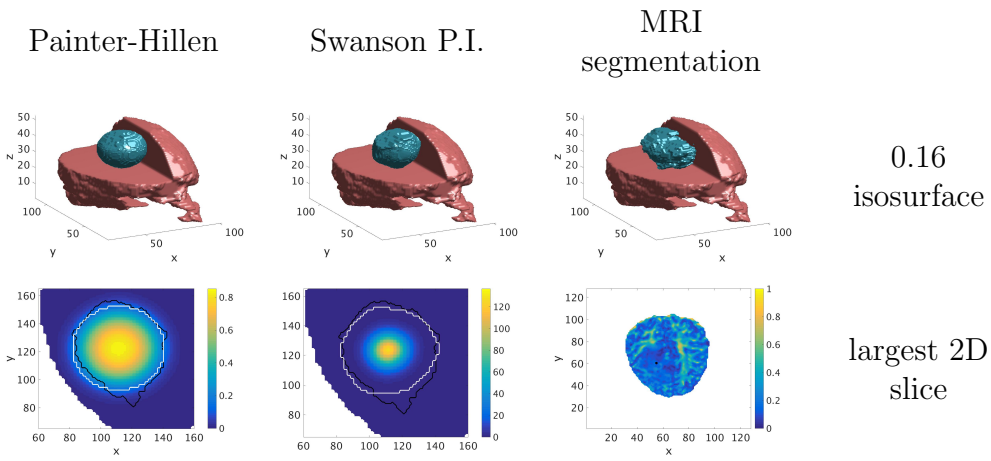


Figure 5.16: 3D Patient 4. Simulation results for Patient 4 in three dimensions. The first column shows the results for the Painter-Hillen model, the second column for the Swanson P.I. model. The third column shows the tumour segmentation in the first row, and the initial condition overlaid onto the FA in the second row.

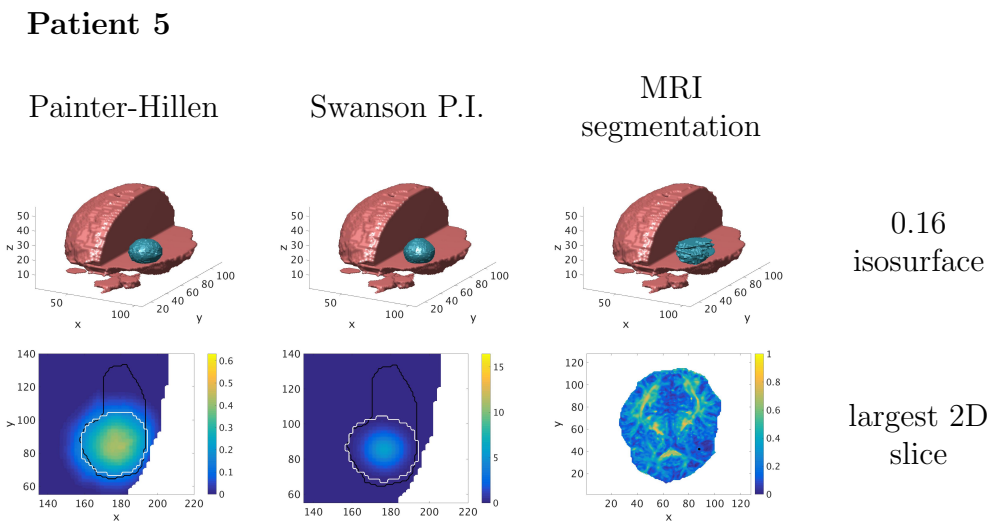


Figure 5.17: 3D Patient 5. Simulation results for Patient 5 in three dimensions. The first column shows the results for the Painter-Hillen model, the second column for the Swanson P.I. model. The third column shows the tumour segmentation in the first row, and the initial condition overlaid onto the FA in the second row.

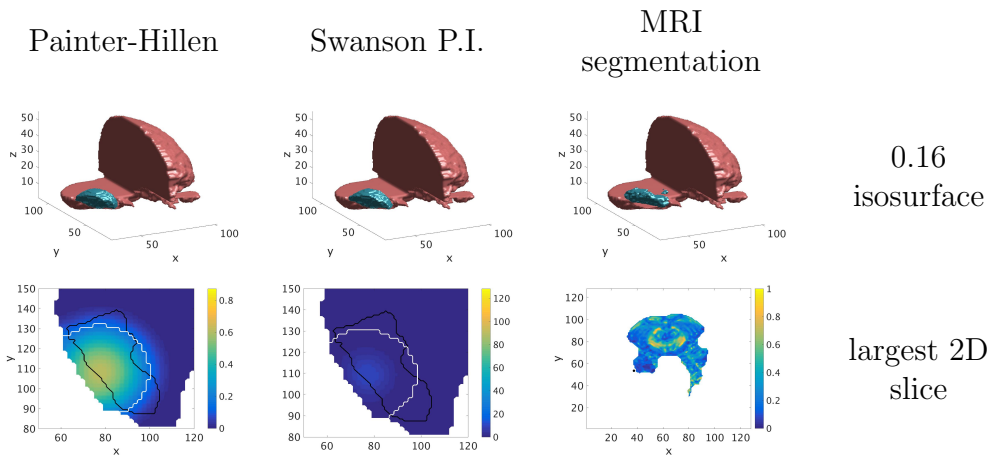


Figure 5.18: 3D Patient 6. Simulation results for Patient 6 in three dimensions. The first column shows the results for the Painter-Hillen model, the second column for the Swanson P.I. model. The third column shows the tumour segmentation in the first row, and the initial condition overlaid onto the FA in the second row.

**Patient 7**

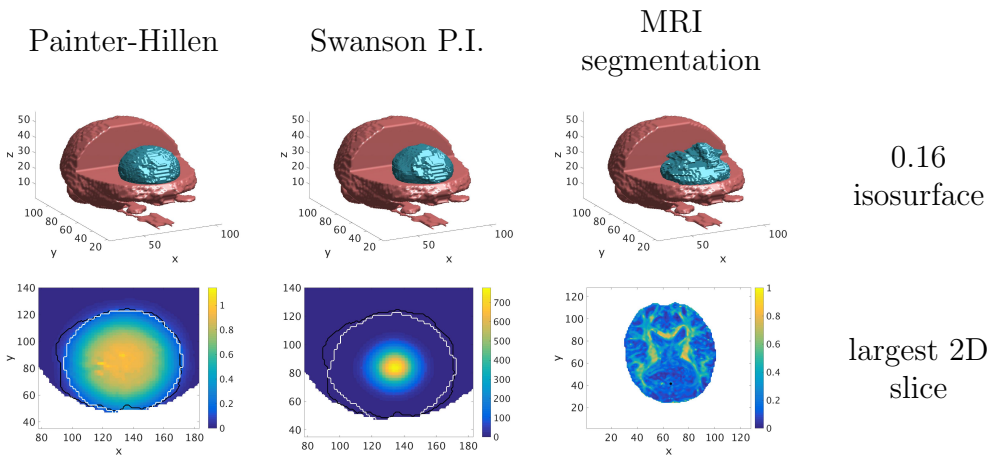


Figure 5.19: 3D Patient 7. Simulation results for Patient 7 in three dimensions. The first column shows the results for the Painter-Hillen model, the second column for the Swanson P.I. model. The third column shows the tumour segmentation in the first row, and the initial condition overlaid onto the FA in the second row.

**Patient 8**

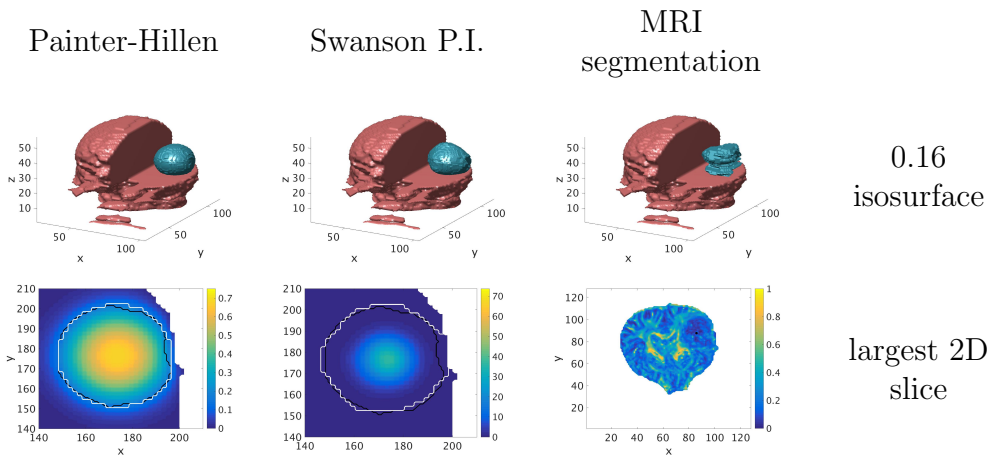


Figure 5.20: 3D Patient 8. Simulation results for Patient 8 in three dimensions. The first column shows the results for the Painter-Hillen model, the second column for the Swanson P.I. model. The third column shows the tumour segmentation in the first row, and the initial condition overlaid onto the FA in the second row.

**Patient 9**

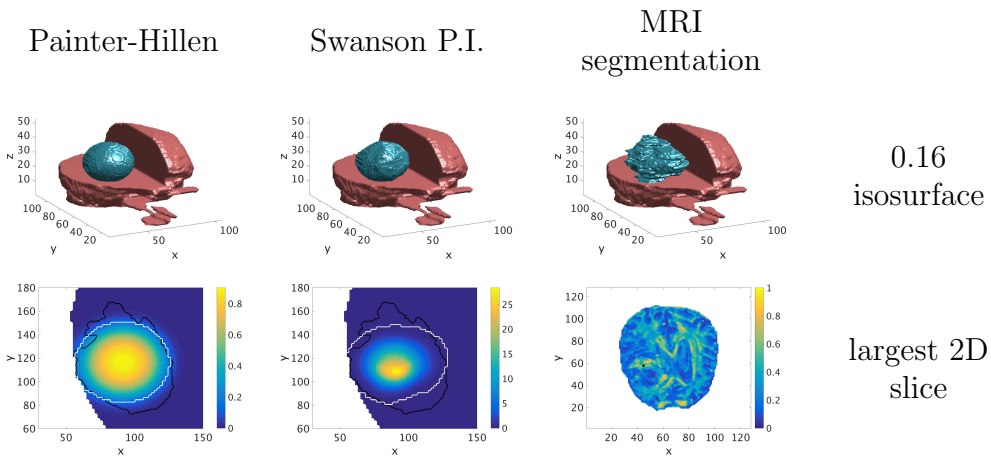


Figure 5.21: 3D Patient 9. Simulation results for Patient 9 in three dimensions. The first column shows the results for the Painter-Hillen model, the second column for the Swanson P.I. model. The third column shows the tumour segmentation in the first row, and the initial condition overlaid onto the FA in the second row.

**Patient 10**

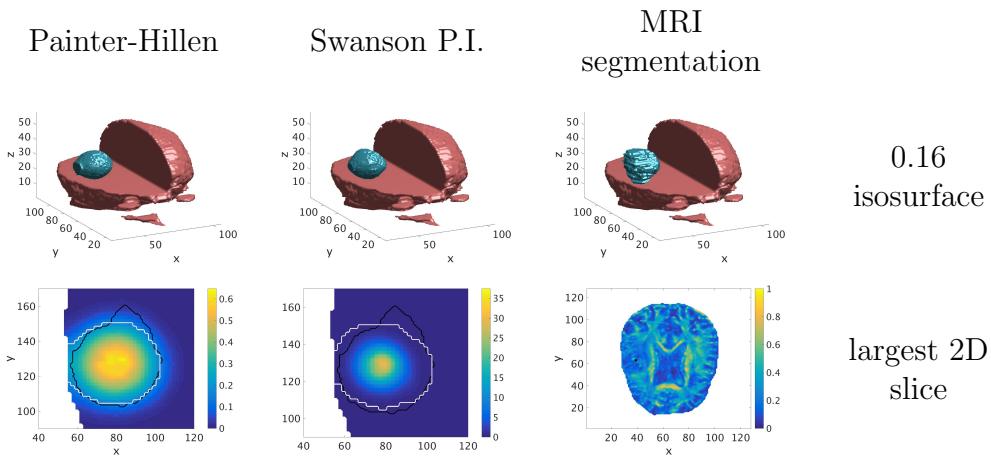


Figure 5.22: 3D Patient 10. Simulation results for Patient 10 in three dimensions. The first column shows the results for the Painter-Hillen model, the second column for the Swanson P.I. model. The third column shows the tumour segmentation in the first row, and the initial condition overlaid onto the FA in the second row.

### 5.3.1 Summary of Three-dimensional Results

The results of the three-dimensional simulations are summarized in Table 5.2. The Jaccard Index for the best fit for each patient for both the Painter-Hillen and the Swanson P.I. model are shown. Additionally, the value of the anisotropy parameter $\kappa$ that achieved the best fit for the Painter-Hillen model is shown.

| Patient | Anisotropic | $\kappa$ | Swanson |
|---|---|---|---|
| 1 | 0.6506 | 0.5 | 0.7002 |
| 2 | 0.6063 | 5.5 | 0.5669 |
| 3 | 0.4888 | 8 | 0.4357 |
| 4 | 0.6887 | 1 | 0.6332 |
| 5 | 0.6663 | 4.5 | 0.6453 |
| 6 | 0.4912 | 1 | 0.4794 |
| 7 | 0.6664 | 4 | 0.6149 |
| 8 | 0.6368 | 0 | 0.5930 |
| 9 | 0.6275 | 0.5 | 0.5719 |
| 10 | 0.7399 | 2.5 | 0.7156 |

Table 5.2: 3D Results. Table showing the Jaccard Indices for each of 10 patients for both the Painter-Hillen model and the Swanson P.I. model in three dimensions. The corresponding $\kappa$ value that maximized the Jaccard Index for the Painter-Hillen is also shown.

We can draw two conclusions from these results, the first is that the Painter-Hillen model does now reliably perform better than the Swanson P.I. model. The second is that frequently, a $\kappa$ value close to 0 optimizes the fit, meaning that the anisotropic model does best when it is tuned to isotropic spread! Fortunately, there is a good explanation for this phenomenon. Looking back to figure 5.1, we observe that the fibre networks within the tumours are displaced or destroyed, leaving behind tissue that is in many cases almost isotropic. Running the model using this DTI data then does not give much advantage over an isotropic method, which is not surprising. This issue will be addressed

and remedied in the section following the 3-D results.

### 5.3.2 Interpretation of Three-dimensional Results

The first thing of note for the three-dimensional results is that the Painter-Hillen model was able to achieve an improved fit in nine out of ten cases over the Swanson P.I. model. Because the Painter-Hillen model includes more of the biological details, this is as we would expect. These results then indicate that the Painter-Hillen model could potentially offer an improvement in therapeutic outcomes if implemented clinically.

Looking deeper at these results, we can see that generally the anisotropy parameter was higher than in two dimensions, giving tumour shapes that are more dependent on the brain architecture. Overall, however, we notice that the fits are quantitatively poorer than they were in two dimensions. This is due to the difficulty in fitting the full three-dimensional model, as this amounts to simultaneously fitting many axial slices. With that said, many of the Jaccard Indices achieved an impressive level of accuracy.

Looking specifically at Patient 2, i.e. Figure 5.14, we can see that both model fits are significantly smoother than the segmented tumour. This is due to the fact that segmentations are done on individual two-dimensional slices and then recombined to form the three-dimensional tumour. As such, the simulation results for both the Painter-Hillen model and the Swanson model offer an advantage over the segmentation. Looking at the slices through the middle of the tumour for Patient 2, shown in the second row of Figure 5.14, we can see that while there is not a dramatic improvement in Jaccard Index with the Painter-Hillen model, qualitatively the model does a better job at capturing the tumour shape. Also of note for all of the patients is the difference in cell

density ranges. Due to the exponential growth of the Swanson model, the resultant tumours possess very dense cores that drop off in density rapidly. The exponential growth also generates very high density values, vs. the Painter-Hillen model that will not grow at densities greater than 1.

The anisotropy of the Painter-Hillen model offers a large improvement in fit for Patient 3, as can be seen in Figure 5.15. Because the cells are able to follow the fibres of the brain, some of the elongation of the tumour is captured. An interesting artifact is seen in the tumour of Patient 5. While the majority of the tumour appears almost spherical, the central slice is very elongated, and juts out from the rest of the tumour segmentation, as can be seen in the first row of Figure 5.17. It appears then that an error occurred in the automated segmentation algorithm.

We encounter a failure of the model with Patient 6, as we did in two dimensions. We can see in the third column of the second row of Figure 5.18 that the initial condition is not actually contained within the brain, which is obviously not realistic. This occurred due to the objective nature of the model fit, as this was the configuration that gave the highest Jaccard Index. The main problem is that both the Painter-Hillen model and the Swanson model will show an overgrowth at the boundary. In reality, a growing tumour would experience a "push-back", or pressure buildup as it compressed the tissue next to the skull, slowing its progression in this direction. Neither of these models contain this effect, and this "mass effect" will be addressed in Chapter 6.

## 5.4 Reflected-DTI

We saw above that there is an issue with using patient data. The problem is that most patients who receive DTI and MRI scans already have a tumour,

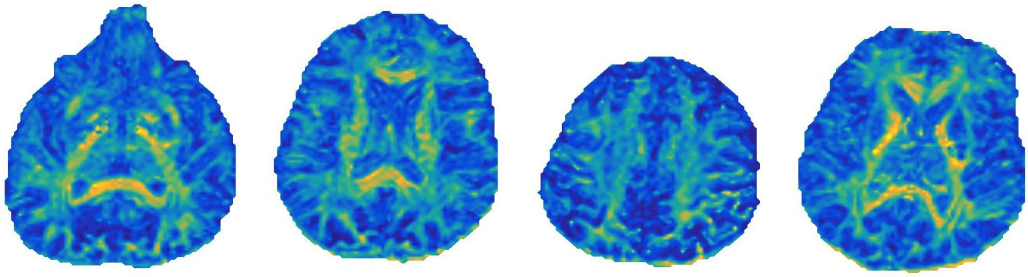

Figure 5.23: Sample Tumour-Free Slices. A sampling of axial slices that do not contain a tumour from the 10 patient dataset. Fractional anisotropy is plotted in order to show the symmetry.

thus it is impossible to obtain an appropriate set of DTI data that accurately describes the initial anisotropic tumour growth. Looking back at Figure 5.1, we can see that within the tumour segmentations (black), there is not a lot of variation in the fractional anisotropy. This is because, as the tumours grew, they changed the brain structures, pushing nerve fibres out of the way, or destroying them altogether. If we then use this DTI data to simulate tumours, we cannot expect to achieve realistic results. This brain looks completely different than it did at the time the tumour started growing. As a remedy for this, we want to estimate the missing data. While we could use Atlas data, we would rather use the symmetry of the brain when it is healthy. As an example, Figure 5.23 shows a sampling of axial slices that do not contain a tumour The slices come from the same 10 patients studies before, where we have chosen slices well above or well below the tumour. The fractional anisotropy is plotted in order to show the symmetry displayed.

Because of the symmetry, we reflect the DTI data from the healthy side across the brain's centreline, into the tumour segmentation. Doing so will allow our simulations to run on a more realistic domain more closely resembling what the brain looked like at the time that the tumour began growing. There were

some simulations above that achieved very good fits even with the original DTI data. We select the 5 patients with the lowest Jaccard Indices from Table 5.1 and try to improve them by implementing the reflected DTI technique. This will thus be done for Patients 2, 3, 5, 6 and 9. The patients whose model fits had a high Jaccard Index had tumours that were often quite regular or spherical in shape, hence little benefit would be obtained by reflecting the DTI data in these cases. The resulting fractional anisotropy after these reflections is shown in Figure 5.24 along with the original tumour segmentations of Figure 5.1. The top row shows the tumour segmentations over the original fractional anisotropy, while the bottom row shows the tumour segmentations over the reflected fractional anisotropy data.

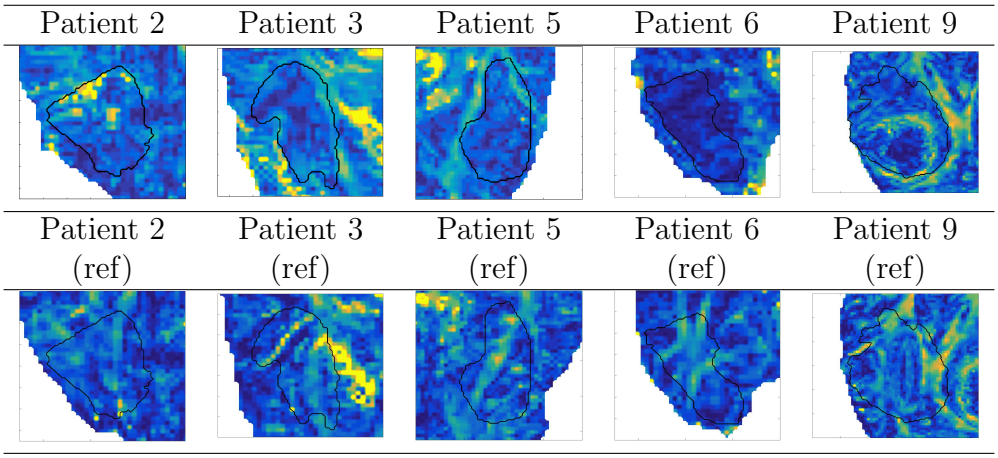


Figure 5.24: Reflected Segmentations. Top: Segmentations through the largest two-dimensional slice of each patient's glioma plotted over top of the original fractional anisotropy. Bottom: The same segmentations shown plotted on top of the fractional anisotropy that has been reflected from the other brain hemisphere.

### 5.4.1 Two-dimensional Reflected DTI Results

We present here the results for the two-dimensional simulations for each of the five patients described above. The simulations are now run using the reflected data in an attempt to obtain a better fit. As before, the results of the Painter-Hillen model are shown on the left while the results of the Swanson P.I. model are shown on the right.

**Patient 2**

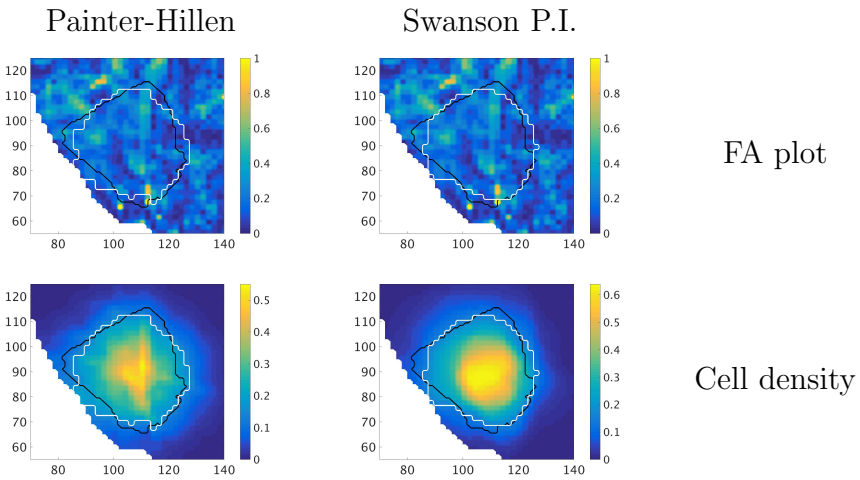


Figure 5.25: 2D Patient 2 Reflected DTI. Two-dimensional simulation results for Patient 2 using reflected DTI data. The result on the left is the result for the Painter-Hillen model, while the result on the right is from the Swanson P.I. model.

**Patient 3**

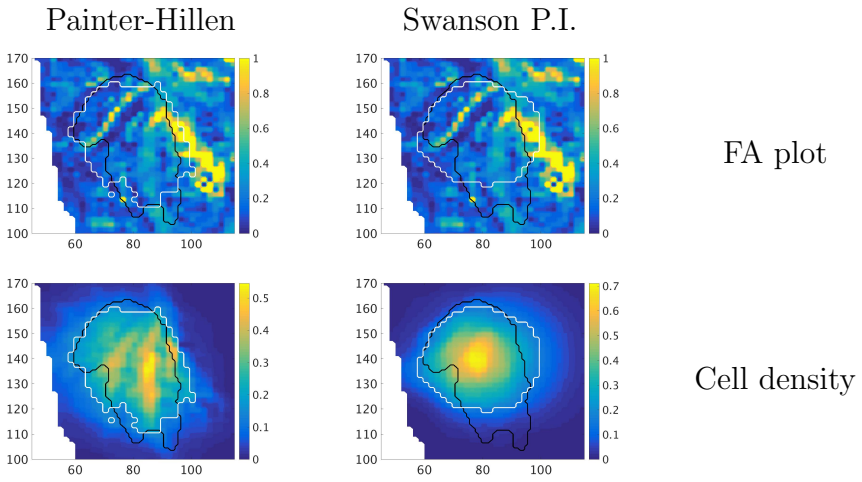


Figure 5.26: 2D Patient 3 Reflected DTI. Two-dimensional simulation results for Patient 3 using reflected DTI data. The result on the left is the result for the Painter-Hillen model, while the result on the right is from the Swanson P.I. model.

**Patient 5**

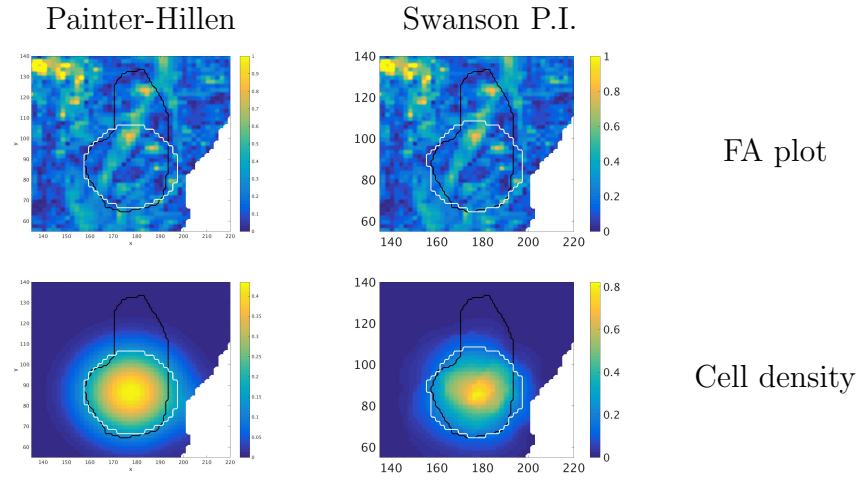


Figure 5.27: 2D Patient 5 Reflected DTI. Two-dimensional simulation results for Patient 5 using reflected DTI data. The result on the left is the result for the Painter-Hillen model, while the result on the right is from the Swanson P.I. model.

**Patient 6**

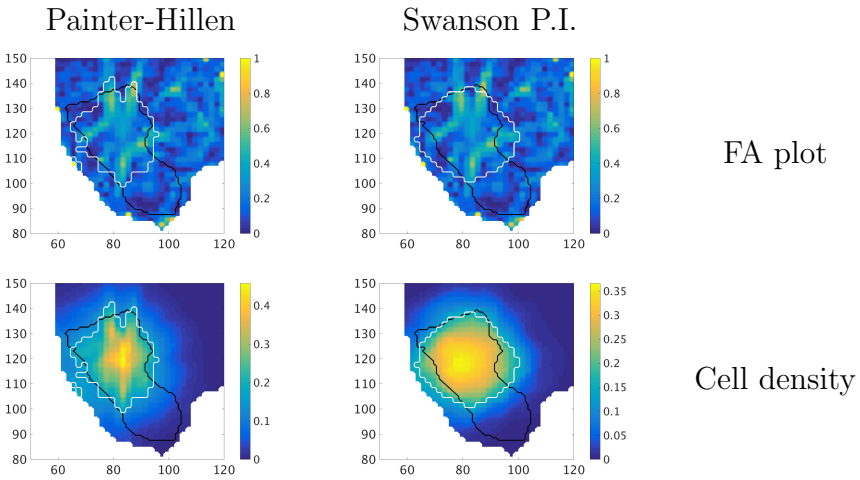


Figure 5.28: 2D Patient 6 Reflected DTI. Two-dimensional simulation results for Patient 6 using reflected DTI data. The result on the left is the result for the Painter-Hillen model, while the result on the right is from the Swanson P.I. model.

**Patient 9**

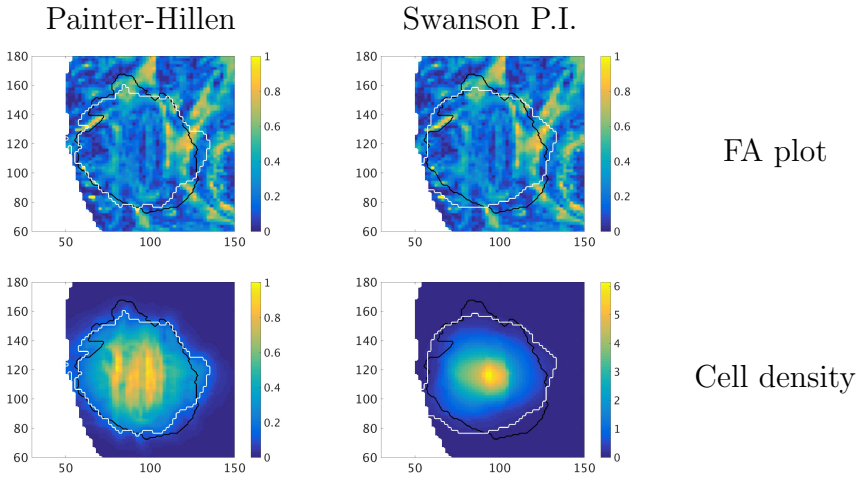


Figure 5.29: 2D Patient 9 Reflected DTI. Two-dimensional simulation results for Patient 9 using reflected DTI data. The result on the left is the result for the Painter-Hillen model, while the result on the right is from the Swanson P.I. model.

### 5.4.2 Summary of Two-dimensional Reflected DTI Results

Here we present a summary of all of the two-dimensional results, including those from the original DTI data for comparison. These results are shown in Table 5.3. The Jaccard Indices for both the Painter-Hillen model and the Swanson model are presented, for both the original DTI data and the reflected DTI data. Additionally, the anisotropy parameters $\kappa$ that provided the optimal fit for the Painter-Hillen model are included.

| Patient | Painter-Hillen | $\kappa$ | P.-H. + Ref. | $\kappa$ | Swanson | S. + Ref. |
|---|---|---|---|---|---|---|
| 1 | 0.8811 | 0 | - | - | 0.8803 | - |
| 2 | 0.7809 | 3 | 0.7886 | 6 | 0.7786 | 0.8284 |
| 3 | 0.6467 | 1 | 0.7194 | 9.5 | 0.5639 | 0.6356 |
| 4 | 0.8633 | 1 | - | - | 0.8377 | - |
| 5 | 0.6426 | 0 | 0.6156 | 0 | 0.6582 | 0.6301 |
| 6 | 0.6269 | 5 | 0.5571 | 6.5 | 0.6072 | 0.5437 |
| 7 | 0.9241 | 0.5 | - | - | 0.9057 | - |
| 8 | 0.9075 | 0.5 | - | - | 0.8819 | - |
| 9 | 0.7990 | 0.5 | 0.8209 | 6.5 | 0.7689 | 0.7869 |
| 10 | 0.8406 | 2.5 | - | - | 0.7581 | - |

Table 5.3: 2D Reflected Domain Results. Table showing the Jaccard Indices for 10 patients for the Painter-Hillen model and the Swanson P.I. model in two dimensions. The corresponding $\kappa$ value that maximized the Jaccard Index for the Painter-Hillen model is also shown. Additionally, results for a subset of five patients using the reflected DTI method are shown.

### 5.4.3 Interpretation of Two-dimensional Reflected DTI Results

Application of the reflected DTI technique improved the results for three out of the five patients for which it was attempted. It should be noted that the two for which it did not lead to an improvement were the same two patients

for which the models failed originally, i.e. Patients 5 and 6. For Patient 2, as can be seen in Figure 5.25, the increase in the Jaccard Index was almost negligible, however the qualitative fit seen in Figure 5.25 is better than that of Figure 5.4, which does not use reflection.

Patient 3 is perhaps the most successful application of this technique, and was also one of the most challenging patients to fit initially. It is interesting to look at the FA plot in the top row of Figure 5.26, and to see how the tumour segmentation matches up to the fibre directions. One can almost visualize how the tumour grew along the fibres. Comparing this to the cell density plot in the bottom row of Figure 5.26, the tumour cells seem to collect along the fibres in the same manner as was seen in the simplified domain simulations of Chapter 3. Quantitatively speaking, the improvement in Jaccard Index was dramatic, as can be seen in Table 5.3.

Finally, for Patient 9, a slight improvement in Jaccard Index was seen when the reflected DTI technique was implemented. Again, the qualitative improvement in this case was significant, as can be seen by comparing Figures 5.11 and 5.29. Overall, these results seem to indicate that for more challenging, more anisotropic tumour shapes, filling in the DTI data by reflecting it over the brain's centreline seems to offer the potential for improved model performance.

### 5.4.4 Three-dimensional Reflected DTI Results

In this section, we show the results of applying the Painter-Hillen model of Equation (1.12) in three dimensions, using the reflected-DTI data. The top row shows the $u = 0.16$ isosurface of the cell density, with the first column corresponding to the Painter-Hillen simulations, and the centre column corresponding to the Swanson P.I. simulations. The third column shows the tumour

segmentation in three dimensions. The second row shows the slice containing the maximum tumour volume through the centre of the three-dimensional simulation. The colours correspond to cell density, with yellow=high and blue=low. The white contour shows the model-predicted boundary, while the black contour shows the tumour segmentation.

**Patient 2**

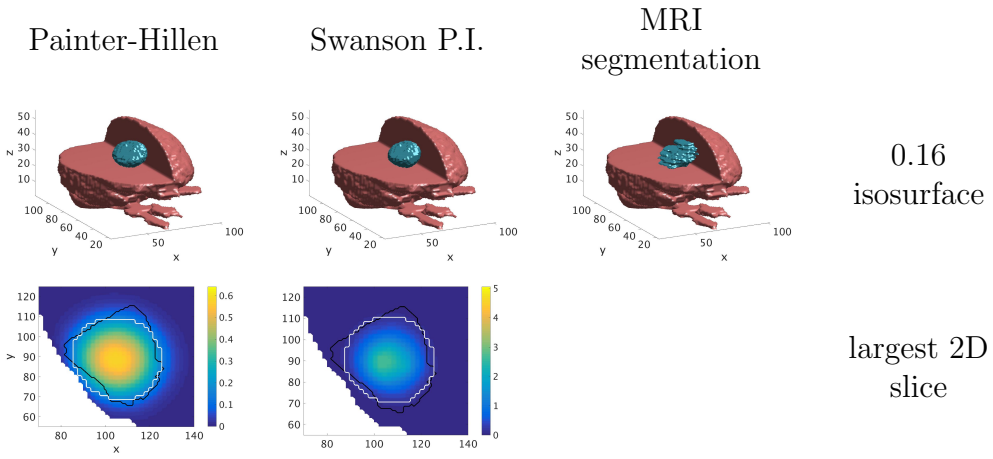


Figure 5.30: 3D Patient 2 Reflected DTI. Three-dimensional simulation results for Patient 2 using reflected DTI data. The first column shows the results for the Painter-Hillen model, the second column for the Swanson P.I. model. The third column of the first row shows the automatic tumour segmentation.

**Patient 3**

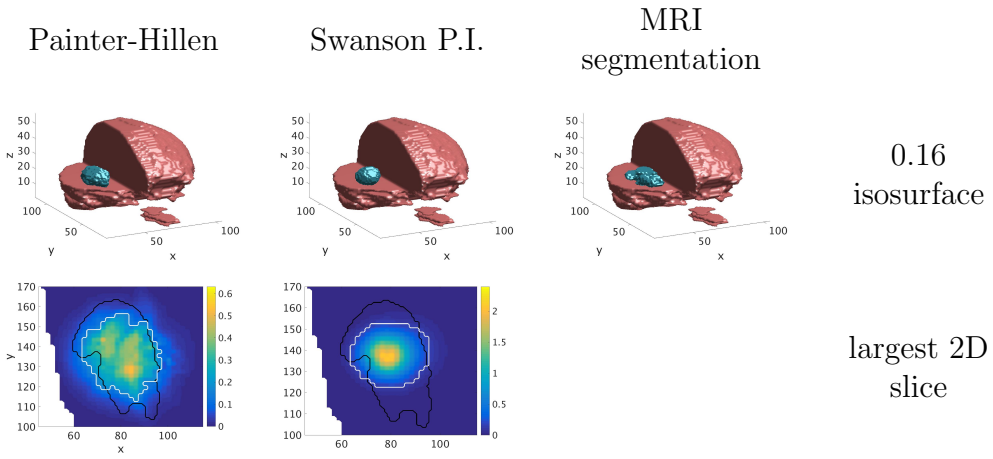


Figure 5.31: 3D Patient 3 Reflected DTI. Three-dimensional simulation results for Patient 3 using reflected DTI data. The first column shows the results for the Painter-Hillen model, the second column for the Swanson P.I. model. The third column of the first row shows the automatic tumour segmentation.

**Patient 5**

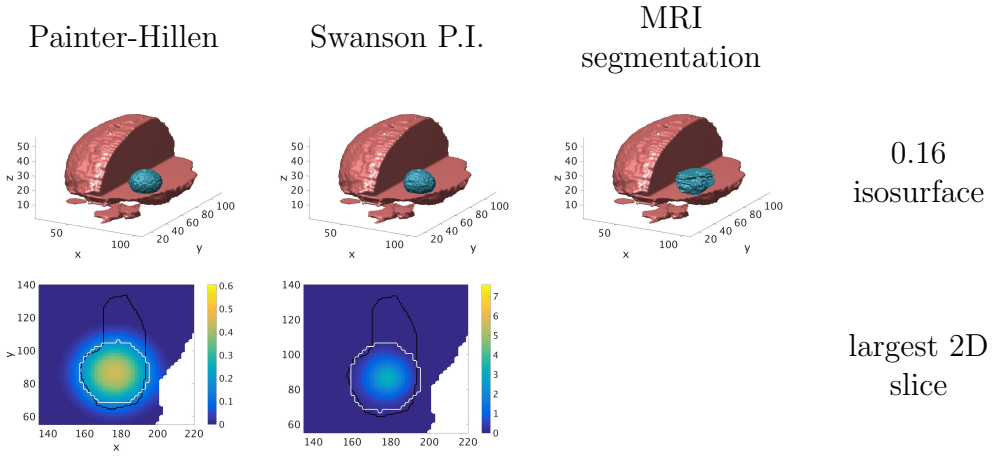


Figure 5.32: 3D Patient 5 Reflected DTI. Three-dimensional simulation results for Patient 5 using reflected DTI data. The first column shows the results for the Painter-Hillen model, the second column for the Swanson P.I. model. The third column of the first row shows the automatic tumour segmentation.

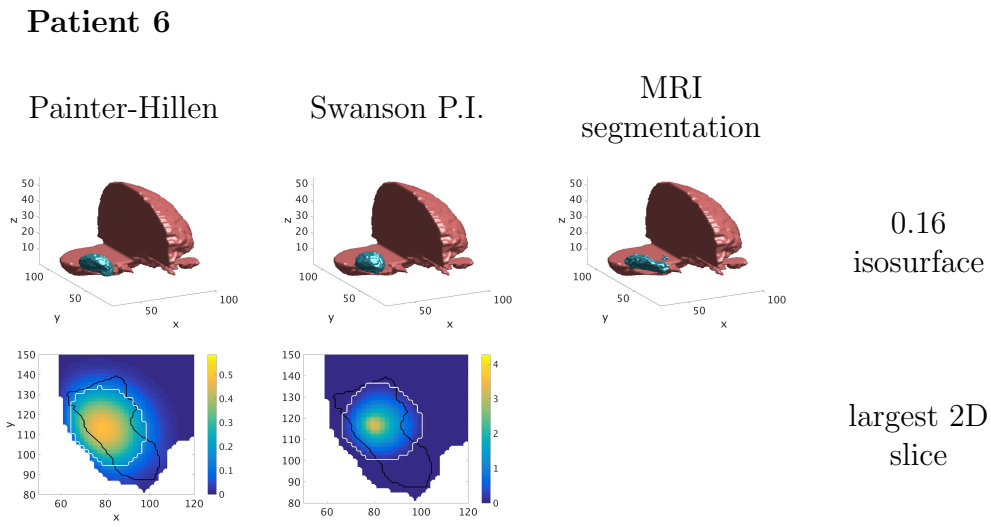


Figure 5.33: 3D Patient 6 Reflected DTI. Three-dimensional simulation results for Patient 6 using reflected DTI data. The first column shows the results for the Painter-Hillen model, the second column for the Swanson P.I. model. The third column of the first row shows the automatic tumour segmentation.

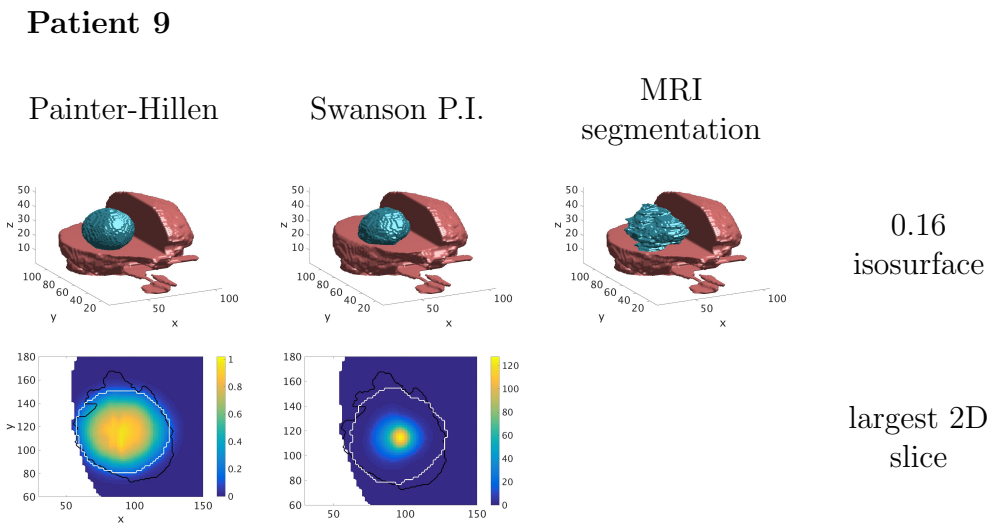


Figure 5.34: 3D Patient 9 Reflected DTI. Three-dimensional simulation results for Patient 9 using reflected DTI data. The first column shows the results for the Painter-Hillen model, the second column for the Swanson P.I. model. The third column of the first row shows the automatic tumour segmentation.

### 5.4.5 Summary of Three-dimensional Reflected DTI Results

| Patient | Painter-Hillen | $\kappa$ | P.-H. + Ref. | $\kappa$ | Swanson | S. + Ref. |
|---|---|---|---|---|---|---|
| 1 | 0.6506 | 0.5 | - | - | 0.7002 | - |
| 2 | 0.6063 | 5.5 | 0.6146 | 1 | 0.5669 | 0.5837 |
| 3 | 0.4888 | 8 | 0.4900 | 7 | 0.4357 | 0.4658 |
| 4 | 0.6887 | 1 | - | - | 0.6332 | - |
| 5 | 0.6643 | 4 | 0.6567 | 1 | 0.6453 | 0.6516 |
| 6 | 0.4912 | 1 | 0.4576 | 0 | 0.4794 | 0.4220 |
| 7 | 0.6664 | 4 | - | - | 0.6149 | - |
| 8 | 0.6368 | 0 | - | - | 0.5930 | - |
| 9 | 0.6275 | 0.5 | 0.6371 | 2 | 0.5719 | 0.6206 |
| 10 | 0.7399 | 2.5 | - | - | 0.7156 | - |

Table 5.4: 3D Reflected Domain Results. Table showing the Jaccard Indices for 10 patients for the Painter-Hillen model and the Swanson P.I. model in three dimensions. The corresponding $\kappa$ value that maximized the Jaccard Index for the Painter-Hillen model is also shown. Additionally, results for a subset of five patients using the reflected DTI method are shown.

### 5.4.6 Interpretation of Three-dimensional Reflected DTI Results

For the three-dimensional case, we are able to further improve the fits in three out of the five cases. Overall, there does not seem to be as much of an advantage to using the reflected-DTI technique in three dimensions. This is likely due to the fact that in two dimensions, when a fibre is pushed out of the plane of consideration, it is gone completely. In three dimensions, when a fibre is moved, it is still contained within the domain. Therefore, while the result may be distorted due to the movement of fibres, the tendency of the fibre direction is still included.

Once again, Patients 5 and 6 proved a challenge when it came to fitting the

model. The results seem to indicate that in order to fit the model to patients whose tumours are in close proximity to the skull, a mass effect will need to be included.

For Patients 2, 3 and 9, however, an advantage was gained by using the reflected DTI data to fit the model. This can be seen not only quantitatively in Table 5.4.5, but also qualitatively, as is seen in Figures 5.30, 5.31 and 5.34. In particular, the Painter-Hillen model seems to do a good job of capturing the overall shape of the tumour in Figure 5.31, even though the Jaccard score is low. It is a very irregularly shaped tumour, and as such it is very challenging to get a good model fit for Patient 3.

## 5.5 Treatment Regions

The goal of the Painter-Hillen model is to simulate glioma invasion in a manner that will be useful to clinicians during treatment planning. In this section we outline how the Painter-Hillen model may be used to delineate planning target volumes for radiation therapy.

As was mentioned in Chapter 1, typical radiation treatment for glioma involves treating the visible tumour as well as an extension to account for microscopic disease spread. Clinically, these are referred to as the Gross Tumour Volume (GTV) and the Clinical Target Volume (CTV), respectively [42]. The GTV is defined as the mass that "can be seen, palpated or imaged" [42]. The CTV is harder to define, as it is where there is assumed to be microscopic spread that cannot be seen or imaged. In particular, for glioma patients, this region is typically taken to be a uniform extension of the GTV. Additionally, clinicians define a Planning Target Volume, or PTV, which consists of a slight extension of the GTV to accommodate inconsistencies between imaging

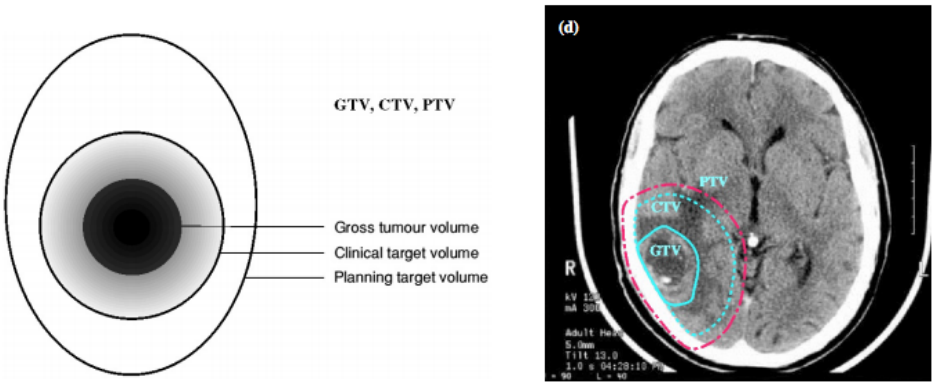


Figure 5.35: GTV, CTV and PTV. Left: Outline of the different treatment volumes. Taken from [75]. Right: An example of a GTV, CTV and PTV for a glioblastoma patient, delineated using a CT scan. GTV outlines the visible tumour, CTV accounts for invisible spread, and PTV allows for uncertainties in the delivery of the dosage. Modified from [42].

modalities and limitations of the machines that deliver the prescribed dose. The PTV is mainly used to ensure that the prescribed radiation is actually delivered to the CTV as desired [42]. These three volumes may of course receive different doses, as they are expected to contain different cancer cell concentrations. An example of these three volumes for a given glioblastoma patient is shown in Figure 5.35. Additionally, radiotherapy planning must take into account critical biological structures, avoiding delivering too high of a dose where possible [42]. For example, in the abdomen, clinicians may try to avoid the lungs where they are not involved. In the brain, this may mean avoiding critical brain structures. These tissues are referred to as organs at risk (OR's) [42].

Defining the CTV for a glioma patient is not a trivial task, and is done in a naive, non-patient-specific manner with the goal of targeting as much microscopic spread as possible. Without being able to see this spread via imaging, or what would be a very invasive biopsy, clinicians use post mortem

data from previous patients to estimate the maximum spread of the cells [42]. While this is a valid method, having a model that is capable of simulating microscopic spread can better advise clinicians about where they might expect to find malignant cells. In particular, we use a level set of the cancer cell density function to define a revised CTV. We then compare this region to the traditional uniform extension that would typically be used. While, for tumours with a low $\kappa$ value that exhibit mostly isotropic spread (i.e. Patient 8), these regions will be similar, for patients with a more anisotropic tumour (i.e. Patient 2), there may be large discrepancies.

Figure 5.36 outlines the GTV in black, the traditional CTV in white, and the modified CTV in red for Patients 2 and 8. The modified CTV was drawn using a level set of the Painter-Hillen simulation results, while the traditional CTV is simply a 2 $c$m extension of the segmented tumour. The appropriate level set was chosen so that the regions contained the same area. Patient 8 was chosen because the Painter-Hillen model obtained a very good fit for this case, and the anisotropy parameter $\kappa$ was 0.5, which corresponds to nearly isotropic spread. The purpose of including this patient is to demonstrate that for this case, the two CTV regions are nearly identical. For Patient 2, however, there is a big difference between the classical CTV in white, and the modified, model-determined CTV in red. Note that the reflected-DTI results were used to determine this treatment region.

## 5.6 Chapter Summary

In this chapter, we showed simulation results for ten patients from the Cross Cancer Institute for both the Swanson P.I. model of Equation 5.1 and the Painter-Hillen model of Equation 1.12. We thus began by describing the

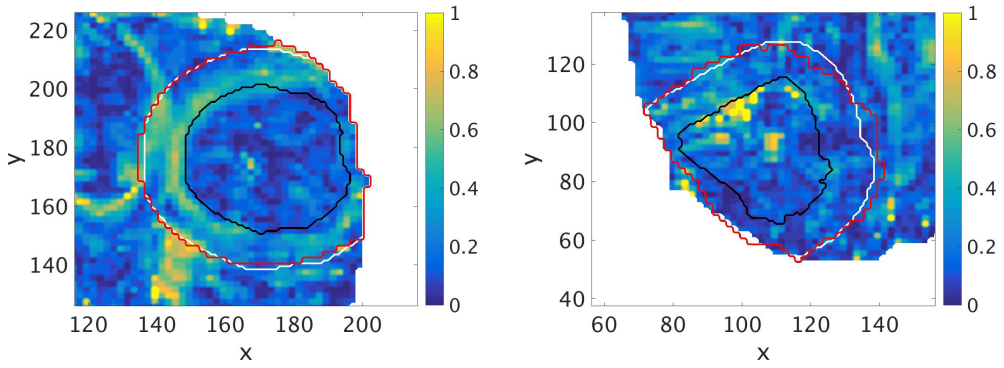


Figure 5.36: Treatment Region Recommendations. The GTV in black, traditional CTV in white and modified CTV in red are shown for Patients 8 (left) and 2 (right) in two dimensions. We see that for some patients whose tumours display more isotropic spread, there is little difference between the traditional and modified CTV's, however some patients show a large discrepancy between the two.

Swanson P.I. model in more detail, and described how to implement it numerically. We then showed the Jaccard Index values for both models in both two and three dimensions, for all ten patients. The results were that in both two and three dimensions, the Painter-Hillen model outperformed the Swanson P.I. model in nine out of ten cases. Additionally, we showed the cell density plots along with the automatic tumour segmentations, so that we could also comment on the qualitative nature of the model fits.

While the results of the simulations seemed to indicate that the Painter-Hillen model offered an advantage over the Swanson P.I. model, many of the fits featured anisotropy parameter $\kappa$ values that were low, indicating that there wasn't a huge advantage over the isotropic model. The reason for this was that the DTI data was altered within the tumour segmentations, with many of the fibre tracts missing as they had been pushed out of the way by the growing tumour, or destroyed completely. To remedy this, we proposed to take advantage of the symmetry present in a healthy brain, reflecting the DTI

data from the other brain hemisphere to approximate the missing data.

We considered the results of simulating both the Swanson P.I. model and the Painter-Hillen model on the reflected data for a subset of five patients, in both two and three dimensions. To choose this subset, we took the lowest five Jaccard Indices, to see if the reflected-DTI technique could improve upon the fits. In the two-dimensional case, this process improved the Jaccard index for three out of the five patients. In some cases, the advantage was substantial, particularly where the tumours had an elongated shape. In three dimensions, the advantage wasn't so substantial, with the reflected-DTI technique improving the Jaccard Index in once again three out of the five patients. The improvement , however, was more slight than what was seen in the two-dimensional case. We postulated that this was due to the fact that in two dimensions, when the fibres were pushed out of the way, they were no longer present in the plane of consideration. In three dimensions, while the fibre network may have been distorted, the displaced fibres remained within the domain.

The results of this chapter indicated that the Painter-Hillen model, in conjunction with the reflected-DTI technique, offers the potential to improve upon current standards of treatment for glioma patients. As such, we outlined how a model for the cell density could be useful for clinicians in designing patient treatment plans.

# Chapter 6

# The Mass Effect

In the model thus far, there is no feedback effect as the mass grows, deforming the brain around it. The absence of this effect is especially obvious when the simulated tumours get close to the skull. In reality, we would expect that as the tissue becomes compressed between the tumour and the skull, a force would be induced, and this force would push back on the tumour, hindering further growth. This can be seen in the real tumour segmentations, as rarely do the actual tumours grow right up against the skull. By contrast, the simulated tumours tend to overestimate the cell densities close to the boundary.

To remedy this, we will incorporate a "Mass Effect" into the model. We will model two cell populations: the healthy host cells, and the cancer cells, and derive a mass balance equation for each constituent. These mass balance equations play the same role as our original model (Chapter 3), but will now include an advection term that is induced by the forces within the brain. The biggest challenge in modelling this effect is determining the appropriate velocity fields, which is done via the appropriate momentum equations.

## 6.1 Scientific Background

The mass effect as it applies to brain tumour modelling has been studied in some detail, with many different models being explored by various research groups. Each of these models is based on the mechanics of the tissues, incorporating the growing tumour mass as a stress or a pressure. Here we provide a brief summary of some of the more important modelling strategies that have been employed.

The first group's work that we discuss here will also form the basis for the mass effect model derived here. Preziosi and collaborators [76–81] have worked extensively on mechanical models for tumour growth. They have focussed primarily on multiphase models, which is what will be implemented in this thesis. Multiphase models treat a tissue as a mixture of multiple "constituents", including cancer cells, healthy cells, extracellular network, or extracellular fluid. A modeller can break the tissue into as many constituents as they wish, incorporating the individual characteristics of each. The general framework for deriving a multiphase model begins by deriving a mass balance equation for each constituent, followed by a corresponding momentum equation to close the system. This process will be explored in far more detail in the remainder of this chapter, or can be seen in an assortment of papers from Preziosi et al. including Byrne et al. 2002 [76], Ambrosi and Preziosi 2002 [77], Preziosi and Tosin 2008 [78], and Preziosi and Vitale 2010 [79].

The second group's whose work that we discuss here is that of Lowengrub and collaborators [82–84]. They have investigated detailed models for tumour growth that include aspects of the tumour microenvironment such as oxygen levels, nutrient levels and mechanical response of the tissue, as well as the effect of these quantities on the resulting tumour [82]. This is done through a

system of equations modelling the cancer cells themselves, as well as growth factors and nutrient distributions. The mechanical aspect was incorporated by modelling pressure directly and applying Darcy's law [82]. The results of such an investigation have implications for therapeutic interventions, such as interrupting the nutrient supply to a tumour. They went on to extend this modelling, incorporating cell-cell adhesion into the model in the form of a Helmholtz free energy term. They also generalized the Darcy's law framework for the cell velocities [83, 84].

Another group that has worked on mechanical aspects of tumour growth is Clatz et al. [8]. They used atlas data to set up a brain domain, incorporating diffusion tensors for the spread of the cancer cells. They modelled tumour growth as an exponential function, with growth ceasing when a density of 1 is reached. The mass effect was included via a classical constitutive equation framework, by deriving the strain and expressing the stress as a function of strain. Overall, this work served to incorporate growth, diffusion, and mechanical deformation into a tumour growth model, and serves as a good basis for future models that combine all of these components.

## 6.2 Introduction to Continuum Mechanics

Before deriving the system, we discuss some introductory ideas from continuum mechanics that are crucial for making sense of the system. In particular, we focus on how to think of matter as a continuum, as well as the idea of stress in three dimensions.

### 6.2.1 Matter as a Continuum

We have made reference to the fact that we will be using continuum mechanics to model the mass effect, however, matter is certainly not a continuum. At a small scale, it is made up of many individual molecules, and subsequently, atoms. At the appropriate scales however, it can be reasonably assumed that matter approximates a continuum. Consider, for example, water. If you were to look at water on a molecular level, you would see that it is made up of many individual particles. Most people however will never consider water on this scale, and instead we think of it on a much larger scale. At these larger scales, water behaves much like a continuum.

To make this more precise, consider an example from [80]. We will use this example to discuss more precisely how to define density as a continuum. Define $M_0$ to be the amount of mass contained in some volume $U_0$. Let the volume of $U_0$ be $V_0$, and let $P$ be some point contained within this volume. In order to define the density *at* the point $P$, let $\{U_0, U_1, U_2, \ldots, U_n, \ldots\}$ be a sequence of subvolumes converging on $P$ with

$$U_n \subset U_{n-1}, \quad P \in U_n, \quad (n = 0, 1, 2, \ldots).$$

Define the volume of $U_i$ to be $V_i$, and the amount of mass contained in $U_i$ to be $M_i$. Then if

$$\lim_{n\to\infty} \frac{M_n}{V_n}, \qquad \text{as } V_n \to 0,$$

exists, then we define the density of the mass distribution at this point $P$ to be this limiting value. See figure 6.1.

There is a slight problem with this definition, however. Because we are applying a mathematical concept to a real-world situation, there are certain

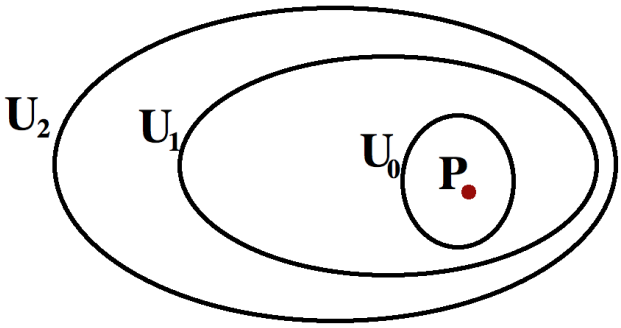


Figure 6.1: Subvolume Sequence. Figure showing the first few volumes in a sequence of subvolumes converging on a point $P$.

allowances that must be made. When taking $V_n \to 0$, eventually there will be a subvolume so small that it is actually contained within a molecule, or subsequently an atom. This will result in oscillations in the density value such that no limiting value can be said to exist in a mathematical sense. As such, the limit is taken with the following caveat, taken directly from [80]:
*"We consider the ratio $M_n/V_n$. Let $U_n$ become smaller and smaller but always remain so large that it contains a large number of particles in it."*

### Volume Ratio

In formulating the multiphase modelling system, we will be referring to volume ratios. These quantities describe the fraction of the volume that is taken up by a given constituent. In this thesis, we will be considering the following constituents:

- $\phi_h(\mathbf{x}, t)$ : volume ratio of the healthy host cells,
- $\phi_c(\mathbf{x}, t)$ : volume ratio of the cancer cells, and
- $\phi_m(\mathbf{x}, t)$ : volume ratio of the extra-cellular network (ECN) (i.e. extra-

cellular matrix (ECM) + blood vessels).

Note that extracellular liquid, $\phi_\ell(\mathbf{x}, t)$ is also present, however we do not explicitly model it. It is assumed that it is present though to facilitate cell growth. Then

$$\phi_h + \phi_c + \phi_m \leq 1.$$

Note that in determining the volume ratios, a similar limiting phenomenon occurs as in our density example. Preziosi and Vitale provide a nice graphical representation of this in [80] where it appears at Figure 1.1. We include it here as Figure 6.2. You can see in this figure the constant limiting value before the volume becomes too small, and the volume ratio oscillates.

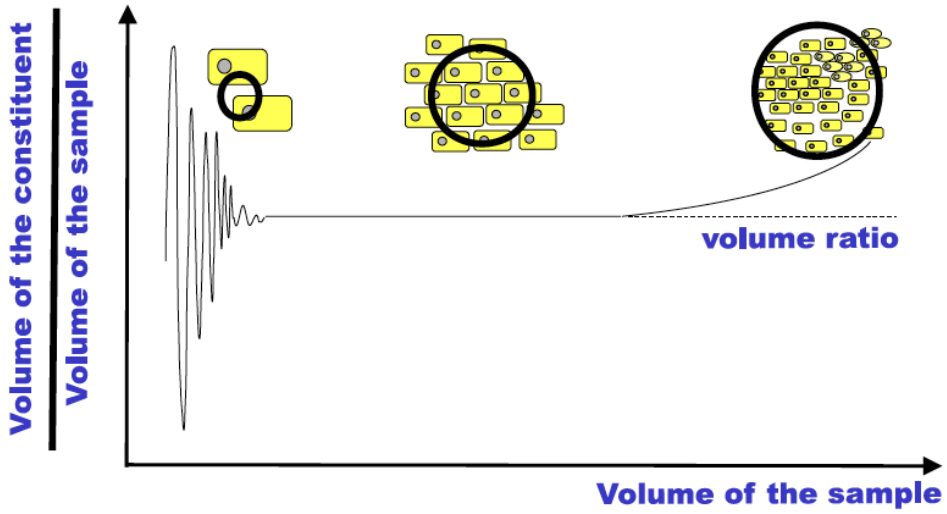


Figure 6.2: Constituent Density Limit. Plot of the volume ratio of the constituent as a function of sample volume size. There is a constant limiting value that occurs before the sample size becomes too small and no longer contains enough particles, and the ratio oscillates.

### 6.2.2 Stress Tensors

The momentum equations of the next section make use of *stress tensors*, an important concept in continuum mechanics that allow us to describe the stress experienced in three dimensions at a point within the brain. Before getting to the three-dimensional case, we consider examples in one and two dimensions, summarized from [85].

As a first example of stress within the body, consider a tendon. Tendons are made up of fibrous connective tissue, and serve to connect muscles to bone. These tendons are capable of withstanding *stress*, with larger tendons being able to withstand larger amounts of stress. We therefore define as a first example of stress

$$\sigma = F/A,$$

where $\sigma$ is defined to be the stress in the tendon, $F$ is the force, and $A$ is the cross-sectional area. In the simple case of a tendon experiencing a force in only one direction, a scalar quantity suffices to define stress. In the context of biomechanics, stress quantifies the interaction of tissue in one part of the body with tissue in another part of the body.

A next example to consider (also from [85]) involves the stress that acts on a surface. For this example, we look at a volume $S$ within a larger volume $B$. We consider an infinitesimal surface element $\Delta S$ on the surface of $S$, and express the force exerted on $\Delta S$ by the material in $B$ as $\Delta\vec{F}$. Note that this force is now a vector. We then define

$$\frac{d\vec{F}}{dS} = \lim_{\Delta S \to 0} \frac{\Delta\vec{F}}{\Delta S},$$

and

$$\vec{T} = \frac{d\vec{F}}{dS}$$

is the *stress vector*.

Generalizing the examples above, we extend our definition to include the stress acting in all directions at a particular location within the brain. To fully describe stress in three dimensions, it is necessary to use a rank-2 tensor. We define this tensor by considering a volume element in the form of a cube, analogous to the surface element in the previous example. We will assume the cube is aligned with the standard coordinate axes as in Figure 6.3, which is taken from [86]. We will then define $\Delta S_i$ to be the surface normal to the positive $x_i$ axis. Now, let the stress vector (as defined above) acting on $\Delta S_1$ be $T^1$. Resolving this vector into three components with respect to the standard basis, we can obtain $T^1 = (\sigma_{xx}, \tau_{xy}, \tau_{xz})$. The same can be done for $\Delta S_2$ and $\Delta S_3$, giving $T^2$ and $T^3$. Assembling these three stress vectors into a matrix gives the stress tensor for a given point:

$$T = \begin{pmatrix} \sigma_{xx} & \tau_{xy} & \tau_{xz} \\ \tau_{yx} & \sigma_{yy} & \tau_{yz} \\ \tau_{zx} & \tau_{zy} & \sigma_{zz} \end{pmatrix}.$$

A comment about notation: Components of the stresses that are normal to the surfaces $\Delta S_i$ are called *normal stresses* ($\sigma_{xx}$, $\sigma_{yy}$, $\sigma_{zz}$), while the other components ($\tau_{x_i x_j}$ with $i \neq j$) are called *shear stresses* [61].

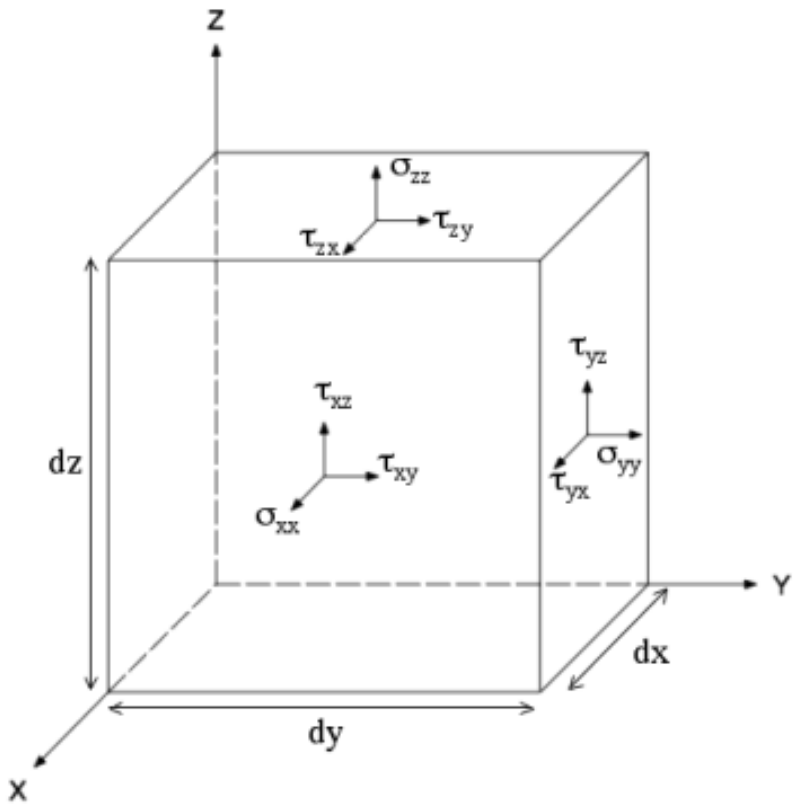


Figure 6.3: 3D Stress Tensor. Figure showing the volume element used to define the stress tensors, in alignment with the standard coordinate axes.

## 6.3 The Multiphase Framework

We introduced earlier that we will be modelling $\phi_h$, $\phi_c$, and $\phi_m$, or the healthy host cells, cancer cells and ECN, respectively. We will also consider the extracellular fluid as $\phi_\ell$, with

$$\phi_\ell = 1 - \phi_t - \phi_h - \phi_c.$$

We will however not explicitly model this quantity, but must assume that it is present to foster cell growth. To simplify notation, we will instead use $c = \phi_c$ to represent the cancer cell density, $h = \phi_h$ for the healthy cells, and $m = \phi_m$ for the ECN.

To describe the time evolution of these densities, we use a system involving a mass conservation equation and a momentum equation for each constituent. The mass conservation equations describe the evolution of the populations in time, while the momentum equations help to determine the advective velocites. We begin by deriving the system of equations. The ideas that are used here are primarily taken from Preziosi et al. [76–80].

### 6.3.1 Mass Conservation

To derive the mass balance equations, we consider a fixed volume $V$ with boundary $\partial V$, and let $\boldsymbol{n}$ be an external normal to the boundary. Consider first only cancer cells $c(\boldsymbol{x}, t)$, as the process is very similar for the other constituents. We begin by writing down an equation for total mass in the volume $V$. This is given by [80]

$$M = \int_V \rho c \, dV,$$

where $\rho$ is the density of the cancer cells. Now consider the possible manners in which the mass within this volume can change. There are only two ways in which this can happen: (i) flux through the boundary, or (ii) creation or deletion of cells (birth or death). In the form of an equation, this means [80]

$$\frac{dM}{dt} = \underbrace{-\int_{\partial V} \rho c \boldsymbol{v}_c \cdot \boldsymbol{n} d\Sigma}_{\text{Flux}} + \underbrace{\int_V \rho \Gamma_c dV}_{\text{Birth/Death}}, \tag{6.1}$$

where $\boldsymbol{v}_c$ gives the cell velocity, and $\Gamma_c$ gives the net growth rate of the cells. The first term on the right hand side of Equation (6.1) models the decrease in cell mass via flux over the boundary. The second term models the change in cell population via cell division and cell death. The first term lends itself very well to the divergence theorem, which upon application gives [80]

$$\int_V \left[ \frac{\partial}{\partial t}(\rho c) + \nabla \cdot (\rho c \boldsymbol{v}_c) - \rho \Gamma_c \right] dV = 0, \tag{6.2}$$

where we are now requiring $dM/dt = 0$ to ensure mass conservation. Because we have not specified the volume $V$, the relation in Equation (6.2) must hold for all arbitrary volumes $V$. This can only be true if the integrand itself is 0, hence we have [80]

$$\frac{\partial}{\partial t}(\rho c) + \nabla \cdot (\rho c \boldsymbol{v}_c) - \rho \Gamma_c = 0.$$

Under the assumption that $\rho$ is constant, and equal to the density of water, we arrive at the mass-balance equation for cancer cells: [80]

$$\frac{\partial c}{\partial t} + \nabla \cdot (c \boldsymbol{v}_c) = \Gamma_c. \tag{6.3}$$

We can then easily write down a mass balance for the healthy host cells, as

the derivation is exactly the same:

$$\frac{\partial h}{\partial t} + \nabla \cdot (h\boldsymbol{v}_h) = \Gamma_h. \tag{6.4}$$

For the ECN, the derivation is the same, except we assume that it is non-remodelling, i.e. that there is no net growth/death. This gives the following mass balance:

$$\frac{\partial m}{\partial t} + \nabla \cdot (m\boldsymbol{v}_m) = 0.$$

### 6.3.2 Momentum Conservation

While the mass balance equations tell us how to update the volume fractions in time, we still need to determine the velocity fields for each constituent. Determining these velocities is not trivial, and is the most crucial part of modelling the mass effect. The velocities are found by determining the appropriate momentum balance for each constituent, which is where the stress tensors, discussed previously, come into the model.

In order to determine the momentum balance equations, we will follow a similar process as for the mass conservation equations. We will once again consider only the cancer cells $c(\boldsymbol{x}, t)$ initially, then extend the results to the other two constituents. First, as per [80], we determine the expression for total momentum within an arbitrary test volume $V$:

$$\text{Total Momentum} = \int_V \rho c \boldsymbol{v}_c dV.$$

Now we consider how this momentum can change. Again, as per [80], this momentum can change in any of the following ways:

1. momentum flux of cells through the boundary,

2. contact forces with other cells through the boundary, n the direction of $\boldsymbol{n}$, the unit normal to the boundary

3. contact forces due to the interaction of cells with other constituents, i.e. friction,

4. momentum change due to mass exchange among constituents, and

5. body forces, i.e. gravity, chemotaxis.

We can then formulate momentum conservation as an integral equation as we did for the mass conservation case. The resulting equation is [80]

$$\frac{d}{dt}\int_V \rho c\boldsymbol{v}_c dV = -\underbrace{\int_{\partial V} \rho c\boldsymbol{v}_c(\boldsymbol{v}_c\cdot\boldsymbol{n})d\Sigma}_{1} + \underbrace{\int_{\partial V} cT_c^{\mathrm{T}}\boldsymbol{n}d\Sigma}_{2} + \underbrace{\int_V \boldsymbol{m}_c dV}_{3}$$

$$+\underbrace{\int_V \rho\Gamma_c\boldsymbol{v}_c dV}_{4} + \underbrace{\int_V \rho c\boldsymbol{b}_c dV}_{5},$$

where $T_c$ is the stress tensor for cancer cells, and $\boldsymbol{m}_c$ is the interaction force for cancer cells. The body force is given by $\boldsymbol{b}_c$. As before, we use the divergence theorem on terms 1 and 2 on the right hand side in order to write all of the integrals over $V$. We then combine all the terms into a single integral, where the time derivative becomes a partial derivative when it is brought inside the integral. This gives [80]

$$\int_V \left[\frac{\partial}{\partial t}(\rho c\boldsymbol{v}_c) + \nabla\cdot(\rho c\boldsymbol{v}_c\otimes\boldsymbol{v}_c - cT_c) - \rho c\boldsymbol{b}_c - \boldsymbol{m}_c - \rho\Gamma_c\boldsymbol{v}_c\right]dV = 0.$$

Because the volume of integration ($V$) is arbitrary, the integrand must

vanish, giving [80]

$$\frac{\partial}{\partial t}(\rho c \boldsymbol{v}_c) + \nabla \cdot (\rho c \boldsymbol{v}_c \otimes \boldsymbol{v}_c) = \nabla \cdot (cT_c) + \rho c \boldsymbol{b}_c + \boldsymbol{m}_c + \rho \Gamma_c \boldsymbol{v}_c.$$

Using Equation (6.3) to simplify, we obtain [80]

$$\rho c \left( \frac{\partial \boldsymbol{v}_c}{\partial t} + \boldsymbol{v}_c \cdot \nabla \boldsymbol{v}_c \right) = \nabla \cdot (cT_c) + \rho c \boldsymbol{b}_c + \boldsymbol{m}_c. \tag{6.5}$$

The term on the left hand side is referred to as the total time derivative, or inertial term. Because of the large discrepancy between the time scales of tumour growth vs. tissue deformation , this term can be neglected. The time scale of tumour growth is days or months, while the time scale of tissue deformation, or inertia, is only seconds. The tissue deformations can be assumed to be at quasi-steady state in terms of the time scale of tumour growth. As such, Equation (6.5) reduces to [80]

$$\nabla \cdot (cT_c) + \rho c \boldsymbol{b}_c + \boldsymbol{m}_c = 0.$$

Finally, we can neglect the body force term $\boldsymbol{b}_c$, as these forces do not play a large role in the tissue deformation. The final momentum equation for cancer cells is therefore [80]

$$\nabla \cdot (cT_c) + \boldsymbol{m}_c = 0. \tag{6.6}$$

Similarly, the derivation of the momentum equations for healthy host cells and for ECN would be the same, thus giving

$$\nabla \cdot (hT_h) + \boldsymbol{m}_h = 0, \tag{6.7}$$

and

$$\nabla \cdot (mT_m) + \boldsymbol{m}_m = 0,$$

respectively.

### 6.3.3 Closing the System

In order to fully define the momentum equations that we have just derived, we must specify both an interaction force ($\boldsymbol{m}_i$) and a stress tensor ($T_i$) for each constituent. Before doing this, we will make an assumption that will simplify the model.

**Assumption 1:** It is assumed that the ECN is rigid. Then

$$m(\boldsymbol{x}, t) = m(\boldsymbol{x}),$$

i.e. $\boldsymbol{v}_m = 0$ for all $\boldsymbol{x}$. We thus do not need to consider the momentum equation for $m$ as the velocity field is known. This is equivalent to treating the brain like a rigid porous medium [78]. It also means that we need not worry about the mass conservation equation, as we are assuming that the ECN does not change with time. We are thus now only considering the equations for the healthy host cells and for the cancer cells. It is still necessary to assume that the ECN is present, however, so that all of the interaction forces balance appropriately. We then proceed with the modelling by determining the interaction force and stress tensor for both the healthy cells and the cancer cells.

#### The Interaction Forces

In order to determine the interaction forces, we employ a classic assumption of multiphase flows [78, 81].

**Assumption 2:** Assume that the interaction force acting on the cells is taken to be proportional to their velocity:

$$\boldsymbol{m}_i = -K_i^{-1}\boldsymbol{v}_i,$$

where the $K_i$ are passive anisotropy tensors that translate a stress into a net displacement according to the tissue structure. The tensor $K_i$ is referred to as a motility tensor.

Employing Assumption 2 and substituting it back into the momentum Equations (6.6) and (6.7), we obtain [78]

$$\boldsymbol{v}_c = K_c \nabla \cdot (cT_c), \tag{6.8}$$

$$\boldsymbol{v}_h = K_h \nabla \cdot (hT_h). \tag{6.9}$$

Now we have a definition for the velocity fields in terms of two tensors: $K_i$ and $T_i$. There are a few ways to choose $K_i$. The simplest choice is to choose $K_i$ proportional the identity matrix. This causes the stress to be distributed isotropically, and translates a stress directly into a net displacement. Alternatively, we can incorporate the tissue architecture into the stress distribution. If we use tensors with the same eigenvectors as the DTI data, then this allows the forces to be distributed along the fibres, which is more realistic than the isotropic distribution. For simplicity, and for a first approximation, here we will use $K_i$ proportional to the identity. The constant of proportionality will be discussed in a later section.

### The Stress Tensors

Similarly, there are a number of ways to specify the stress tensors. We will use the technique of Preziosi et al. [77, 78], taking the stress to be a function $\Sigma$ of the cell densities:

$$T_c(\boldsymbol{x}, t) = -\Sigma_c(c + h)\mathbb{I}, \tag{6.10}$$

$$T_h(\boldsymbol{x}, t) = -\Sigma_h(c + h)\mathbb{I}, \tag{6.11}$$

where $\mathbb{I}$ is the identity tensor, so that the stress at a given location is dependent on the total cell density at that location. Of course, this raises the question of how to choose the functions $\Sigma_c$ and $\Sigma_h$. Choosing $\Sigma_c$ and $\Sigma_h$ will be addressed in the following section where the model is fully specified. We now combine Equations (6.3), (6.4), (6.8), (6.9), (6.10) and (6.11). Additionally, we specify the growth functions. Since $h(\boldsymbol{x}, t)$ represents the healthy cells, we expect that in general they would have no net growth, hence we set $\Gamma_h = 0$. For the cancer cells, we employ a logistic growth (in the entire cell population), as well as include the anisotropic diffusion term. The result is a system of coupled PDE's for the cancer cells $c(\boldsymbol{x}, t)$ and the healthy cells $h(\boldsymbol{x}, t)$:

$$\frac{\partial c}{\partial t} - \nabla \cdot (cK_c\nabla(c\Sigma_c(c + h))) = \nabla\nabla : (D_c c) + r_c c(1 - (c + h)), \tag{6.12}$$

$$\frac{\partial h}{\partial t} - \nabla \cdot (hK_h\nabla(h\Sigma_h(c + h))) = 0. \tag{6.13}$$

## 6.4 Numerical Methods

To get an idea of how the model evolves with time, it is useful to simulate it numerically in one dimension. We use a conservative flux discretization scheme, using operator splitting and employing one scheme for the advective

term, and another for the diffusive term. These schemes are as outlined in Hundsdorfer's lecture notes [87]. For an advection equation having the form

$$u_t + (a(x,t)u)_x = 0, \tag{6.14}$$

we can discretize in space via [87]

$$w_i'(t) = \frac{1}{h}\left(f_{i-\frac{1}{2}}(t, w(t)) - f_{i+\frac{1}{2}}(t, w(t))\right),$$

where $i = 1, \ldots, m$, and the fluxes $f_{i-\frac{1}{2}}$ and $f_{i+\frac{1}{2}}$ are defined by

$$f_{i-\frac{1}{2}}(t,w) = a^+(x_{i-\frac{1}{2}}, t)\left[w_{i-1} + \psi(\theta_{i-1})(w_i - w_{i-1})\right] + a^-(x_{i-\frac{1}{2}}, t)\left[w_i + \psi\left(\frac{1}{\theta_i}\right)(w_{i-1} - w_i)\right],$$

and

$$f_{i+\frac{1}{2}}(t,w) = a^+(x_{i+\frac{1}{2}}, t)\left[w_i + \psi(\theta_i)(w_{i+1} - w_i)\right] + a^-(x_{i+\frac{1}{2}}, t)\left[w_{i+1} + \psi\left(\frac{1}{\theta_{i+1}}\right)(w_i - w_{i+1})\right],$$

Notationally, Hunsdorfer [87] uses $w_i(t)$ to refer to the approximate value of $u(x,t)$ at $x_i$. The scheme can be adjusted and tuned via the flux limiter function $\psi(\theta)$, however we will take $\psi \equiv 0$ for simplicity, giving a first order upwind scheme [87]. An in depth discussion of various flux limiter functions and their respective merits can be found in [74]. For the diffusion equation, we consider then standard divergence form

$$u_t = (d(x,t)u_x)_x, \tag{6.15}$$

and employ the following discretization courtesy of Hundsdorfer [87]:

$$w_i'(t) = \frac{1}{h^2}(d(x_{i-\frac{1}{2}}, t)(w_{i-1}(t) - w_i(t)) - d(x_{i+\frac{1}{2}})(w_i(t) - w_{i+1}(t))).$$

Of particular importance is the fact that these schemes allow for both $a$ and $d$ to depend on both space and time, as is the case here. In order to simulate the models derived in this chapter then, we must derive the appropriate advective velocities and diffusion coefficients corresponding to the forms of Equations (6.15) and (6.14).

## 6.5 Specifying the Model

Now, we will consider two separate models based on how the stress-tensors, and subsequently the velocities are defined. The first model is a more classic choice, following the Preziosi derivations. We call this the **Non-Aggressive Model**, and it will be discussed in Section 6.5.1. Simulations of this model, however, did not behave as would be expected of a growing tumour system. This will be seen in Section 6.5.2. As such, in Section 6.5.3 we have derived an alternative model that better corresponds to the reality of a growing tumour, based on the derivative of the cancer cell density. As such, we call this the **Aggressive-Invasion Model**. In both cases, the resulting PDE's are similar in type to Burger's equation, hence we assume existence and uniqueness, however further analysis beyond the scope of this thesis would be required to verify this. Simulations of the aggressive-invasion model are shown in Section 6.5.4.

### 6.5.1 Non-Aggressive Model

To define the non-aggressive model, we specify the functions $\Sigma_c$ and $\Sigma_h$. These functions should describe how the cells respond to the growing mass. The non-aggressive model assumes that the two different cell types respond in the same way to the increasing pressure. Because it is assumed that the tissue has a "natural" state, under which the cells are relaxed, we define a threshold density $\phi_0$ representing the relaxed state. The stress then increases as the total cell density exceeds $\phi_0$. We therefore define

$$\Sigma_c(c+h) = \Sigma_h(c+h) = E(c+h-\phi_0),$$

where the factor $E$ is Young's modulus for the brain, which quantifies how the tissue responds to stress. The resulting model is then given by

$$\frac{\partial c}{\partial t} - KE\nabla \cdot (c\nabla(c(c+h-\phi_0))) = \nabla\nabla : (D_c c) + r_c c(1-(c+h)), \quad (6.16)$$

$$\frac{\partial h}{\partial t} - KE\nabla \cdot (h\nabla(h(c+h-\phi_0))) = 0. \quad (6.17)$$

Note that we are assuming $K_h = K_c = K$ to be constant in space, hence both $K$ and $E$ are brought outside of the derivative.

The numerical methods discussed above can be applied to simulate the non-aggressive model. Considering the model (6.16)-(6.17) in one dimension we get

$$\frac{\partial c}{\partial t} - KE\frac{\partial}{\partial x}\left(c\frac{\partial}{\partial x}(c^2+ch-c\phi_0)\right) = \frac{\partial^2}{\partial x^2}(d_c c) + r_c c(1-(c+h)), \quad (6.18)$$

$$\frac{\partial h}{\partial t} - KE\frac{\partial}{\partial x}\left(h\frac{\partial}{\partial x}(h^2+ch-h\phi_0)\right) = 0, \quad (6.19)$$

where $d_c$ is the diffusion coefficient. Expanding Equations (6.23) and (6.24) into divergence form gives

$$\frac{\partial c}{\partial t} - \frac{\partial}{\partial x}\left(\left(KEc\frac{\partial h}{\partial x} + \frac{\partial d_c}{\partial x}\right)c\right) = \frac{\partial}{\partial x}\left((d_c + KEc(2c + h - \phi_0))\frac{\partial c}{\partial x}\right) + r_c c(1 - (c + h)),$$

$$\frac{\partial h}{\partial t} - \frac{\partial}{\partial x}\left(\left(KEh\frac{\partial c}{\partial x}\right)h\right) = \frac{\partial}{\partial x}\left((KEh(c + 2h - \phi_0))\frac{\partial h}{\partial x}\right)$$

and so we have that

$$\begin{aligned} a_c &= -KEc\frac{\partial h}{\partial x} + \frac{\partial d_c}{\partial x}, \\ a_h &= -KEh\frac{\partial c}{\partial x}, \\ d_c &= d_c + KEc(2c + h - \phi_0), \\ d_h &= KEh(c + 2h - \phi_0). \end{aligned}$$

The coefficients $a_c$ and $a_h$ define the advective velocities for cancer cells and healthy cells, respectively, needed for the advective scheme discussed in Section 6.4, as per Equation (6.14). The diffusion coefficients $d_c$ and $d_h$ correspond to the diffusion of cancer cells and healthy cells, respectively, and are input into the numerical scheme as per Equation (6.15). The growth term is implemented in the same manner as for the Painter-Hillen model as in Equation (3.8), using a simple Euler scheme. No-flux boundary conditions are implemented

by setting

$$\begin{aligned} c(0) &= c(1), \\ c(m+1) &= c(m), \\ h(0) &= h(1), \\ h(m+1) &= h(m). \end{aligned}$$

Recall that both $c$ and $h$ are discretized in $x$ from $i = 1, \ldots, m$. The boundary points are thus given by $i = 0$ and $i = m + 1$.

### 6.5.2 Non-Aggressive Model Results

For the non-aggressive model given in Equations (6.16) and (6.17), we show results for $t = 0$, $t = 160$, $t = 320$, $t = 480$, $t = 640$ and $t = 800$. Parameter values were chosen as $r_c = 0.12$, $d_c = 0.0013$, $KE = 0.001$. These quantities roughly correspond to realistic values for the brain, however they would have to be more carefully tuned if applied to patient data. We chose $\phi_0 = 0.7$, meaning that any increase in density over this value creates a pressure driving the invasion. If the total density were to dip below this value, there would be a force in the opposite direction as the tissue would try to fill this region in. The results of these simulations are shown in Figure 6.4. The red line corresponds to the cancer cells, the blue line corresponds to the healthy cells, and the green line corresponds to the total $(c + h)$. The initial condition was chosen to represent a tumour sitting inside healthy tissue.

There are two immediate observations in these simulations. The first is the formation of the shocks at the invasion front. This occurs because the speed of

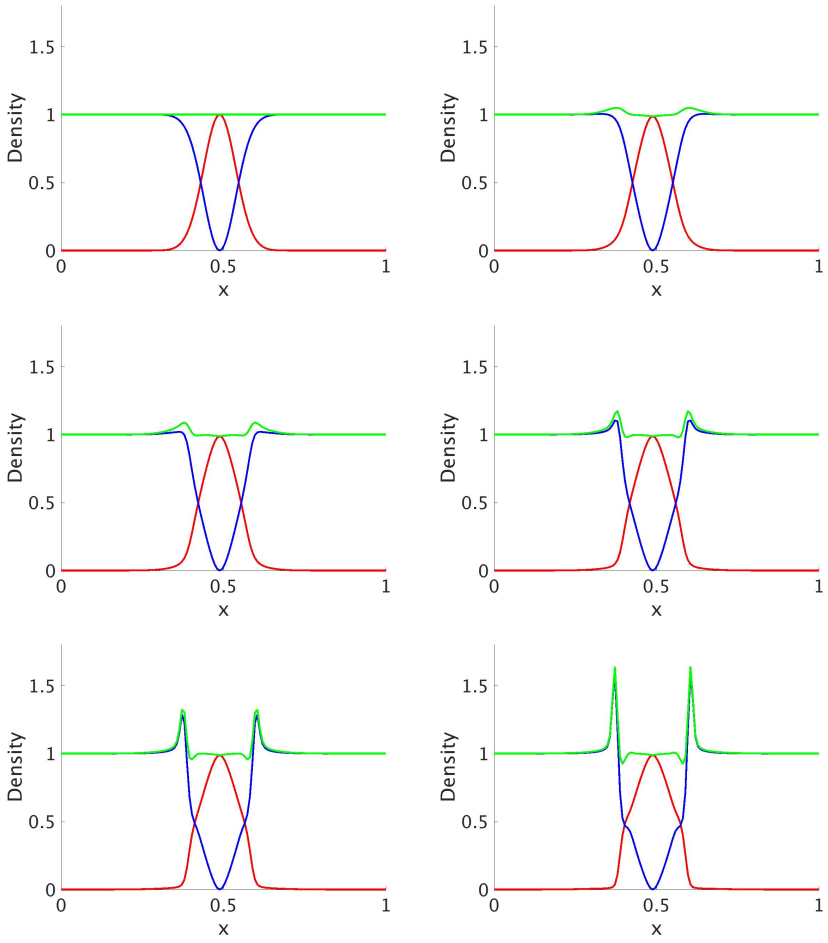


Figure 6.4: Non-Aggressive Model Results. Results of simulating the non-aggressive model in one dimension. Results are shown for $t = 0$, $t = 160$, $t = 320$, $t = 480$, $t = 640$ and $t = 800$. The red line corresponds to the cancer cells, the blue line corresponds to the healthy cells, and the green line corresponds to the total $(c + h)$. The initial condition was chosen to represent a tumour sitting inside healthy tissue.

the higher density tissue is higher than that of the lower density tissue, so the density builds up here, increasing more and more and eventually resulting in instability. This issue was remedied in the aggressive-invasion model through the use of a diffusion perturbation. Additionally, in the non-aggressive model, the cancer population seems unable to properly invade into the healthy tissue. This was also remedied in the aggressive-invasion model by increasing the aggressiveness of the cancer population.

### 6.5.3 Aggressive-Invasion Model

It turns out that simulations of the non-aggressive model don't exactly correspond to the reality of an invading tumour, as was outlined above. There was both the issue of shock-formation, and of the cancer population not being aggressive enough to invade the healthy tissue. Ideally, we would like to see the cancer cells invading and "pushing" the healthy tissue out of the way. In order to achieve this, we will generalize the function $\Sigma(c+h)$ to $\Sigma(c,h)$ so that the stress response can depend on the two populations independently. Since cancer is so much more aggressive than healthy tissue, using stress functions that depend on the populations independently gives more flexibility so that the increased aggression of the cancer cells can be included. Additionally, we will incorporate the effect when the total cell density exceeds $\phi_0$ through the constant of proportionality for $K$. As such, we define the tensors $K_c$ and $K_h$ from Equations (6.8) and (6.9) as

$$K_h = K_c = KE(c + h - \phi_0)\mathbb{I}, \tag{6.20}$$

where the scalar constant $E$ once again corresponds to Young's modulus for the brain, and $K$ remains as a constant. We now define the functions $\Sigma_c(c,h)$

and $\Sigma_h(c,h)$ of Equations (6.10) and (6.11), this time independently. The dominating pushing effect of a growing brain tumour is produced by the relative size of the tumour population. Hence for the stress magnitude $\Sigma_i$, we assume that it is proportional to the relative proportion of constituent $i$ with respect to constituent $c$, i.e.

$$\Sigma_c(c,h) = \frac{c}{c} = 1,$$

$$\Sigma_h(c,h) = \frac{h}{c},$$

so that they represent the relative size with respect to the cancer cells. Effectively, we have given the cancer cells a more aggressive nature. The resulting model (in one dimension) is given by

$$\frac{\partial c}{\partial t} - \frac{\partial}{\partial x}\left(cK_c\frac{\partial c}{\partial x}\right) = \frac{\partial^2}{\partial x^2}\left(d_c c\right) + r_c c(1-(c+h)), \tag{6.21}$$

$$\frac{\partial h}{\partial t} - \frac{\partial}{\partial x}\left(hK_h\frac{\partial c}{\partial x}\right) = 0, \tag{6.22}$$

where $K_c$ and $K_h$ are as given in Equation (6.20). Running simulations of this model, we observe the formation of shocks near the healthy/tumour transition region. This is related to the fact that the advection term in Equation (6.22) is a cross diffusion term. To remedy the occurrence of shocks, we introduce a small diffusion perturbation to the velocities in Equations (6.8) and (6.9) to diffuse the shocks. The final model then is given by

$$\frac{\partial c}{\partial t} - \frac{\partial}{\partial x}\left(c\left(K_c\frac{\partial c}{\partial x} + \epsilon\left(\frac{\partial c}{\partial x} + \frac{\partial h}{\partial x}\right)\right)\right) = \frac{\partial^2}{\partial x^2}\left(d_c c\right) + r_c c(1-(c+h)), \tag{6.23}$$

$$\frac{\partial h}{\partial t} - \frac{\partial}{\partial x}\left(h\left(K_h\frac{\partial c}{\partial x} + \epsilon\left(\frac{\partial c}{\partial x} + \frac{\partial h}{\partial x}\right)\right)\right) = 0, \tag{6.24}$$

where $\epsilon$ is a small parameter that can be used to tune the model. We can simulate the aggressive-invasion model using the numerics discussed above, by first rewriting Equations (6.21) and (6.22) in divergence form

$$\frac{\partial c}{\partial t} - \frac{\partial}{\partial x}\left(\left(KE(c+h-\phi_0)\frac{\partial c}{\partial x} + \frac{\partial d_c}{\partial x} + \epsilon\left(\frac{\partial c}{\partial x} + \frac{\partial h}{\partial x}\right)\right)c\right) = \frac{\partial}{\partial x}\left(d_c\frac{\partial c}{\partial x}\right) + r_c c(1-(c+h)),$$

$$\frac{\partial h}{\partial x} - \frac{\partial}{\partial x}\left(\left(KE(c+h-\phi_0)\frac{\partial c}{\partial x} + \epsilon\left(\frac{\partial c}{\partial x} + \frac{\partial h}{\partial x}\right)\right)h\right) = 0,$$

and so we have

$$\begin{aligned} a_c &= -KE(c+h-\phi_0)\frac{\partial c}{\partial x} - \frac{\partial d_c}{\partial x} - \epsilon\left(\frac{\partial c}{\partial x} + \frac{\partial h}{\partial x}\right) \\ a_h &= -KE(c+h-\phi_0)\frac{\partial c}{\partial x} - \epsilon\left(\frac{\partial c}{\partial x} + \frac{\partial h}{\partial x}\right) \\ d_c &= d_c, \\ d_h &= 0. \end{aligned}$$

The coefficients $a_c$ and $a_h$ define the advective velocities for cancer cells and healthy cells, respectively, needed for the advective scheme discussed in Section 6.4, as per Equation (6.14). The diffusion coefficients $d_c$ and $d_h$ correspond to the diffusion of cancer cells and healthy cells, respectively, and are input into the numerical scheme as per Equation (6.15). Once again, no-flux boundary

conditions are implemented via

$$\begin{aligned} c(0) &= c(1), \\ c(m+1) &= c(m), \\ h(0) &= h(1), \\ h(m+1) &= h(m). \end{aligned}$$

### 6.5.4 Aggressive-Invasion Model Results

Simulations for the aggressive-invasion model of Equations (6.21) and (6.22) are shown for time points $t = 0$, $t = 2400$, $t = 4800$, $t = 7200$, $t = 9600$ and $t = 12000$. The time scales for this model are longer since there is no shock formation and blow up. Parameter values were chosen as $r_c = 0.12$, $d_c = 0.0053$, $KE = 0.007$, $\phi_0 = 0.7$ and $\epsilon = 0.005$. The results of these simulations are shown in Figure 6.5. The red line corresponds to the cancer cells, the blue line corresponds to the healthy cells, and the green line corresponds to the total $(c + h)$. The initial condition was chosen to represent a tumour sitting inside healthy tissue.

It can be seen in these simulations that the cancer population is growing and filling the space in the centre. Additionally, it is invading to the left and right, and moving the healthy tissue out of the way. Applying this model in two dimensions then would allow for a build-up of tissue between a tumour mass and the boundary, inducing the pressure that is seen in the real patient segmentations. This model thus warrants further investigation in the modelling of gliomas.

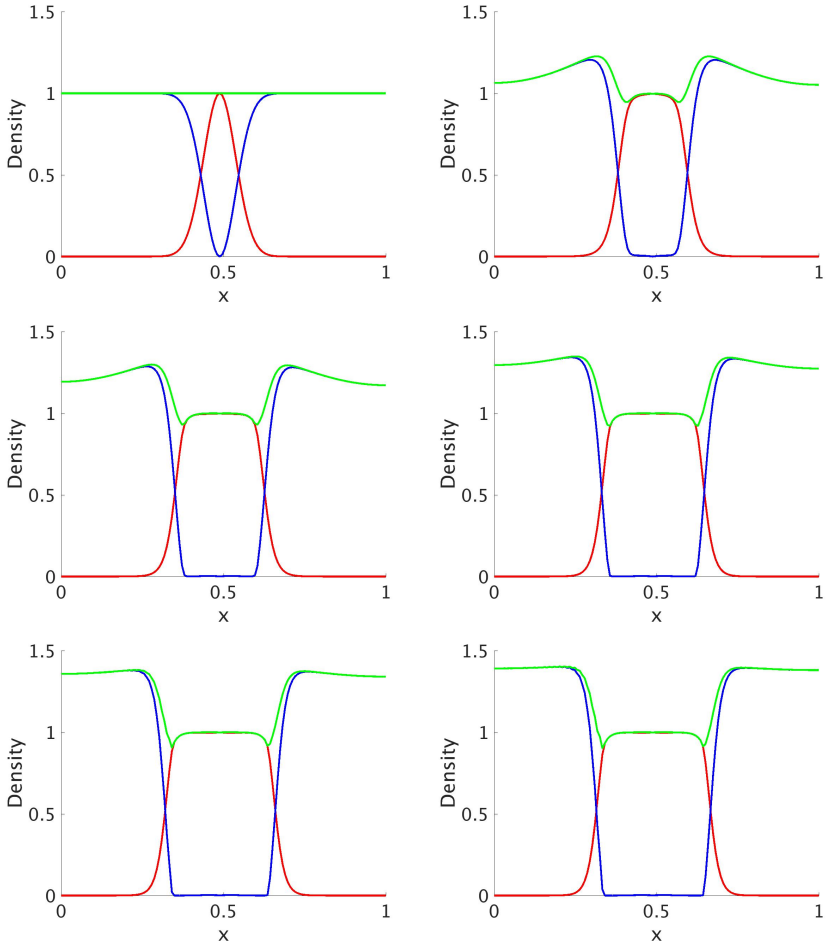


Figure 6.5: Aggressive-Invasion Results. Results of simulating the aggressive-invasion model in one dimension. Results are shown for $t = 0$, $t = 2400$, $t = 4800$, $t = 7200$, $t = 9600$ and $t = 12000$. The red line corresponds to the cancer cells, the blue line corresponds to the healthy cells, and the green line corresponds to the total $(c + h)$. The initial condition was chosen to represent a tumour sitting inside healthy tissue.

## 6.6 Chapter Summary

In this chapter, we began an investigation of the mass effect that is seen in tumour growth within the brain. Because the skull provides a fixed boundary, any increase in mass within the brain from a growing tumour causes an increase in pressure. This increase in pressure can then affect how the tumour proceeds to grow, in a feedback effect.

Before deriving a mechanical model for tumour growth, a basic understanding of continuum mechanics was necessary. This included an understanding of how to think of matter as a continuum, and how to think about the density "at a point". Stress was also an important concept to understand, and we introduced this through the use of a simple one-dimensional example before discussing three-dimensional stress tensors.

We derived a system of equations for both the cancer cells and the healthy cells through the use of a multiphase model, following the work of Preziosi et al. [80]. This began with a consideration of conservation of mass and momentum for the system, and the system was closed by deriving the corresponding constitutive equations. When the initial, more classically derived model did not display the behaviour we would expect, we derived a modified model based on the aggressiveness of the cancer population. The models differed in how the stress tensors, and subsequently the velocities were defined. For the non-aggressive model, the cancer and healthy cells were equally weighted with equal velocities. This model did not show the invasive behaviour characteristic of a growing tumour, hence we defined the aggressive-invasion model. In this model, the stress tensors were defined so that the cancer cells displayed a more aggressive tendency, and the velocities for the cancer cells and healthy cells differed.

Finally, we showed simulation results for both the non-aggressive model of Equations (6.23) and (6.24) and the modified aggressive-invasion model of Equations (6.21) and (6.22). While the non-aggressive model did not behave as expected, the aggressive-invasion model demonstrated the expected behaviour of a tumour invading the healthy tissue surrounding it. This model therefore offered the potential for application using patient data in higher dimensions, and could represent a further improvement to the existing Painter-Hillen model.

# Chapter 7

# Model with Direction-dependent Turning Rate

## 7.1 Transport Model Set-up

This section is an aside to the development of the Painter-Hillen model, and will not be used for simulations. However, it derives from an interesting fundamental idea, and has slightly different biological implications, thus we discuss its derivation with the intention of future development.

In the discussion of the mesoscopic model of Chapter 2, we assumed that the turning rate $\mu$ has a constant value. This is a reasonable assumption for our purposes, however it is interesting to consider the case where the rate $\mu$ depends on the direction that a cell is travelling. For example, it would seem reasonable that a cell that is travelling on a fibre is less likely to change its direction than a cell that is travelling perpendicular to a fibre. In this

Chapter then, we consider the case where $\mu$ depends on the cell orientation, i.e. $\mu = \mu(\boldsymbol{v})$.

To derive this model, we perform a similar derivation to what was done in Chapter 2, but now we allow $\mu$ to depend on velocity. We show that this derivation is consistent with the previous case, since allowing $\mu$ to be constant produces the same results as in Chapter 2.

Following the procedure described in Chapter 2 for the case of a constant turning rate, we begin with the same transport equation (Equation (2.1)):

$$p_t(t, \boldsymbol{x}, \boldsymbol{v}) + \boldsymbol{v} \cdot \nabla p(t, \boldsymbol{x}, \boldsymbol{v}) = \mathcal{L}p(t, \boldsymbol{x}, \boldsymbol{v}).$$

Recall that the terms on the left hand side describe simple transport of the cells with advective velocity $\boldsymbol{v}$, while the term on the right is the turning operator. We now define $\mathcal{L}$ in a slightly different manner than the definition in Equation (2.2). The turning operator is now given by

$$\mathcal{L}p(t, \boldsymbol{x}, \boldsymbol{v}) = -\mu(\boldsymbol{v})p(t, \boldsymbol{x}, \boldsymbol{v}) + \int_V \mu(\boldsymbol{v'})q(t, \boldsymbol{x}, \boldsymbol{v}, \boldsymbol{v'})p(t, \boldsymbol{x}, \boldsymbol{v'})d\boldsymbol{v'},$$

where the first term describes cells turning out of velocity $\boldsymbol{v}$ with turning rate $\mu(\boldsymbol{v})$, and the second term is a kernel term describing cells turning into velocity $\boldsymbol{v}$ from all other directions $\boldsymbol{v'}$. Since the turning rate depends on the direction that a particle is travelling, it appears inside the integral. The turning distribution, or turning kernel is given by $q(t, \boldsymbol{x}, \boldsymbol{v}, \boldsymbol{v'})$, which defines the probability that a cell at time $t$, spatial location $\boldsymbol{x}$ and travelling with velocity $\boldsymbol{v'}$ will turn into velocity $\boldsymbol{v}$. As was done in Chapter 2, we will make some assumptions on the turning kernel:

(A1) The turning distribution is fixed in time, and the probability of turning

into velocity $\boldsymbol{v}$ is independent of a cell's previous velocity, i.e., $q(t, \boldsymbol{x}, \boldsymbol{v}, \boldsymbol{v}') \approx q(\boldsymbol{x}, \boldsymbol{v})$.

(A2) $q$ is a probability density, so it integrates to 1: $\int_V q(\boldsymbol{x}, \boldsymbol{v}) d\boldsymbol{v} = 1$, and it is non-negative: $q(\boldsymbol{x}, \boldsymbol{v}) \geq 0$.

(A3) We do not distinguish between travelling "up" a fibre vs. "down" a fibre, hence $q$ is symmetric: $q(\boldsymbol{x}, \boldsymbol{v}) = q(\boldsymbol{x}, -\boldsymbol{v})$.

It turns out that it is not just the direction $\boldsymbol{v}$ the cell is moving in that is important, but also the relation of this direction to the underlying structure $q$. For example, if a cell is travelling in a direction that is very different from the fibre direction, it should have a higher turning rate, whereas if it is travelling in a direction that is aligned with the fibre, it should experience a lower turning rate. As such, the turning rate will depend on both $\boldsymbol{v}$ and $q$, i.e., $\mu = \mu(\boldsymbol{v}, q(\boldsymbol{x}, \boldsymbol{v}))$. We have now, however, added an implicit $\boldsymbol{x}$-dependence to the turning rate, and must be careful how this is handled in the analysis. Before doing the scaling, we will assume that changes in $q$ are small with respect to changes in $\boldsymbol{x}$, and consider the scaling on subdomains where the changes in $q$ are very small. We now define these assumptions more rigourously.

We will consider a neighbourhood $U(\boldsymbol{x})$, and look at a ball of radius $\delta$, $\mathbb{B}_\delta(\boldsymbol{x}) \subset U(\boldsymbol{x})$ such that whenever $\boldsymbol{y} \in \mathbb{B}_\delta(\boldsymbol{x})$, i.e., whenever $|\boldsymbol{x} - \boldsymbol{y}| < \delta$, then $|q(\boldsymbol{x}, \boldsymbol{v}) - q(\boldsymbol{y}, \boldsymbol{v})| < \tilde{\epsilon}$. The assumption then is that $\tilde{\epsilon} \ll \delta$, and consequently that $|Dq(\boldsymbol{y}, \boldsymbol{v})| \ll 1$ and $|Hq(\boldsymbol{y}, \boldsymbol{v}))| \ll 1$, where $Dq$ is a vector containing the partial derivatives (gradient) with respect to $\boldsymbol{x}$, and $Hq$ is the Hessian matrix of $q$ with respect to $\boldsymbol{x}$. Note that we are using $\tilde{\epsilon}$ to distinguish it from the $\epsilon$ that appeared in the parabolic scaling of Chapter 2, and that we will use later

in this Chapter. Now, substituting $\boldsymbol{y} = \boldsymbol{x} + \boldsymbol{h}$ with $|\boldsymbol{h}| < \delta$, we have

$$\mu(\boldsymbol{v}, q(\boldsymbol{x}, \boldsymbol{v})) = \mu(\boldsymbol{v}, q(\boldsymbol{y} - \boldsymbol{h}, \boldsymbol{v})),$$

and Taylor expanding $q$ gives

$$\mu(\boldsymbol{v}, q(\boldsymbol{y} - \boldsymbol{h}, \boldsymbol{v})) = \mu(v, q(\boldsymbol{y}, \boldsymbol{v}) - \boldsymbol{h}Dq(\boldsymbol{y}, \boldsymbol{v}) + \frac{1}{2}\boldsymbol{h}^T Hq(\boldsymbol{y}, \boldsymbol{v})\boldsymbol{h} + h.o.t.).$$

Now expanding $\mu$, we have

$$\mu(\boldsymbol{v}, q(\boldsymbol{y}-\boldsymbol{h}, \boldsymbol{v})) = \mu(\boldsymbol{v}, q(\boldsymbol{y}, \boldsymbol{v}))+\left(-\boldsymbol{h}Dq + \frac{1}{2}\boldsymbol{h}^T Hq\boldsymbol{h}\right)\frac{d\mu}{dq}(\boldsymbol{v}, q(\boldsymbol{y}, \boldsymbol{v}))+h.o.t.,$$

but we have already assumed that $|Dq(\boldsymbol{y})| \ll 1$ and $|Hq(\boldsymbol{y}))| \ll 1$, hence we obtain the approximation

$$\mu(\boldsymbol{v}, q(\boldsymbol{x}, \boldsymbol{v})) \approx \mu(\boldsymbol{v}, q(\boldsymbol{y}, \boldsymbol{v})) \qquad \forall \boldsymbol{y} \in \mathbb{B}_\delta(\boldsymbol{x}). \tag{7.1}$$

This means that when the stated assumptions are satisfied, $\mu$ is approximately constant in $\boldsymbol{x}$ on small subsets of the domain. Let $\boldsymbol{y}_i$ be a set of representative points in the domain $\Omega$, and $U(\boldsymbol{y}_i)$ be a collection of open, convex neighbourhoods such that $q(\boldsymbol{x}, \boldsymbol{v}) \approx q(\boldsymbol{y}_i, \boldsymbol{v})\ \forall \boldsymbol{x} \in U_i(\boldsymbol{y}_i)$ where $\bigcup_i U_i \supseteq \Omega$. We state this formally as another assumption:

(A4) Changes in $q$ are small in relation to changes in $\boldsymbol{x}$, so that $q$ may be assumed constant on the appropriate subdomains, i,e.

$$\mu(\boldsymbol{v}, q(\boldsymbol{x}, \boldsymbol{v})) \approx \mu(\boldsymbol{v}, q(\boldsymbol{y}_i, \boldsymbol{v})) \quad \forall \boldsymbol{x} \in U_i(\boldsymbol{y}_i), \text{ with } \Omega \subseteq \bigcup_i U_i.$$

## 7.2 Parabolic Scaling

Now that we have defined the subdomains over which we will perform the scaling, we will consider the transport equation

$$\begin{aligned} &p_t(t,\boldsymbol{x},\boldsymbol{v}) + \boldsymbol{v}\cdot\nabla p(t,\boldsymbol{x},\boldsymbol{v}) \\ &\qquad = -\mu(\boldsymbol{v},q)p(t,\boldsymbol{x},\boldsymbol{v}) + q(\boldsymbol{x},\boldsymbol{v})\int_V \mu(\boldsymbol{v}',q(\boldsymbol{x},\boldsymbol{v}'))p(t,\boldsymbol{x},\boldsymbol{v}')d\boldsymbol{v}', \quad (7.2) \end{aligned}$$

on a given $U_i$. Note that since $q(\boldsymbol{x},\boldsymbol{v})$ did not depend on $\boldsymbol{v}'$, we brought it out of the integral. Now we let $\tilde{\boldsymbol{x}}$ denote the vector distance from the point $\boldsymbol{y}_i$, i.e. $\tilde{\boldsymbol{x}} = \boldsymbol{x} - \boldsymbol{y}_i$, and scale space via

$$X = \epsilon\tilde{\boldsymbol{x}}.$$

Note that whenever $\boldsymbol{y}_i + X \in U_i(\boldsymbol{y}_i)$, then also $\boldsymbol{y}_i + \epsilon X \in U_i(\boldsymbol{y}_i)$ since the $U_i$ are convex. The scaling factor $\epsilon$ is as defined in Chapter 2, and used in the same manner as in Equation (2.3). It is not to be confused with $\tilde{\epsilon}$ mentioned earlier in this chapter. Then, since the biological scales are the same as in Chapter 2, we again perform a parabolic scaling and scale time by a factor of $\epsilon^2$, i.e.

$$\tau = \epsilon^2 t.$$

Applying these scalings to Equation (7.2), we obtain

$$\begin{aligned} &\epsilon^2 p_\tau(\tau,X,\boldsymbol{v}) + \epsilon\boldsymbol{v}\cdot\nabla p(\tau,X,\boldsymbol{v}) \\ &\qquad = -\mu(\boldsymbol{v},q)p(\tau,X,\boldsymbol{v}) + q(\boldsymbol{x},\boldsymbol{v})\int_V \mu(\boldsymbol{v}',q)p(\tau,X,\boldsymbol{v}')d\boldsymbol{v}', \quad (7.3) \end{aligned}$$

where the gradient is applied with respect to $X$. Now we take an asymptotic

expansion of $p(\tau, X, \boldsymbol{v})$:

$$p(\tau, X, \boldsymbol{v}) = p_0(\tau, X, \boldsymbol{v}) + \epsilon p_1(\tau, X, \boldsymbol{v}) + \epsilon^2 p_2(\tau, X, \boldsymbol{v}) + O(\epsilon^3). \tag{7.4}$$

We can derive a closed form expression for the leading-order term $p_0(\tau, X, \boldsymbol{v})$ for this expansion, summarized in the following theorem.

**Theorem 7.1.** *Let the assumptions (A1)-(A4) be satisfied. Given the transport equation of Equation (7.2) then the leading-order term $p_0(\tau, X, \boldsymbol{v})$ of Equation (7.4) satisfies*

$$p_0(\tau, X, \boldsymbol{v}) = \frac{q(X, \boldsymbol{v})}{\mu(\boldsymbol{v}, q)} \bar{p_0}_\mu(\tau, X),$$

*and $\bar{p_0}_\mu(\tau, X)$ satisfies the non-homogeneous and non-isotropic parabolic equation*

$$c(X)(\bar{p_0}_\mu)_\tau(\tau, X) = \nabla\nabla : (D(X)\bar{p_0}_\mu(\tau, X)),$$

*where $c(X)$ is the mean runtime along the fibres given by*

$$c(X) = \int_V \frac{q(X, \boldsymbol{v})}{\mu(\boldsymbol{v}, q)} d\boldsymbol{v},$$

*and $D(X)$ is the variance-covariance matrix of the mean distance travelled, given by*

$$D(X) = \int_V (\tau(X, \boldsymbol{v})\boldsymbol{v})(\tau(X, \boldsymbol{v})\boldsymbol{v})^T q(X, \boldsymbol{v}) d\boldsymbol{v},$$

*with $\tau(X, \boldsymbol{v}) = 1/(\mu(\boldsymbol{v}, q))$ the mean runtime in direction $\boldsymbol{v}$.*

*Proof.* Upon substituting the Hilbert expansion of Equation (7.4) into Equation (7.3), we match coefficients of orders of $\epsilon$, as was done in Chapter 2. Before this order matching, we establish some properties of the turning operator that will be necessary to solve the resulting equations. The first step

is to compute the kernel of $\mathcal{L}$ in order to determine the space on which the operator can be inverted. A function $\phi(\boldsymbol{v})$ is in $\ker \mathcal{L}$ if it satisfies

$$\begin{aligned} &\mathcal{L}\phi(\boldsymbol{v}) = 0 \\ \Leftrightarrow\ &-\mu(\boldsymbol{v},q)\phi(\boldsymbol{v}) + q(X,\boldsymbol{v}) \int_V \mu(\boldsymbol{v},q)\phi(\boldsymbol{v})d\boldsymbol{v} = 0 \\ \Leftrightarrow\ &\mu(\boldsymbol{v},q)\phi(\boldsymbol{v}) = q(X,\boldsymbol{v}) \int_V \mu(\boldsymbol{v},q)\phi(\boldsymbol{v})d\boldsymbol{v}. \end{aligned} \tag{7.5}$$

For convenience, we define

$$\bar{\phi}_\mu := \int_V \mu(\boldsymbol{v},q)\phi(\tau,X,\boldsymbol{v})d\boldsymbol{v}, \tag{7.6}$$

which has a useful biological interpretation. To see this, define $\bar{\mu}_\phi$ to be the mean turning rate over the entire population, i.e.

$$\bar{\mu}_\phi := \frac{\int_V \mu(\boldsymbol{v},q)\phi(\boldsymbol{v})d\boldsymbol{v}}{\bar{\phi}} = \frac{\bar{\phi}_\mu}{\bar{\phi}},$$

where $\bar{\phi}$ is the total mass of $\phi$ as was defined in Equation (2.6). Then

$$\bar{\phi}_\mu = \underbrace{\bar{\mu}_\phi}_{\substack{\text{mean turning} \\ \text{rate}}} \cdot \underbrace{\bar{\phi}}_{\substack{\text{total} \\ \text{mass}}},$$

and thus $\bar{\phi}_\mu$ represents the mean number of cells turning per unit of time. Using this definition, we rewrite Equation (7.5) as

$$\mu(\boldsymbol{v},q)\phi(\boldsymbol{v}) = q(X,\boldsymbol{v})\bar{\phi}_\mu,$$

and finally

$$\phi(\boldsymbol{v}) = \bar{\phi}_\mu \frac{q(X,\boldsymbol{v})}{\mu(\boldsymbol{v},q(X,\boldsymbol{v}))}.$$

Because $\bar{\phi}_\mu$ is independent of $\boldsymbol{v}$, the kernel of $\mathcal{L}$ is given as the span of $q(X,\boldsymbol{v})/\mu(\boldsymbol{v},q(X,\boldsymbol{v}))$:

$$\ker \mathcal{L} = \left\langle \frac{q(X,\cdot)}{\mu(\cdot,q(X,\cdot))} \right\rangle.$$

Notice that the spatial coordinate $X$ appears as a parameter in the kernel of $\mathcal{L}$. i.e., the kernel might change from point to point, however we use assumption (A4) such that $\ker \mathcal{L}$ is approximately constant on each subdomain $U_i(\boldsymbol{y}_i)$. We define a weighted $L^2$ space, denoted $L^2_{\frac{\mu}{q^2}}(V)$, upon which we define a norm:

$$||\phi(\boldsymbol{v})||_{L^2_{\frac{\mu}{q^2}}} = \int_V |\phi(\boldsymbol{v})|^2 \frac{\mu^2(\boldsymbol{v},q)}{q(X,\boldsymbol{v})} d\boldsymbol{v}.$$

Finally, we define the pseudo inverse on the complement of the kernel. We can therefor invert $\mathcal{L}$ on $\left\langle \frac{q(X,\cdot)}{\mu(\cdot,q(X,\cdot))} \right\rangle^\perp$. To derive the inverse, let $\phi \in \left\langle \frac{q}{\mu} \right\rangle^\perp$, $\psi \in \left\langle \frac{q}{\mu} \right\rangle^\perp$ be such that

$$\begin{aligned} &\mathcal{L}\phi = \psi \\ \Leftrightarrow\ &-\mu(\boldsymbol{v},q)\phi(\boldsymbol{v}) + q(X,\boldsymbol{v})\bar{\phi}_\mu = \psi. \end{aligned} \tag{7.7}$$

Computing $\bar{\phi}_\mu$:

$$\begin{aligned} \bar{\phi}_\mu &= \int_V \mu(\boldsymbol{v},q)\phi(\boldsymbol{v}) d\boldsymbol{v} \\ &= \int_V \phi(\boldsymbol{v}) \frac{q(X,\boldsymbol{v})}{\mu(\boldsymbol{v},q)} \frac{\mu^2(\boldsymbol{v},q)}{q(X,\boldsymbol{v})} d\boldsymbol{v} \\ &= \left\langle \phi(\boldsymbol{v}), \frac{q(X,\boldsymbol{v})}{\mu(\boldsymbol{v},q)} \right\rangle_{L^2_{\frac{\mu^2}{q}}}, \end{aligned}$$

but since $\phi \in \left\langle \frac{q}{\mu} \right\rangle^{\perp}$, this inner product is 0 by orthogonality. Thus $\bar{\phi}_\mu = 0$. Substituting this back into Equation (7.7), we obtain

$$\begin{aligned} -\mu(\boldsymbol{v}, q)\phi(\boldsymbol{v}) &= \psi \\ \Leftrightarrow \phi(\boldsymbol{v}) &= -\frac{1}{\mu(\boldsymbol{v}, q)}\psi, \end{aligned}$$

and so

$$\left(\mathcal{L}|_{\frac{q}{\mu^2}^{\perp}}\right)^{-1} = -\frac{1}{\mu(\boldsymbol{v}, q)}. \tag{7.8}$$

Substituting the Hilbert expansion in Equation (7.4) into the scaled transport equation in Equation (7.3), we proceed with matching orders of $\epsilon$, as was done in Chapter 2:

$\epsilon^0$ :

$$\begin{aligned} 0 &= \mathcal{L}p_0 \\ \Leftrightarrow -\mu(\boldsymbol{v}, q)p_0(\tau, X, \boldsymbol{v}) + q(X, \boldsymbol{v})\bar{p_0}_\mu(\tau, X) \\ \Leftrightarrow p_0(\tau, X, \boldsymbol{v}) &= \frac{q(X, \boldsymbol{v})}{\mu(\boldsymbol{v}, q)}\bar{p_0}_\mu(\tau, X), \end{aligned} \tag{7.9}$$

where $\bar{p_0}_\mu$ is defined as in Equation (7.6). Proceeding with $\epsilon^1$:

$$\epsilon^1 : \qquad \boldsymbol{v} \cdot \nabla p_0(\tau, X, \boldsymbol{v}) = \mathcal{L}p_1(\tau, X, \boldsymbol{v}). \tag{7.10}$$

In order to isolate and solve for $p_1$, we must invert the turning operator $\mathcal{L}$. We established above that this can only be done on $\left\langle \frac{q}{\mu} \right\rangle^{\perp}$, hence we first must verify that the left hand side of Equation (7.13) is in the correct space.

To do so, we compute the inner product

$$\begin{aligned}\left\langle \boldsymbol{v}\cdot\nabla p_0(\tau,X,\boldsymbol{v}),\frac{q}{\mu}\right\rangle &= \int_V \boldsymbol{v}\cdot p_0(\tau,X,\boldsymbol{v})\frac{\cancel{q(X,\boldsymbol{v})}}{\cancel{\mu(\boldsymbol{v},q)}}\frac{\mu(\boldsymbol{v},q)\cancel{^2}}{\cancel{q(X,\boldsymbol{v})}}d\boldsymbol{v}\\ &= \int_V \boldsymbol{v}\cdot\nabla p_0(\tau,X,\boldsymbol{v})\mu(\boldsymbol{v},q)d\boldsymbol{v}.\end{aligned}$$

Substituting in the formula for $p_0$ given in Equation (7.9), we have

$$\left\langle \boldsymbol{v}\cdot\nabla p_0(\tau,X,\boldsymbol{v}),\frac{q}{\mu}\right\rangle = \int_V \boldsymbol{v}\cdot\nabla\left(\bar{p_0}_\mu(\tau,X)\frac{q(X,\boldsymbol{v})}{\mu(\boldsymbol{v},q)}\right)\mu(\boldsymbol{v},q)d\boldsymbol{v}. \tag{7.11}$$

Now we apply the assumption that was made on $q$ as per Equation (7.1). We first apply a product rule to the gradient operator:

$$\begin{aligned}&\nabla\left(\bar{p_0}_\mu(\tau,X)\frac{q(X,\boldsymbol{v})}{\mu(\boldsymbol{v},q)}\right)\\ &\qquad= \nabla\left(\bar{p_0}_\mu(\tau,X)q(X,\boldsymbol{v})\right)\frac{1}{\mu(\boldsymbol{v},q)} + \bar{p_0}_\mu(\tau,X)q(X,\boldsymbol{v})\nabla\left(\frac{1}{\mu(\boldsymbol{v},q)}\right),\end{aligned}$$

but

$$\begin{aligned}\nabla\left(\frac{1}{\mu(\boldsymbol{v},q)}\right) &= -\frac{1}{\mu(\boldsymbol{v},q)^2}\nabla\mu(\boldsymbol{v},q)\\ &= -\frac{1}{\mu(\boldsymbol{v},q)^2}\frac{\partial\mu}{\partial q}\nabla q.\end{aligned} \tag{7.12}$$

Since we assumed in (A4) that on each subdomain upon which we are applying the scaling, $|Dq| \ll 1$, the quantity on the right hand side of Equation (7.12) will be approximately 0. Hence

$$\nabla\left(\bar{p_0}_\mu(\tau,X)\frac{q(X,\boldsymbol{v})}{\mu(\boldsymbol{v},q)}\right) \approx \nabla\left(\bar{p_0}_\mu(\tau,X)q(X,\boldsymbol{v})\right)\frac{1}{\mu(\boldsymbol{v},q)},$$

and Equation (7.11) simplifies to

$$\left\langle \boldsymbol{v} \cdot \nabla p_0, \frac{q}{\mu} \right\rangle \approx \int_V \boldsymbol{v} \cdot \nabla \left( \bar{p_0}_\mu(\tau, X) q(X, \boldsymbol{v}) \right) d\boldsymbol{v}.$$

Since $\bar{p_0}_\mu$ is independent of $\boldsymbol{v}$, it can be brought outside the integral, and since $\boldsymbol{v}$ doesn't depend on $X$, we can rewrite the gradient as a divergence:

$$\left\langle \boldsymbol{v} \cdot \nabla p_0, \frac{q}{\mu} \right\rangle = \nabla \cdot \int_V \boldsymbol{v} q(X, \boldsymbol{v}) d\boldsymbol{v} \bar{p_0}_\mu(\tau, X).$$

We assumed in (A3) that $q$ is symmetric, hence

$$\mathbf{E}_q = \int_V \boldsymbol{v} q(X, \boldsymbol{v}) d\boldsymbol{v} = 0$$

$$\Rightarrow \left\langle \boldsymbol{v} \cdot \nabla p_0, \frac{q}{\mu} \right\rangle = 0,$$

and $\boldsymbol{v} \cdot \nabla p_0$ is in the appropriate space, $\left\langle \frac{q}{\mu} \right\rangle^\perp$, to invert the turning operator. Therefore

$$p_1(\tau, X) = -\frac{1}{\mu(\boldsymbol{v}, q)} (\boldsymbol{v} \cdot \nabla p_0(\tau, X)), \tag{7.13}$$

where we have applied the inverse operator of Equation (7.8). Now for $\epsilon^2$:

$\epsilon^2$ :

$$(p_0)_\tau(\tau, X, \boldsymbol{v}) + \boldsymbol{v} \cdot p_1(\tau, X, \boldsymbol{v}) = \mathcal{L} p_2(\tau, X, \boldsymbol{v}).$$

We integrate the whole equation over $V$:

$$\int_V (p_0)_\tau(\tau, X, \boldsymbol{v}) d\boldsymbol{v} + \int_V \boldsymbol{v} \cdot p_1(\tau, X, \boldsymbol{v}) d\boldsymbol{v} = \int_V \mathcal{L} p_2(\tau, X, \boldsymbol{v}) d\boldsymbol{v}, \tag{7.14}$$

and consider each integral individually. Beginning with the term on the right

hand side:

$$\begin{aligned}\mathcal{L}p_2(\tau, X, \boldsymbol{v}) &= -\int_V \mu(\boldsymbol{v}, q)p_2(\tau, X, \boldsymbol{v})d\boldsymbol{v} + \int_V q(X, \boldsymbol{v})\bar{p_2}_\mu(\tau, X)d\boldsymbol{v} \\ &= -\bar{p_2}_\mu + \bar{p_2}_\mu \underbrace{\int_V q(X, \boldsymbol{v})d\boldsymbol{v}}_{=1} \\ &= 0, \end{aligned} \tag{7.15}$$

where we have used Assumption (A3). Now we turn our attention to the first integral on the left hand side of Equation (7.14). Substituting in Equation (7.9) for $p_0$, we have

$$\begin{aligned}\int_V (p_0)_\tau(\tau, X, \boldsymbol{v})d\boldsymbol{v} &= \int_V \frac{q(X, \boldsymbol{v})}{\mu(\boldsymbol{v}, q)}(\bar{p_0}_\mu)_\tau(\tau, X)d\boldsymbol{v} \\ &= (\bar{p_0}_\mu)_\tau(\tau, X)\int_V \frac{q(X, \boldsymbol{v})}{\mu(\boldsymbol{v}, q)}d\boldsymbol{v} \\ &= c(X)(\bar{p_0}_\mu)_\tau(\tau, X), \end{aligned} \tag{7.16}$$

where

$$c(X) := \int_V \frac{q(X, \boldsymbol{v})}{\mu(\boldsymbol{v}, q)}d\boldsymbol{v}.$$

Just as $\bar{p_0}_\mu$ had a biological interpretation as the mean number of cells turning per unit time, $c(X)$ has a meaning in a biological context too. If we define

$$\tau(X, \boldsymbol{v}) := \frac{1}{\mu(\boldsymbol{v}, q(X, \boldsymbol{v}))}, \tag{7.17}$$

to be the mean runtime in direction $\boldsymbol{v}$, then

$$c(X) = \int_V \tau(X, \boldsymbol{v})q(X, \boldsymbol{v})d\boldsymbol{v},$$

is the mean runtime along the fibres. Finally, we compute the second integral from the left hand side of Equation (7.14). Applying the definitions for $p_0$ and $p_1$ from Equations (7.9) and (7.13), we have

$$\begin{aligned}
\int_V \boldsymbol{v}\cdot\nabla p_1 d\boldsymbol{v} &= \int_V \boldsymbol{v}\cdot\nabla\left(-\frac{1}{\mu(\boldsymbol{v},q)}(\nabla\cdot\boldsymbol{v})p_0(\tau,X,\boldsymbol{v})\right)d\boldsymbol{v}\\
&= \nabla\cdot\int_V \boldsymbol{v}\left(-\frac{1}{\mu(\boldsymbol{v},q)}\boldsymbol{v}\cdot\nabla\left(\bar{p_0}_\mu(\tau,X)\frac{q(X,\boldsymbol{v})}{\mu(\boldsymbol{v},q)}\right)\right)d\boldsymbol{v}\\
&= \nabla\nabla:\int_V \boldsymbol{v}\boldsymbol{v}^T\left(-\frac{q(X,\boldsymbol{v})}{\mu^2(\boldsymbol{v},q)}\right)d\boldsymbol{v}\bar{p_0}_\mu\\
&= -\nabla\nabla:\left(D(X)\bar{p_0}_\mu\right), \qquad (7.18)
\end{aligned}$$

where

$$\begin{aligned}
D(X) &= \int_V \boldsymbol{v}\boldsymbol{v}^T\left(\frac{q(X,\boldsymbol{v})}{\mu^2(\boldsymbol{v},q)}\right)d\boldsymbol{v}\\
&= \int_V \boldsymbol{v}\boldsymbol{v}^T\tau^2(X,\boldsymbol{v})q(X,\boldsymbol{v})d\boldsymbol{v}\\
&= \int_V (\tau(X,\boldsymbol{v})\boldsymbol{v})(\tau(X,\boldsymbol{v})\boldsymbol{v})^T q(X,\boldsymbol{v})d\boldsymbol{v}.
\end{aligned}$$

Recall that $\tau$ is as defined in Equation (7.17), and since $\tau(X,\boldsymbol{v})$ is the mean runtime in direction $\boldsymbol{v}$, $\tau(X,\boldsymbol{v})\boldsymbol{v}$ is the mean distance travelled in direction $\boldsymbol{v}$. Defining then a new quantity

$$\chi(X,\boldsymbol{v}) := \tau(X,\boldsymbol{v})\boldsymbol{v},$$

we can rewrite the tensor $D(X)$:

$$D(X) = \int_V \chi(X,\boldsymbol{v})\chi(X,\boldsymbol{v})^T q(X,\boldsymbol{v})d\boldsymbol{v},$$

and we can see that the tensor $D(X)$ is the variance-covariance matrix of the

mean distance travelled. Now combining Equations (7.14), (7.15), (7.16) and (7.18), we obtain a closed form PDE for $\bar{p_{0}}_{\mu}$

$$\underbrace{c(X)}_{\substack{\text{mean}\\ \text{runtime}\\ \text{along}\\ \text{fibres}}} (\bar{p_{0}}_{\mu})_{\tau}(\tau, X) = \nabla\nabla : ( \underbrace{D(X)}_{\substack{\text{variance in}\\ \text{distance}\\ \text{travelled}}} \cdot \underbrace{\bar{p_{0}}_{\mu}(\tau, X)}_{\substack{\text{mean number}\\ \text{of cells}\\ \text{turning per}\\ \text{unit time}\\ \text{at } X}} ).$$

□

Simplifying notation, we will again use $t$ and $\boldsymbol{x}$, recalling that these are now the macroscopic time and spatial variables, respectively. Also, recalling that $p_0$ is the first approximation to the mesoscopic density $p(\tau, X, \boldsymbol{v})$ in the Hilbert expansion of Equation (7.4), we will simplify notation and let $p_{\mu}(t, x) = \bar{p_{0}}_{\mu}(\tau, X)$ be the number of cells turning per unit time at time $t$ and spatial location $\boldsymbol{x}$. The resulting PDE then is

$$c(\boldsymbol{x})(p_{\mu})_{t}(t, \boldsymbol{x}) = \nabla\nabla : (D(\boldsymbol{x})p_{\mu}(t, \boldsymbol{x}))\,. \tag{7.19}$$

### 7.2.1 Limiting Case: Constant Turning Rate

Since this model should be considered a generalization of the Painter-Hillen model derived in Chapter 2, we expect that if we set $\mu$ to be constant everywhere, we will recover the model in Equation (2.14). Here we verify that this is the case.

First, let $\mu(\boldsymbol{v}, q) = \mu$ constant. Then

$$\begin{aligned} p_\mu &= \mu\bar{p}, \\ c(\boldsymbol{x}) &= \frac{1}{\mu}\int_V q(\boldsymbol{x}, \boldsymbol{v})d\boldsymbol{v} = \frac{1}{\mu}, \\ \tau &= \frac{1}{\mu} \Rightarrow \chi = \frac{\boldsymbol{v}}{\mu}, \\ D(\boldsymbol{x}) &= \frac{1}{\mu^2}\int_V \boldsymbol{v}\boldsymbol{v}^T q(\boldsymbol{x}, \boldsymbol{v})d\boldsymbol{v}. \end{aligned}$$

Then the left hand side of Equation (7.19) reduces to

$$c(\boldsymbol{x})(p_\mu)_t = \frac{1}{\mu}\mu\bar{p}_t = \bar{p}_t,$$

and the right hand side of Equation (7.19) reduces to

$$\begin{aligned} \nabla\nabla : (D(\boldsymbol{x})p_\mu(t, \boldsymbol{x})) &= \frac{1}{\mu^2}\,\mu\,\nabla\nabla : \left(\int_V \boldsymbol{v}\boldsymbol{v}^T q(\boldsymbol{x}, \boldsymbol{v})\bar{p}\right) \\ &= \nabla\nabla : (D_c(\boldsymbol{x})\bar{p}), \end{aligned}$$

where $D_c(\boldsymbol{x})$ is the tensor defined in Equation (2.13). Thus we see that for the case where the turning rate is constant, we recover the results of Chapter 2.

## 7.3 Chapter Summary

While this chapter should be seen as a tangential exploration to the main narrative of this thesis, the derivation of this model offers the potential for further development. The motivation for this model stemmed from the fact that within a population of cells, the turning rate may not be constant. If a cell is travelling along a fibre, it is likely to change its direction far less frequently

than a cell that is travelling through isotropic brain material. As such, we postulated that the turning rate should depend both on a cell's velocity $\boldsymbol{v}$, and the underlying brain structure at its current location $q(\boldsymbol{x}, \boldsymbol{v})$.

In order to perform the appropriate scaling calculation, it was necessary to make an assumption on the turning distribution $q(\boldsymbol{x}, \boldsymbol{v})$. Namely, we assumed that changes in $q$ were small relative to changes in $\boldsymbol{x}$. To achieve this, we split the domain into many small subdomains upon which we could assume that $q$ was approximately constant in $\boldsymbol{x}$. Upon this division of the domain, a parabolic scaling could be applied on each subdomain.

We began by formulating a new transport equation that incorporated a generalization of the constant turning rate. This was given by

$$p_t(t, \boldsymbol{x}, \boldsymbol{v}) + \boldsymbol{v} \cdot \nabla p(t, \boldsymbol{x}, \boldsymbol{v}) = \mathcal{L}p(t, \boldsymbol{x}, \boldsymbol{v}),$$

with turning operator

$$\mathcal{L}p(t, \boldsymbol{x}, \boldsymbol{v}) = -\mu(\boldsymbol{v}, q)p(t, \boldsymbol{x}, \boldsymbol{v}) + \int_V \mu(\boldsymbol{v}', q(\boldsymbol{x}, \boldsymbol{v}'))q(t, \boldsymbol{x}, \boldsymbol{v}, \boldsymbol{v}')p(t, \boldsymbol{x}, \boldsymbol{v}')d\boldsymbol{v}'.$$

After applying a parabolic scaling to this transport equation (i.e. $X = \epsilon\boldsymbol{x}$, $\tau = \epsilon^2 t$), we arrived at a new PDE model for macroscopic behaviour:

$$c(\boldsymbol{x})(p_\mu)_t(t, \boldsymbol{x}) = \nabla\nabla : (D(\boldsymbol{x})p_\mu(t, \boldsymbol{x}))\,,$$

where $p_\mu$ represents the mean number of cells turning at time $t$ and location $\boldsymbol{x}$, $c(\boldsymbol{x})$ gives the mean runtime along fibres, and $D(\boldsymbol{x})$ is the variance-covariance matrix in distance travelled with respect to the turning distribution $q$.

At this point, we made note that when $\mu$ is constant, this PDE reduced to the Painter-Hillen anisotropic diffusion model of Equation (2.14), as expected.

# Chapter 8

# Conclusions

## 8.1 Discussion

Developing novel cancer therapies is at the forefront of medical science, inspiring scientists across many disciplines, from molecular biology to mathematics. Innovations can come from unexpected places, with mathematical models offering the potential to help clinicians in designing treatment plans on an individualized basis. Swanson et al. [6, 44–46, 49, 51–54] has had a good deal of success by implementing mathematical models for glioma spread clinically, however the potential for improvement always exists. In this thesis, we review the derivation of the Painter-Hillen [5] model of Equation (1.12), describing all of the underlying fundamentals, with the goal of demonstrating its utility. Perhaps the most important component of the derivation of the Painter-Hillen model is the choice for the turning distribution. We make use of a von Mises distribution (two dimensions) and a Fisher distribution (three dimensions) to include the tissue architecture into the diffusion model. The use of this distribution introduces a patient-specific parameter, the anisotropy parameter $\kappa$,

that allows the Painter-Hillen model to be specifically tuned to each patient.

To demonstrate the applicability of the Painter-Hillen model, we compare it directly to the Swanson P.I. model [6] by applying both models to real patient data from the Cross Cancer Institute, provided by Dr. Albert Murtha. The purpose of this comparison is to demonstrate that the inclusion of a fully anisotropic diffusion operator, coupled with diffusion tensors specific to each patient, gives an improved model fit over the isotropic P.I. model. The Painter-Hillen model offers an improved fit in almost every case. Upon observing these results, it can be noted that white matter tracts are not present in the scans in the region occupied by the tumour mass, as the growing mass either pushes them out of the way or destroys them. Taking this into account, we implement a "reflected DTI" technique to fill in data that is missing, using this technique to try to improve some of the poorer model fits. This process offers a further improvement to both of the models for certain patients. The benefits of improving the accuracy of the Swanson P.I. model for glioma spread can potentially be implemented into patient therapy. If the Swanson P.I. model is extended to include anisotropy, the hope is that the improved performance of the model will translate into an improvement in patient outcomes.

Mathematical modelling often consists of many successive iterations, with each iteration offering a slight improvement over the last version. This is what we do here with the Painter-Hillen model. In mathematical biology, successive iterations of a model typically include more and more of the biological details. For example, in this case, the Painter-Hillen model is built from the Swanson model through the inclusion of anisotropic diffusion tensors. Additionally, the growth term is modified in an attempt to simulate more realistic tumour growth. Often it is not clear if a new iteration of a model will offer an improvement, as more complicated models are not always better, however the results

of this thesis seem to indicate that the inclusion of the tissue architecture, through anisotropic diffusion, leads to better model fits.

We also propose a framework for the next iteration of this model, which will include a mass effect, as was discussed in Chapter 6. Including mechanical responses of the tissue should reduce the overgrowth at the skull that is seen in some of the simulations. It is our hope that after full development of the mass effect model in two and three dimensions, a further improvement in model fit will be seen.

## 8.2 Mathematical Challenges

In deriving the models contained in this thesis, as well as implementing them, there are a number of mathematical challenges that are encountered. The first challenge that is encountered is the computations of the moments of the von Mises and Fisher distributions. We were not able to find existing formulas for some of these quantities in the literature, and computing them explicitly is not trivial. Applying the divergence theorem allows for straightforward computation, giving us the appropriate formulas for the cancer cell diffusion tensors.

The numerical method for simulating the Painter-Hillen model comes with its own set of challenges, particularly due to the irregular nature of the brain domain. The combination of the fully anisotropic diffusion operator and the irregular boundary makes mass conservation difficult. A careful derivation is required, by taking the double sum (in two dimensions) and triple sum (in three dimensions) over the finite difference scheme. While the computation is a challenge, the resulting conditions are fairly simple to implement.

In Chapter 6, we discuss the derivation of the mass effect. While much

of the theory was existing, it is a challenge to derive a specific model that displays the behaviour we are looking for. Many different stress functions and parameter values were tested before finding a combination that behaved in a realistic manner.

Finally, in Chapter 7 we derive a generalization to the Painter-Hillen model involving a direction-dependent turning rate. There are multiple challenges associated with this derivation, beginning with determining the necessary assumptions on the turning distribution $q$. We make the assumption that the underlying structure of $q$ changes slowly over space such that an appropriate scaling method can be carried out. As compared with the method in Chapter 2, we consider the weighted $L^2$ space $L^2_{\frac{\mu}{q^2}}(V)$. The resulting PDE is not a diffusion model for $p_0(t, \boldsymbol{x})$, but for $p_{0_\mu}(t, \boldsymbol{x})$, i.e., the 0th order approximation to the number of cells turning per unit of time.

## 8.3 Limitations and Extensions

The work contained herein offers a step forward in mathematical modelling of cancer, however there is much more that can be done. The next step of this research will be to automate the model fitting, so that a clinician can automatically fit the Painter-Hillen model for a specific patient, and use this information when designing a treatment plan. The ultimate goal of this work will be for it to be implemented in a clinical setting, following the work of Swanson et al. [6, 44–46, 49, 51–54].

The mass effect model warrants further development. In Chapter 6, we introduce the mass effect model in one dimension, demonstrating both a more classical multiphase model, and a novel cancer-driven invasion model. Ultimately, the mass effect should be implemented in two and three dimensions

using patient data, working towards a better overall data fit. Additionally, there is the potential for updating the DTI-data in response to the increasing pressure as the tumour grows. Using the reflected-DTI as an initial configuration for the DTI-data, the fibres can be advected with the same velocities derived for the cells. This development should be viewed as the next iteration of the Painter-Hillen model.

In Chapter 7, we consider an extension of the Painter-Hillen model where we allow the turning rate to depend on both the cell's orientation and the underlying fibre structure. Here, we consider only the derivation of this model, however further investigation is needed. Considering specific examples of turning distributions and turning rate functions will allow for deeper understanding of the solutions, and exploration of the underlying biological meaning.

Ultimately, the landscape of cancer research is always changing, with survival times growing longer as new therapies are developed all the time. While many like to think of scientists working towards an all-encompassing "cure" for cancer, the reality is that therapeutic innovations march forward incrementally in the work of many researchers around the world. It is our hope that the work contained in this thesis will represent an incremental step forward in the treatment of gliomas.

# Bibliography

[1] D. Hanahan and R.A. Weinberg. The Hallmarks of Cancer. *Cell*, 100: 57–70, 2000.

[2] Breast cancer survival rates, by stage. http://www.cancer.org/cancer/breastcancer/detailedguide/breast-cancer-survival-by-stage. Accessed: 2016-04-24.

[3] Survival rates for prostate cancer. http://www.cancer.org/cancer/prostatecancer/detailedguide/prostate-cancer-survival-rates. Accessed: 2016-04-24.

[4] Survival statistics for brain tumours. http://www.cancerresearchuk.org/about-cancer/type/brain-tumour/treatment/statistics-and-outlook-for-brain-tumours. Accessed: 2016-04-24.

[5] K.J. Painter and T. Hillen. Mathematical modelling of glioma growth: the use of diffusion tensor imagining DTI data to predict the anisotropic pathways of cancer invasion. *J. Theor. Biol.*, 323:25–39, 2013.

[6] K.R. Swanson, E.C. Alvord Jr., and J.D. Murray. A quantitative model

for differential motility of gliomas in grey and white matter. *Cell Proliferation*, 33:317–329, 2000.

[7] A. Jbabdi, E. Mandonnet, H. Duffau, L. Capelle, K.R. Swanson, M. Pelegrini-Issac, R. Guillevin, and H. Benali. Simulation of anisotropic growth of low-grade gliomas using diffusion tensor imaging. *Mang. Res. Med.*, 54:616–624, 2005.

[8] O. Clatz, M. Sermesant, P.Y. Bondiau, H. Delignette, S.K. Warfield, G. Malandain, and N. Ayache. Realistic simulation of the 3D growth of brain tumors in MRI images coupling diffusion with biomechanical deformation. *IEEE Trans. Med. Imag.*, 24(10):1334–1346, 2005.

[9] E. Konukoglu, O. Clatz, P.Y. Bondiau, H. Delignette, and N. Ayache. Extrapolating glioma invasion margin in brain magnetic resonance images: Suggesting new irradiation margins. *Medical Image Analysis*, 14:111–125, 2010.

[10] C. Hogea, C. Davatzikos, and G. Biros. An image-driven parameter estimation problem for a reaction-diffusion glioma growth model with mass effects. *J. Math Biol.*, 56(6):793–825, June, 2008.

[11] P.Y. Bondiau, O. Clatz, M. Sermesant, P.Y. Marcy, H. Delingette, M. Frenay, and N. Ayache. Biocomputing: numerical simulation of glioblastoma growth using diffusion tensor imaging. *Physics in Medicine and Biology*, 53:879–893, 2008.

[12] P. Mosayebi, D. Cobzas, A. Murtha, and M. Jagersand. Tumor invasion margin on the Riemannian space of brain fibers. *Medical Image Analysis*, 16(2):361–373, 2011.

[13] C. Engwer, T. Hillen, M. Knappitsch, and C. Surulescu. A DTI-based multiscale model for glioma growth including cell-ecm interactions. *J. Math. Biol.*, 2014.

[14] P. Kleihues, F. Soylemezoglu, B. Schäuble, B.W. Scheithauer, and P.C. Burger. Histopathology, classification, and grading of gliomas. *Glia*, (15): 211–221, 1995.

[15] J.S. Rao. Molecular mechanisms of glioma invasiveness: The role of proteases. *Nature Reviews: Cancer*, 3:489–501, July 2003.

[16] http://www.abta.org/.

[17] D.N. Louis, H. Ohgaki, O.D. Wiestler, W.K. Cavanee, P.C. Burger, A. Jouvet, B.W. Scheithauser, and P. Kleihues. The 2007 WHO Classification of Tumours of the Central Nervous System. *Acta Neuropathol*, 114:97–109, 2007.

[18] H. Ohgaki, A. Peraud, Y. Nakazato, K. Watanabe, and A. von Deimling. Giant cell glioblastoma. *Pathology and Genetics of Tumours of the Nervous System*, 2000.

[19] J.R. Perry, L.C. Ang, J.M. Bilbao, and P.J. Muller. Clinicopathologic Features of Primary and Postirradiation Cerebral Gliosarcoma. *Cancer*, 75(12):2910–2918, 1995.

[20] Justin D. Lathia, Stephen C. Mack, Erin E. Mulkearns-Hubert, Claudia L. L. Valentim, and Jeremy N. Rich. Cancer stem cells in glioblastoma. *Genes and Development*, 29:1203–1217, 2015.

[21] A.J. Levine. p53, the Cellular Gatekeeper for Growth and Division. *Cell*, 88(3):323–331, 1997.

[22] P.B. Kingsley. Introduction to Diffusion Tensor Imaging Mathematics: Part I. Tensors, Rotations and Eigenvectors. *Concepts in Magnetic Resonance Part A*, 28A(2):101–122, 2006.

[23] D. Purves, G.J. Augustine, D. Fitzpatrick, W.C. Hall, A.S. LaMantia, J.O. McNamara, and L.E. White. *Nneuroscience, 4th edition.* Sinauer Associates, 2008.

[24] B. Kolb and I.Q. Whishaw. *Ffundamentals of Human Neuropsychology, Ffifth Edition.* Worth Publishers, 2003.

[25] A. Giese and M. Westphal. Glioma invasion in the central nervous system. *Neurosurgery*, 39(2):235–252, 1996.

[26] P.G. Gritsenko, O. Ilina, and P. Friedl. Interstitial guidance of cancer invasion. *Journal or Pathology*, 226:185–199, 2012.

[27] P.J. Basser. *Diffusion and diffusion tensor MR imaging: fundamentals. In: Atlas, S.W. (Ed.), Magnetic Resonance Imaging of the Brain and Spine.* Lippincott Williams, Philadelphia, 2008.

[28] T. Hillen and A. Swan. *The diffusion limit of transport equations in biology.* book chapter, CIME lectures, Springer.

[29] D.K. Jones and P.J. Basser. "Squashing Peanuts and Smashing Pumpkins": How Noise Distorts Diffusion-Weighted MR Data. *Magnetic Resonance in Medicine*, 52:979–993, 2004.

[30] E. Berry and A. Bulpitt. Fundamentals of MRI: An Interactive Learning Approach. *Series in Medical Physics and Biomedical Engineering, CRC Press*, 2009.

[31] Public domain. https://commons.wikimedia.org/w/index.php?curid=2130068. Accessed: 2016-04-22.

[32] T.A. Gould. How mri works, HowStuffWorks.com. *How MRI works*.

[33] S.L. Talagala and I.J. Lowe. Introduction to Magnetic Resonance Imaging. *Concepts in Magnetic Resonance*, (3):145–159, 1991.

[34] J. Ainali Own work. Cc by 3.0. https://commons.wikimedia.org/w/index.php?curid=3546051. Accessed: 2016-04-21.

[35] A.L. Alexander, J.E. Lee, M. Lazar, and A.S. Field. Diffusion tensor imaging of the brain. *Neurotherapeutics*, 4(3):316–329, July, 2007.

[36] D.K. Jones and A. Leemans. Diffusion tensor imaging. *Methods in Molecular Biology*, 711:127–144, 2011.

[37] D. Le Bihan, J.F. Mangin, C. Poupon, C.A. Clark, S. Pappata, N. Molko, and H. Chabriat. Diffusion Tensor Imaging: Concepts and Applications. *Journal of Magnetic Resonance Imaging*, 13:534–546, 2001.

[38] Peter C.M. van Zijl Jinsuh Kim Godfrey D. Pearlson Susumu Mori Hangyi, Jiang. Dtistudio: Resource program for diffusion tensor computation and finer bundle tracking. *Computer Methods and Programs in Biomedicine*, 81:106–116, 2006.

[39] P.B. Kingsley. Introduction to Diffusion Tensor Imaging Mathematics: Part II. Anisotropy, Diffusion-Weighting Factors, and Gradient Encoding Schemes. *Concepts in Magnetic Resonance Part A*, 28A(2):123–154, 2006.

[40] H. Hatzikirou, A. Deutsch, C. Schaller, M. Simaon, and K. Swanson. Mathematical modelling of glioblastoma tumour development: A review. *Math. Models Meth. Appl. Sci.*, 15(11):1779–1794, 2005.

[41] Treatment for Gliomas.
http://www.hopkinsmedicine.org/neurology_neurosurgery/centers_clinics/brain_tumor/center/glioma/treatment.html
Accessed: 2016-04-23

[42] N.G. Burnet, S.J. Thomas, K.E. Burton, and S.J. Jefferies. Defining the tumour and target volumes for radiotherapy. *Cancer Imaging*, (4):153–161, 2004.

[43] D. Sanghvi. Post-treatment imaging of high-grade gliomas. *Indian Journal of Radiology and Imaging*, 25(2):102–108, May, 2015.

[44] C.H. Wang, J.K. Rockhill, M. Mrugala, D.L. Peacock, A. Lai, K. Jusenius, J.M. Wardlaw, T. Cloughesy, A.M. Spence, R. Rockne, E.C. Alvord Jr., and K.R. Swanson. Patient-Specific Mathematical Neuro-Oncology: Using a Simple Proliferation and Invasion Tumor Model to Inform Clinical Practice. *Cancer Research*, 69(23):846–856, 2009.

[45] R. Rockne, J.K. Rockhill, M. Mrugala, A.M. Spence, I. Kalet, K. Hendrickson, A. Lai, T. Cloghesy, E.C. Alvord Jr., and K.R. Swanson. Predicting the efficacy of radiotherapy in individual glioblastoma patients *in vivo*: a mathematical modeling approach. *Physics in Medicine and Biology*, 55:3271–3285, 2010.

[46] M.L. Neal, A.D. Tanner, T. Cloke, R. Sodt, S. Ahn, A.L. Baldock, C.A. Bridge, A. Lai, T.F. Cloughesy, M.M. Mrugala, J.K. Rockhill, R.C.

Rockne, and K.R. Swanson. Discriminating Survival Outcomes in Patients with Glioblastoma Using a Simulation-Based, Patient-Specific Response Metric. *PLOSone*, 8(1):1–7, 2013.

[47] A.R. Anderson and M.A. Chaplain. Continuous and discrete mathematical models of tumor-induced angiogenesis. *Bulletin of Mathematical Biology*, 60(5):857–899, 1998.

[48] S.R. McDougall andA.R.A. Anderson, M.A.J. Chaplain, and J.A. Sherratt. Mathematical Modelling of Flow Through Vascular Networks: Iimplications for Tumour-induced Angiogenesis and Chemotherapy Strategies. *Bulletin of Mathematical Biology*, 64:673–702, 2002.

[49] K.R. Swanson, C. Bridge, J.D. Murray, and E.C. Alvord Jr. Virtual and real brain tumors: using mathematical modeling to quantify glioma growth and invasion. *Journal of the Neurological Sciences*, 216:1–10, 2003.

[50] M. Marusic, Z. Bajzer, J.P. Freyer, and S. Vuk-Pavlovic. Analysis of growth of multicellular tumour spheroids by mathematical models. *Cell Proliferation*, 27:73–94, 1994.

[51] K.R. Swanson, R.C. Rostomily, and E.C. Alvord Jr. A mathematical modelling tool for predicting survival of individual patients following resection of glioblastoma: a proof of principle. *British Journal of Cancer*, 98:113–119, 2008.

[52] S. Gu, G. Chakraborty, K. Champley, A.A. Alessio, J. Claridge, R. Rockne, M. Muzi, K.A. Krohn, A.M. Spence, E.C. Alvord Jr., A.R.A. Anderson, P.E. Kinahan, and K.R. Swanson. Applying a patient-specific bio-mathematical model of glioma growth to develop virtual [18F]-

FMISO-PET images. *Mathematical Medicine and Biology*, 29(1):31–48, 2012.

[53] D. Corwin, C. Holdsworth, R.C. Rockne, A.D. Trister, M.M. Mrugala, J.K. Rockhill, R.D. Stewart, M. Phillips, and K.R. Swanson. Toward Patient-Specific, Biologically Optimized Radiation Therapy Plans for the Treatment of Glioblastoma. *PLoS ONE*, 8(11):e79115, 2013.

[54] P.R. Jackson, J. Juliano, A. Hawkins-Daarud, R.C. Rockne, and Kristin R. Swanson. Patient-Specific Mathematical Neuro-Oncology: Using a Simple Proliferation and Invasion Tumor Model to Inform Clinical Practice. *Bulletin of Mathematical Biology*, 77:846–856, 2015.

[55] E. Konukoglu, O. Clatz, P. Bondiau, H. Delignette, and N. Ayache. Extrapolating tumor invasion margins for physiologically determined radiotherapy regions. *MICCIA*, 2006.

[56] K. Painter T. Hillen and A. Swan. Moments of von Mises and Fisher Distributions. *In preparation*.

[57] T. Hillen, K.J. Painter, and M. Winkler. Anisotropic diffusion in oriented environments can lead to singularity formation. *European Journal of Applied Mathematics*, 24(3):371–413, June 2013.

[58] T. Hillen. Transport equations with resting phases. *European Journal of Applied Mathematics*, 14(5):613–636, 2003.

[59] T. Hillen. $M^5$ mesoscopic and macroscopic models for mesenchymal motion. *J. Math. Biol.*, 53(4):585–616, 2006.

[60] T. Hillen and K. Painter. Transport and anisotropic diffusion models for movement in oriented habitats. in M. lewis, P. maini, and S. petrovskii,

editors. *Dispersal, individual movement and spatial ecology: A mathematical perspective*, page 46, Heidelberg, 2012. Springer.

[61] L.E. Malvern. *Introduction to the Mechanics of a Continuous Medium*. Prentice-Hall Series in Engineering of the Physical Sciences, 1969.

[62] L.C. Evans. *Partial Differential Equations*. American Mathematical Society, 2010.

[63] J.C. Robinson. *Infinite-Dimensional Dynamical Systems: An Introduction to Dissipative Parabolic PDEs and the Theory of Global Attractors*. Cambridge University Press, 2001.

[64] W.H. Press, S.A. Teukolsky, W.T. Vetterling, and B.P. Flannery. *Nnumerical Recipes in C*. Cambridge University Press, 1992.

[65] I. Diaz, P. Boulanger, R. Greiner, B. Hoehn, L. Rowe, and A. Murtha. An Automatic Brain Tumor Segmentation Tool. *Conf. Proc. IEEE Eng. Med. Biol. Soc.*, pages 3339–3342, 2013.

[66] M.B. Salah, I. Diaz, R. Greiner, P. Boulanger, B. Hoehn, and A. Murtha. Fully Aautomated Brain Tumor Segmentation using two MRI Modalities. *Chapter in: Advances in Visual Computing, Springer Berlin Heidelberg*, 27:30–39, 2013.

[67] D. Cobzas, P. Mosayebi, A. Murtha, and M. Jagersand. Tumor invasion margin on the Riemannian space of brain fibers. *MICCAI*, 2009.

[68] N. Just. Improving tumour heterogeneity MRI assessment with histograms. *British Journal of Cancer*, 111(12):2205–2213, 2014.

[69] Gerda de Vries, Thomas Hillen, Mark Lewis, Johannes Müller, and Birgitt Schönfisch. *A Course in Mathematical Biology: Quantitative Modeling with Mathematical and Computational Methods*. SIAM, 2006.

[70] G. Bertorelle, A. Benazzo, and S. Mona. ABC as a flexible framework to estimate demography over space and time: some cons, many pros. *Molecular Ecology*, 19:2609–2625, 2010.

[71] S. Mori and P.C.M. van Zijl. Fiber tracking: principles and strategies - a technical review. *NMR in Biomedicine*, (15):468–480, 2012.

[72] C. Lebel and C. Beaulieu. Longitudinal Development of Human Brain Wiring Continues from Childhood into Adulthood. *The Journal of Neuroscience*, 31(30):10937–10947, 2011.

[73] S.V. Patankar. *Numerical Heat Transfer and Fluid Flow*. MgGraw-Hill Book Company: series in computational methods in mechanics and thermal sciences, 1980.

[74] W. Hundsdorfer and J.G. Verwer. *Numerical Solution of Time-Dependent Advection-Diffusion-Reaction Equations*. Springer Series in Computational Mathematics, 2003.

[75] Icru. Prescribing, Recording and Reporting Photon Beam Therapy. Report 50. Bethesda, MD: International Commission on Radiation Units and Measurements. 1999.

[76] H.M. Byrne, J.R. King, D.L.S. McElwain, and L. Preziosi. A Two-Phase Model of Solid Tumour Growth. *Applied Mathematics Letters*, 16:567–573, 2002.

[77] D. Ambrosi and L. Preziosi. On the closure of mass balance models for tumor growth. *Mathematical Models and Methods in Applied Sciences*, 12 (5):737–754, 2002.

[78] L. Preziosi and A. Tosin. Multiphase modelling of tumour growth and extracellular matrix interaction: mathematical tools and applications. *Journal of Mathematical Biology*, 58:625–656, 2008.

[79] L. Preziosi and G. Vitale. A multiphase model of tumor and tissue growth including cell adhesion and plastic reorganization. *Mathematical Models and Methods in Applied Science*, 21(9):1901–1932, 2011.

[80] L. Preziosi and G. Vitale. Mechanical Aspects of Tumour Growth: Multiphase Modelling, Adhesion, and Evolving Natural Configurations. *Oxford University Press.*

[81] S. Astanin and L. Preziosi. Multiphase Models of Tumour Growth. *Chapter in: Selected Topics in Cancer Modeling*, pages 1–31, 2008.

[82] P. Macklin and J. Lowengrub. Nonlinear simulation of the effect of microenvironment on tumor growth. *Journal of Theoretical Biology*, 245: 677–704, 2007.

[83] S.M. Wise, J.S. Lowengrub, H.B. Frieboes, and V. Cristini. Three-dimensional multi species nonlinear tumor growth - I Model and numerical method. *Journal Theoretical Biology*, 253:524–543, 2008.

[84] H. Youssefpour, X. Li, A.D. Lander, and J.S. Lowengrub. Multispecies model of cell lineages and feedback control in solid tumors. *Journal Theoretical Biology*, 304:39–59, 2012.

[85] Y.C. Fung. *Biomechanics Mechanical Properties of Living Tissues*. Springer, 1993.

[86] http://large.stanford.edu/courses/2007/ph210/rosen2/.

[87] W. Hundsdorfer. Numerical Solution of Advection-Diffusion-Reaction Equations. *Lecture notes, Thomas Stieljes Institute*, 2000.